Учреждение Российской академии наук
ИНСТИТУТ ЯДЕРНЫХ ИССЛЕДОВАНИЙ РАН

ТРУДЫ XII МЕЖДУНАРОДНОГО СЕМИНАРА ПО ЭЛЕКТРОМАГНИТНЫМ ВЗАИМОДЕЙСТВИЯМ ЯДЕР

ЭМИН-2009

Москва, Сентябрь 17-20, 2009

Москва-2010

RUSSIAN ACADEMY OF SCIENCES
INSTITUTE FOR NUCLEAR RESEARCH

PROCEEDINGS OF THE XII INTERNATIONAL SEMINAR ON ELECTROMAGNETIC INTERACTIONS OF NUCLEI

EMIN-2009

Moscow, September 17-20, 2009

Moscow 2010

УДК 539.17

Труды XII Международного семинара
по электромагнитным взаимодействиям ядер
ЭМИН-2009

В сборник включены доклады, представленные на XII Международный семинар по электромагнитным взаимодействиям ядер EMIN-2009 и подготовленные авторами к публикации.

Proceedings of the XII International Seminar
on Eletctromagnetic Interactions of Nuclei
EMIN-2009

Materials of the XII International Seminar EMIN-2009 (including the talk presentations) one can find at the site http://www.inr.ac.ru/~pnlab/emin2009/Welcome.html

ISBN 978-5-94274-127-3

Contents

MESON PHOTOPRODUCTION AT GRAAL

C. Schaerf for the Graal collaboration*
Dipartimento di Fisica, Università degli Studi di Roma "Tor Vergata" and
INFN – Sezione di Roma Tor Vergata

The Graal collaboration has measured beam polarization asymmetries in the photoproduction of mesons on protons and neutrons using the linearly polarized and tagged gamma-ray beam produced by the backward Compton scattering of laser light on the high energy electrons circulating in the ESRF storage ring. The tagged gamma-ray spectrum covers the range 600-1487 MeV and has an energy resolution of 16 MeV (FWHM). Its polarization is close to 1 at the highest energy and remains higher than 0.6 on the entire spectrum using a Green (514.5 nm) and UV (351.1 nm) laser line.

The beam characteristic and the experimental apparatus are described in reference[i].

Beam polarization asymmetries have been produced in the reactions:

$\gamma + p \rightarrow p + \pi^\circ$

$\gamma + p \rightarrow n + \pi+$

$\gamma + p \rightarrow p + \eta$

$\gamma + n \rightarrow n + \pi^\circ$

$\gamma + n \rightarrow n + \eta$

$\gamma + n \rightarrow p + \pi^-$

$\gamma + p \rightarrow K^+ + \Lambda$

$\gamma + p \rightarrow K^+ + \Sigma^\circ$

In the last two reactions we have also measured double-polarization beam-recoil observables.

We have studied the reactions on the proton with a liquid hydrogen target and those on the neutron with liquid deuterium. We have detected the two reacting particles in the final state and for the deuterium we have treated, with the Impulse Approximation (IA), the proton as a spectator and the target neutron as a quasi-free particle. In the same deuterium runs we have collected data on the quasi-free proton treating the neutron as a spectator. We have compared the asymmetries on the free proton (in Hydrogen) with those on the quasi-free proton (in Deuterium) and those on the quasi-free proton with those on the quasi-free neutron. In this way we can reasonably assume that in the reactions where the asymmetries on the free and quasi-free protons are in good agreement, the asymmetries on the quasi-free neutron can be assumed to be a very good approximations to those on the free neutron.

The data on the free protons have been analyzed selecting the events when the two particles in the final state satisfy the constraints of a two-body kinematics. For those on the deuteron we have used a similar procedure with less stringent constraints. For the events with a π° or an η in the final state the first requirement has been that the invariant mass of the two decay photons is close to that of a π° or an η respectively.

In fig. 1a we have compared the coplanarity of the two particles in the final state for the free and quasi free proton. In fig. 1b we have the calculated distribution of the Fermi momentum of the spectator before and after the imposition of the two-body kinematical constraints for the reaction on quasi free nucleons.

---

* V. Bellini, J. P. Bocquet, L. Casano, A. D'Angelo, R. Di Salvo, A. Fantini, D. Franco, G. Gervino, F. Ghio, G. Giardina, B. Girolami, A. Giusa, A. S. Ignatov, A. M. Lapik, P. Levi Sandri, A. Lleres, F. Mammoliti, G. Mandaglio, M. Manganaro, D. Moricciani, A. N. Mushkarenkov, V. G. Nedorezov, C. Randieri, D. Rebreyend, N. V. Rudnev, G. Russo, C. Schaerf, M. L. Sperduto, M. C. Sutera, A. Turinge and V. Vegna.

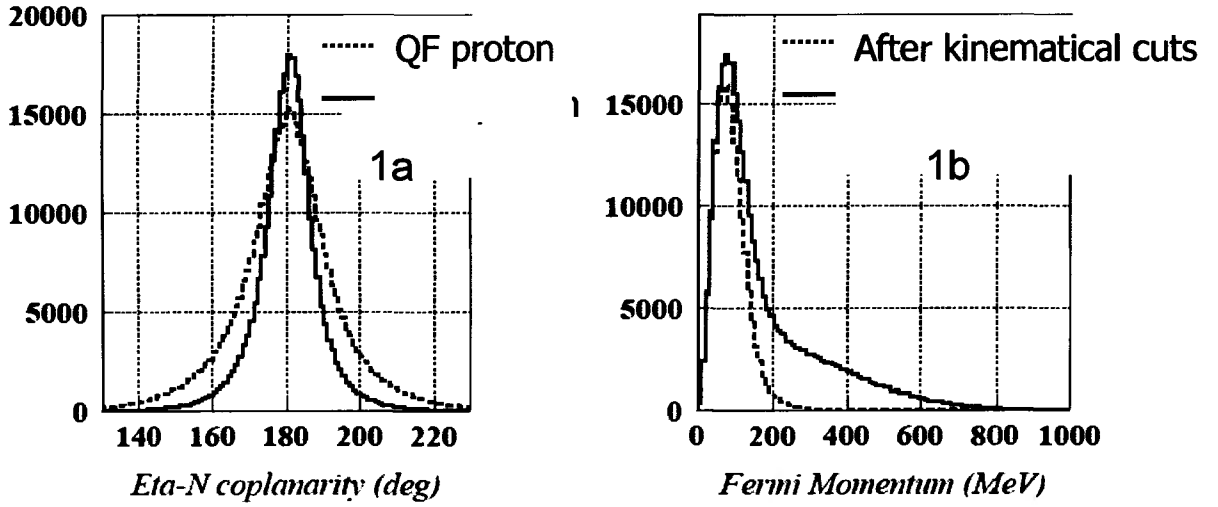

Fig. 1. a) coplanarity of the two particles in the final state for free and quasi-free proton; b) Fermi momentum of the spectator calculated before and after the kinematical cuts.

In Fig. 2 we have indicated the invariant mass of the two photons around the η mass before and after the quasi-two body kinematical cuts and our estimate of the background from competing processes.

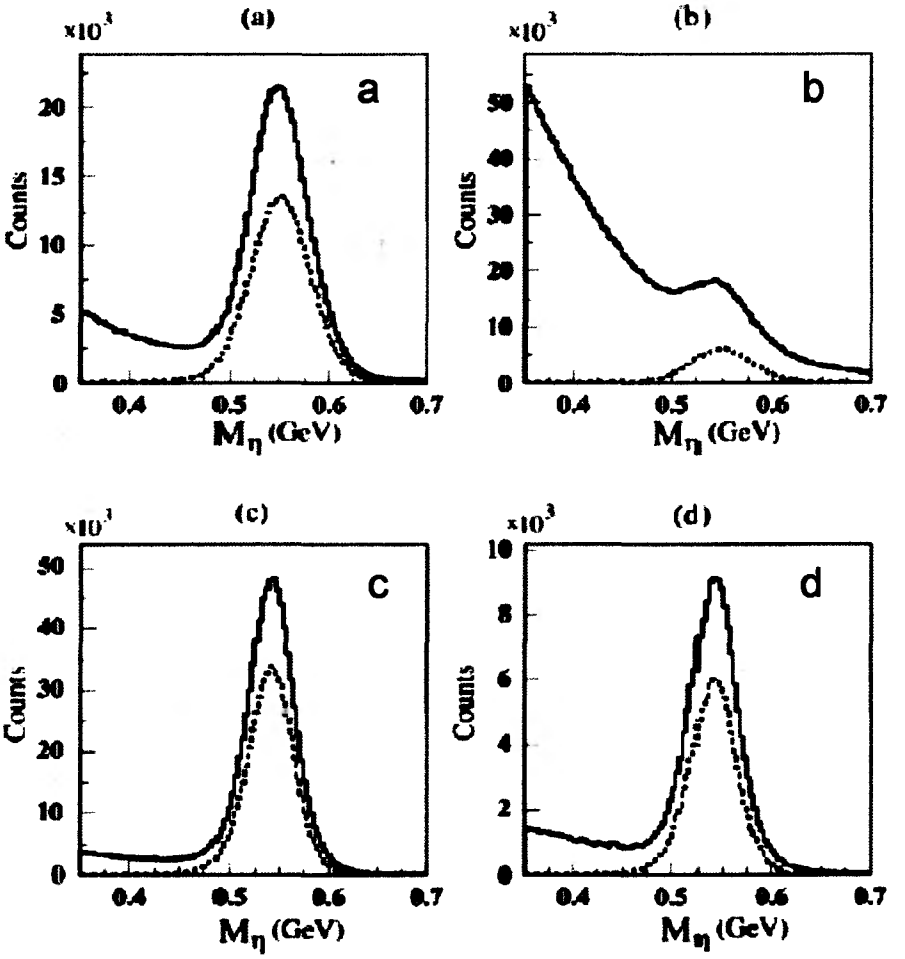

Fig. 2. The invariant mass of the two-photon system around the η mass calculated before (solid curve) and after (dotted curve) the two-body kinematical cuts. a) proton in the BGO; b) neutron in the BGO; c) proton in the forward direction; d) neutron in the forward direction.

In the next figures (3-5) we show the beam polarization asymmetry, Σ, for η meson photoproduction reactions in Hydrogen (free proton) and Deuterium (quasi-free proton and quasi-free neutron).

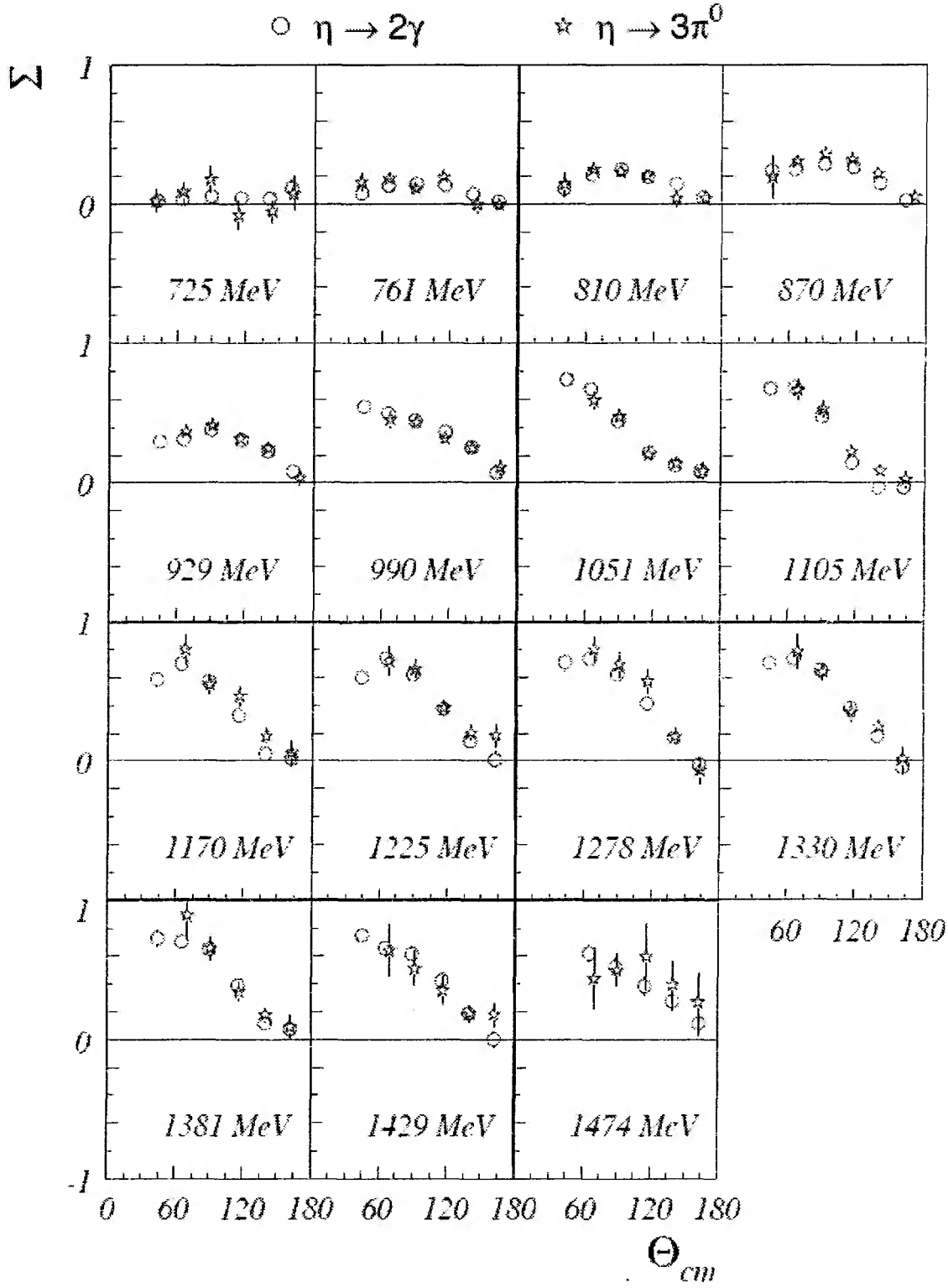

Fig. 3. Beam polarization asymmetries, Σ, for the photoproduction of η on the proton. $\gamma + p \rightarrow p + \eta$. The results obtained for the two main neutral decay channels are compared. The 3π° decay requires the detection of six photons in the BGO: η → 3π° → 6γ.

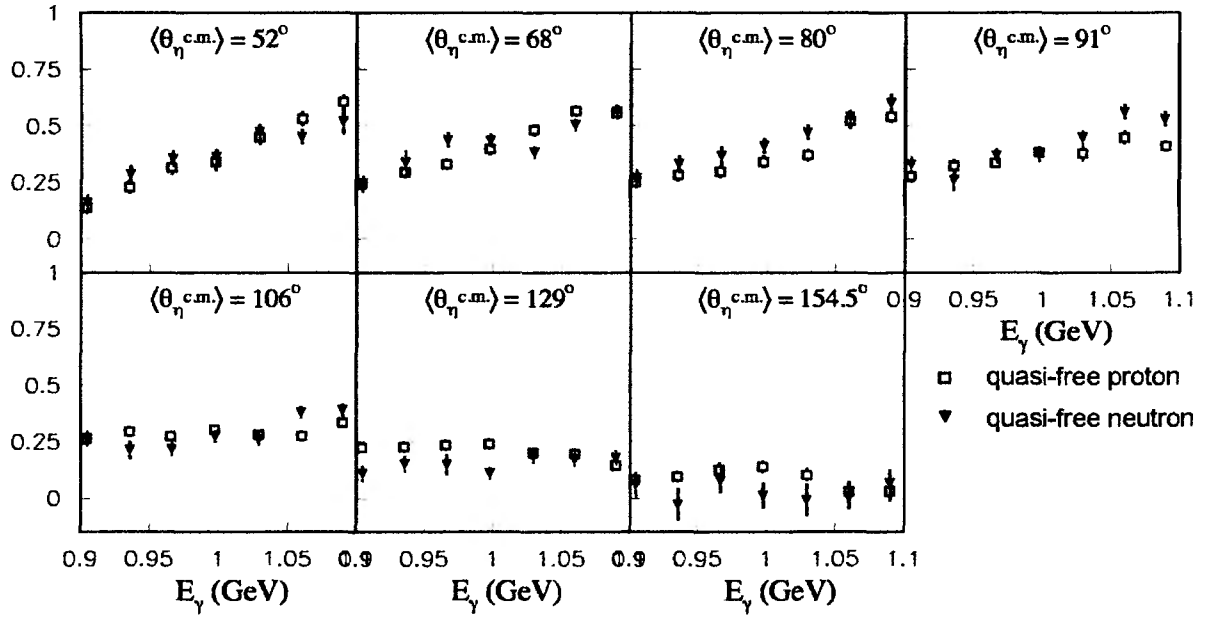

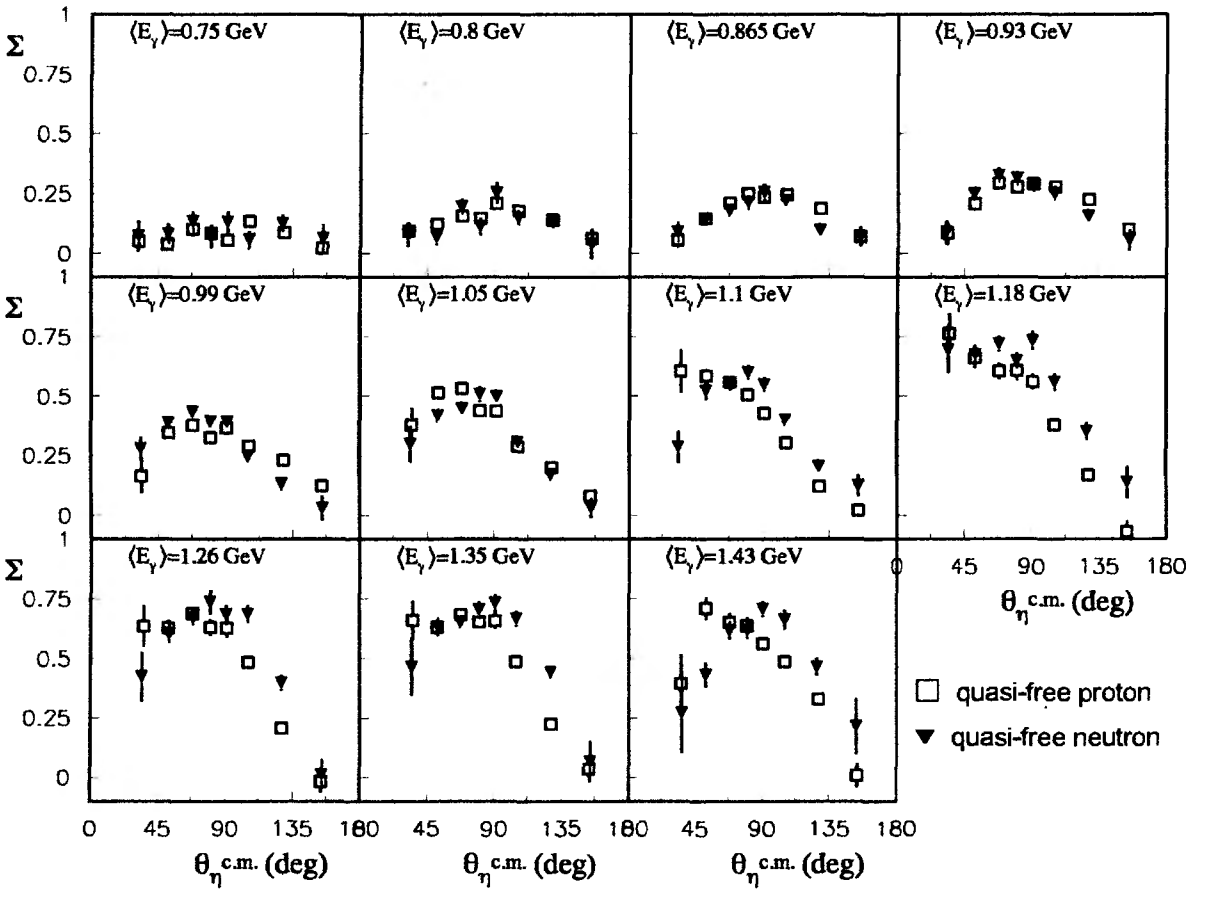

Fig. 5. Beam polarization asymmetries for the photoproduction of η on quasi-free proton and quasi-free neutron in the deuteron. Open squares proton, full inverted triangles neutron. The data are presented for different gamma-ray energies as a function of the CM angle of the η. The neutron asymmetries appear more symmetrical around 90°.

The beam polarization asymmetries for the photoproduction of π° on the proton and the neutron are indicated in fig. 6 at constant CM angles as a function of the gamma-ray energy.

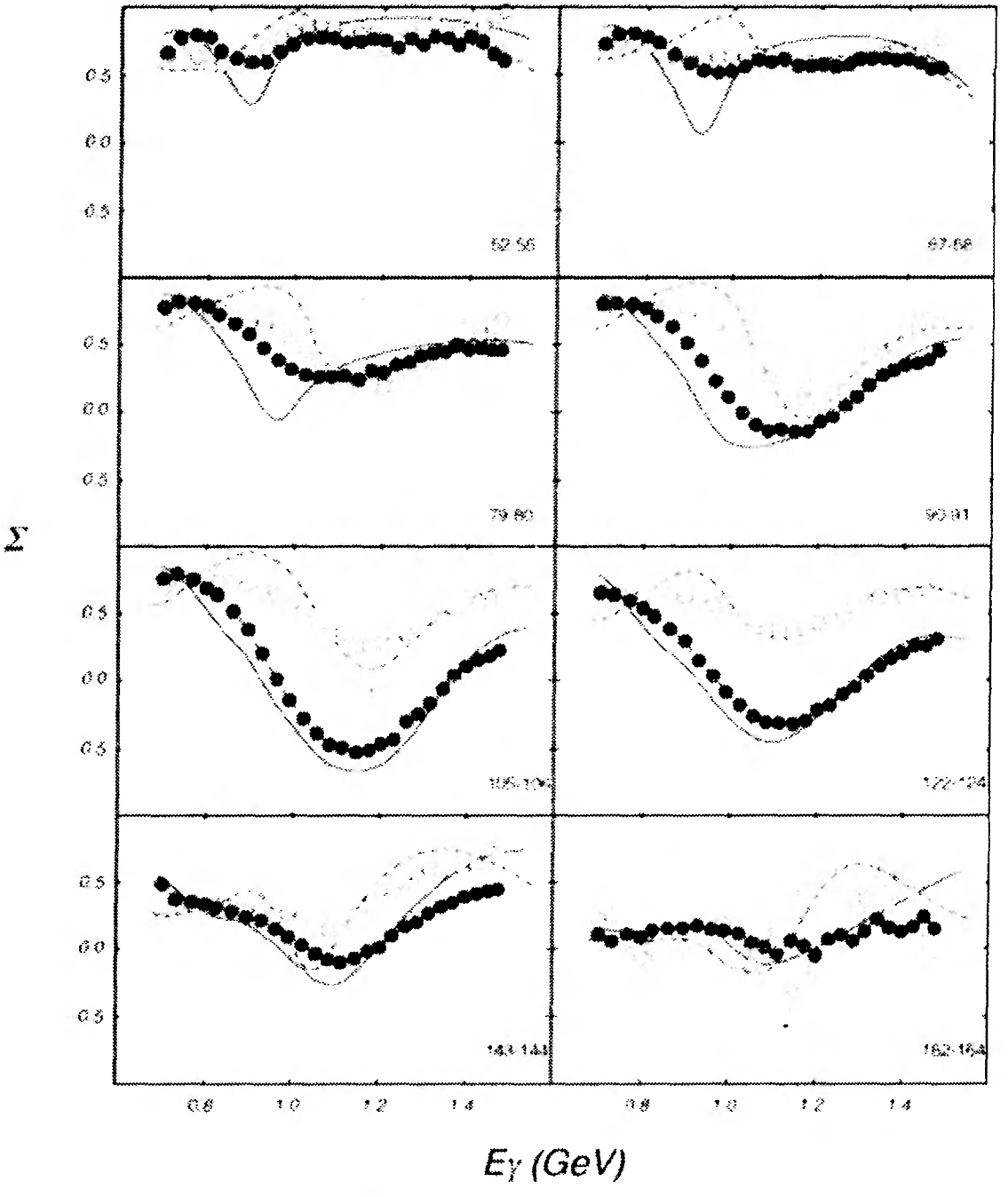

Fig. 6. Σ beam asymmetry for the π° photoproduction on the quasi-free proton (full dots) and quasi-free neutron (open dots) as a function of the photon energy at fixed π° center-of-mass angles, compared to the results of partial-wave analysis from modified MAID2007[ii] (full line: proton, dashed line: neutron). Where not visible, errors bars lie within the data point spots.

In fig. 7 are reported our very preliminary results for the beam-polarization asymmetries for the reaction $\gamma + p \rightarrow \omega + p$. We present the results for the radiative and charged ω decay modes: $\omega \rightarrow \pi^\circ + \gamma$ (blue full circles) and $\omega \rightarrow \pi^\circ + \pi^+ + \pi^-$ (red inverted full triangles). These two results have been obtained with different selection criteria for the events and therefore are statistically independent and can be combined to give our global result. For comparison we present also the results of one previous experiment[iii] and a previous independent analysis[iv] of a subset of Graal data.

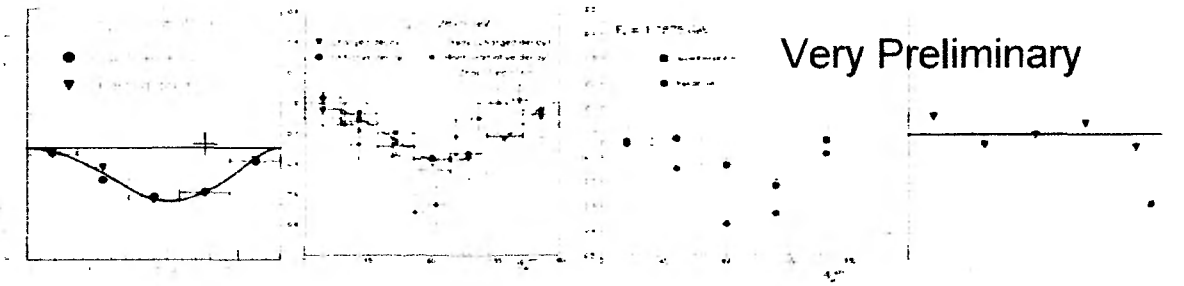

Fig. 7. Angular distribution of the beam-polarization asymmetries for ω photoproduction on the proton at a gamma-ray energy of 1.2875 GeV. Our results are compared with those of previous experiments[3] and a previous analysis of a subset of Graal data[4]. The theoretical curves have been provided by Q. Zhao[6].

In fig. 8 we report our very preliminary results for the beam-polarization asymmetry for the photoproduction of π^- p on the neutron.

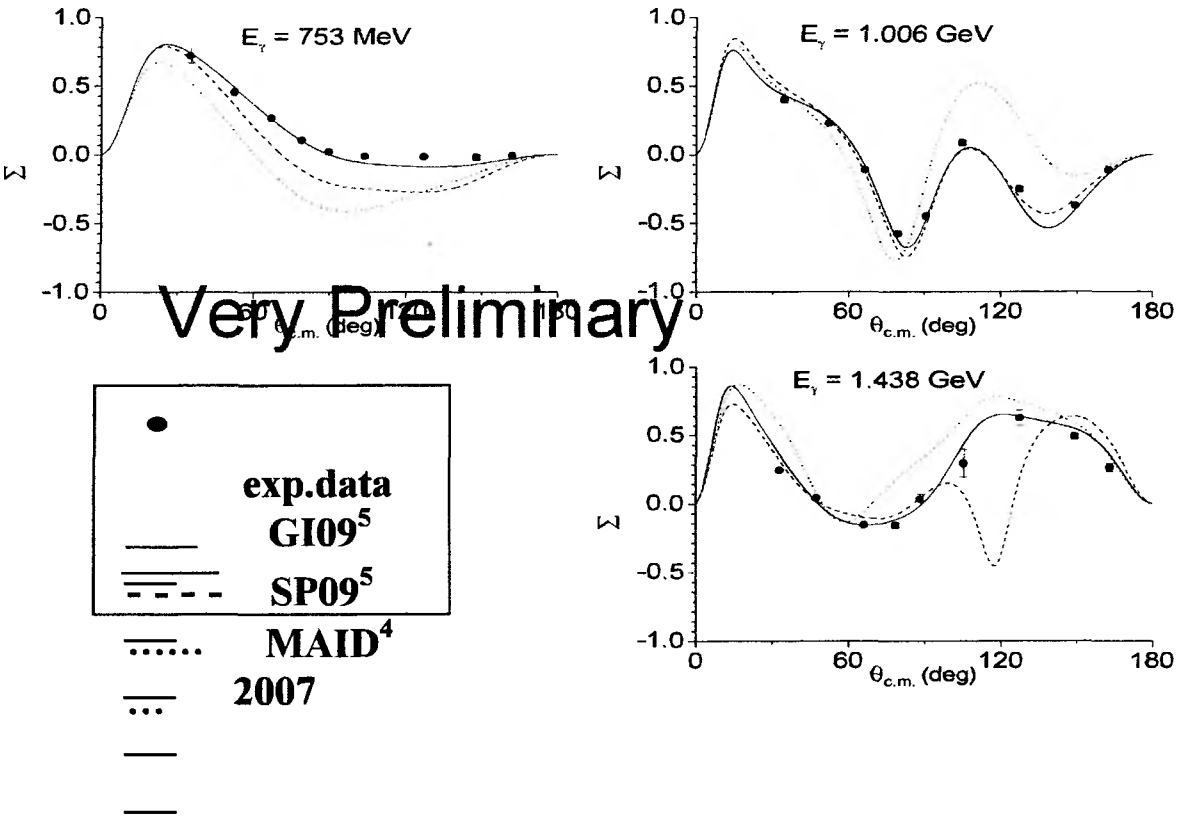

Fig. 8. Preliminary results for the beam-polarization asymmetries for the reaction $\gamma + n \rightarrow \pi^- + p$ are compared with three theoretical models.

---

[i] O. Bartalini *et al.*, Eur. Phys. J. A **26**, 399 (2005).
[ii] http://wwwkph.kph.uni-mainz.de/MAID//maid2007/polariz.html
[iii] F. Klein *et al.*, Phys. Rev. D **78**, 117101 (2008)
[iv] J. Ajaka *et al*,. Phys. Rev. Lett. **96**, 132003 (2006).
[5] http://gwdac.phys.gwu.edu/analysis/pr_analysis.html
[6] Q. Zhao, Phys. Rev. C **63**, 25203 (2001) and private communication.

RECENT RESULTS FROM THE CB@MAMI COLLABORATION

Evangeline J. Downie[1] for the A2 Collaboration

[1] *Institut für Kernphysik, Johannes Gutenberg Universität, Mainz, Germany*

1 Introduction & motivation

Due to quark confinement, there exists no way to dissect the nucleon and directly study its internal architecture and components. Instead, the excitation spectra of protons and neutrons are carefully measured and deconstructed into their constituent excitations, thereby revealing the underlying structure. Presently, there is insufficient experimental data available to fully constrain this decomposition process. Therefore, in order to unambiguously determine exactly which resonances contribute to the nucleon excitation spectrum, it is imperative to measure not simply differential cross sections, but also multiple single and double polarisation observables over a variety of outgoing channels.

In order to achieve such an experimental programme, one requires a polarised beam and target and the ability to determine the polarisation of the recoiling nucleus. With the successful construction of the Mainz Frozen Spin Target, the CB@MAMI detector setup now satisfies all of these criteria in addition to having a high flux photon beam, which provides a well understood initial state, and a 4π highly segmented detector system with well developed particle identification capability. The combination of this high photon flux beam and large acceptance detector is ideal for the measurement of rare final states and those involving a high photon multiplicity.

2 Experimental apparatus

2.1 Photon beam

MAMI C consists of a three stage cascaded racetrack microtron system followed by the Harmonic Double-Sided Microtron (HDSM). It can provide an electron beam with 100% duty cycle, current of up to 100 μA and electron polarisation of 85%. The HSDM designed output energy of 1508.4 MeV has been surpassed by the optimisation of the system as a whole and, as of 16th September 2009, MAMI can supply an electron beam of up to 1604 MeV.

The A2 photon beam is derived from the production of Bremsstrahlung photons during the passage of the MAMI electron beam through a thin radiator. The resulting photons can be circularly polarised, when using the polarised electron beam, or linearly polarised, in the case of a crystalline radiator. The degree of polarisation achieved is dependent on the energy of the incident photon beam (E_0) and the energy range of interest, but currently peaks at $\sim$75% for linear polarisation (Fig. 1) and $\sim$85% for circular polarisation (Fig.1). The maximum degree of linear polarisation should be further improved by 5 to 10% by the end of 2009 when the collimation and beam monitoring systems will be optimised for MAMI-C during the installation of the Frozen Spin Target. The Glasgow Photon Tagger (Fig 2) provides energy tagging of the photons by detecting the post-radiating electrons and can determine the photon energy with a resolution of 2 to 4 MeV depending on the incident beam energy, with a single-counter time resolution $\sigma_t = 0.117$ ns [1]. Each counter can operate reliably to a rate of $\sim$1 MHz, giving a photon flux of 2.5×10^5 photons per MeV. Photons can be tagged in the momentum range from 4.7 to 93.0% of E_0.

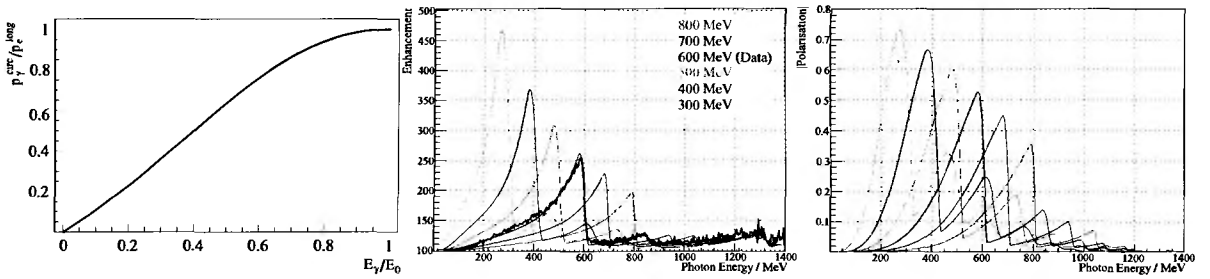

Figure 1: Left: Helicity transfer from the electron to the photon beam as function of the energy transfer. The MAMI beam polarisation is $P_e \approx 85\%$. Centre and right: Linear polarisation available with the current collimation system for a variety of crystal orientations. The thin black lines are data obtained during recent MAMI-C runs.

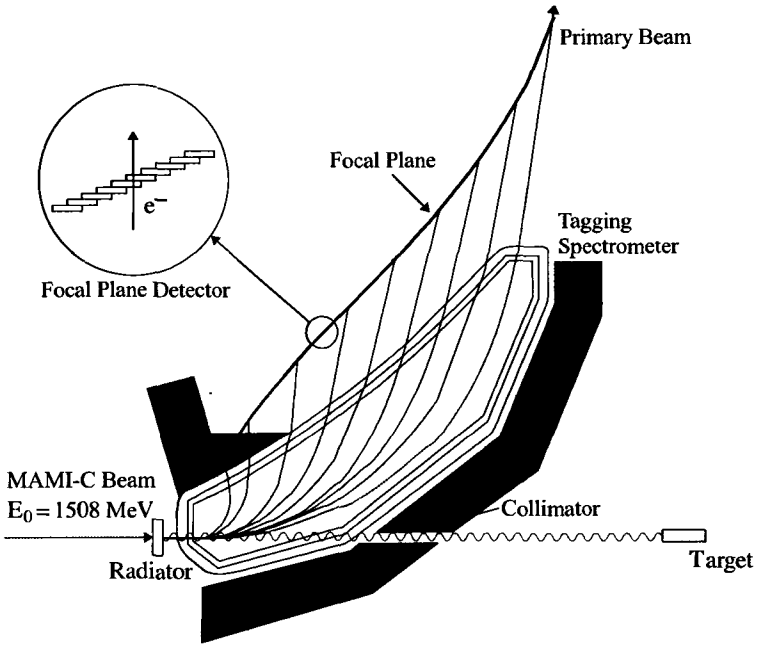

Figure 2: The Glasgow photon tagging spectrometer.

To augment the standard focal plane detector system and make use of the Tagger's intrinsic energy resolution of 0.4 MeV (FWHM), there exists a scintillating fibre detector ('Tagger Microscope') that can improve the energy resolution by a factor of about 6 for a ~100 MeV wide region of the focal plane (dependent on its position) [2].

2.2 Crystal Ball detector system

The central detector system consists of the Crystal Ball calorimeter combined with a barrel of scintillation counters for particle identification and two coaxial multiwire proportional counters for charged particle tracking. This central system provides position, energy and timing information for both charged and neutral particles in the region between 21° and 159° in the polar angle (θ) and over almost the full azimuthal (ϕ) range. At forward angles, less than 21°, reaction products are detected in the TAPS forward wall. The full, almost hermetic, detector system is shown schematically in Fig. 3.

The Crystal Ball detector (CB) is a highly segmented 672-element NaI(Tl), self-triggering photon spectrometer constructed at SLAC in the 1970's. Each element is a truncated triangular

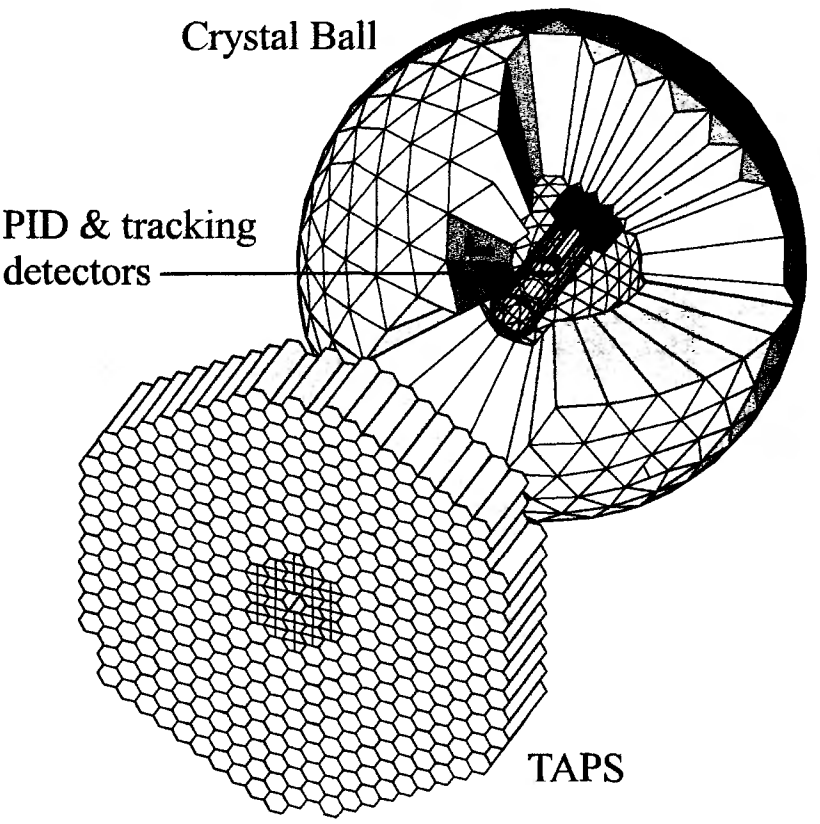

Figure 3: The A2 detector setup: The Crystal Ball calorimeter, with cut-away section showing the inner detectors, and the TAPS forward wall.

pyramid, 41 cm (15.7 radiation lengths) long. The Crystal Ball has an energy resolution of $\Delta E/E = 0.020 \cdot E[GeV]^{0.36}$, and angular resolutions of $\sigma_\theta = 2 \ldots 3^\circ$ and $\sigma_\phi = \sigma_\theta / \sin\theta$ for electromagnetic showers [3].

In order to distinguish between neutral and charged particles species detected by the Crystal Ball, the system is equipped with PID2, a barrel detector of twenty-four 50 mm long, 4 mm thick scintillators, arranged so that each PID2 scintillator subtends an angle of 15° in ϕ. By matching a hit in the PID2 with a corresponding hit in the CB, it is possible to use the locus of the $\Delta E, E$ combination to identify the particle species (Fig. 4). This is primarily used for the separation of charged pions, electrons and protons. The PID2 covers from 15° to 159° in θ.

The excellent CB position resolution for photons stems from the fact that a given photon triggers several crystals and the energy-weighted mean of their positions locates the photon position to better than the crystal pitch. For charged particles which deposit their energy over only one or two crystals, this is not so precise. Here the tracks of charged particles emitted within the angular and momentum acceptance of the CB detector will be reconstructed from the coordinates of point of intersections of the tracks with two coaxial cylindrical multiwire proportional chambers (MWPCs) with cathode strip readout. The expected angular resolution (rms) is ~2° in the polar emission angle θ and ~3° in the azimuthal emission angle ϕ.

2.3 TAPS Forward Wall

The TAPS forward wall is composed of 384 BaF_2 elements, each 25 cm in length (12 radiation lengths) and hexagonal in cross section, with a diameter of 59 mm. The face of every TAPS element is covered by a 5 mm thick plastic veto scintillator. The single counter time resolution is

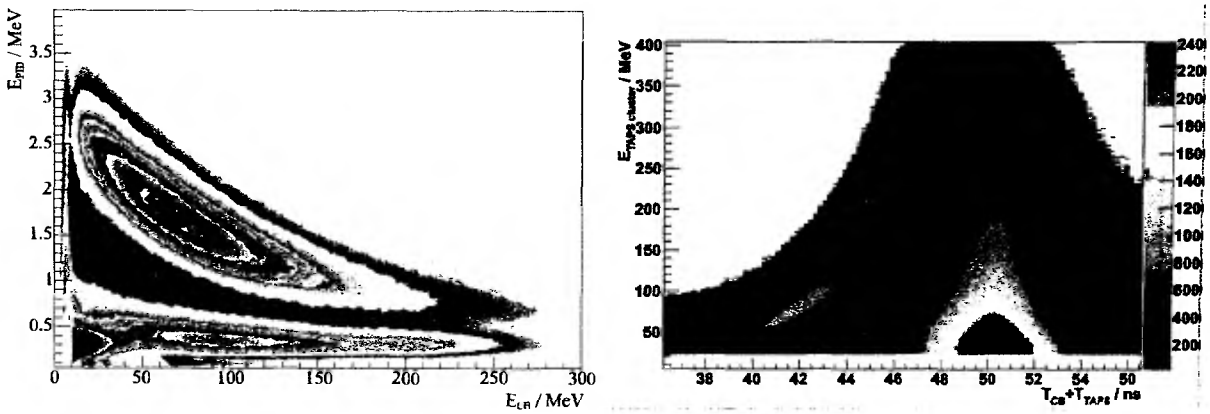

Figure 4: Left: A typical $\Delta E/E$ plot from the Crystal Ball and the PID2 detector. The upper curved region is the proton locus, the lower region contains the pions and the peak towards the origin contains mostly electrons. Right: A typical Time of Flight identification plot from TAPS, the vertical band being photons, the curved band to the left, nucleons.

$\sigma_t = 0.2$ ns, the energy resolution can be described by $\Delta E/E = 0.018 + 0.008/E[GeV]^{0.5}$. The angular resolution in the polar angle is better than 1°, and in the azimuthal angle it improves with increasing θ, being always better than $1/R$ radian, where R is the distance in centimetres from the central point of the TAPS wall surface to the point on the surface where the particle trajectory meets the detector [3]. The TAPS readout was custom built for the beginning of the CB@MAMI program and is effected in such a way as to allow particle identification by Pulse Shape Analysis (PSA), Time Of Flight (TOF) (see Fig. 4) and $\Delta E/E$ methods (using the energy deposit in the plastic scintillator to give ΔE). The two inner rings of 18 BaF_2 elements have been replaced recently by 72 $PbWO_4$ crystals each 20 cm in length (22 radiation lengths). The higher granularity improves the rate capability as well as the angular resolution. The crystals are operated at room temperature. The energy resolution for photons is similar to BaF_2 under these conditions [4].

3 Recent Results

3.1 Photoproduction of π^0 mesons

The photoproduction of π^0 mesons occurs with almost equal probability on both protons and neutrons over the whole volume of the nucleus, making it an ideal probe of the nuclear matter distribution. The cross section for coherent π^0 photoproduction is then almost a Fourier Transform of the mass distribution, with the position of the minima giving the matter radius of the nucleus. At low outgoing pion energies, the probability of final state interactions (FSI) between the outgoing pion and the residual nucleus is reduced and handling of the FSI effects is more straightforward. A measurement of π^0 photoproduction was performed for a series of nuclei, including ^{12}C, ^{16}O, ^{40}Ca and ^{208}Pb [5].

3.1.1 Incoherent π^0photoproduction

It was found that it was possible to separate the incoherent π^0 photoproduction cross section by tagging on the 4.4 MeV photon produced by the de-excitation of the 2+ excited state of ^{12}C. This was the first ever study to produce differential cross sections for the production of a

specific excited state, and the data, which are reported in [6], are sensitive to the propagation of the Δ in medium and matter transition form factors.

3.1.2 Coherent π^0 photoproduction

With the ability to isolate the production of these excited states, comes the ability to produce an incredibly clean sample of purely coherent events. These events have been used to produce differential cross sections for the coherent production of π^0 mesons on ^{208}Pb. The careful analysis of this data in combination with the use of two different models of final state interactions allows the neutron skin thickness of ^{208}Pb to be determined with an accuracy of $\sim$0.05 fm [5]. This information is important for the equation of state of neutron rich matter and also has astronomical significance in the physical description of neutron stars and their possible cooling mechanisms.

3.1.3 Radiative π^0 photoproduction

Due to the incredibly short lifetime of the $\Delta^+(1232)$, it is impossible to measure its static electromagnetic properties in the normal way used for longer-lived particles. Instead, the resulting large Breit Wigner width of the $\Delta(1232)$ makes it is possible to create a Δ at the upper end of this mass range which can then decay to a Δ of lower mass, with the emission of a photon. The lower-mass Δ subsequently decays to a nucleon and a pion, giving an overall process of $\gamma p \rightarrow \gamma\pi N$. The $\Delta \rightarrow \Delta\gamma$ process amplitude is sensitive to the magnetic dipole moment of the Δ (μ_{Δ^+}). However, as the same final state can also be reached by Bremsstrahlung from the in- and outgoing charged particles, models of the process [7, 8] must be used to extract the contribution due to the $\Delta \rightarrow \Delta\gamma$ transition and ultimately extract μ_{Δ^+}. After a proof-of-principle measurement [9], the CB@MAMI collaboration acquired 800 hours of data on this reaction in 2004/5.

The separation of the signal from background in this reaction is an experimental challenge as the background processes ($\gamma p \rightarrow p\pi^0$ and $\gamma p \rightarrow p\pi^0\pi^0$) have cross sections more than two orders of magnitude greater than the signal of interest. The separation of the the signal from the background has been achieved and a collection of $\sim$30,000 events recorded, with the production of differential cross sections [10] of much higher statistical significance than the proof-of-principle measurement and the first ever determination of the linearly polarised photon asymmetry [11]. The increased precision cross section measurement and the measurement of additional observables are key steps in the constraint of the theory and an extraction of the magnetic dipole moment of the $\Delta^+(1232)$.

3.2 Photoproduction and decay of the η and η' mesons

As the $S_{11}(1535)$ is the only major resonance involved in η production in the region around its threshold and peak, the analysis of η production in this region acts as a filter to enable the study of this specific resonance despite the presence of several other broad overlapping resonances. The photoproduction and decay amplitudes of the η are described in Chiral Perturbation Theory (ChiPT). Due to its isospin breaking nature, the decay $\eta \rightarrow 3\pi^0$, has an amplitude proportional to the mass difference between the up and down quark in the lowest order of ChiPT. This term can be accessed by looking at the slope parameter α of the reaction Dalitz plot. The slope parameter can be obtained by plotting all of the entries in the Dalitz plot as a function of their distance from the centre of the Dalitz plot. For pure phase space decays, this would give a perfectly flat distribution. When this phase-space result is passed through the detector

acceptance, it acquires some slope and the ratio of the measured Dalitz plot to this phase-space simulation passed through the detector acceptance gives the measured slope parameter. This was measured with incredibly high precision with both MAMI B [12] and MAMI C [3] data.

The ratio of $\eta' \to 3\pi^0$ to $\eta' \to \eta\pi^0\pi^0$, the primary decays of the η', gives information on $\eta\pi^0$ mixing, and the dalitz plots of these reactions contain information on the $\pi\pi$ and $\pi\eta$ scattering lengths. Other, rarer, decays of the η and η' test the higher orders of ChiPT. Rare η decays under study currently include $\eta \to e^+e^-\gamma, 4\pi^0, \pi^0\gamma, 2\pi^0\gamma, 3\pi^0\gamma$. The decays $\eta' \to \pi^0e^+e^-$, $\eta' \to 3\gamma$ and $\eta' \to 4\pi^0$ are currently under investigation for their role in CP symmetry violation. In all, it is expected that the CB@MAMI detector system will measure $3 \times 10^8\eta$ and $3 \times 10^6\eta'$ within only a few years, providing an "eta factory" for the investigation of precision observables and fundamental symmetry breaking.

3.3 Photoproduction of $\eta\pi^0$ in the region of the $D_{33}(1700)$

A recent high precision measurement of $\eta\pi^0$ photoproduction by the A2 Collaboration [13] has been very well described by a very simple model including only the $D_{33}(1700)$ resonance [14]. This implies that, in $\eta\pi^0$ photoproduction, the $D_{33}(1700)$ shows the same dominance as the $P_{33}(1232)$ in pion photoproduction and the $S_{11}(1535)$ in η production. Underneath the dominant $D_{33}(1700)$ contribution, are believed to lie other contributions from several P-wave resonances. In order to extract the contributions of these less dominant resonances, detailed angular distributions and polarisation measurements must be made, for which the new Frozen Spin Target will be an essential and valuable tool.

4 Future prospects

4.1 Frozen-spin target

In order to perform double polarisation experiments with the CB@MAMI detector setup, it was decided to build a high density solid state frozen spin target which would allow the performance of experiments on polarised protons and deuterons using Butanol and deuterated Butanol as the target material. To achieve the low temperatures required to produce the desired polarisation degree of of 90% for protons and 80% for the deuteron (giving a neutron polarisation of 50%) a specially designed, large horizontal ^{3}He/^{4}He dilution refrigerator was built in cooperation with the Joint Institute for Nuclear Research (JINR) Dubna. The target material is polarised via the Dynamic Nuclear Polarisation method by irradiating it with microwaves in a 2.5 Tesla magnetic field. The polarisation is then orientated and held using a superconducting internal holding coil in either longitudinal (with a solenoidal coil) or transverse (with a saddle coil) orientation. The target is currently fully operational and has reached a nucleon polarisation of 50% in a test run. The detector systems in the experimental hall are currently being made mobile in order to allow access to the target for re polarisation and first experimental runs with the completed target assembly are expected to take place in early 2010.

4.2 Vector spin polarisabilities of the nucleon

The scalar polarisabilities of the nucleon, α and β are fundamental structure constants which describe the spin response of the nucleon to a static electromagnetic field. They are relatively well known for the proton. The vector polarisabilities of the nucleon are fundamental quantities

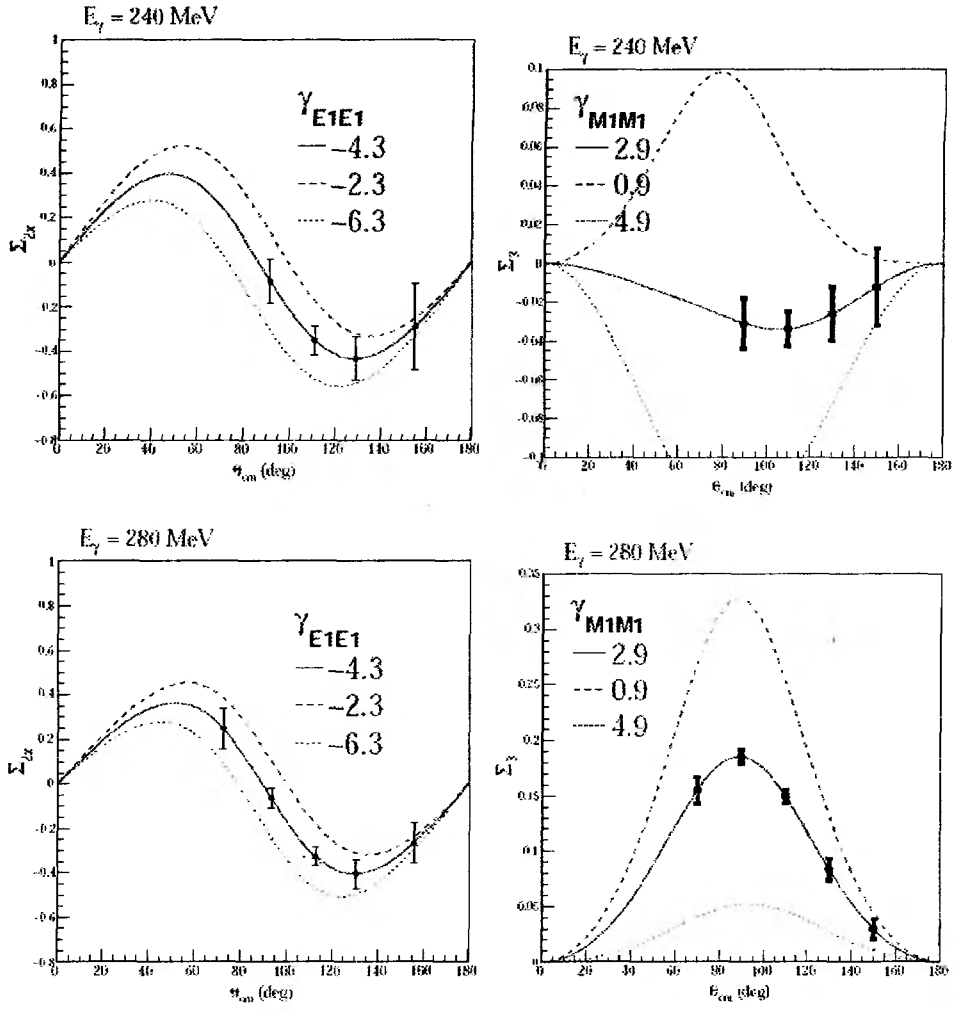

Figure 5: Illustrative plots showing the sensitivity of the planned measurements to two of the four spin polarisibilities. The left panels illustrate the sensitivity of Σ_{2x} to γ_{M1M1} and the right panels illustrate the sensitivity of Σ_3 to γ_{M1M1}. The error bars shown are those predicted for 300 hours (Σ_{2x}) and 100 hours (Σ_3) of measurement. These are produced by varying only one polarisability, additional studies illustrating the effect of varying multiple polarisabilities show similarly promising results.

that describe the spin response of the nucleon to a changing electromagnetic field e.g. an incident photon. These quantities, known as γ_{M1M1}, γ_{E1E1}, γ_{E1M2}, γ_{M1E2} (where the subscript refers to the initial and final photon state), have never been individually extracted from experiment. They appear in the Effective Interaction Hamiltonian of Compton Scattering at the third order. To access them, we plan to measure the Compton Scattering asymmetries Σ_3 (linearly polarised photon beam and unpolarised target), Σ_{2x} (circularly polarised photon beam and transversely polarised target) and Σ_{2z} (circularly polarised photon beam and a longitudinally polarised target). It is clear from simulation, that it will be possible to satisfactorily separate the desired coherent Compton scattering events from the background processes of coherent and incoherent π^0 photoproduction and quasi free Compton scattering on the heavier nuclei on the target. The vector polarisabilities will then be extracted by performing a simultaneous fit over all three asymmetries with predictions from Dispersion Relations [15] and Chiral Perturbation Theory [16]. The predicted sensitivities, as illustrated in Fig 5, and the fundamental nature of these quantities make the outcome from this experiment very promising indeed.

5 Conclusions

The CB@MAMI detector system is a highly flexible and sensitive 4π detector system. In combination with the high quality MAMI C electron beam and Glasgow Photon Tagger, it is well adapted for the accurate measurement of the nucleon resonance spectrum, polarisation observables and rare final states. It has already produced results of great interest involving studies of the $P_{33}(1232)$, the $S_{11}(1535)$ and the $D_{33}(1700)$. The new polarised target capability and recoil polarimeter system will enable an interesting and varied range of new resonance studies.

References

[1] J. C. McGeorge et al. *Eur. Phys. J. A*, 2008.

[2] A. Reiter et al. *Eur. Phys. J. A*, 2006.

[3] S. Prakhov et al. *Phys. Rev. C*, 79:035204, 2009.

[4] R. Novotny et al. *Nucl. Instrum. Meth. A*, 486:131, 2002.

[5] C. M. Tarbert. PhD thesis, University of Edinburgh, 2007.

[6] C. M. Tarbert et al. *Phys. Rev. Lett.*, 100:132301, 2008.

[7] W. Chiang et al. *Physical Review C*, 71(015204), 2005.

[8] V. Pascalutsa and M. Vanderhaeghen. *Phys. Rev. D*, 77:014027, 2008.

[9] M Kotulla et al. *Physical Review Letters*, 89, 2002.

[10] S. Schumann et al. Radiative π^0 photoproduction on protons in the $\Delta(1232)$ region. In Preparation.

[11] E. J. Downie et al. A first meaurement of Σ for radiative π^0 photoproduction on the proton in region of the $\Delta(1232)$. In Preparation.

[12] M. Unverzagt et al. *Eur. Phys. J. A.*, 2009.

[13] V. Kashevarov et al. Accepted for publication in EPJA. arXiv:0901.3888.

[14] A. Fix, M. Ostrick, and L.Tiator. *Eur. Phys. J. A.*, 36:61–72, 2008.

[15] B. Pasquini, M. Drechsel, and M. Vanderhaeghen. *Phys. Rev. C*, 76:015203, 2007.

[16] Vladimir Pascalutsa et al. *JETP Lett.*, 89:108–113, 2009.

EMIN2009 – Contribution

INVERSE DIPROTON PHOTODISINTEGRATION WITH ANKE AT COSY

Hans Ströher, Institut für Kernphysik and Jülich Center for Hadron Physics,
Forschungszentrum Jülich, 52425 Jülich, Germany

Abstract:

The paper gives a brief introduction into the COSY-facility, the currently used detector systems (ANKE, TOF and WASA) and the targets (cluster jet, pellet and ABS). It presents and discusses the results of recent measurements of the reaction pp → $\{pp\}_s \gamma$ (inverse diproton photodisintegration) which were obtained with ANKE/COSY and subsequently at WASA-Promice/TSL.

Introduction:

Photoabsorption on two-nucleon systems in nuclei at intermediate energies (a few 100 MeV) allows one to probe fundamental properties of nuclei at short distances, for example through the photo-disintegration of the simplest nucleus, the deuteron. Much less is known about the other simplest process, i.e. $\gamma + \{pp\}_s \rightarrow p + p$, where $\{pp\}_s$ is a proton pair in the $^1S_0$ state. It is obvious that different features of the underlying dynamics will be revealed by studying both systems since different amplitudes contribute to deuteron and diprotons, respectively. In the absence of a free diproton, the cleanest way to study the above reaction is the inverse channel with the production of a free $^1S_0$ diproton: $p + p \rightarrow \{pp\}_s + \gamma$.

Such an experiment has been performed with the ANKE detector system at an internal beam of the Cooler Synchrotron COSY that will be discussed further below; before, however, a brief overview of the COSY facility is provided.

Apparatus:

- COSY [Ref. 1]
  The COoler SYnchrotron COSY is an accelerator and storage ring at the Institute for Nuclear Physics (IKP) of the Forschungszentrum Jülich (FZJ). It is in operation since the beginning of the 90's and is now in a mature state, providing high intensity proton and deuteron beams, which may also be polarized, for both internal experiments (ANKE, WASA (see below), in previous times also COSY-11 and EDDA) and to external target stations (now TOF (see below), earlier also BIG KARL (GEM, MOMO)). The maximum beam momentum is 3.7 GeV/c, typical beam intensities are a few times 10^{10} for unpolarized particles, and about an order of magnitude less, if the beams are polarized.

- Detectors
  - ANKE [Ref. 2]

    ANKE is the name of a magnetic forward spectrometer inside the ring of the Cooler Synchrotron COSY. It comprises 3 dipole magnets D1-D3, which impose a small chicane to the COSY ring. D1 deflects the beam out of the nominal orbit onto a target (see below) in front of D2, and D3 reflects the magnet back onto the nominal orbit. D2 is the large spectrometer magnet, which separates the reaction products from the beam. The magnet is movable perpendicular to the beam direction in order to detect particle momenta independent of the beam momentum. Forward, positive and negative side detection systems allow to track, identify and momentum analyze the particles. For experiments with deuterium (used as effective neutron targets), silicon tracking telescopes near the target are implemented to detect slow recoil protons ("spectator protons").
  - TOF [Ref. 3]

    The time-of-flight spectrometer TOF is a non-magnetic detector at an external target position, combining excellent tracking capabilities with large acceptance and full azimuthal coverage. It consists of a large vacuum tank, covered with scintillators inside, and a near target tracking system for decay vertex detection and triggering. Recently, a low-mass budget tracking detector, based on straw-chambers has been implemented to improve the momentum resolution. TOF is optimized for detection of final states with strangeness.
  - WASA [Ref. 4]

    The "Wide Angle Shower Array", originally set up at the CELSIUS accelerator in Uppsala (Sweden), is a close-to-4π detector for neutral and charged particles, which is operated at the internal COSY beam. WASA comprises an electro-magnetic calorimeter (~1000 CsI crystals), a very thin superconducting solenoid (~0.18 X_0), inner and forward tracking detectors and a frozen pellet target (see below).
- Targets
  - Cluster Jet [Ref. 5]

    For measurements with unpolarized hydrogen or deuterium targets, a cluster jet is used, crossing the circulating COSY beam at right angles. The density of the target reaches ~10^{15} atoms/cm^2 for hydrogen and (2-5)x10^{14} atoms/cm^2 for deuterium. It is used at ANKE.
  - Pellet [Ref. 6]

    For high luminosity unpolarized experiments with internal targets, a stream of frozen pellets (diameter ~ 20-50 μm, pellet rate up to 10 kHz) through the circulating beam is the target of choice. The vertex is well defined, but the interaction rate is not as smooth as with cluster jets. In addition the large

energy loss leads to fast "heating" of the beam, which must be compensated by cooling methods. This target is employed at WASA.

- Polarized atomic beam source [Ref. 7]
  The polarized internal target for the ANKE experiment utilizes a polarized atomic beam source to feed a storage cell with polarized hydrogen or deuterium atoms. The nuclear polarization is measured with a Lamb-shift polarimeter. The commissioning of the target in the COSY ring has been done, and first double polarized experiments are scheduled for 2009.
- Liquid hydrogen/deuterium target [Ref. 8]
  The TOF liquid hydrogen/deuterium target has been constructed with an extremely small amount of passive material. The standard target cell is 6 mm in diameter and has a length of 4 mm. The working pressure is 200 mbar, which allows to use very thin target windows of only 0.9 μm Mylar foil.

Recent results on inverse diproton photodisintegration:

The fundamental reaction pp → $\{pp\}_s$ γ was observed in an experiment of an incident beam of unpolarized protons (T_p = 353, 500, and 550 MeV; note that the corresponding γ-energy is equivalent to about $T_p/2$) on an unpolarized proton cluster jet target inside the COSY ring [Ref. 9]. The produced two protons in the final state were registered in the forward detection system of the magnetic spectrometer ANKE. To identify diprotons, it was requested that the excitation energy E_{pp} of the two protons was less than 3 MeV. The photon final state was selected through a missing mass analysis, i.e. pp → pp X (X = γ): at the lowest beam energy a clean separation between γ and π^0 was achieved. For larger beam energies the photon peak was sitting on top of the much larger π^0-contribution, which, however, could be easily subtracted.

The differential cross sections measured for c.m. angles θ_{pp} between 0° and 20° exhibit a steep increase with angle that is compatible with E1 and E2 multipole contributions. The ratio of measured cross sections to those of np → dγ is on the 10^{-3} to 10^{-2} level. The observed cross section increase with T_p might reflect the influence of the Δ(1232) resonance. It should be noted that there is no direct contribution from S-wave ΔN intermediate states and M-odd multipoles are forbidden. In addition only the spin-flip contribution to the E1 operator survives.

Motivated by this result, an experiment performed at TSL CELSIUS (Uppsala, Sweden) with the WASA-Promice set-up has been analyzed and published [Ref. 10]. The measurement was performed at the incident proton beam energy of 310 MeV, and the $^1S_0$ diproton state was identified by a final state pp missing mass peak where the excitation energy was less than 3 MeV. The advantage of this measurement is the complete coverage of the photon c.m. angle θ_γ. The linear behaviour observed in $\cos^2\theta_\gamma$ indicates that there is almost no influence of an E2 multipole at this energy, and that the E1 and M2 must be of similar size.

For more details, I refer to the orginal publications [Refs. 9, 10].

Summary, Outlook:

Two recent experiments [Ref. 9, Ref. 10] have been performed to investigate inverse diproton photo-disintegration at intermediate energies, i.e. in the region of the Δ-resonance. Such an approach (pp → $\{pp\}_s$ γ) is advantageous compared to other techniques, for example studying the photoabsorption (γ, pp)-reaction with emission of two fast protons on light nuclei. Due to the different quantum numbers and involved multipoles compared to deuteron photodisintegration, this reaction provides valuable additional information about NN-systems.

More recently, the excitation function has been studied at ANKE throughout the Δ-resonance region, and a clear indication for its excitation has been observed [Ref. 11].

There are also analysis efforts going on for ANKE data to enlarge the angular range [Ref. 12].

Finally, it is planned to exploit polarized COSY proton beams for this reaction.

Acknowledgements:

The presented results have been obtained by the ANKE-collaboration at COSY-Jülich [Ref. 13]. I owe much credit to the Dubna-group, i.p. S. Dymov and D. Tsirkov as well as to V. Komarov who initiated this research. Many discussions with A. Kacharava, K. Nakayama and C. Wilkin are gratefully acknowledged. This work is supported by the BMBF-JINR joint agreement, by DFG grants, by JCHP-FFE and by VI-QCD.

References:

[Ref. 1] R. Maier et al., Nucl. Instrum. Meth. A 390 (1997) 1

[Ref. 2] S. Barsov et al., Nucl. Instrum. Meth. A 462 (2001) 364

[Ref. 3] A. Böhm et al., Nucl. Instrum. Meth. A 443 (2000) 35

[Ref. 4] Chr. Bargholtz et al., Nucl. Instrum. Meth. A 594 (2008) 339

[Ref. 5] A. Khoukaz et al., Eur. Phys. J. D 5 (1999) 275

[Ref. 6] C. Ekström (CW Collaboration), Phys. Scr. T99 (2002) 169

[Ref. 7] H. Kleines et al., Nucl. Instrum. Meth. A 560 (2006) 503

[Ref. 8] S. Abdel-Samad *et al.*, Nucl. Instrum. Meth. A 556 (2006) 20

[Ref. 9] V. Komarov et al., Phys. Rev. Lett. 101, 102501 (2008)
See also: Ann. Rep. JCHP/IKP Forschungszentrum Jülich 2008, p.7

[Ref.10] A. Johansson and C. Wilkin, Phys. Lett. B 673 (2009) 5

[Ref.11] D. Tsirkov, private communication (2009)

[Ref.12] S. Dymov, private communication (2009)

[Ref.13] ANKE-collaboration
See : http://www.fz-juelich.de/ikp/anke/de/index.shtml

Total photoabsorption on quasi free nucleons at 600 – 1500 MeV

N.Rudnev, A.Ignatov, A.Lapik, A.Mushkarenkov, V.Nedorezov, A.Turinge
for the GRAAL collaboration
Institute for Nuclear Research RAS, Moscow, 117312

Experimental data on the nuclear total photo-absorption cross section above P_{33} (1520) resonance (E_γ > 500 MeV) are scarce, especially for the quasi-free neutrons. There exist the T.A.Armstrong data for the proton [1] and deuteron [2] and partly (below 1.2 GeV) N.Bianchi for different nuclei [3]. New precise experimental results for the free proton were published recently by the GRAAL collaboration [4]. They are in a good agreement with the old (1972) Armstrong data. Aim of this work is to present new experimental results for the quasi free neutron, especially.

Almost all the existing data for the total photo-absorption in the nucleon resonance energy region were obtained with the bremsstrahlung tagged gamma beams. To reduce the electromagnetic backgrounds different methods were used. For example, Cherenkov counters were applied for identification of charge particles in the hadron yield etc. At GRAAL facility we used the Compton back scattered laser photons, so the low energy gamma tail was significantly reduced by the collimation. The scheme of GRAAL experiment is shown on fig.1.

Scheme of the GRAAL experiment

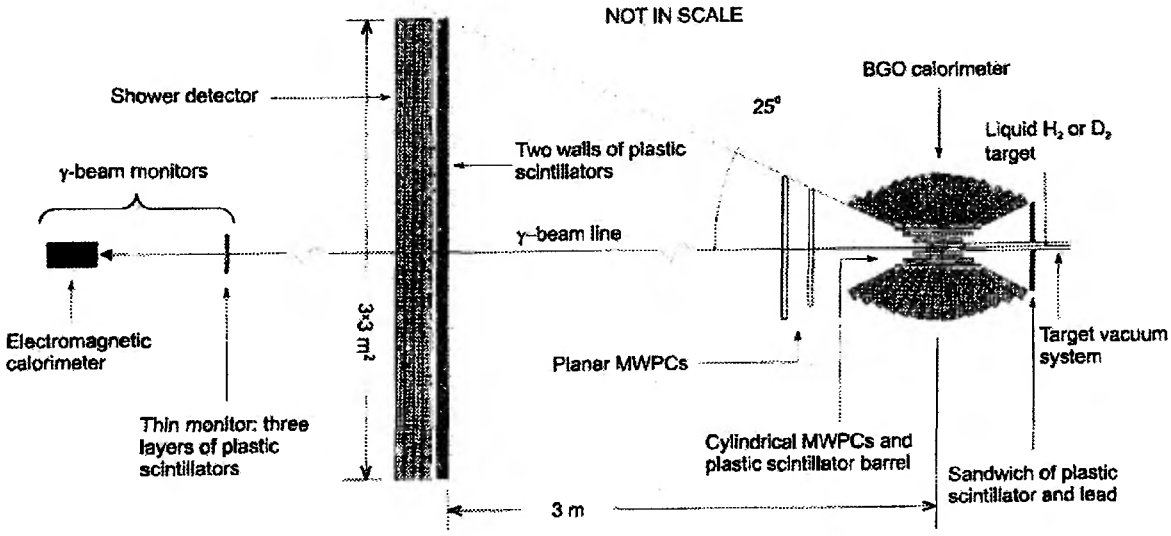

Fig.1.

An important feature of the GRAAL beam is the possibility to change the gamma energy range changing the laser wave length during the experiment. For example, the gamma energy ranges (E_γ = 500 -1100 MeV and 800 – 1500 MeV for green and UV lines, respectively) were used. Measurement of the yield in the overlapping energy regions allows us to evaluate the systematic errors precisely. Fig.2 shows an example of such measurements where the accuracy of 5% can be demonstrated.

Here we present new data for the deuteron and carbon targets separating the processes on quasi-free protons and neutrons. These data were obtained by two independent methods, namely the summing of partial cross sections and subtraction of the backgrounds, to improve the systematic accuracy. Both mentioned methods were separately used earlier in the bremsstrahlung experiments independently at Frascati and Mainz [5,6].

The detailed description of the GRAAL facility was done particularly in our previous paper [4] devoted to measurement of the total cross section on the free proton. The cross sections in absolute scale were evaluated by measuring the total hadron yield, the fluxes, and target thickness. The measurement efficiency was determined by simulations. Due to large solid angle of the GRAAL detector closed to 4π the geometrical efficiency was high.

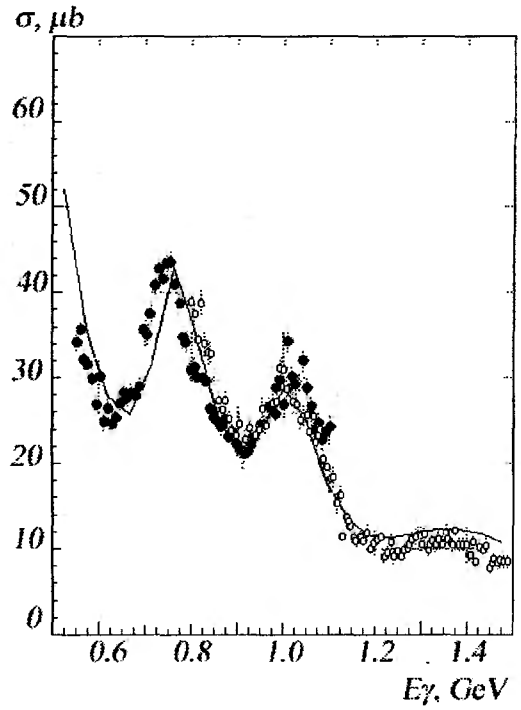

Fig.2.Partial π^0 photo-production cross section on the proton, measured with different wave length laser light. Full dots and circles correspond to 514 and 340 nm, respectively. Curve represents the prediction of SAID [6].

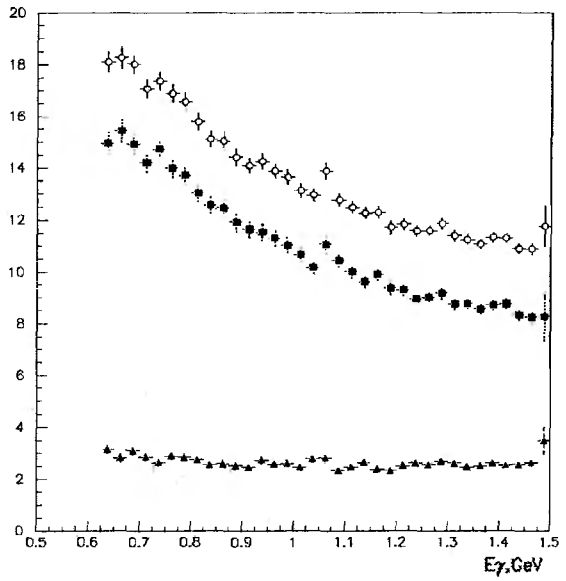

Fig.3. Results obtained by the subtraction method for the carbon target. Total yield from the full target (open circles), empty target (full triangles) and their difference (full squares) are shown.

Let's describe both methods mentioned above in details. The first one is the subtraction of the background which contribution was evaluated using the empty target measurement. The subtraction method is illustrated in fig.3. Total cross section is the difference between two total hadron yields from full and empty target normalized on the corresponding fluxes. Taking into account the target thickness, we obtain the total cross section in absolute scale.

Second method is the summing of partial meson photo-production cross sections. It is available due to almost 4π solid angle and low background conditions of the GRAAL experiment. At first, here we took into account the single and double π–mesons and η–meson photo-production on the proton and neutron using the deuteron target. The products of π^0 decay (2γ) were detected in BGO-detector, nucleons and charged mesons were measured in both BGO and front scintillation wall detectors. Time of flight measurement for the forward detector was applied to separate nucleons and charged mesons. Simulation was done for each partial reaction providing the algorithm for data analysis. The contribution of neighborous channels to the any selected yield does not exceed 1%.

Energy of charged mesons were evaluated knowing their angles in two body kinematics. An example of the proton and pion selection for the reaction $\gamma n \Rightarrow p\,\pi^-$ using two-dimension distributions is shown in fig.4. The result of experiment was in a good agreement with simulations.

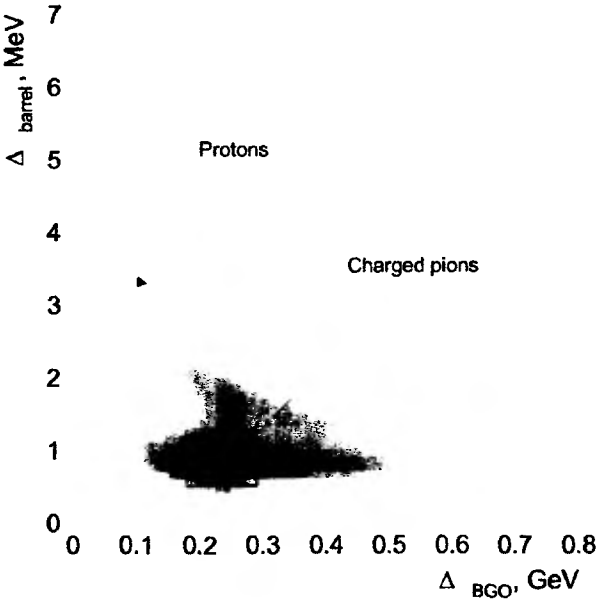

Fig.4. Selection of a proton and charged pion in BGO detector

Difference between calculated and measured angles of nucleons for the experimental (solid line) and simulated (dashed line) data for reaction $\gamma n \Rightarrow p \pi^-$ is shown in fig.5. For the reaction $\gamma p \Rightarrow n \pi^+$ it looks very similar. Difference between measured by TOF and calculated energy of nucleon and the energy is shown in fig.6. Vertical lines indicate the cuts for event

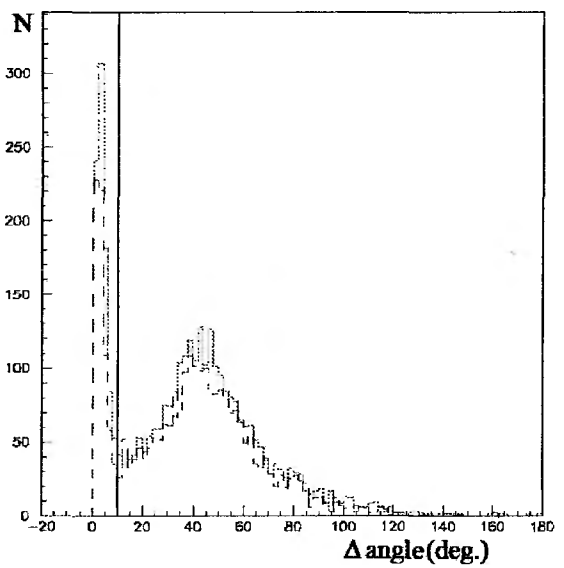

Fig.5.Angle between calculated and measured angles of the nucleon (reaction $\gamma n \Rightarrow \pi^- p$)

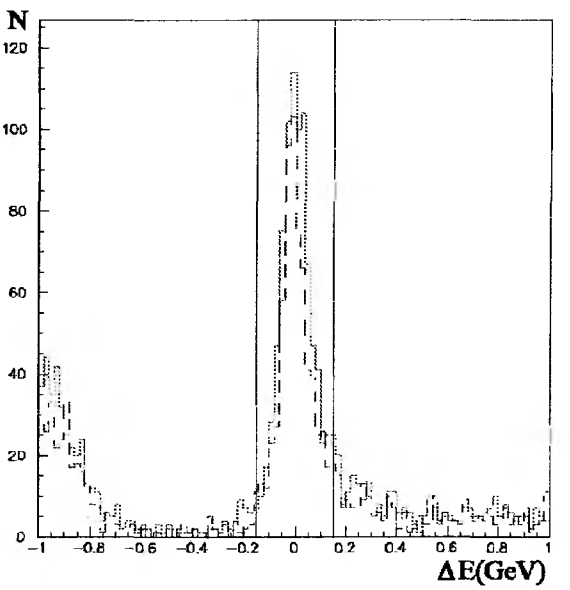

Fig.6. Difference between calculated and measured energies of the forward nucleon (reaction $\gamma n \Rightarrow p \pi^-$)

Selection of particles in BGO detector was done using the cut on cluster size which depends on the type of particle. For neutrons the cluster size is minimal being equal to 1 crystal dominantly. There where four criteria of event selection for the reactions $\gamma p \Rightarrow p \pi^0$ and $\gamma n \Rightarrow n, \pi^0$: invariant mass of two γ-quanta (fig.7), missing mass of two γ-quanta (fig.8), difference between calculated and measured angles of nucleon (similar one is shown in fig.5) and the difference between calculated energy of nucleon and the energy measured by TOF as was shown in fig.6.

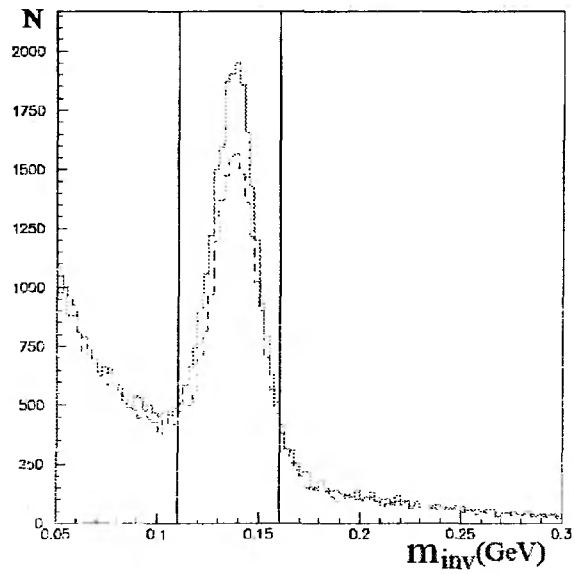

Fig.7. Invariant mass of two γ-quanta in BGO detector (reaction $\gamma p \Rightarrow p\pi^0$)

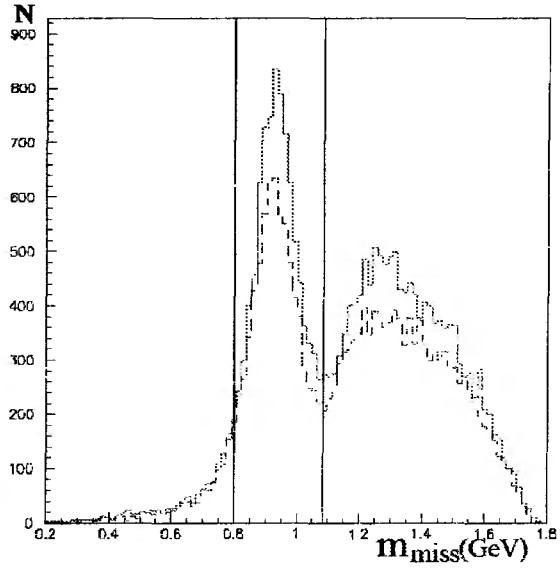

Fig.8. Missing mass of two γ-quanta in BGO detector (reaction $\gamma p \Rightarrow p\pi^0$).

Selection of events for η-meson photo production was done practically by the same way as for π^0 photo production, except that the cuts the invariant mass of two γ-quanta (only this channel of η–decay was considered) corresponded to the mass of η-meson.

Selection of events for double π^0 photo production was done almost the same as for reactions of single π^0 photo production. The only difference was to use the two dimension distributions of invariant masses of two pars of γ-quanta corresponding to two π^0.

Events with one neutral and one charged meson was done using invariant masses of two γ-quanta. Then energy and momentum of the missing mass were calculated. Energy of charged meson was evaluated so the missing mass of the neutral and charged meson was equal to the mass of nucleon. Then the angle and energy of the nucleon was evaluated and compared with the measured values.

The most difficult case was to separate the reaction of two charged mesons photo production. If nucleon hits the BGO detector we can't measure the energies of all three particles. Therefore, in order to decrease background, the events with nucleon, coming in forward direction where separated. Energy and momentum of the nucleon and its missing mass were calculated. Energy of one charged meson was evaluated, so the missing mass of nucleon and this meson was equal to the mass of second meson. Then angle of second meson was calculated and compared with the measured value.

Outputs for each of twelve mentioned above reactions were collected in several dozen million events. For the same runs the corresponding fluxes were evaluated as was described in [1]. Examples of spectra and flux distributions are shown in fig.9a and fig.9b, respectively.

The measurement efficiency for any reaction was evaluated by simulations using LAGGEN, LAGDIG, PREAN codes (see details in [1]). The efficiency is the product of three factors: geometrical efficiency (probability of particle to hit the detector), physical efficiency (the probability of particle to be measured) and calculating efficiency (the probability of measured particle to be counted). The efficiency changes from several tenths of percent for the reaction of two charge pion photo production up to several tens for the reaction $\gamma p \Rightarrow p\pi^0$, as seen in fig.9c.

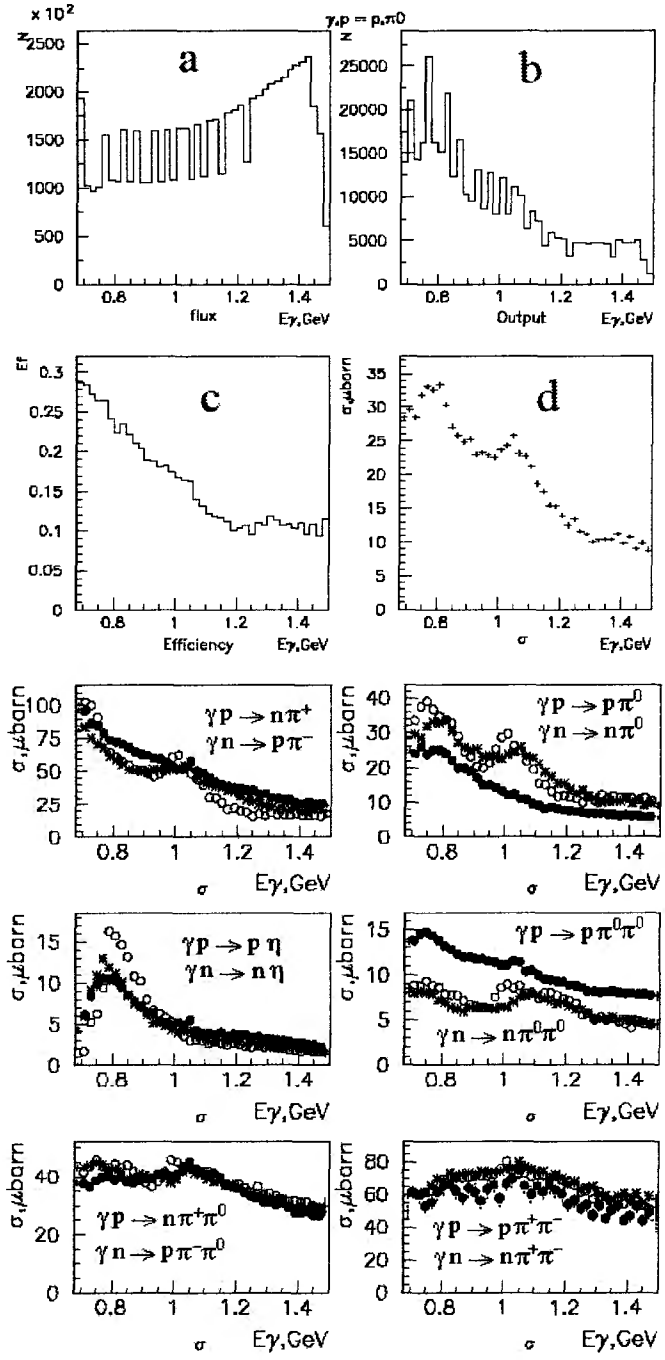

Fig.9.Photon flux (a), hadron yield (b),
measurement efficiency (c) for reaction $\gamma p \Rightarrow p\pi^0$. Cross section (d) is obtained by division of the yield on the flux, and normalized on the measurement efficiency and thickness of the target

Fig.10.Partial cross sections for one and double π and η mesons photo-production on free and quasi-free proton and quasi-free neutron. Open circles– free proton, stars – quasi-free proton, full dots – quasi-free neutron

Total photo-absorption cross sections for the deuteron, obtained by subtraction and summing method in comparison with literature Armstrong data are shown on fig.11. It is seen that the results obtained by two different methods coincide within 5% error bars in the energy region up to 1.2 GeV. Above this energy, there is seen a noticeable disagreement, which is explained by the triple meson production channels contribution which was not included in the present evaluation of partial channels. We see the similar relative behavior for proton and neutron, especially presence of the F15 (1680) resonance in both cross sections, obtained by subtraction and summing methods in contradiction with the Armstrong data [2].

Total photo-absorption cross section for the ^{12}C nuclei is shown in Fig.12. Results for the carbon were obtained by subtraction method only. Good agreement with earlier published results and the "universal curve" is seen but the error bars are much less.

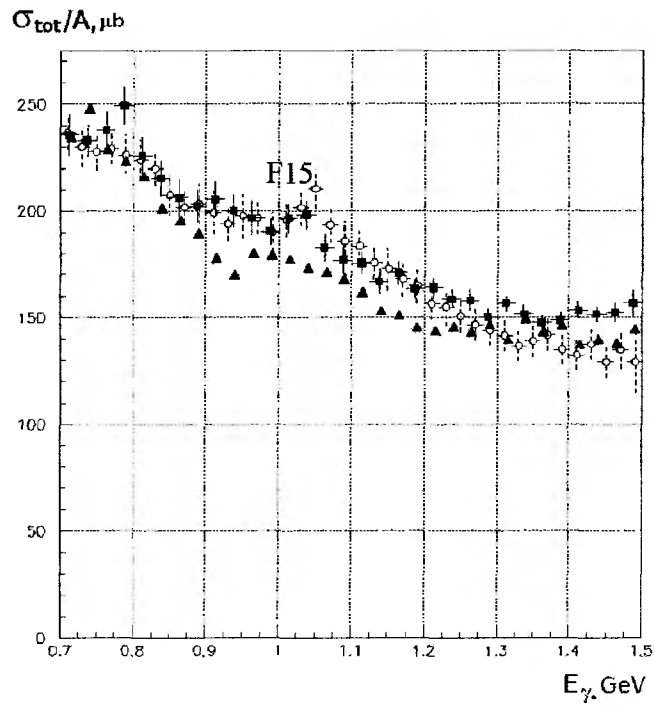

Fig.11.Total photo-absorption cross section for the deuteron, obtained by subtraction (open points) and summing method (full points) in comparison with literature Armstrong data [2] (full triangles)

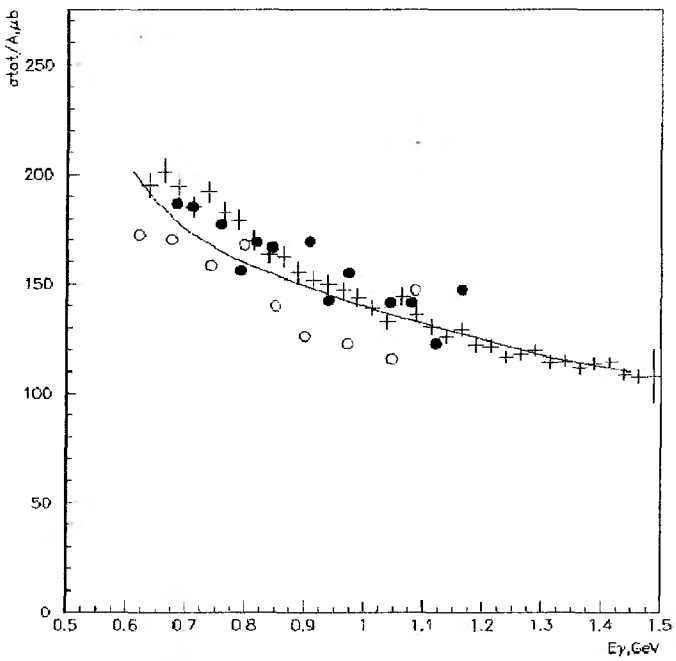

Fig.12. Total photo-absorption cross section for the 12C. Crosses correspond to GRAAL data, obtained by the subtraction method. Full and open points are taken from Bianchi [3] e. a. and Mirazita [4] e. a. data, respectively. "Universal curve" is marked by the full line

Final GRAAL results for the free proton, deuteron and carbon target are shown in fig.13. We can see that carbon cross section is practically coincides with "Universal curve" (Fig.12) but the cross sections for free proton and deuteron are approximately 30% more.

From fig.14 one can see that there is a difference between the proton and neutron (deuteron target) cross sections within 5% error bars. Slight but systematic difference in the absolute scale above 1 GeV is caused, presumably, by the neutron efficiency uncertainty. The neutron efficiency is the most important factor for the systematic accuracy as it was studied carefully in details.

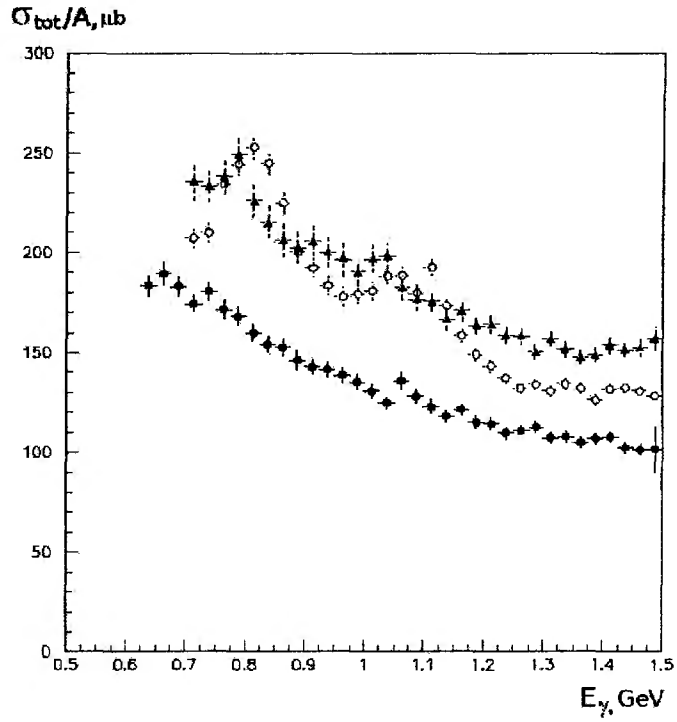

Fig.13. Comparison of the total photo-absorption cross sections for the proton (full triangles), deuteron (open points) and carbon (full points) – GRAAL data

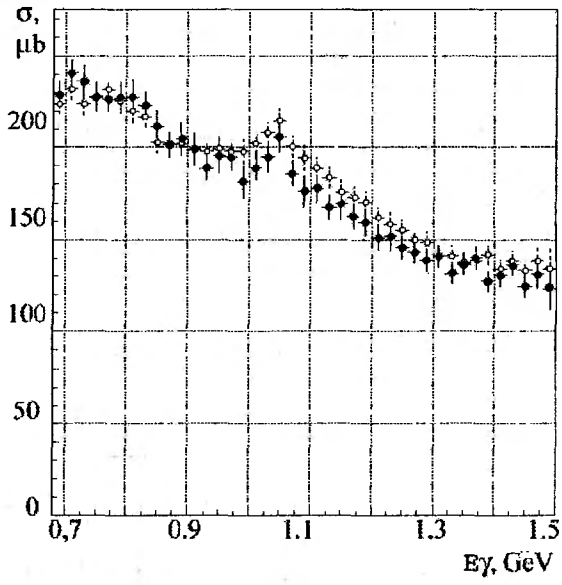

Fig.14. Total photo-absorption cross section on the bound proton (open points) and neutron (full points) obtained by the summing method (deuteron target)

Comparison of total photo-absorption cross sections on free and quasi-free proton for different nuclei including actinide ones [11] is shown in fig.15. Evidently, the conclusions of the work [11] concerning actinide nuclei would be revised. It is seen that GRAAL data for carbon is practically coincide with SEBAF data for the actinide nuclei. In fig.15 we can see the difference between free proton and quasi-free proton as well.

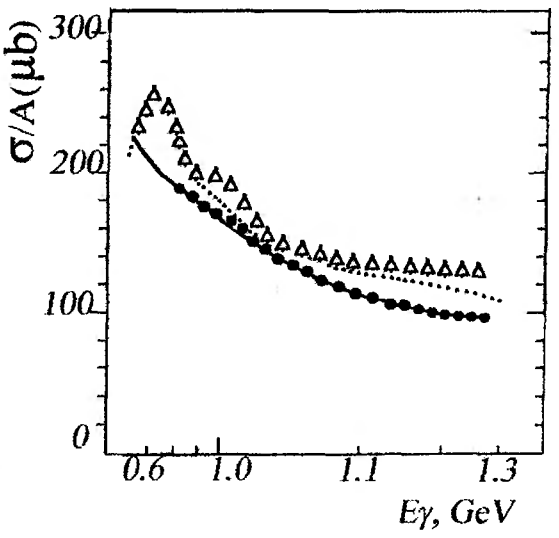

Fig.15. Total photoabsorption cross section for Free proton (dotted line and triangles correspond. To Armstrong and GRAAL data, respectively), full points – GRAAL data for carbon, solid line – actinide nuclei (CEBAF data)

This work is supported by RFBR, grant 08-02-00648-a

References:

1. О. Барталини и др. ЯФ 71, 1 (2008).
2. C. S. Armstrong *et.al.*, Nucl. Phys. B 41, 445 (1972).
3. N. Bianchi *et.al.*, Phys.Lett. B 309, 5 (1993).
4. M. Mirazita *et.al.*, Phys.Lett. B 407, 225 (1997).
5. M. McCormick *et.al.*, Phys. Rev. C 53, 41 (1996).
6. L. Mazzaschi *et.al.*, NIM A 346, 441 (1994).
7. M.Castoldi *et.al.*, NIM A 403, 22 (2002).
8. O. Bartalini *et.al.*, NIM A 448, 12 (2006).
9. T. A. Armstrong *et.al.*, Phys. Rev. D 5, 1640 (1972).
10. J. Ahrens *et.al.*, Nucl. Phys. A 446, 229 (1985).
11. I.Pshenichnov e.a. Archive: nucl-th/0303070

ON EVIDENCE FOR EXOTIC DIBARYON $d_1{}^*(1956)$ IN SELECTED TWO-NUCLEON-TWO-PHOTON REACTIONS

S.B. Gerasimov

Joint Institute for Nuclear Research, Dubna, Russia

Abstract

The narrow, NN-decoupled dibaryon resonance with a mass about 1956 MeV was reported in 2000 by DIB2γ Collaboration (JINR,Dubna) on the basis of the measurement of the two-photon energy spectrum in the reaction $pp \to pp2\gamma$ at 216 MeV. The most probable quantum numbers $J^P = 1^+$ prevent the resonance from decaying into two protons due to the exclusion principle while the pionic decays are impossible energetically. The significance of this resonance (called $d_1^*(1956)$) for the interpretation of a few other exclusive and inclusive reactions connected with the photon(s) production in nucleon collisions with nucleons and nuclei at different energies is discussed. The importance is stressed of on-going and planned studies of the elastic and inelastic Compton scattering on the lightest nuclei for collecting information on the structure and dynamics of $d_1^*(1956)$ which can shed light on its nature.

Contents:

1. Multiquark systems involve more complicated colour sub-systems which cannot be studied in the simplest meson and baryon systems. Therefore, multi-q's are principally important for a full study of the low energy typical hadronic-scale behavior of QCD and the structure of strongly interacting matter. The theory of strong interaction, QCD, is still unable to predict the properties of the multiquark systems such as nuclei or other possible bound states of hadron clusters. Even in the simplified case of $SU(2)$ gauge symmetry, the lattice calculation of the four-quark systems (*e.g.*,[1] and references therein) are still in the initial phase though the results already obtained show the principally important effects of mutual screening of gluon flux-tubes connecting the quarks.

There are also arguments telling us that explicit gluon degrees of freedom may be involved in the description of all such multiquark states [2]. Therefore, the reliable experimental identification of even one multiquark state, *e.g.*, the long-sought-for six-quark dibaryon, would play the role of the necessary prompting for theory.

Among different possibilities,the nonstrange NN-decoupled dibaryons with small widths could be the most promising and easy for experimental searches.

2. The new experimental method using the two-photon mechanism of the production and subsequent decay of the NN-decoupled (6q)-resonance(s) in proton-proton collisions was proposed to facilitate the identification and further study of the exotic nature of these resonances [3]. This method is free of inherent difficulties of many earlier used reactions connected with the participation or production of multihadron states in the initial or final states. The specific experimental signature of the production and decay of nonstrange dibaryon , having mass below the pionic decay modes, was indicated and discussed [4]. On the basis of this method, the Dib2γ Collaboration (JINR) observed the specific structure in the spectrum of final photons which was interpreted as the production and decay of the narrow dibaryon with the mass $\simeq 1950 \div 1960$ MeV [5]. The diagramme in Fig.1 with the double line representing an intermediate resonance may serve as an illustration to different processes touched upon in the subsequent sections. With the solid lines in

Fig.1, representing free nucleons, it describes the double photon production in the nucleon-nucleon collisions (Section 2); if all nucleons are bound inside nuclei, it may be considered as the photon scattering on the correlated pair of nucleons in a nucleus, or just as the Compton scattering on the deuteron (Section 3b); and if the initial photon line is replaced by any meson line this diagramme can be referred to as the photon production in a meson capture by a correlated nucleon pair accompanied by the resonance excitation or just as a part of the resonance excitation process induced via the strong initial nucleon-nucleus interaction (Section3a).

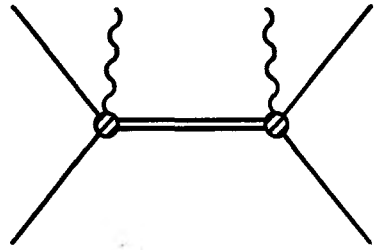

Fig.1

The energy spectrum for coincident high energy photons ($\omega_\gamma > 10$ MeV) emitted from the process $pp \to \gamma\gamma X$ at an energy of 216 MeV, measured by the DIB2γ Collaboration, consists of a narrow peak at a photon energy of about 24 MeV and a relatively broad peak at an energy around 65 MeV with the statistical significance 5.3σ and 3.5σ, respectively [5].

In the overall center-of-mass system the energy of the photon ω^F associated the resonance production (formation) is determined by the mass M_R of the resonance and the energy of colliding nucleons $W = \sqrt{s}$ as

$$\omega^F = \frac{W^2 - M_R^2}{2W} \tag{1}$$

It is clear that owing to narrowness of the considered dibaryon resonance the energy distribution of these photons should also be very narrow. The energy of the photon ω^D arising from the three-particle decay of the resonance d_1^* in its rest frame is given by

$$\omega^D = \frac{M_R^2 - M_{NN}^2}{2M_R} \tag{2}$$

where M_{NN} is the invariant mass of the final NN state which is determined by the relative momentum of the nucleons in this state. Since the momentum distribution of M_{NN} is closely connected with interaction between these nucleons, the energy distribution of photons from the resonance decay will be strongly sensitive to NN final state interactions (FSI).

The KVI-Group(Groningen) accumulated a large sample of the 2γ-events at lower energy of the incident proton beam 190 MeV. In their published work [6], they prefer to interpret the similar structure of the photon spectral distribution as due to a nonresonance mechanism of the double bremsstrahlung. In principle, the initial kinetic energy of proton $T_p = 190MeV$ is sufficient to produce the $d_1^*(1956)$-resonance together with the photon energy $\omega^F \simeq 12MeV$ which is two times lower than the photon energy in the JINR experiment. However, due to lower energy of the initial proton in the KVI experiment, the cross-section of the resonance excitation is markedly ($\sim 2^3 = 8$) lower than in the Dubna experiment and the nonresonance mechanism, *i.e.* ordinary double-bremsstrahlung of photons, appears to become comparable with the resonance mechanism and interferes with it preventing the reliable separation of two mechanisms.

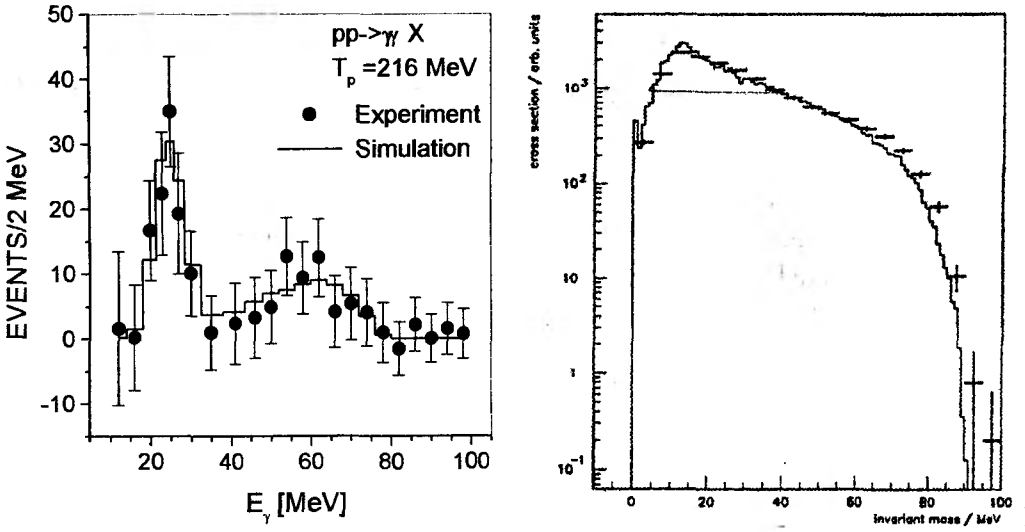

Fig.2a(b)

Taking for granted the resonance mass $M(d_1^*) = 1956$ MeV one gets the maximal value $M_{\gamma\gamma} \simeq 63$ MeV coming as the result of the resonance excitation at $T_p = 190MeV$, while the experimental distribution in the KVI-experiment shown in Fig.2b [6] extends for significantly higher values testifying to significant non-resonance two-photon production.

The resolution of the question about the relative contributions of the resonance and non-resonant mechanisms would consist in the long ago suggested way of checking the sign of the resonance presence, namely, in the repetition of the experiment at several initial proton energies below the π^o-threshold to observe the quantitatively calculable shift of the narrow peak.

Two more exclusive experiments should be mentioned which deal with the photon production in the proton-proton reactions at higher energies. First, the CELSIUS-WASA Collaboration [7] analyzing its pp-bremsstrahlung data collected at 200 and 310 MeV claimed that it did not find the signal of narrow dibaryon in the mass range from 1900 to 1960 MeV. Further, rather recently, the same CELSIUS-WASA Collaboration reported on a study of the exclusive reaction $pp \to pp\gamma\gamma$ at energies of 1.36 and 1.2 GeV [8] which resulted in the measurements of the invariant mass spectra of photon pairs emitted from this reaction. These measurements enable one to construct the invariant mass spectrum ($M_{\gamma\gamma}$) of its photon pairs. The surprising feature of the measured spectra is that they both contain pronounced resonant structures located at about 280 MeV. The conservative estimates of the statistical significance amount to 4.5σ for the spectrum measured at T_p =1.36 GeV and 3.2σ at T_p=1.2 GeV. We made a simple model-dependent analysis showing that it is the dibaryon mechanism of the two-photon production in pp collisions $pp \to \gamma d_1^* \to pp\gamma\gamma$ that bears the responsibility for these structures at higher energies [9] and why the same mechanism and the adopted experimental cuts did not discover the signal of the $d_1^*(1956)$ in the pp bremsstrahlung data accumulated in measurements at 310 MeV which are most full and reliable.

. Briefly, the model assumptions are illustrated by a sequence of transitions in the matrix element of the process

$$M(p_1p_2 \to \gamma_1\gamma_2p_1'p_2') = M_F M_I M_D \tag{3}$$

$$M_F = M_F(p_1p_2 \to \gamma(k1\ \epsilon_1)_{M1}, \Delta_1(1231)_{virt}\ p_2)$$

$$M_I = M_I(\Delta_1(1231)_{virt}\ p_2 \to d_1^*(1956) \to \Delta_1'(1231)_{virt}\ p_2')$$

$$M_D = M_D(\Delta_1'(1231)_{virt} \to p_1'\gamma(k2\ c_2)_{M1})$$

The ingredients of the quantum-mechanical (*i.e.*, non-covariant) calculation have been the spin-angular and radial parts of the total $\Delta(1231)N$-wave function, the usual structure of the dominating spin-dependent $\Delta \to N\gamma$-radiative transition vertex, and the initial and final antisymmetric pp-continuum wave functions. The fitting parameters of the quasi-bound ΔN wave function resulted

in the ratio $\sqrt{< r^2 >_d / < r^2 >_{d_1^*}} \simeq 3.6$, which means that the average distance between the baryon constituents in the $d_1{}^*(1956)$ is markedly less than in the deuteron and that a significant overlap of internal quark structures of the virtual Δ and nucleon inside the d_1^*-resonance has to take place. In turn, this hint can be of importance in construction of more detailed QCD-based dynamical models of the $d_1{}^*(1956)$-resonance.

Leaving the absolute normalization of the cross-section arbitrary, i.e. normalized to experiment, we present only the calculated distribution of $M_{\gamma\gamma}$ in comparison with that measured at the proton energy 1.36 GeV[?] and at proton energy .31 GeV [7] in comparison with the distribution from the π^o-decays. Being very close to each other as seen in Fig.3b, both kinds of last events were dropped of registration because both were considered as the background. Hence, the conclusion about absence of the d_1^*-excitation traces has to follow.

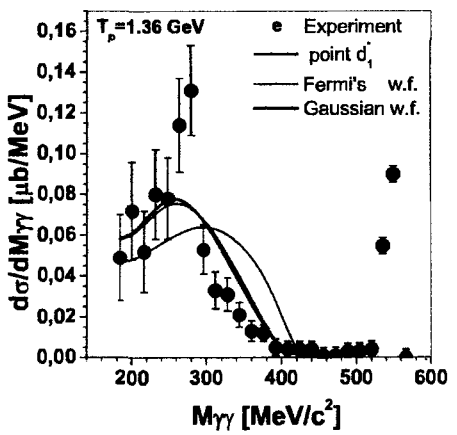

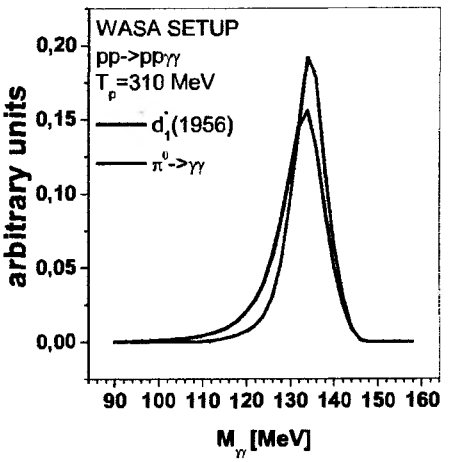

Fig.3a(b)

3a. The last example refers to the inclusive reaction $pd \to \gamma X$ and $pC \to \gamma X$ below the π^o -threshold, where the inclusion of the $d_1^*(1956)$ excitation and its radiative decay in addition to an ordinary mechanism of single photon bremsstrahlung helps describing the measured photon energy distribution [10]. Note that $BR(d_1^* \to \gamma pn) \simeq 1$, which means that the allowed, in principle, resonance excitation in the *strong* pd -interaction turns out to be of the order of the NN -bremsstrahlung cross-section which is the lowest order *electromagnetic* process (*i.e.*, of the order $\mathcal{O}(\alpha_{em})$).

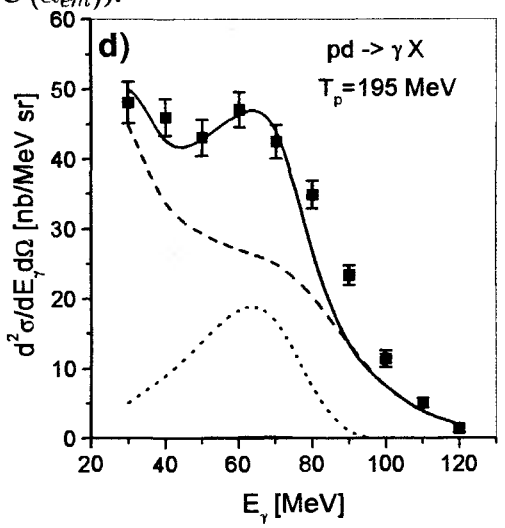

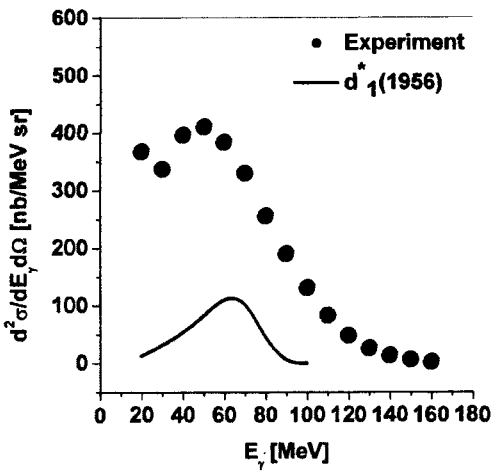

Fig.4a(b)

The experimental data and theoretical curve (the dashed line) are taken from Refs.[11] and [12] in Fig.4a, and from [13] in Fig.4b.

3b. Presently, much of the information on the fundamental properties of the neutron has to be extracted from the processes including atomic nuclei. In particular, this refers to the coefficients of electric and magnetic polarizabilities of the neutron. Naturally, data on the elastic and quasi-elastic Compton scattering on the deuteron are the most accurate and easily interpretable by the theory. The amplitude $T_{\gamma\gamma}(s,t)$ of the Compton scattering

$$T = (\vec{\varepsilon'} \cdot \vec{\varepsilon}) A_1(s,t) + ...$$

depends, in the low-energy limit, on static properties of a given target particle and its coefficients of the electric (α) and magnetic (β) polarizabilities. Omitting the spin-dependent terms and higher polinomials in ω, we have

$$A = -\frac{(eQ_N)^2}{m_N} + 4\pi(\alpha_N + \beta_N cos\theta)\omega^2 \qquad (4)$$

The data that have been accumulated for many years from different processes and been gradually improving with the time are reproduced below (the units are $10^{-4}\ fm^3$) [14]:

reaction	$\alpha_{p[n]}$	$\beta_{p[n]}$
$\gamma p \to \gamma p$	12.1(.3)	1.6(.4)
n+Pb$\to$ n+Pb	[12.0(1.5)]	–
$\gamma d \to \gamma d$	[8.8(2.4)]	[6.5(2.4)]
$\gamma d \to \gamma np$	[12.5(1.8)]	[2.7(1.8)]

Encoded into the effective lagrangian,

$$\mathcal{L} = -\frac{1}{m^2}(\alpha+\beta)\partial_\mu(\bar{\psi})(\partial_\nu\psi)F_{\mu\lambda}F_{\nu\lambda} + \frac{1}{2}\beta F_{\mu\nu}F_{\mu\nu}\bar{\psi}\psi$$

the "meson" polarizabilities of nucleons can be used in different low-energy reactions, such as the Compton effect on heavier nuclei, *etc*. The study of $\gamma d \to \gamma d$ enables one to extract the "isoscalar(vector)" polarizabilities of the nucleon $\alpha^{s,v} = (1/2)(\alpha_p \pm \alpha_n)$ and $\beta^{s,v}$. The lower-energy extractions from experiments at $\omega = 49$ and 69 MeV (Urbana Uni.) and at 55 and 69 MeV (Lund, MAXLab) are consistent with small iso-vectorial polarizabilities [14]. The treatment of the higher-energy $\omega = 94$ MeV experiment (SAL, Saskatoon) with the earlier theoretical calculations [15] gives

$$(\alpha^s - \beta^s) = 2.6 \pm 1.8$$

instead of expected value $\simeq 9.0$ (in units of $10^{-4}\ fm^3$). More recent and corrected calculation of the same authors, presented as the contributed paper at EMIN-2009, essentially removed this discrepancy.

In view of available data and planned experiments on the $\gamma d \to \gamma d$ reaction we stress its utility to inquire on new information and/or constraints on characteristics of $d_1^*(1956)$, in this "formation-type" resonance excitation process. The contributions of possible NN-decoupled dibaryon resonances to the photon-deuteron processes like $\gamma d \to \gamma d$ or $\gamma d \to \pi^- pp$ have earlier been considered in [16].The emphasis was made there on the isoscalar resonances with quantum numbers $I = 0, J^P = 0^\pm, 1^-$. Continuing our earlier line of discussion [17], we focus here on the $d_1^*(I = 1, J^P = 1^+)$-resonance and present some additional comments aiming to attract more attention to the specifics of the explication of this resonance in the energy range pertinent to the forthcoming new data on the Compton scattering from deuteron and $He-3$. We have in view the

ongoing investigation of the γd -reaction in MAXLab, where the tagged-photon facility will be used to measure the scattered photon angular distribution between 60^o and 150^o over the photon energy range $60 \div 115$ MeV in 5 MeV steps [18].

Below we give the estimation of the contribution of the photoexcitation of d_1^* into the averaged differential γd -scattering cross-section and to the real part of the dynamic magnetic polarizability of the deuteron which should, in principle, be added to the meson polarizabilities of bound nucleons as an additional structure-dependent effect that might influence the observables of the γd-elastic scattering, around the photon energies close to $\omega_{lab}^{res} \simeq 82MeV$, the resonance photoexcitation energy of $d_1^*(1956)$. The second mentioned estimation can be done with the help of the known dispersion sum rule

$$\Re\delta\beta(\omega) = \frac{1}{2\pi^2} P \int d\omega' \frac{\sigma^{BW}{}_{M1}(\omega')}{\omega'^2 - \omega^2} \tag{5}$$

where the cross-section of the magnetic-dipole radiative transition $\gamma d \to d_1^* \to X$ is taken in the standard Breit-Wigner form, in which one should define $\Gamma_{tot}(d_1^*)$ and $BR(d_1^* \to \gamma d) \leq 1$. The data of the SAL Collaboration [19] on γd -scattering at $\omega_{lab} \simeq 94MeV$ have the scale of 12-18 nb/sr, with variations of approximately 2 nb/sr in energy bins of $\Delta W \simeq 3MeV$. The distance of their energy from the presumed $\omega_{lab}^{res} \simeq 82MeV$ is much larger than $\Gamma_{tot}(d_1^*)$ and this enables one to get an upper bound of $\Gamma(d_1^* \to \gamma d) \leq 5KeV$ which is rather weak one. Much stronger bounds will follow from the forthcoming data of MAXLab measurements in the resonance region $\omega_{res} \pm 2 \simeq 82 \pm 2$ MeV . For instance, if we take maximally large $BR(d_1^* \to \gamma d) = 1$ then the resonance enhancement of the cross-section, averaged over $\Delta W \simeq 3MeV$, by amount,say,of $5 \cdot \delta < d\sigma/d\Omega >= 10nb/sr$ will result in the total width estimate of $\Gamma_{tot}(d_1^*) \simeq 1\ eV$. Hence, either $\Gamma_{tot}(d_1^*)$ acquires the values of the order of $\mathcal{O}(eV)$, as estimated within the soliton model of the narrow NN-decoupled dibaryons [22], or the $BR(d_1^* \to \gamma d) \ll 1$, which would still need proper dynamic justification. The evaluated $\Re\delta\beta(\omega)$ reveals the cross-over at $\omega = \omega_{res} \simeq 82MeV$, but as it is proportional to the value of $\Gamma_{tot}(d_1^*)$, the maximal difference of its values before the crossing zero and after the crossing is of per-cent order as compared to typical experimental uncertainty of $\beta_{p(n)}$ itself, that is negligibly small.

Returning to the discussed $pp-2\gamma pp$ -processes exhibiting the positive signs of the $d_1^*(1956)$ excitation and decay, it is natural to expect that the effective strength in the vertex $\mathcal{V}((pp)_{J^P,I=1};\gamma;d_1^*)$ may be quite different (in fact, higher) as compared to effective coupling in the vertex $\mathcal{V}(d_{J^P=1^+,I=0};\gamma;d_1^*)$. This will result in a quantitatively different effect of the resonance explication in the Compton scattering on ^3He or on ^4He comparatively to the Compton scattering on deuteron target. This means, therefore, that the resonance effect should be estimated and properly taken into account in the extraction of the neutron polarizabilities from the planned studies of the elastic γ^3He -scattering, either in the spin/polarization independent experimental set-up (*e.g.*, [20]), or in experiments aiming to measure the spin-dependent electromagnetic polarizabilities which are under preparation at TUNL(USA) [21].

4. We briefly discuss here the question of probable $d_1^*(1950 \div 1960)$ quantum numbers.

•. Among theoretical models predicting dibaryon resonances with different masses there is one giving the state with $IJ^P = 11^+$ and the mass value ($\sim 1940MeV$) surprisingly close to the value ($\simeq 1956MeV$) extracted from the observed maximum of the $pp \to pp2\gamma$-reaction. This is the chiral soliton model[22] applied to the sector with the baryon number $B = 2$. The theoretical uncertainty at the level of $\pm 30MeV$ might be taken here because the model gives this numerical (unrealistic) value for the mass difference of the deuteron and the singlet level.However the estimated radiative width of the order $\sim \mathcal{O}(eV)$ may seem to be too low.

•. There is also a kind of the hadron-constituent oriented models, *e.g.*, the relativistic dynamic πNN-interaction model based on the Faddeev-type equations with the specifically chosen ansatz

for the off-mass-shell pion-nucleon interaction amplitude [23]. Specific feature of the last-mentioned approach is the statement about the relative orbital moment $l = 1$ and isospin $I = 2$ for the most strongly bound cluster configuration $P_{33}(\pi N) + N$ of the considered three-body πNN-system. Yet the estimated resonance mass is different from the value suggested by experiment.

• In the composite models, the cluster decomposition $(6q) = (3q) \times (3q)$ or $(6q) = (qq) \times (qq) \times (qq)$,or $(6q) = (qq) \times (qqqq)$ can be assumed. The fractional-parentage expansions of colour-singlet 6-quark states in a cluster model were considered in several works (*e.g.*, [24]).

For qualitative estimations one can choose the $N\Delta$ - model with possible values of spin(S) and isospin (I) $S(I) = 1$ or 2. In fact, this model was used in our calculations of the 2γ-invariant mass distribution to be compared with data of the CELSIUS-WASA Collaboration. The quantum numbers of relevant dibaryons within the 3-diquark model, which are consistent with the Bose-nature of diquarks and $L = 0$ for total orbital moment, require two axial-vector ($J^P = 1^+$)-diquarks with isospin $I = 1$ and one (iso)scalar diquark ($J^P = 0^+$).This model gives the following combinations of the total spin and isospin for the lowest mass dibaryons: ($I = 1, J = 0$, *i.e.*, the quantum numbers of the "virtual" NN-state), ($I = 0, J = 1$, *i.e.*, the quantum numbers of the deuteron), ($I = 2, J = 1$ - the exotic, NN-decoupled quantum numbers for narrow dibaryon) ($I = 1, J = 2$ coinciding with the quantum numbers of known ${}^1D_2(2.17)$ -resonance, lying close to the $N\Delta$-threshold). The overlap of possible NN-decoupled quantum numbers with $L = 0$ following from either $N\Delta$- or diquark model select as more probable isospin and spin values $I = 2, J = 1$ for our low-lying d_1^*-resonance. However, one can escape a potentially problematic situation with the long-lived iso-tensor ($I = 2$) dibaryon if one unites, following Refs.[25, 26], one axial-vector diquark (A_2) and one scalar diquark (S_2) into a single four-quark cluster ($A_4 = S_2 \otimes A_2$) which should be the color-triplet iso-vector ($I = 1$) and spin-parity $J^P = 1^+$. Hence, as most perspective we would suggest for $d_1^*(1956)$ the following configuration structure: $|d_1^*(1956) >= c_0|N, \Delta > + c_{\bar{3}_c 3_c}|S_2(\bar{3}_c, 0^+), A_4(3_c, 1^+) >$.

The presence of the color-octet 3q-baryons is associated in the decomposition of Ref.[24] with the antisymmetric radial wave function, hence with the negative parity and,therefore, we drop it. Needless to say in conclusion that deciphering and testing of such a complex structure would require further development of the theory and new experimental data.

The author wishes to thank Dr. A.I. L'vov for the important comment and the Organizing Committee of EMIN-2009 for the invitation and support.

References

[1] A.M. Green and P. Pennanen, Phys. Rev. **C 57** 3384 (1998)

[2] H.J. Lipkin, Phys. Lett. **B 113** 490 (1982).

[3] S.B. Gerasimov and A.S. Khrykin, Mod.Phys.Lett.**A8** (1993) 2457.

[4] S.B.Gerasimov, S.N.Ershov and A.S.Khrykin,Yad.Fiz. **58** (1995) 911.

[5] A.S. Khrykin, et al, Phys.Rev. **C 64** (2001) 034002; nucl-ex/0012011.

[6] R. Ĉaplar, J.C.S. Bacear, et al., Fizika **B12** 81 (2003)

[7] H. Calen, et al., Phys. Lett. **B427**, 248 1998.

[8] M. Bashkanov, H. Clement et al. Int.J.Mod.Phys. **A20**, 554(2005);hep-ex/0406081.

[9] A.S. Khrykin and S.B. Gerasimov, in: Proceedings of the 11th Conference on Meson-Nucleon and the Structure of the Nucleon (MENU 2007),Jülich, Germany, Sep. 10-14, 2007, pp.250; hep-ph/0710.3331.

[10] A.S. Khrykin, Nucl.Phys. **A721**, 625c (2003); nucl-ex/0211034.

[11] J. Clayton, et al.,Phys. Rev. **C45**,1810 (1992)

[12] K.Nakayama, Phys.Rev.**C45**, 2039 (1992)

[13] J.A. Pinston, et al., Phys. Lett. **B 249**, 402 (1990)

[14] M.Schumacher, Prog. Part. Nucl. Phys. **55**, 567 (2005); hep-ph/0501167.

[15] M.I. Levchuk and A.I. L'vov, Nucl. Phys. **A 674**, 449 (2000); nucl-th/9909066 and contributed paper at the EMIN-2009 (to be published).

[16] D.M. Akhmedov and L.V. Fil'kov, Nucl. Phys. **A554**, 692 (1992)

[17] S.B. Gerasimov, Czech.J.Phys. **51** (2001) A153; nucl-th/9812077; JINR-E1,2-2001-291, Dubna, 2001, p.166;

[18] G.Feldman, et al., Few Body Syst. **44**, 325 (2008).

[19] D.L. Hornidge et al., Phys.Rev.Lett., **84**, 2334 (2000).

[20] D. Choudhury, et al., Phys. Rev. Lett., **98**, 232303 (2007).

[21] H.R. Weller, et al. , Prog. Part. Nucl. Phys. **62**, 257 (2009).

[22] V.B.Kopeliovich, Yad. Fiz. bf 58, 1317 (1995) (Phys. Atom. Nucl.**58** (1995) 1237) J.Exp.Theor.Phys. **93** (2001) 435; (Zh.Eksp.Teor.Fiz. **120**(2001) 499); hep-ph/0103336.

[23] A. Matsuyama, Phys. Lett. **B 408**, 25 (1997).

[24] M. Harvey, Nucl. Phys. **A 352** (1981) 301.

[25] R. L. Jaffe, Phys. Rev. **D 72**, 074508 (2005).

[26] L.A. Kondratyuk, et al., Yad.Fiz., **45**, 1252 (1987).

Photoreactions with Polarized HD target at SPring-8

M. Fujiwara, K. Fukuda, T. Hotta, K. Kohri, T. Kunimatsu, C. Morisaki, T. Ohta, K. Ueda, M. Uraki, M. Utsuro, and M. Yosoi

Research Center for Nuclear Physics, Osaka University, Mihogaoka 10-1, Ibaraki, Osaka, 567-0047 Japan

J.-P. Didelez and G. Rouillé

IN2P3, Institut de Physique Nucléair, Orsay, France

S. Bouchigny

CEA LIST, Fontenay-aux-Roses, France

M. Tanaka

Kobe Tokiwa University, Kobe, 654-0838, Japan

Su-Yin Wang and W.C. Chang

Institute of Physics, Academia Sinica, Taipei, Taiwan, 11529, Republic of China

Abstract

Double polarization measurement for ϕ photoproduction with the polarized target and a polarized photon-beam is a sensitive means to investigate small and exotic amplitudes, such as an $s\bar{s}$-quark content of nucleons. In order to realize the double polarization measurements to study the $s\bar{s}$-quark content as well as exotic hadron structures involving s-quarks, we started to construct a frozen-spin polarized HD target at the laser-electron photon facility (LEPS) facility on the new basis of recent technology developments in cryogenic and high magnetic field from 2004. At SPring-8 BL33LEP beam-line (LEPS facility), the linearly-polarized photons were produced by Backward-Compton scattering. A polarized target plays a very crucial role in upgrading the LEPS experiments. The physics motivation for producing HD polarized target and the present status of its development are discussed. Especially, we discuss the experiment for ϕ-meson photoproduction for the double polarization asymmetry measurement.

1 Introduction

It is generally accepted that the low-energy properties of nucleon is well described in terms of u and d quarks. The constituent quark model predicts that the ratio (μ_n/μ_p) of the neutron and proton magnetic moments is $-2/3$, which agrees with the experimental value -0.685. However, the results from the experiments of lepton deep inelastic scattering introduce a serious controversial situation. The magnetic moments from constituent quarks only contribute 10%. Measurements of the nucleon spin structure functions indicate that there may be non-negligible strange quark content and that the strange quarks give 10–20% contributions to the nucleon spin [1, 2, 3].

A similar conclusion has been drawn from the elastic νp scattering at BNL [4]. Analysis of the pion nucleon sigma term also suggests that proton might contain an admixture of 20% strange quarks [5, 6]. Experiments on annihilation reactions $p\bar{p} \to \phi X$ at rest [7, 8, 9] show a strong violation of the OZI rule [10]. It has also been argued that such experimental

results could be understood with little or no strangeness content in the nucleon. Recently, some important experiments to measure the parity-violation ep scattering (the anapole moment of proton) have been performed at Bates [11], at Mainz [12], and at Jefferson Laboratory [13, 14, 15, 16], indicating a small strangeness content in proton.

These experimental as well as theoretical situations still remain a puzzle "Does the the $s\bar{s}$ content exist in a nucleon?" This puzzle is a long-standing problem in physics [17], and deeply relates our understanding of the quark generation; Is the three generation of quarks distinctive without any generation mixing? The controversy should be solved by providing new experimental information on the $s\bar{s}$ content of nucleon.

The ϕ-meson photoproduction is one of the promising reactions to give direct experimental data for studying the $s\bar{s}$ contents of nucleon. The wave function of ϕ meson consists of the almost pure $s\bar{s}$ component. Thus, there is a possibility of pinning down the $s\bar{s}$ components in a nucleon through the knockout process, where the $s\bar{s}$ pair couples to the photon is knocked out as a ϕ meson. Although the $s\bar{s}$ knockout amplitude is much smaller than that from the dominant Pomeron exchange process in the ϕ meson photoproduction, it is predicted that double polarization asymmetries with a polarized proton target and a polarized beam are sensitive to the $s\bar{s}$ content via an interference effect. Theoretical calculations suggest that the effect of the $s\bar{s}$ content is detectable via beam-target asymmetry C_{BT} measurements at $E_\gamma \sim 2$ GeV [18], and that the LEPS energy region ($E_\gamma = 1.5 \sim 2.4$ GeV) is suitable to perform the C_{BT} measurement. The afore mentioned discussion is concerned with the "hidden strangeness content" study via the $\vec{\gamma}\vec{p} \longrightarrow \phi p$ or $\vec{\gamma}\vec{n} \longrightarrow \phi n$ measurement.

There are also other interesting subjects to be studied via the double polarization measurements. One is the mystery related to the bump structure in excitation energy observed in ϕ meson photoproduction [19]. Although theories predict that the cross sections of the ϕ meson photoproduction increase monotonically from the threshold as a function of photon energy [20, 21], the SPring-8 experiment [19] clearly indicates that the ϕ meson photoproduction cross section has a bump structure at around 2.1 GeV. This experimental conclusion is consistent with the SAPHIR result [23], and has been confirmed by the experimental result at the Jefferson Laboratory [24]. The question "Why does the bump structure in the ϕ meson photoproduction cross section appear at around 2.1 GeV?" should be understood theoretically. Additional experimental information from the double polarization measurement will help to confirm the theoretical interpretation and to answer the question. It is interesting to note here that the theory groups in Osaka and Groningen try to explain the bump structure of ϕ meson photoproduction near the threshold by introducing the interference effect [22].

Recently, the results on photoreactions at SPring-8 such as $\vec{\gamma}p \longrightarrow K^+X$ and $\vec{\gamma}p \longrightarrow \eta p$ at SPring-8 have been analyzed and published [25, 26, 19, 27, 28, 29, 30, 31, 32, 33, 34, 35, 36]. Interesting observations are reported on the bump structures at around 2.1 GeV in photoreaction cross sections for producing K-mesons and η mesons, both of which relate to the s-quark production. An interesting fact is that all the bump structures observed in cross sections, mentioned above, appear at around 2.1-2.2 GeV. The questions addressed are; "Are the observed bump structures related to some hidden resonance states at 2.1-2.2 GeV?" or "Do the bumps originated from the interference effect induced by the strong meson-nucleon coupling?". For revealing the hidden resonances at around 2 GeV and for giving the deeper insight of the reaction mechanisms associated with s-quark production, it would be of very importance to have additional new experiments of "double polarization measurement".

In the present report, we describe the double polarization measurement of the ϕ meson

production, as a sample case. We also describe the present development status of the polarized Hydrogen-Deuterium (HD) target at SPring-8.

2 C_{BT} measurement in ϕ-meson photoproduction

The ϕ meson photoproduction consists of three components as

1. diffractive production within the vector-meson-dominance model (VDM) through Pomeron exchange process,
2. conventional meson exchange process, such as one-pion exchange (OPE) in the t channel: This process is strongly suppressed by the OZI rule,
3. the $s\bar{s}$ knockout process: When the proton has the $s\bar{s}$-quark content, the $s\bar{s}$ knockout and uud knockout processes should be taken in to account in the ϕ meson photoproduction.

The main ingredient of the knockout photoproduction mechanism stems from the assumption that the constituent quark wave function of proton contains a configuration with explicit $s\bar{s}$ pair, in addition to the usual three-quark (uud) component. The following wave function for proton is a simple expression given by Titov et al. [18, 37].

$$|P\rangle = \alpha|[uud]^{1/2}\rangle + \beta\{a_0|[[uud]^{1/2} \otimes [s\bar{s}]^0]^{1/2}\rangle + a_1|[[uud]^{1/2} \otimes [s\bar{s}]^1]^{1/2}\rangle\} \quad (1)$$

The detailed description to explain the reason why the double polarization measurement becomes very sensitive to the $s\bar{s}$ content in the proton wave function is given by Ref. [37]. Titov et al. [37] found that the study of cross section of the ϕ meson photoproduction at forward angles is not sensitive to the $s\bar{s}$-quark content. The VDM cross section is ten times larger than the cross section from $s\bar{s}$-quark knockout process. However, it has been found that the beam-target asymmetry is very sensitive to the $s\bar{s}$-quark content. The interference effect between the VDM amplitude and the $s\bar{s}$-quark knockout amplitude gives an clear contribution to indicate the presence of the $s\bar{s}$-quark content.

The beam-target asymmetry is defined as

$$C_{BT} = \frac{d\sigma(\overrightarrow{\rightarrow}) - d\sigma(\overleftarrow{\rightarrow})}{d\sigma(\overrightarrow{\rightarrow}) + d\sigma(\overleftarrow{\rightarrow})} = \frac{d\sigma(\frac{3}{2}) - d\sigma(\frac{1}{2})}{d\sigma(\frac{3}{2}) + d\sigma(\frac{1}{2})} \quad (2)$$

where the arrows represent the spin projections of the incoming photon and the target protons, and the notations $(\rightarrow)$ and $(\leftarrow)$ correspond to the initial states with the total spin equal to $\frac{3}{2}$ and $\frac{1}{2}$, respectively.

The beam-target asymmetry mainly appears as an interference effect between the VDM amplitude and the small $s\bar{s}$ knockout amplitude.

Figure 1 shows the absolute value $|C_{BT}|$, which is calculated by taking into account the $s\bar{s}$-knockout process as a function of initial photon energy at $|t| = 0.1$ GeV^2. For convenience, the beam-target asymmetry for background processes is also shown in Fig. 1. We also show the data point obtained from the work of the HERMES collaboration [38]. One can see that the contribution of the $s\bar{s}$-knockout process decreases monotonically with increasing E_γ, because of the corresponding dynamical factor ("form-factor") which decreases rapidly with increasing E_γ. Thus, we may conclude:

1. The expected effect of the $s\bar{s}$ channel in the beam-target asymmetry in the $\gamma p \to \phi p$ process is large.

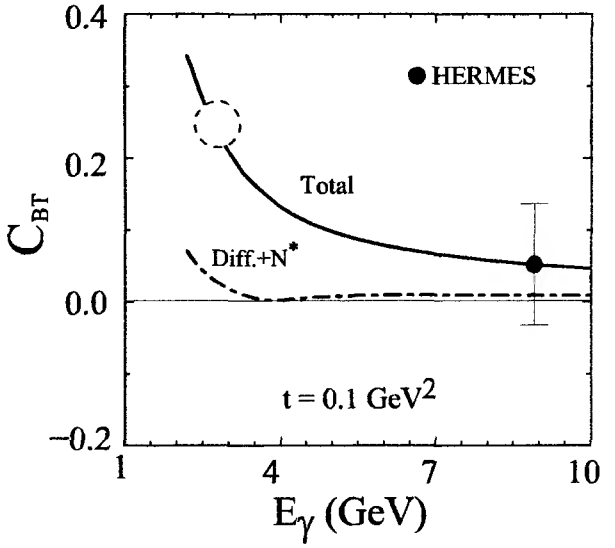

Figure 1: The absolute values of beam-target asymmetry calculated without the $s\bar{s}$-knockout (the dot-dashed curve) and with the $s\bar{s}$-knockout process (the solid line) as a function of E_γ at $|t| = 0.1$ GeV^2. The data point is taken from Ref. [38]. The formulation for the calculations are given in Refs. [18, 37, 39]. Note that the nearly pure $s\bar{s}$ wave function for the ϕ meson and the $s\bar{s}$ content of 1% in the proton are assumed. The data point expected to be measured at SPring-8 is indicated by the dashed circle at around 2.4 GeV.

2. The optimum region for the study of this effect is $E_\gamma = 2 \sim 3$ GeV and $|t| \leq 0.4$ GeV^2.

This conclusion gives a strong support to perform the double polarization measurement of ϕ meson photoproduction at E_γ~2 GeV at forward angles. At present, such an experiment will be performed at SPring-8 or at Jefferson Laboratory, where the preparation of the polarized HD target is now in progress.

3 Estimations for Experiment

In order to obtain the reliable C_{BT} value in ϕ-meson photoproduction, the key issue is a reliable measurement of beam-target asymmetry. The beam-target asymmetry (C_{BT}) is calculated by

$$C_{BT} = \frac{(\sigma_P - \sigma_{BG}) - (\sigma_A - \sigma_{BG})}{(\sigma_P - \sigma_{BG}) + (\sigma_A - \sigma_{BG})} = \frac{\sigma_P - \sigma_A}{\sigma_P + \sigma_A - 2\sigma_{BG}}, \tag{3}$$

where σ_P (σ_A) represents the spin parallel (anti-parallel) cross section from a HD target and σ_{BG} describes a common background contribution mainly from an unpolarized deuteron. The advantage of using the polarized HD target comes from the fact that 50% of dilution factor is achieved in case of the HD target, and we do not have no serious background from carbon and nitrogen in measuring a small cross section for ϕ meson photoproduction. The powerfulness of using the polarized HD target has been well demonstrated by the LEGS experiment at BNL [40].

Defining the ratio R= $\frac{\sigma_{BG}}{(\sigma_P+\sigma_A)/2}$ using the background cross section σ_{BG} and an averaged cross section $(\sigma_P + \sigma_A)/2$, we obtain a relation between σ_P and σ_A as $\sigma_A = \frac{1-C_{BT}(1-R)}{1+C_{BT}(1-R)}\sigma_P$. If it is assumed that σ_P and σ_A will be measured with the same precision, $\Delta\sigma_A$ is written as $\frac{1-C_{BT}(1-R)}{1+C_{BT}(1-R)} \cdot \Delta\sigma_P$. By using these relations, the following equation is obtained:

$$\frac{(\Delta C_{BT})^2}{C_{BT}^2} = \frac{\{1 - C_{BT}^2(1-R)\}^2 + C_{BT}^2 R^2}{2C_{BT}^2(1-R)^2} \cdot \frac{(\Delta\sigma_P)^2}{\sigma_P^2} + \frac{R^2}{(1-R)^2} \cdot \frac{(\Delta\sigma_{BG})^2}{\sigma_{BG}^2}. \tag{4}$$

Titov suggested that 1% of strange quark contents would produce $C_{BT} = 0.3$ in a small $|t|$ region [18]. The fraction R depends not only on coherent and incoherent cross sections from deuteron but on an off-line cut for a missing mass of K^+ and K^- tracks, which will be affected by Fermi motion in deuteron. If R is assumed to be 0.5, Eqn. 4 is rewritten as $\frac{(\Delta C_{BT})^2}{C_{BT}^2} = 20.8 \cdot \frac{(\Delta\sigma_P)^2}{\sigma_P^2} + 1.0 \cdot \frac{(\Delta\sigma_{BG})^2}{\sigma_{BG}^2}$. This means that 10% (20%) precision of C_{BT} requires 2.2% (4.4%) measurement of σ_P, for example, by neglecting the second term. If only statistical error is taken into account, ~2000 (~500) events of ϕ photoproductions has to be collected for the successful measurement.

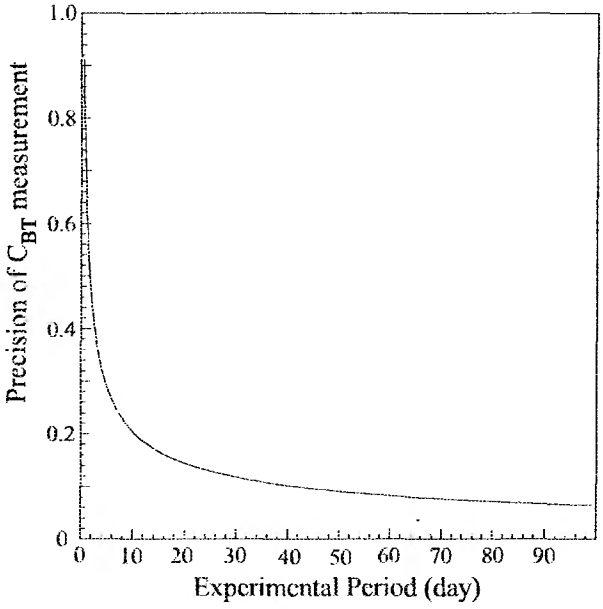

Figure 2: Expected precision for the beam-target asymmetry measurement as a function of the experimental period. In order to obtain the 10% error for the C_{BT} value, we need the experimental run time of about 40 days in case of the SPring-8 where the counting rate of the ϕ mesons amounts to about 3 counts/hour with a 5 cm long H_2 liquid target.

In the LEPS experiment, it is possible to produce about 2000 events of ϕ photoproductions within 40 days in a K^+ and K^- detection mode by using a 5 cm-long LH_2 target (For the ϕ meson photoproduction, see the recent publication [19]). Since the counting rate of ϕ mesons are about 3 counts/hour with a 5 cm long H_2 liquid target, the 10% accuracy for the experimental C_{BT} value will be achievable within 40 days.

Figure 2 shows an expected precision of a beam-target asymmetry measurement as a function of the experimental period. We conclude that the accuracy of the C_{BT} measurement reaches at 10% level within a beam time of 40 days. Since the photoproduction cross sections of Λ and Σ particles are the same order of 1 μbarn at forward angles, the C_{BT} values for K^+ photoproduction also become available with reasonable good accuracy.

4 Installation of the HD target

As the first stage of the HD target development, we clean up the existing building for the cryogenic system at RCNP. Twenty years ago, this building was used to produce liquid He for the superconducting solenoid magnet. But, the equipment became old and it was not used for about 15 years. The building was almost empty. This building was very suitable for our purpose to produce the HD target at RCNP. The infrastructure such as the power line and air conditioning system were improved to fit to the aim of the HD target production. This was also officially good since the building was not used in the correct way for the cryogenic purposes for a long time. Fortunately, it was decided at RCNP that this building could used for the HD target from 2004. It should be noted

that the essential mechanism of polarizing protons in the cooled HD solid and keeping the long relaxation of polarization has been already discussed by Refs. [42, 43, 44].

We started the actual design for the installation of the HD target in 2004. The HD target project has been approved by Japanese government as the five year project, and started from 2005. Among all the equipments necessary to produce and exploit polarized HD, the key ingredient is the ^{4}He+^{3}He dilution refrigerator equipped with a high field superconducting coil. This type of equipment is commercially available and can be delivered within one year after the contract.

Firstly, we prepared the experimental house with a hole to install the ^{4}He+^{3}He dilution refrigerator to cool the HD target down to around 10 mK. The deepness of this hole is 6 m and the diameter is 0.9 m. We started the actual construction of the HD production facility from 2005. The dilution refrigerator (DR) introduced at RCNP was a newly designed one from Leiden cryogenics Co. LTD, the Netherlands with a cooling power of about 2700 μW at 100 mK and with a lowest achievable temperature of 10 mK. Although the roots pumps were used to evacuate the ^{4}He and ^{3}He gases for dilution cooling in the past, we employed turbo molecular pumps instead of the noisy roots pumps. This helps us a lot for a stable long-run operation of the DR without any serious problem.

In order to polarize protons in the HD target, a 17 Tesla superconducting magnet was assembled with this new DR. This 17 Tesla magnet was fabricated in Japan with the help of the JASTEC Co. LTD. In order to reduce the cost of liquid ^{4}He for a long run of the DR, we installed a pipe line for ^{4}He gas recovery by connecting the DR to the central ^{4}He liquefier of Osaka University. This ^{4}He recycling system gives us a great merit to reduce the ^{4}He gas cost by 90%. Since there are many parts which are necessary to be developed at the RCNP side, we started the developments of small devices such as the NMR system from 2004.

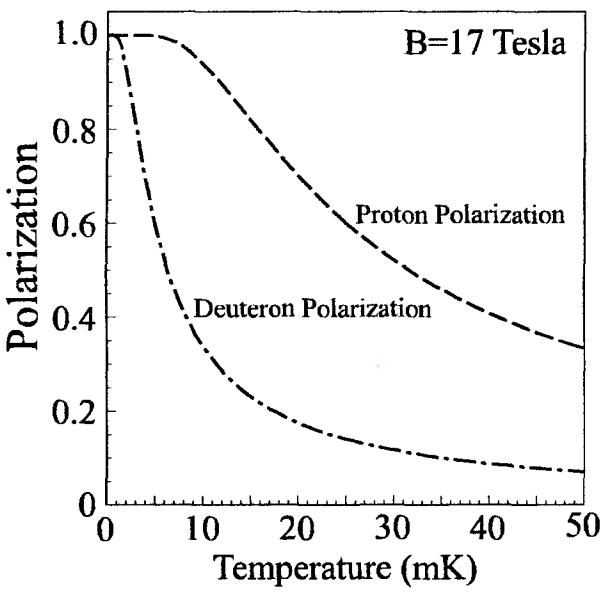

Figure 3 shows the polarizations for proton and deuteron as a function of temperature at 17 Tesla. With the advantage of a high magnetic field of 17 T and a low temperature of around 14 mK, we can achieve the proton polarization of 85%. If we take into account the state-of-the-art technology for the polarized HD target,

1. one can follow the protocol to transport the polarized HD target into the In Beam Cryostat (IBC) which is now rather well established by numerous polarization runs

at Brookhaven [41],

2. one can use a double distilled HD gas with a high quality, for which the distillation apparatus already installed at RCNP and its performance is checked. In collaboration with the ORSAY group, we have exported the HD-gas distillation still from ORSAY [46], and are developing furthermore the still in order to get a purity HD gas better than 10^{-3} with a relatively fast speed.

The IID solid is a heat insulator, making a difficulty to cool down the inside of the solid HD. To solve the bad heat conductivity of the HD, thin wires with purified Al materials are introduced to cool down the inside of the HD. There is an alternative idea to solve this problem. Normally, the solid HD consists of policrystal, in which small HD crystals are assembled with a random direction. If we can make the monocrystal HD, it is possible to let the HD solid have a heat conductivity much better than the policrystal HD. It is expected that the heat conductivity of monocrystal HD is 100 times better than that of the policrystal IID. Thus, if we can make a large monocrystal HD target, we can remove the Al wires as heat sink of the HD target. Technically, it is feasible to make such a monocrystal HD. At RCNP, we promote this development in making a monocrystal and in measuring the heat conductivity of the monocrystal HD [47]

The development of the NMR system to measure the absolute polarization is also in progress: we have achieved the HD polarization by using the DR with 17 T magnet. After about one month operation, we obtained a proton polarization of about 40%. We have confirmed that the relaxation time of the proton polarization has reached at about 3 months. The detailed description about the afore-mentioned developments is partly described in Ref. [48].

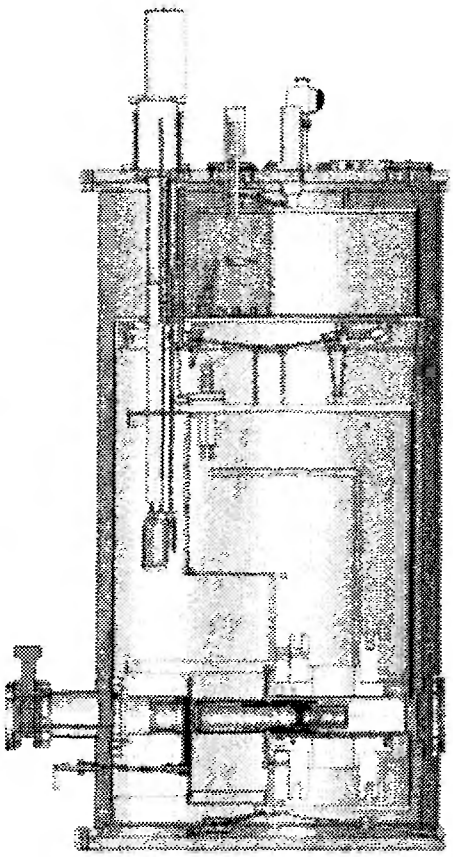

Figure 4: A design drawing of the in beam cryostat (IBC) for the C_{BT} measurement at SPring-8. The HD target is cooled down to about 250 mK to keep the long relaxation time of polarization. Two superconducting Helmholtz coils are arranged around the HD target: One Helmholtz coil generates a vertical magnetic field with a strength of 1 Tesla and the other horizontal coil generates a horizontal magnetic filed of 1 Tesla. By combining the two magnetic fields, we can change the spin direction of polarized proton without any loss of polarization.

Figure 4 shows the schematic drawing of the In-Beam Cryostat (IBC) for the C_{BT} measurement, which has been installed for the LEPS experiment at SPring-8. The cooling

system of the IBC is on the basis of the ^{4}He+^{3}He dilution. The HD target will be be cooled down till 0.25 K. In order to greatly reduce the consumption of liquid ^{4}He, we use a cryogenerator for re-condensation of evaporated ^{4}He gas. Although it increases the original fabrication cost, we can save the operational cost of using liquid ^{4}He. The cooling ability around 0.25 K is extremely attractive to increase the relaxation times of the HD polarization.

The polarization of the HD target is kept in the magnetic field generated by the two sets of 1 Tesla Helmholtz coils: One is arranged in the transverse direction, and the other is arranged in the vertical direction. By changing the currents for the two Helmholtz coils, it is possible to change the applied magnetic field from the transverse to the vertical direction, and also possible to change the field direction to the opposite side. According to this manipulation of the magnetic field, the spin direction of polarized proton or deuteron can be changed. In principle, this change of the polarization direction can be performed without any loss of the HD polarization if the relaxation time is long enough.

At SPring-8, photons generated by Compton back-scattering are linearly polarized because of the 100% laser polarization. The linear polarization is easily manipulated to convert into the circular polarization, which has been demonstrated in the test experiment at SPring-8. Therefore, it is possible for us to measure the complete polarization observables with various combination of spin degrees of freedom for the beam and target spin directions.

We have already installed The transfer cryostat (TC) and storage cryostat (SC) for moving the polarized HD target from the dilution cryostat to the IBC without any serious loss of the obtained polarization. At present, all the installed devises are tested for the LEPS experiment with the HD target. The LEPS experiment has been scheduled to be performed in the year 2010.

5 Final Remarks

We started to construct a polarized HD target for photoproduction experiments at LEPS facility at SPring-8, where a polarized photon beam is available in the energy region from 1.5 to 2.4 GeV with a photon intensity of a few times 10^6/sec. We aim to perform the experiment of ϕ photoproduction off a nucleon at forward angles as a main motive force. Measurement of the double polarization asymmetries for the ϕ photoproduction with the polarized target and the circularly polarized photon beam enables us to investigate small and exotic amplitudes via the interference with dominant amplitudes. We can study the interesting subjects such as the $s\bar{s}$-quark content of nucleons, which is currently considered to be non-negligible. A measurement of a beam-target asymmetry at small $|t|$ (forward angles) with a $1.5 - 2.4$ GeV photon beam is promising to extract a small component via a large interference effect.

Other subjects in hadron physics, such as the spin-determination of the pentaquark particle can be also accessible in a clear method via the polarization observables by using the HD target. An interesting subject is the study of the Θ^+ pentaquark particle [49, 50]. The existence of the Θ^+ pentaquark particle at 1540 MeV itself is in the controversial situation [51]. Theoretically, the problems addressed stem from the fact that the spin and parity values are not uniquely determined: The candidates are $1/2^+$, $1/2^-$, $3/2^+$, $3/2^-$, depending on the theoretical models. In order to determined the spin and parity values of the Θ^+, the polarization measurements are discussed theoretically [52, 53]. Experimentally, the spin-parity determination is difficult because of the poor statistics of

the measured Θ^+ yields. However, if the HD polarized target becomes available with a long relaxation time, it is possible to make a complete measurements of the polarization observables for the Θ^+ particles with a long run at SPring-8. We should await long to perform this kind of a long run experiment after the final setup of the HD target.

Double polarization measurements to detect K mesons yielding the Λ and Σ particles would be also the interesting subjects to be studied in view of the reaction dynamics involving strange quarks and also in view of the hidden resonances expected with the mass of 2-3 GeV. These measurements are rather easily performed as a short term program after the completion of the HD target, and some interesting results will be reported soon.

In 2010, the 5 years budget for the construction of all the devises for the HD target project will be terminated. During these 5 years, all the designed devises have been fabricated and many tests have been done to confirm the devise performances. We plan to have the first test experiment with the polarized HD target in 2010.

6 Acknowledgment

We thank T. Nakano and all the LEPS collaborators for promoting the HD project. We also thank H. Toki, and T. Kishimoto the director of RCNP, for supporting the project. We also thank A.I. Titov for discussion on the double polarization measurement of ϕ meson photoproduction. The present work was supported in part by the Japan Society for the Promotion of Science (JSPS) under the Joint Research Project in the Japan-France Scientific Cooperation Program.

References

[1] J. Ashman *et al.,* (European Muon Collaboration), Phys. Lett. B **206**, 364 (1988).

[2] D. Adams *et al.,* (Spin Muon Collaboration), Phys. Lett. B **329**, 399 (1994)

[3] K. Abe *et al.,* (E143 Collaboration), Phys. Rev. Lett. **74**, 346 (1995).

[4] L. A. Ahrens *et al.,*, Phys. Rev. D **35**, 785 (1987).

[5] J. F. Donoghue and C. R. Nappi, Phys. Lett. B **168**, 105 (1986).

[6] J. Gasser, H. Leutwyler, and M. E. Sainio, Phys. Lett. B **253**, 252 (1991).

[7] J. Reifenroether *et al.,* [ASTERIX Collaboration], Phys. Lett. B **267**, 299 (1991).

[8] C. Amsler *et al.,* [Crystal Barrel Collaboration], Phys. Lett. B **346**, 363 (1995).

[9] A. Bertin *et al.,* [OBELIX Collaboration], Phys. Lett. B **388**, 450 (1996).

[10] S. Okubo, Phys. Lett. **5**, 165 (1963).

[11] D.T. Spayde *et al.,* (SAMPLE Collaboration), Phys. Lett. B **583**, 79 (2004).

[12] F.E. Maas *et al.,* Phys. Rev. Lett. **94**, 152001 (2005).

[13] D.S. Armstrong *et al.,* (G0 collaboration), Phys. Rev. Lett. 95, 092001 (2005).

[14] A. Acha *et al.,* (HAPPEX collaboration), Phys. Rev. Lett. 98, 032301 (2007).

[15] K.A. Aniol *et al.,* (HAPPEX collaboration), Phys. Lett. B **635**, 275 (2006).

[16] K.A. Aniol *et al.,* (HAPPEX collaboration), Phys. Rev. C **69**, 065501 (2004).

[17] P. Wang, D.B. Leinweber, A.W. Thomas and R.D. Yong, Phys. Rev. C **79**, 065202 (2009).

[18] A. I. Titov, Y. Oh, and S. N. Yang, Phys. Rev. Lett. **79**, 1634 (1997).
[19] T. Mibe *et al.*, (LEPS collaboration) Phys. Rev. Lett. **95**, 182001 (2005).
[20] A.I. Titov and T.-S. Lee, Phys. Rev. C **67**. 065205 (2003).
[21] Q. Zhao, B. Saghai, and J.S. Al-Khalili, Phys. Lett. B **509**, 231 (2001).
[22] S. Ozaki *et al.*, Phys. Rev. C **80**, 035201 (2009).
[23] J. Barth *et al.*, Eur. Phys. J. A 17, 269 (2003).
[24] D. Tedeschi, private communication.
[25] R.G.T. Zegers *et al.*, (LEPS collaboration) Phys. Rev. Lett. **91**, 092001 (2003).
[26] T. Ishikawa *et al.*, (LEPS collaboration) Phys. Lett. B **608**, 215 (2005).
[27] M. Sumihama *et al.*, (LEPS collaboration) Phys. Rev. C **73**, 035214 (2006).
[28] H. Kohri *et al.*, (LEPS collaboration) Phys. Rev. Lett. **97**, 082003 (2006).
[29] M. Sumihama *et al.*, (LEPS collaboration) Phys. Lett. B **657**, 32 (2007).
[30] K. Hicks *et al.*, (LEPS collaboration) Phys. Rev. C **76**, 042201 (2007).
[31] W.C. Chang *et al.*, (LEPS collaboration) Phys. Lett. B **658**, 209 (2008).
[32] M. Niiyama *et al.*, (LEPS collaboration) Phys. Rev. C **78**, 035202 (2008).
[33] K. Hicks *et al.*, (LEPS collaboration) Phys. Rev. Lett. **102**, 012501 (2009).
[34] N. Muramatsu *et al.*, (LEPS collaboration) Phys. Rev. Lett. **103** 012001 (2009).
[35] H. Kohri *et al.*, (LEPS collaboration) arXiv:0906.0197 (2009).
[36] M. Sumihama *et al.*, (LEPS collaboration) submitted (2009).
[37] A.I. Titov, Y. Oh, S. N. Yang, and T. Mori, Phys. Rev. C **58**, 2429 (1998).
[38] A. Airapetian *et al.*, (HERMES Collaboration), Phys. Lett. B **666**, 446 (2008).
[39] Y. Oh, A.I. Titov, S. N. Yang, and T. Mori, Phys. Lett. **B 462**, 23 (1999).
[40] S. Hoblit *et al.*, (LEGS-Spin Collaboration) Phys. Rev. Lett. **102**, 172002 (2009).
[41] A. M. Sandorfi *et al.*, in Proc. NSTAR 2005: Physics of Excited Nucleons, edited by S. Capstick, V. Crede, and P. M. Eugenio (World Scientific, New Jersey, 2006).
[42] M. Bloom, Physica **23**, 767 (1957).
[43] W.N. Hardy and J.R. Gaines, Phys. Rev. Lett. **17**, 12781 (1966).
[44] A. Honig, Phys. Rev. lett. **19**, 1009 (1967).
[45] P.C. Souers and P.A. Fedders, Phys. Rev. B **41**, 8643 (1990).
[46] S. Bouchigny, J.-P. Didelez, F. Dubois, G. Rouillé, Nucl. Instrum. Methods in Phys. Res., A **607**, 271 (2009).
[47] K. Kuwai, M. Utsuro *et al.*, RCNP Annual Report p.10 (2007).
[48] Wang Su-Yin, Master thesis, Department of Physics, National Kaohsiung Normal University (2009).
[49] T. Nakano *et al.*, (LEPS collaboration), Phys. Rev. Lett. 91, 012002 (2003).
[50] T. Nakano *et al.*, (LEPS collaboration), Phys. Rev. C **79**, 025210 (2009).
[51] K. Hicks, Prog. Part. Nucl. Phys. **55**, 647 (2005).
[52] C. Hanhart, J. Haidenbauer, K. Nakayama, and U.-G. Meissner, Phys. Lett. B **606**, 67 (2005).
[53] A.I. Titov, H. Ejiri, H. Haberzetti, and K. Nakayama, Phys. Rev. C 71, 035203 (2005).

New frozen-spin target for experiments at MAMI C

G.M.Gurevich
Institute for Nuclear Research of the Russian Academy of Sciences, 119312 Moscow, Russia
(for A2 collaboration)

Abstract

A new frozen-spin polarized target intended for experiments at the polarized photon beam of the MAMI C accelerator in combination with Crystal Ball detector having high angular acceptance is described. The central part of the target apparatus is a horizontal ^{3}He/^{4}He dilution refrigerator providing target temperature about 25 mK which ensures a polarization relaxation time up to 1000 hours. A superconducting holding coil integrated into the target cryostat provides 0.5 T longitudinal/transverse magnetic field to maintain the target polarization in the frozen-spin mode. The main goals of the experimental program using this polarized target represent a test of the Gerasimov-Drell-Hearn (GDH) sum rule for the nucleons at photon energies up to 1500 MeV as well as an investigation of the helicity structure of partial reaction channels.

1. Introduction

The study of the spin structure of the nucleon represents an important part of the physics program for the MAMI C accelerator. This will be attacked by doing double polarized experiments with the use of linearly or circularly polarized energy marked photons in combination with the new polarized solid state target and the Crystal Ball detector which will allow the determination of polarization observables with high accuracy.

In the study of spin-dependent reactions on the nucleon the experimental verification of the Gerasimov-Drell-Hearn (GDH) sum rule [1,2] and in more general terms a study of polarized photon cross-sections in a wide photon energy region from 140 to 1500 MeV is of special interest. The GDH sum rule relates static properties of the nucleon to the difference of the total photoabsorption cross sections for parallel (σ_p) and antiparallel (σ_a) photon-nucleon spin configurations:

$$\int_{\nu_{th}}^{\infty} (\sigma_p - \sigma_a)\frac{d\nu}{\nu} = \frac{2\pi^2\alpha}{m^2}k^2, \qquad (1)$$

where ν_{th} is the pion photoproduction threshold, α is the fine-structure constant, m and k are the nucleon mass and its magnetic moment. Since the model independent derivation of the GDH sum rule is based on very fundamental physical principles and the widely accepted no-subtraction hypothesis an experimental test of the sum rule also represents an experimental check of the underlying assumptions used in its derivation, if the integrand can be determined over whole energy range.

Apart from measurements of polarized total cross sections, which are needed for a test of the GDH sum rule, the determination of the polarized partial cross-sections of all meson photoproduction channels on proton and neutron is an important goal of the experiments. Polarized cross-sections of γN channels allow one to verify predictions of various nucleon models in a very detailed way. This certainly will lead to a development of improved nucleon models and to a growing understanding about the structure of the nucleon and its resonances.

To test experimentally the GDH sum rule the total cross section of circularly polarized photons on longitudinally polarized nucleons has to be measured. Circularly polarized photons are obtained as a result of the bremsstrahlung process of longitudinally polarized electrons and energy marked in the Glasgow-Edinburgh-Mainz tagger with a resolution of 2

MeV. The photon polarization is determined by a Møller polarimeter and the photon beam intensity is about $5 \cdot 10^5$ s^{-1}. These conditions require the use of a solid state target having a high density of polarized nucleons (of the order of 10^{23} cm^{-3}). The main detector system includes the Crystal Ball, consisting of 672 NaJ(Tl) crystals, in combination with the TAPS detector for the forward angles, leading to an angular acceptance close to 4π. To match the detector geometry the horizontal alignment of the refrigerator was used so that the beam axis coincides with the refrigerator axis. A general view of the experimental set-up at Mainz is shown in Fig. 1.

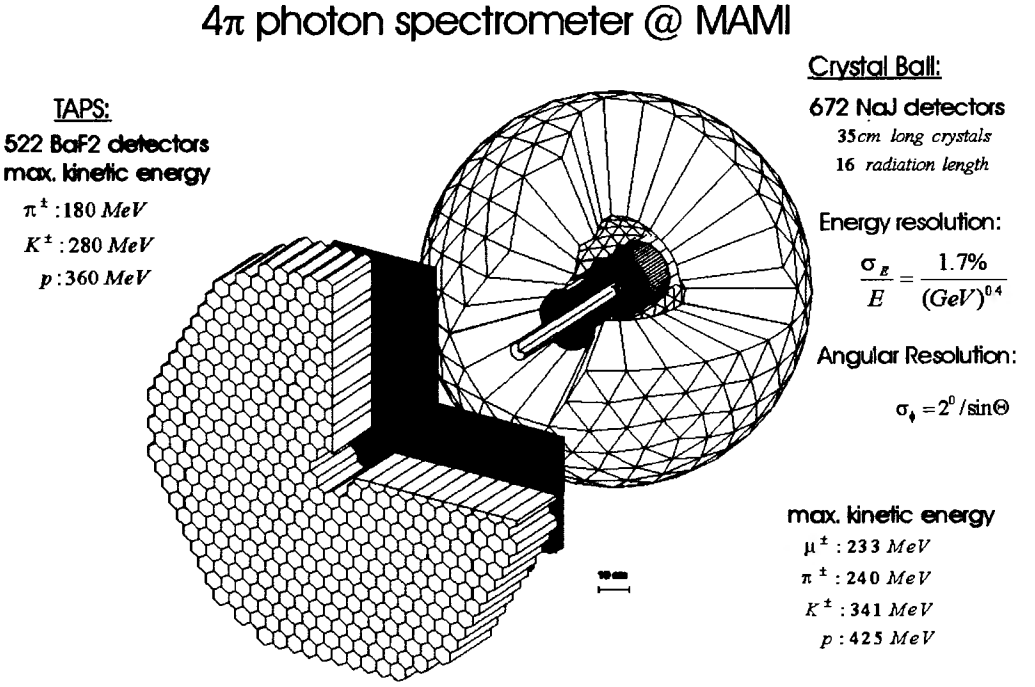

Fig. 1. General view of the experimental set-up at Mainz

2. Frozen spin target principle

In the thermal equilibrium the general form of the polarization degree for particles with spin S at absolute temperature T in external magnetic field B is given by the Brillouin function

$$P_S = \frac{2S+1}{2S}\coth\left(\frac{2S+1}{2S}\frac{g\mu BS}{kT}\right) - \frac{1}{2S}\coth\left(\frac{g\mu BS}{kT}\right) \qquad (2)$$

where g is the g-factor, μ the magnetic moment and k the Boltzmann constant. As follows from equation (2), in a magnetic field of 2.5 T at absolute temperature 1 K the polarization degree for electrons is more than 92% while for protons it is only 0.25% and for deuterons even less than 0.05%. A magnetic field of approximately 10 T and temperatures of 20 mK are necessary to polarize protons to a degree of 47%, the polarization degree of deuterons is then still only 10%. This way of polarizing protons and deuterons is called "brute force method". To obtain these conditions is very difficult and expensive, in addition detectors and outgoing particles are affected by the high magnetic field. Moreover, the build-up time for the final nucleon polarization in thermal equilibrium is some weeks due to the weak spin-lattice interaction. To overcome all these problems the nucleon polarization is enhanced by the principle of the dynamic nuclear polarization (DNP) [3,4]. In this method the coupled electron-nucleon system has to be considered. A double spin-flip transition of electron and nucleon is produced by the application of an external microwave field with the proper

frequency. The electron flips its orientation back in some milliseconds, while the nucleon at a temperature of 300 mK and a magnetic field 2.5 T keeps it for several hours. The electron couples again with another nucleon and the process continues. By this the polarization degree of the target material increases. Depending on the selected hyperfine transition (the microwave frequency), the nucleon spin could be aligned parallel or antiparallel to the external magnetic field. To drive the transition uniformly the target material has to be placed into the magnet with the field homogeneity better than 10^{-4} over the whole target sample (usually a large superconducting solenoid magnet surrounding the target completely is used, which, however, reduces strongly the angular acceptance).

To free the experiment from the constraint of having the target inside a big magnet and to allow large solid angle for observing scattered particles the frozen-spin method was developed [5,6]. The principle of the frozen-spin target is as follows. Once the maximum polarization degree is achieved via the DNP process the microwaves are turned off. At this moment the temperature is driven down to about 50 mK (or below), where the spins get "frozen" and the relaxation time increases drastically. Then the field of the polarizing magnet is reduced and an internal holding coil keeps the magnetic field at about 0.5 T. After that the polarizing magnet is removed and the detector is installed around the target.

As illustrated in Fig. 2, the frozen spin target can be divided into some subsystems: ^{3}He/^{4}He dilution cryostat with the internal holding coil, pumping system, polarizing magnet, microwave system, NMR system, and control system. The following sections will go into details of all these parts for the new Mainz target.

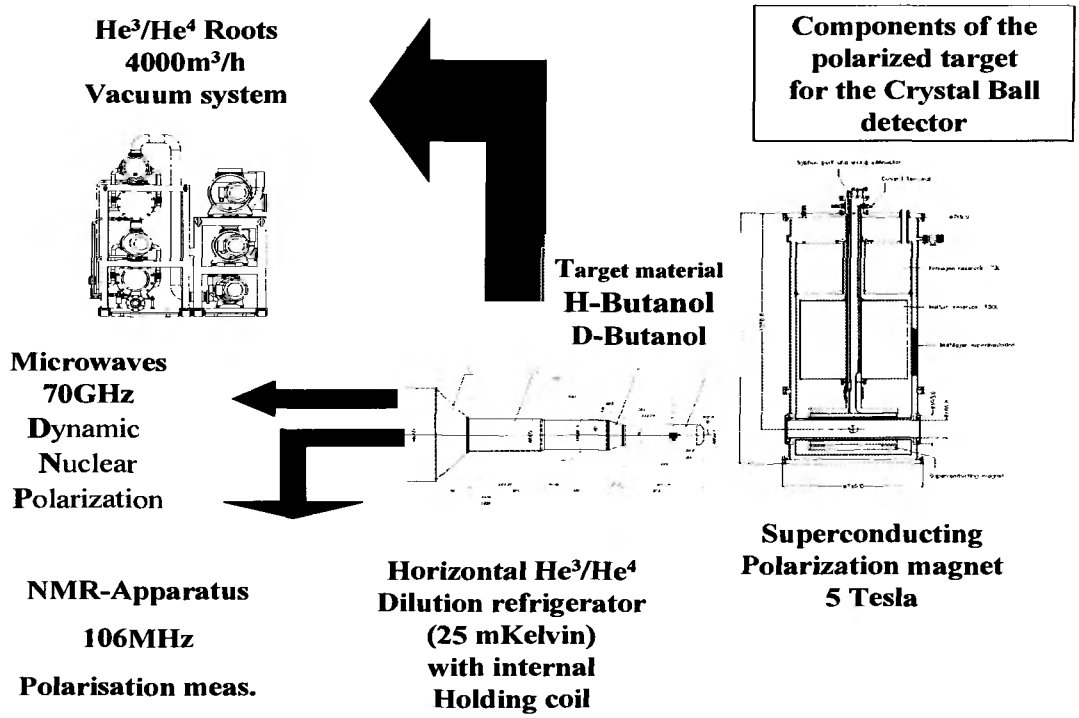

Fig. 2. Sketch of the frozen-spin target with its subsystems

3. ^{3}He/^{4}He dilution refrigerator

A central part of the target apparatus is the ^{3}He/^{4}He dilution refrigerator. In the case of the Mainz A2 real photon facility the beam cases neither serious heating problems nor the radiation damage problem for the target material in a typical experimental conditions. To provide a relaxation time of the order of 1000 hours for the target material in the frozen-spin

mode the refrigerator needs to have a base temperature well below 50 mK (preferably around 30 mK). On the other hand, to meet a requirement of a large thermal load in the DNP mode its cooling power at 200 mK must be over 10 mW.

Thus a horizontal refrigerator with axially symmetric geometry was built, its axis being along the photon beam axis. Total length of the refrigerator cryostat is about 2 meters and its diameter amounts to 65 mm in the target area and to 300 mm in the back part. Console type design was chosen with centering elements providing necessary mechanical rigidity and co-axiality. Cryogenic components are placed symmetrically around the beam tube which is a central part of the refrigerator. The dilution cryostat for the Mainz target was developed in close collaboration with the polarized target group of JINR (Dubna) which has a lot of experience in building this kind of facilities [7-11].

Schematic view of the dilution cryostat is shown in Fig. 3. To reduce a thermal heat load to the low-temperature components they are enclosed by an isolation vacuum and surrounded by two copper radiation shields. The outer shield consists of the upstream part (with the temperature below 80 K) and the downstream part (about 30 K). Two parts of the outer shield are thermally insulated from one another. To decrease a radiation heating a superinsulation is used. A possibility of the initial cooling of the massive upstream part of the outer shield by the liquid nitrogen is foreseen to shorten a pre-cooling period and provide essential economy of liquid ^{4}He. The inner radiation shield has a temperature as low as 1.5 K.

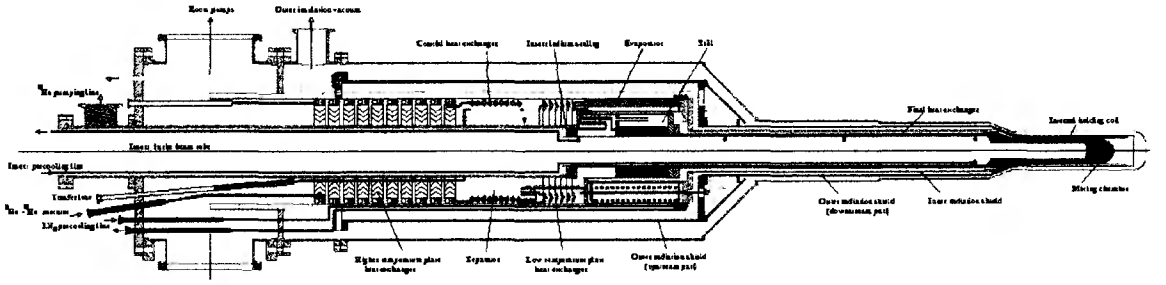

Fig. 3. Schematic view of the dilution cryostat

The dilution cryostat is cooled by the liquid ^{4}He introduced through the transfer line into the separator bath where the helium is separated in two phases: gas and liquid. Cold gas from the separator pumped by 60 m^3/h rotary pump circulates through heat exchangers cooling the outer shield. Another 100 m^3/h rotary pump reduces the vapor pressure above the liquid cooling down the separator to about 4 K.

Liquid ^{4}He from the separator can be supplied to the evaporator bath through the heat exchanger, used to liquefy the incoming ^{3}He, or directly via a bypass, the latter being used during a cool-down process when the flow resistance of the heat exchanger is too large for a warm gas. Two needle valves rule these alternatives. A 250 m^3/h rotary pump, exhausting the helium vapor from the evaporator, reduces its temperature to about 1.5 K. The pumped out vapor is also used to cool down incoming gas flows in respective heat exchangers. The evaporator surrounds and thermally isolates the still bath of the dilution unit.

The ^{3}He gas entering the refrigerator is cooled in a series of counter-current heat exchangers. Depending on the temperature gradient and the absolute temperature different designs of heat exchangers are used. Fig. 4 shows a schematic view of the high-temperature heat exchangers, which pre-cool the ^{3}He gas from room temperature to about 4 K. A tube with the incoming ^{3}He is soldered to a capillary that carries the outgoing ^{4}He gas from the separator. Both tubes are fixed to a perforated copper radiator with ribs which ensure a maximum surface area in contact with the ^{3}He gas pumped out from the still. A total of 7 such radiators are used. Two warmest radiators have conical ribs, other five radiators have

cylindrical ribs. Additionally, an inner tube, used to pump out the cold ^{4}He gas from the evaporator (through an annular space between this tube and the central beam tube), is also anchored to these copper radiators.

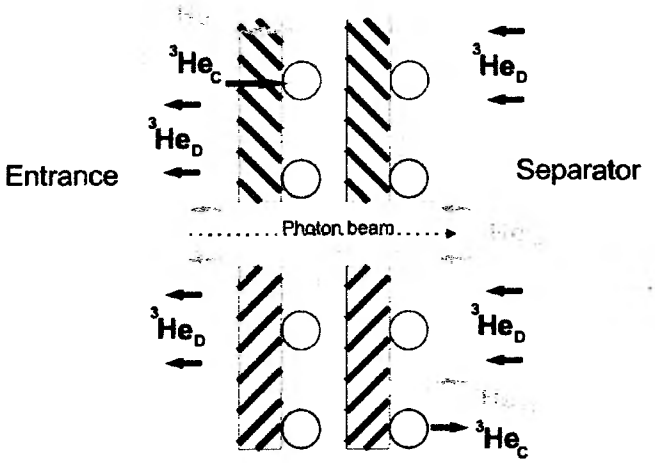

Fig. 4. High-temperature heat exchanger of the ^{3}He pre-cooling stage

The intermediate tube-in-tube heat exchanger consists of seven 2-mm diameter stainless steel capillaries, inserted in 10-mm diameter tube. The incoming ^{3}He moves in the space between the capillaries and the external tube while the liquid ^{4}He from the separator goes out through the capillaries. This heat exchanger is placed between the separator bath and the inner tube used for pumping out the ^{4}He gas from the evaporator.

The final gas heat exchanger, which reduces a temperature of the ^{3}He from 4 K to approximately 2 K, consists of four consecutively connected stages of similar design located between the separator and the evaporator. Each stage includes a perforated copper disk cooled by the ^{3}He gas pumped from the still. Three tubes are spiraled and soldered to the disk. The largest tube contains outgoing cold ^{4}He gas from the evaporator. Warmer ^{4}He from the separator flows through one of smaller tubes; if necessary it can also go directly to the evaporator via a bypass. The incoming ^{3}He flows through the third tube where its condensation starts at about 2.5 K. The liquefied ^{3}He pass first through a helix capillary placed inside the evaporator bath and then through the second helix capillary inside the still that reduces ^{3}He temperature to about 0.8 K.

A temperature in millikelvin range, necessary for normal functioning of the frozen-spin target, is obtained in the dilution unit which consists of the still, the counter-current heat exchangers and the mixing chamber. This unit provides a continuous cooling of the target sample located in the mixing chamber using ^{3}He/^{4}He dilution process. The still bath having a volume about 80 cm^3 contains a heater which helps to obtain the necessary circulation rate of ^{3}He in the DNP and frozen-spin modes. Carbon resistance thermometers are also placed inside the still. Downstream part of the dilution unit with the heat exchangers and the mixing chamber is connected to the still by an indium seal. Base temperature of the refrigerator and its cooling power depend directly on the characteristics of the heat exchangers in the dilution unit. Two heat exchangers are used in our dilution unit: a coiled tube heat exchanger and a sectioned sintered copper heat exchanger. The latter consists of 10 consecutive stages and has a total heat exchanging area about 5 m^2 for both concentrated (^{3}He$_C$) and diluted (^{3}He$_D$) phases. Fig. 5 illustrates schematically a design of the sintered heat exchanger. Using this heat exchanger, the temperature of 25 mK was reached at a ^{3}He circulation rate about 1.5 mmol/s.

The working substance of the target (butanol) is placed in a cylindrical 6-cm^3 container made of Teflon. This container is mounted at the end of an insert which also carries a microwave guide and an NMR cable. By moving the insert inside the beam tube from the

upstream side the container with the target sample is placed inside the mixing chamber of the refrigerator. To insulate the dilution unit against the beam tube vacuum a cold indium seal is used, which is located at a level of the upstream flange of the evaporator. In a procedure of indium sealing remote screwdrivers mounted inside the insert are used. After fixing the insert both the indium seal and the dilution unit are cooled down to helium temperature with a help of a forced cooling line provided in the insert. To minimize the heat load on the mixing chamber by a thermal radiation along the beam tube four 10-μm foils of aluminium-covered Mylar are placed in the insert.

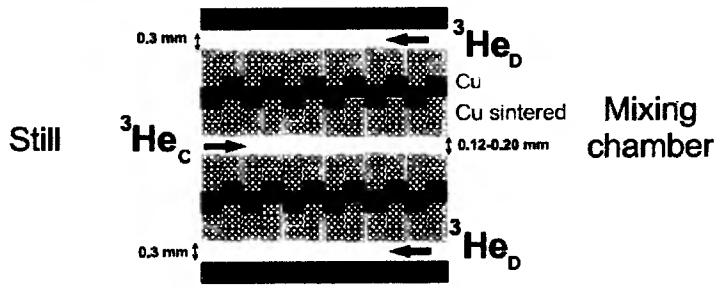

Fig. 5. Sintered copper heat exchanger of the dilution unit

4. ^{3}He pumping and circulation system

The ^{3}He pumping system includes five roots pumps developed by the company Pfeiffer Vacuum. They have a pumping speed of 4000 m^3/h, 2000 m^3/h, 1000 m^3/h, 500 m^3/h and 250 m^3/h respectively. A rotation speed of the biggest one could be changed in order to adjust the ^{3}He flow. They are oil-free pumps and the leak rate is less $5 \cdot 10^{-5}$ mbar·l/s. Pressure sensors are connected before and after each pump to monitor the pressure difference. In order to avoid overheating of the compressed gas, integrated water-cooled gas coolers are placed after the high-pressure stages. This system pumps the outcoming gas from the refrigerator through the valve with a 200-mm diameter hole. The ^{3}He gas from the exit of the pumping system goes through a liquid nitrogen-cooled charcoal trap which cleans the gas from traces of water, oil and air, passes the flow-meter and finally enters the cryostat. Two parallel lines, each containing a cleaning trap, are used which work in turn.

5. Polarizing magnet

In order to polarize the target material a superconducting magnet manufactured by the Cryogenic Limited was used. The magnet is able to produce a magnetic field up to 5 T with a homogeneity $\leq 10^{-4}$. A construction of the magnet is shown in Fig. 6. A superconducting solenoid consists of a single block of multifilamentary NbTi wire wound onto a stainless steel former. The conductor is casted in epoxy resin to prevent wire movement. A cryostat of the magnet contains a 70-l liquid nitrogen bath and a 100-l liquid helium bath. The liquid helium consumption of the magnet at 2.5-T magnetic field used during the polarization build-up is about 2 l/h. The cryostat has a 100-mm diameter warm bore which encloses the target material completely in the DNP mode. After switching to the frozen-spin mode the magnet was removed from the refrigerator in order to place the Crystal Ball detector in the data-taking position (as shown in Fig. 1). The polarizing magnet and the detectors are mounted on a railway system which allows to place them into reproducible positions.

The magnet control system was developed mainly by the Cryogenic Limited. The power supply incorporates a sophisticated microprocessor unit, with all operations being monitored through the internal firmware. It is connected to a PC and is completely controlled by a LabView program. The ramping speed and maximum current can be set, and the induced

magnetic field is continuously displayed. The temperature sensors and the helium level gauge are verified at any time by the program.

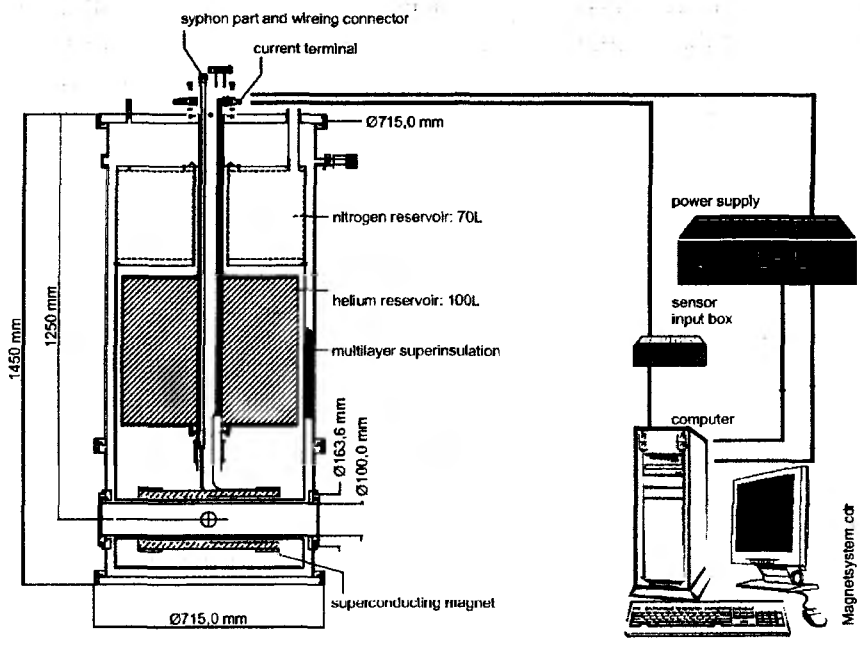

Fig. 6. A design of the polarizing magnet

6. Internal holding coil

A superconducting internal holding coil placed inside the cryostat of the refrigerator keeps the target polarization in the frozen-spin mode when the external magnet is removed. A design of the holding coil is similar to that used in the Bonn frozen-spin target [12]. It is manufactured of 0.227-μm NbTi-wire and consists of four layers, each having 600 turns wound around a 0.3-mm thick copper holder. The holder is in a thermal contact with the evaporator which cools the coil to a temperature below 1.5 T. To load a current from a power supply at room temperature to the coil at about 1.5 K a high-temperature superconducting band from the Trithor company was used. It has a critical current of 70 A at 77 K. A maximum field obtained with this holding coil reached 0.5 T. Two versions of the holding coil (a solenoid and a saddle-shaped coil) permit to support both longitudinal and transverse polarization.

7. Microwave system

The microwave system was designed, tested and successfully used for the Mainz GDH experiment on the neutron in 2003. Since then some minor changes have been made. Fig. 7 illustrates a schematics of the system. A Varactor IMPATT (IMPact ionization Avalanche Transit-Time) diode is used as a microwave source. It is able to deliver about 150 mW with a central frequency of 70 GHz (tunable around ±200 MHz by an external power supply). This corresponds to the Larmor frequency of the electron in a magnetic field of 2.5 T. The Larmor frequencies of the proton and the deuteron for this magnetic field are 106 MHz and 16 MHz respectively. For a fast polarization build-up a microwave power of 2-3 mW/cm^3 is required which amounts to about 15 mW for a 6-cm^3 target.

To obtain a reliable frequency value a frequency counter 598A from Phase Matrix was used. It can measure continuous signals from 100 Hz to 170 GHz and perform pulsed measurements from 250 MHz to 170 GHz. It is steered by a computer. Data are processed in a

LabView program that controls the total set-up. A spectrum analyzer type preselector prevents harmonics and other spurious signals from interfering with the measurement of the desired signal. Additionally, it totally eliminates a noise. The YIG (Yttrium Iron Garnet) filter provides effective power limiting to protect against burnout, and does not reduce sensitivity.

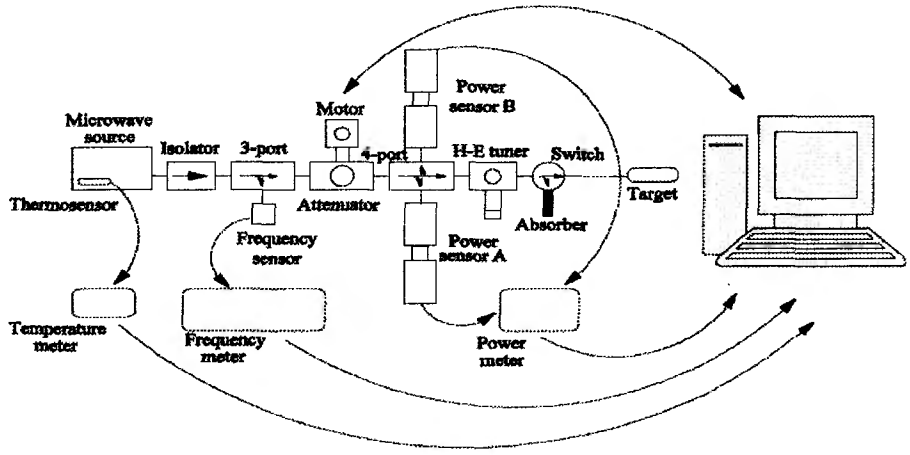

Fig. 7. Microwave system

The system also contains two sensors which measure incoming and reflected microwave power. They are connected to the computer and the signals are processed by the LabView program. With this setup it is possible to control and monitor the power and save all data for later analysis. The time needed to polarize the target material depends on the power, the optimum power can be tuned using an attenuator with a range up to 30 dB. This attenuator controls the power fed into the target material, while the frequency is adjusted by the applied voltage. Finally, an H-E tuner matches impedances of the microwave generator and the transmission waveguide to the cryostat cavity.

A frequency generator modulates the control voltage applied to the microwave source, and therefore the microwave signal. This can optimize the maximum degree of polarization and the polarization build-up rate.

8. NMR system

Since all measured physical asymmetries scale with the degree of the target polarization P, the latter should be measured with the best possible accuracy. A nuclear magnetic resonance (NMR) system is used to determine the P value. For this purpose a coil is placed around the target material. The coil acts as a probe in a serial resonance LC circuit that measures the Q factor. The circuit is driven at the nucleon Larmour frequency to induce transitions between the nucleon Zeeman levels. Changes in the polarization degree induce changes in the magnetic susceptibility of the target material and this will modify the impedance of the coil that can be seen by the Q-meter. NMR signal is obtained by a frequency sweep over the resonance Larmour frequency using Rohde & Schwarz generator capable to produce frequencies from 5 kHz up to 1.5 GHz. In order to increase the signal to noise ratio many sweeps are accumulated (the noise reduces as a square root of the number of sweeps). Initially the NMR system with so-called Liverpool Q-meter was used (Fig. 8). However, the HF Liverpool NMR box is no longer commercially available, and it was replaced by Minicircuits HF components. They create a circuit that amplifies the NMR signal and processes it. The processed signal goes via a PCI-68M I/O M-series board (National Instruments) to the PC, where a LabView program reads and analyzes it.

9. Control system

The subsystems of the frozen-spin target present different requirements to the control system, from the fast NMR readout to the slow control of the cryostat. Another important task is given by safety considerations. The main idea is to have a modular control for each subsystem integrated in the same software in order to allow easy data transfer from one to another. Each of the NMR, polarizing magnet and microwave systems has a dedicated Windows PC with a LabView software installed on it. In the previous sections an explanation of these parts was given, thus in this section an attention will focus on the cryostat control system.

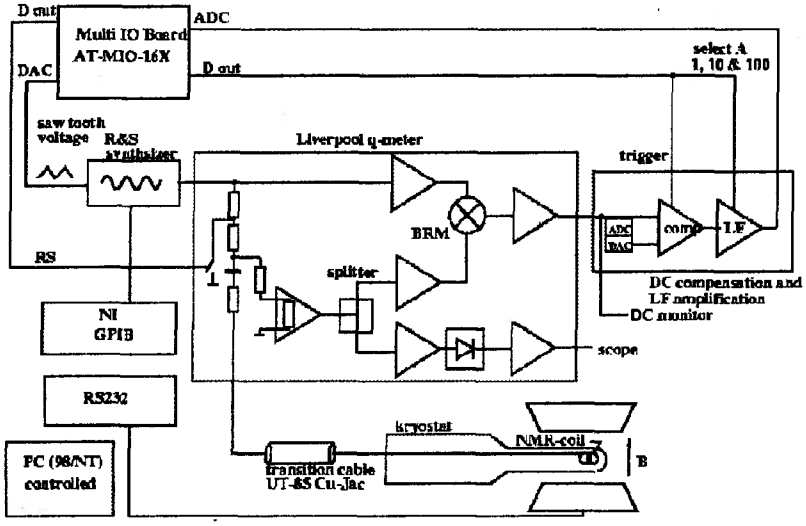

Fig. 8. NMR system with a Liverpool Q-meter

The cryostat control system is showed schematically in Fig. 9. Temperatures inside the cryostat are monitored with secondary thermometers including one calibrated RuO and different PT100, Allen Breadley, Speer and TVO resistors. AVS resistor bridges measure the resistance precisely and without disturbing noise. A Keithley digital voltmeter monitors less important sensors. Both AVS and voltmeter are connected to the computer via GPIB, and the LabView program reads the values. The AVS resistor bridge is optically coupled with the computer to avoid an influence of the GPIB bus clock frequency.

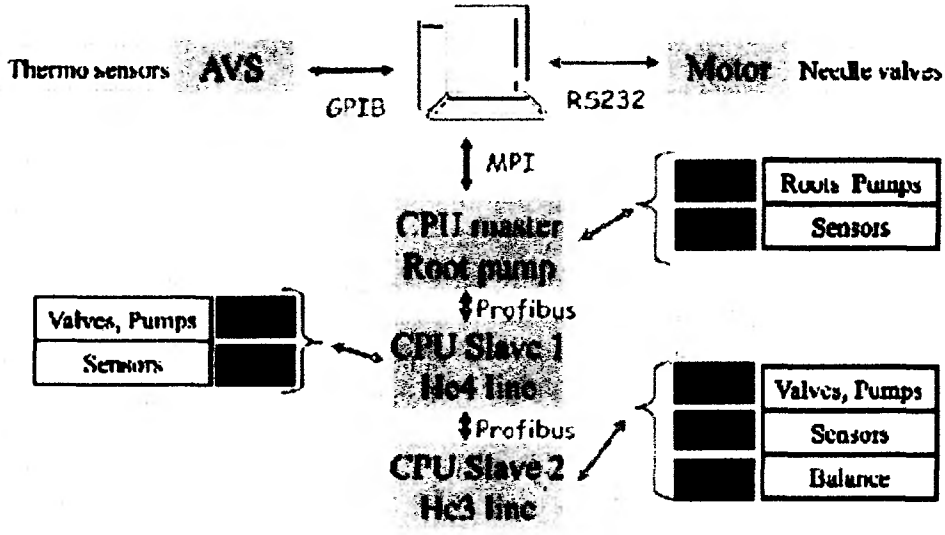

Fig. 9. Schematic view of the cryostat control system

The gas flows in different stages of the refrigerator are adjusted with 5 needle valves, driven by the step motors. A LabView interface was developed that can be used to set the positions of the needle valves in order to optimize the refrigerator functioning. The rest of the valves, pressure gauges, flow meters, and pumps are handled with three Simatic CPUs. One CPU operates the Roots Pumps unit, another runs the ^{4}He pre-cooling stage and the third one controls the ^{3}He line. The CPU of the Roots Pumps unit acts as a master, and it is connected to the two slaves via the Profibus, and to the computer by an MPI cable. Each CPU has some modules for Digital Input/Output and Analog Input/Output signals, which are connected to the CPU that runs the Simatic Step7 control software. An intuitive LabView interface was created, where all the parameters are shown. Step7 and LabView are connected using AGlink software.

10. Summary

The new solid-state polarized target suitable for an investigation of the spin structure of nucleons by doing double polarization experiments at the MAMI C accelerator was developed. The horizontal design of the dilution refrigerator and the use of a thin internal holding coil enable the placement of the Crystal Ball detector directly around the forward end of the refrigerator to keep the high angular acceptance of the detector system. Complete test of the target facility has been performed in July 2009. High proton polarization was achieved and measured. In the frozen-spin mode temperatures well below 30 mK were reached which correspond to long polarization relaxation times (up to 1000 hours). It means that during experiments the nucleon polarization has to be refreshed only about twice a week resulting in more efficient data-taking. First beam test with the frozen-spin target is scheduled for December 2009. Some future experiments are listed below:

- experimental verification of the Gerasimov-Drell-Hearn (GDH) sum rule in the energy range up to 1500 MeV;
- helicity dependence of π^0, $\pi^0\pi^0$, $\pi^0\pi^+$ and η production on the proton in the region of the $D_{13}(1520)$ and $F_{15}(1680)$ resonances (requires circularly polarized photons and longitudinally polarized protons);
- measurement of the G asymmetry in $\gamma p \rightarrow p\pi^0$ and $\gamma p \rightarrow n\pi^+$ (sensitive to the Roper resonance $P_{11}(1440)$; requires linearly polarized photons and longitudinally polarized protons);
- photoproduction of η-mesons on the neutron: measurement of double polarization observable E (sensitive to D_{15} (1675) resonance; requires circularly polarized photons on longitudinally polarized deuterons).

References

1. S. B. Gerasimov. Sov. J. Nucl. Phys. 2 (1966) 430.
2. S. D. Drell and A. C. Hearn. Phys. Rev. Lett. 16 (1966) 908.
3. A. W. Overhauser. Phys. Rev. 92 (1953) 411.
4. T. R. Carver and C. P. Slichter. Phys. Rev. 92 (1953) 212.
5. T. J. Schmugge and C. D. Jeffries. Phys. Rev. 138 (1965) A1785.
6. T. O. Niinikoski and F. Udo. Nucl. Instr. Meth. 134 (1976) 219.
7. B. S. Neganov, N. S. Borisov and M. Yu. Liburg. JETP 50 (1966) 1445.
8. B. S. Neganov. Vestn. Akad. Nauk SSSR 12 (1968) 49.
9. F. Lehar et al. Nucl. Instr. Meth. A356 (1995) 58.
10. N. A. Bazhanov et al. Nucl. Instr. Meth. A402 (1998) 484.
11. Y. Usov. Nucl. Instr. Meth. A526 (2004) 153.
12. C. Bradtke et al. Nucl. Instr. Meth. A436 (1999) 430.

EXPERIMENTAL-THEORETICAL EVALUATION OF PARTIAL PHOTONEUTRON REACTIONS σ(γ,nX) AND σ(γ,2nX) CROSS SECTIONS FOR SN ISOTOPES

V.A. Chetvertkova, B.S. Ishkhanov, V.N. Orlin, V.V. Varlamov

Skobeltsyn Institute of Nuclear Physics and Physics Faculty, Lomonosov Moscow State University
119991 Moscow, Russia

Introduction

Photonuclear reaction data are very important for many basic research such as investigations of structure and dynamic of atomic nucleus and nuclear reaction mechanisms. At the same time they are widely used for variety of applications (radiation shielding design, radiation transport analysis, activation analysis, astrophysical nucleosynthesis, safeguards and inspection technologies, human body radiotherapy absorbed dose calculation, etc.). Various parameters of photonuclear reactions are needed, but reaction cross section energy dependence (excitation function - probability of interaction of definite energy photons with nucleus) is the most important one. After absorption of initial γ-quanta excited nucleus emits nucleons or their combinations. With the most probability one nucleon is emitted, with the less one two and more nucleons are emitted. That circumstance together with the energy threshold values for correspondent reactions define the total photoabsorption cross section

$$\sigma(\gamma,abs) = \sigma(\gamma,n) + \sigma(\gamma,np) + \sigma(\gamma,n2p) + \sigma(\gamma,2n) + \sigma(\gamma,2np) + \sigma(\gamma,2n2p) + \sigma(\gamma,3n) + \sigma(\gamma,3np) + \sigma(\gamma,3n2p) + \ldots + \sigma(\gamma,f) \quad (1)$$

including those for main Giant Dipole Resonance (GDR) decay channels.

Balance of cross sections of reactions with several (primarily 1 and 2) outgoing neutrons is very important characteristic of nucleus photodisintegration processes such as competition of various decay channels, roles of direct and statistical processes, effects of GDR configurational and isospin splitting and many others.

But experimental investigations of photonuclear reactions with various numbers of outgoing products are very complicated because, first of all, closeness (Table 1) of various reactions thresholds [1].

Table 1

Stable Sn isotopes abundances in natural mixture and energy thresholds of main photonuclear reactions

Isotope	Abundance, %	Reaction threshold, MeV								
		B_n	B_p	B_{2n}	B_{2p}	B_{np}	B_{3n}	B_{3p}	B_{2np}	B_{4n}
^{112}Sn	0.97	10.8	7.6	19.0	12.9	17.6	30.2	21.8	25.6	38.9
^{114}Sn	0.65	10.3	8.5	18.0	14.6	17.9	28.8	24.2	25.6	37.0
^{116}Sn	14.53	9.6	9.3	17.1	16.1	18.3	27.4	26.4	25.6	35.2
^{117}Sn	7.68	6.9	9.4	16.5	16.9	16.2	24.1	27.3	25.3	34.4
^{118}Sn	24.23	9.3	10.0	16.3	17.5	18.8	25.8	28.5	25.6	33.4
^{119}Sn	8.59	6.5	10.1	15.8	18.2	16.5	22.8	29.4	25.3	32.3
^{120}Sn	32.59	9.1	10.7	15.6	19.0	19.2	24.9	30.7	25.6	31.9
^{122}Sn	4.63	8.8	11.4	15.0	20.6	19.6	24.1	33.3	25.7	30.6
^{124}Sn	5.79	8.5	12.1	14.4	22.1	20.0	23.3	35.4	25.8	29.4

That is very clear that for energies higher then threshold B_{2n} of reaction (γ,2n) registration of neutron must be accompanied by identification of reaction - (γ,n), (γ,2n), (γ,3n),... – in which that neutron was produced. Without such identification only cross section for the total neutron yield reaction

$$\sigma(\gamma,xn) \approx \sigma(\gamma,n) + 2\sigma(\gamma,2n) + 3\sigma(\gamma,3n) + 4\sigma(\gamma,4n) + \ldots, \quad (2)$$

in which partial reaction cross sections are included with correspondent multiplicities (1, 2, 3, 4, ...) can be determined. One can see from the data of Table 1 that studying photodisintegration of Sn isotopes besides neutron decay channels those in which emission of neutron is accompanied by proton emission must be taken into account. For example for ^{112,114,116}Sn $B_p < B_n$ and for several isotopes $B_{np} \approx B_{2n}$. Because that reason the equation

$$\sigma(\gamma,xn) \approx \sigma(\gamma,nX) + 2\sigma(\gamma,2nX) + 3\sigma(\gamma,3nX) + 4\sigma(\gamma,4nX) \ldots, \quad (3)$$

where "X" means the sum of all processes in which emission of one or two neutrons is accompanied by emission of other particles must be used instead of (2). It must be pointed out that in the energy range investigated (E < 25 MeV) cross sections $\sigma(\gamma,3nX)$ and all the more $\sigma(\gamma,4nX)$ are small and moreover for many Sn isotopes are not well known.

Different methods are used for identification of neutrons from the reactions (γ,nX) and (γ,2nX). In experiments used quasimonoenergetical annihilation (QMA) photons for determination of neutron multiplicity its mean kinetic energy was used. In experiments used bremsstrahlung (BR) for determination of various multiplicity neutron parts the equation of statistical theory of nuclear reaction was used [2].

Essential difference between those methods is the reason for clear disagreements between data obtained in various experiments. Many special works [3 – 6] were devoted to investigation of such systematical disagreements reasons, to development of methods for overcoming such disagreements and to joint evaluation of various experiments results. Results of Sn isotopes investigations [7 – 11] give to one rich experimental material for various experiments joint analysis and evaluation and for obtaining of reliable data for partial reaction cross sections.

In this work the way for such reactions cross sections evaluation free from shortcomings of neutron multiplicity sorting problems is proposed. It uses experimental data for only total photoneutron yield reaction cross sections $\sigma^{exp}(\gamma,xn)$ and theoretically calculated data describing competition of reactions with one, two and more neutrons for determination of their contributions into $\sigma^{exp}(\gamma,xn)$. Such treatment became fruitful at last time because of evident progress in describing of various channels of GDR excitation and decay and their competition for many nuclei and for various Sn isotopes among them [12 – 14]. In the frame of preequilibrium model based on Fermi gas densities [13, 14] it was possible to investigate in details the effects of nucleus deformation and GDR isospin splitting on GDR excitation and decay processes.

1. Experimental data on photoneutron reaction cross sections for ^{112,114,116,117,118,119,120,122,124}Sn

Total photoneutron yield reaction cross sections $\sigma^{exp}(\gamma,xn)$ (3) and separately parts $\sigma^{exp}(\gamma,nX)$ and $\sigma^{exp}(\gamma,2nX)$ for Sn isotopes were obtained in BR- [7 – 9] and QMA- [10, 11] experiments (Table 2).

In BR-experiments (Russia Moscow State University Institute of Nuclear Physics [7 – 9]) partial reaction cross sections were obtained via the following way. At various values of bremsstrahlung photon spectrum end-point energy E^{max} the experimental yields $Y(E^{max})$ for total photoneutron yield reaction (γ,xn) (3) were measured

$$Y(E^{max}) = \alpha \int_{Eth}^{E^{max}} W(E^{max}, E)\sigma(E)dE, \quad (4)$$

where $\sigma(E)$ - is cross section of the reaction $\sigma(\gamma,xn)$ with threshold E_{th} at photon energy E;

$W(E^{max},E)$ - is bremsstrahlung photons spectrum with end-point energy E^{max};

α - is normalization constant.

Table 2

Information about photoneutron reaction cross section experiments for Sn

Isotope	$\sigma^{exp}(\gamma,xn)$		$\sigma^{exp}(\gamma,nX)$		$\sigma^{exp}(\gamma,2nX)$	
	BR	QMA	BR	QMA	BR	QMA
^{112}Sn	[7]		[7]*		[7]**	
^{114}Sn	[8]		[8]*		[8]**	
^{116}Sn	[8]	[10, 11]	[8]*	[10, 11]	[8]**	[10, 11]
^{117}Sn	[8]	[10, 11]	[8]*	[10, 11]	[8]**	[10, 11]
^{118}Sn	[7]	[12, 13]	[7]*	[10, 11]	[7]**	[10, 11]
^{119}Sn	[18, 9]	[10]	[9]*	[10]	[9]**	[10]
^{120}Sn	[7]	[10, 11]	[7]*	[10,11]	[7]**	
^{122}Sn	[8]		[8]*		[8]**	
^{124}Sn	[8]	[10, 11]	[8]*	[10, 11]	[8]**	[10, 11]

* $\sigma^{exp}(\gamma,nX)$ reaction cross section data, obtained (see further (7)) using data [7 - 9].

** $\sigma^{exp}(\gamma,2nX)$, полученные reaction cross section data, obtained (see further (6)) using data [7 - 9].

After that cross section $\sigma(E)$ of reaction (γ,xn) were obtained by the solution of integral equations system (4) using the variable-bin method of Penfold-Leiss. Twiced contribution of $\sigma^{exp}(\gamma,2nX)$ into $\sigma^{exp}(\gamma,xn)$ were taking into account using special corrections obtained in the frame of statistical theory of nuclear reactions [2] and total photoneutron reaction cross sections were obtained:

$$\sigma^{exp}(\gamma,sn) = \sigma^{exp}(\gamma,nX) + \sigma^{exp}(\gamma,2nX) = \sigma^{exp}(\gamma,xn) - \sigma^{exp}(\gamma,2nX). \quad (5)$$

We used published [7 – 9] data for $\sigma^{exp}(\gamma,xn)$ and $\sigma^{exp}(\gamma,sn)$ for determination (symbols «*» and «**» in Table 2) of $\sigma^{exp}(\gamma,nX)$ and $\sigma^{exp}(\gamma,2nX)$:

$$\sigma^{exp}(\gamma,2nX) = \sigma^{exp}(\gamma,xn) - \sigma^{exp}(\gamma,sn), \quad (6)$$

$$\sigma^{exp}(\gamma,nX) = \sigma^{exp}(\gamma,sn) - \sigma^{exp}(\gamma,2nX) = \sigma^{exp}(\gamma,xn) - 2\sigma^{exp}(\gamma,2nX). \quad (7)$$

In QMA-experiments (USA National Lawrence Livermore Laboratory [10] and at France Centre d'Etudes Nucleaires de Saclay [11]) because annihilation photons always are accompanied by positron bremsstrahlung, experiment is carried out by three steps:

1) measurement of the reaction yield $Y_{e+}(E)$ (4) under the action of photons both from positron bremsstrahlung and annihilation;
2) measurement of the reaction yield $Y_{e-}(E)$ (4) under the action of photons from electron bremsstrahlung;
3) subtraction (under appropriate normalization and with assumption that bremsstrahlung spectra are identical for electrons and positrons)

$$Y_{e+}(E) - Y_{e-}(E) = Y(E) \approx \sigma(E) \quad (8)$$

and interpretation of that difference as reaction cross section under investigation.

For separation of partial reaction cross sections $\sigma^{exp}(\gamma,nX)$ and $\sigma^{exp}(\gamma,2nX)$ the dependencies of neutron multiplicity on neutron mean kinetic energy were used. For that at Livermore [10] the "ring-ratio method" was used. In that it was supposed that ratio of counting rate in the outer ring of neutron detectors to that in the inner ring is strong, monotonically increasing function of the energy of photoneutrons. At Saclay [11] the large Gd-loaded liquid scintillator calibrated by means of radioactive source was used for mean photoneutron energy measurement.

2. Systematical disagreements of photoneutron reaction cross sections for $^{112,114,116,117,118,119,120,122,124}Sn$

Things described show that the conditions of various experiments [7 – 11] under discussion are quite different. So it is not so surprisingly that significant disagreements were found out both in shape and value of identical reactions cross sections. It is very important to point out that the differences between experimental cross sections are bigger (in many cases much more) than statistical uncertainties. The most clear are disagreements have place for energies higher threshold B_{2n} of reaction $(\gamma,2nX)$. For example Table 3 contains comparison of partial photoneutron reaction cross section data obtained in two QMA-experiments [10, 11].

Table 3

Data [6] on integrated cross section ratios of reactions (γ,nX) and $(\gamma,2nX)$ obtained at Saclay [11] and Livermore [10] ($E_{int\text{-}min}$ and $E_{int\text{-}max}$ – low and high integration limits)

Nucleus	$E_{int\text{-}min}$, MeV	$E_{int\text{-}max}$, MeV	$R(n) = \sigma^{S}_{int}(\gamma,n)/\sigma^{L}_{int}(\gamma,n)$, arb. units	$R(2n) = \sigma^{S}_{int}(\gamma,2n)/\sigma^{L}_{int}(\gamma,2n)$, arb. units
^{116}Sn	17.1	22.1	1.10	0.92
^{117}Sn	16.7	21.1	1.02	0.93
^{118}Sn	16.3	21.6	1.07	0.86
^{120}Sn	15.6	22.4	1.00	0.86
^{124}Sn	14.6	21.6	0.93	0.94

Typical disagreements between the results of QMA- and BR-experiments are illustrated also on the Fig. 1 (for example data for ^{120}Sn are presented). One can see that i) cross sections $\sigma^{exp}(\gamma,nX)$ from [11] have larger values than those from [10] and [7 – 9] which are close to each other and ii) cross sections $\sigma^{exp}(\gamma,2nX)$ from [11] have smaller values than those from [10] and [7 – 9], the last ones have the biggest values.

Data from the Table 3 generally confirm existence of problems investigated in [3 – 6] and connected with not enough reliability of the QMA-methods for partial reaction separation. In BRA-experiments the main shortcoming for that is using of statistical theory, because it is known [16, 17] that direct processes have noticeable (till 20 %) contribution into photodisintegration of many nuclei.

At the same time from the data of Table 3 and Fig. 1 one can see that for isotopes Sn under investigation disagreements between various experiments are not inadmissibly large and therefore all of them can be compared with evaluated (see further) reaction cross sections $\sigma^{eval}(\gamma,nX)$ and $\sigma^{eval}(\gamma,2nX)$.

3. The new treatment to partial photoneutron reaction cross sections analysis

In connection with all mentioned above the new treatment to joint analysis and evaluation of partial photoneutron reaction cross sections on Sn in definite degree free from

neutron multiplicity sorting shortcomings is proposed. As initial experimental information it is using only data for total neutron yield reaction cross section $\sigma^{exp}(\gamma,xn)$. For evaluation of partial reaction cross sections $\sigma^{eval}(\gamma,nX)$ and $\sigma^{eval}(\gamma,2nX)$ contributions into $\sigma^{exp}(\gamma,xn)$ theoretically calculated [13, 14, 18] cross sections $\sigma^{theor}(\gamma,xn)$, $\sigma^{theor}(\gamma,nX)$ and $\sigma^{thear}(\gamma,2nX)$ are used. In details the equations obtained in the frame of preequilibrium model of photonuclear reaction based on the Fermi gas densities and taking into account the effects of nucleus deformation and Giant Dipole Resonance (GDR) isospin splitting are presented in [15].

In Fig. 2 there is presented the example (^{124}Sn) of cross sections for various reactions calculated [13, 14] till the energy ~ 100 MeV for pure neutron GDR decay channels (γ,0pkn) and for most intensive other decay channels – those with 1 (γ,1pkn) and two (γ,2pkn) protons. One can see various GDR decay channels competition.

In the frame of proposed treatment for separation of reaction with 1 and two outgoing neutrons (γ,nX) and (γ,2nX) reactions cross sections were evaluated by the following way:

- theoretically calculated [13, 14] cross sections $\sigma^{theor}(\gamma,nX)$, $\sigma^{theor}(\gamma,2nX)$,... were combined into the total neutron yield reaction cross section

$$\sigma^{theor}_{(\gamma,xn)}(E) = \sigma^{theor}_{(\gamma,nX)}(E) + 2\sigma^{theor}_{(\gamma,2nX)}(E) + \ldots; \quad (9)$$

- for each energy E special transition multiplicity function F(E) was constructed (Fig. 3)

$$F(E) = \sigma^{theor}_{(\gamma,2nX)}(E)/\sigma^{theor}_{(\gamma,xn)}(E) = \sigma^{theor}_{(\gamma,2nX)}(E)/[\sigma^{theor}_{(\gamma,nX)}(E) + 2\sigma^{theor}_{(\gamma,2nX)}(E)]; \quad (10)$$

- using F(E) and experimental data for total neutron yield reaction cross section $\sigma^{exp}(\gamma,xn)$ (3) evaluated partial reaction cross sections were obtained for each experiments ([7, 8], [10], [11])

$$\sigma_{exp}{}^{eval}_{(\gamma,2nX)}(E) = F(E)\cdot\sigma^{exp.}_{(\gamma,xn)}(E) \quad (11)$$

and

$$\sigma_{exp}{}^{eval}_{(\gamma,nX)}(E) = \sigma^{exp}_{(\gamma,xn)}(E) - 2\sigma_{exp}{}^{eval}_{(\gamma,2nX)}(E) = \sigma^{exp}_{(\gamma,xn)}(E) - 2F(E)\cdot\sigma^{exp}_{(\gamma,xn)}(E) = \\ = (1 - 2F(E))\cdot\sigma^{exp}_{(\gamma,xn)}(E). \quad (12)$$

It must be pointed out that because the model [13, 14] taking into account the main mechanisms that define various GDR decay channels competition function F properties resulted from its definition (10) do this function very comfortable tool for analysis of reliability of 1 and two neutron outgoing processes separation. That can be shown by the following typical features of energy dependencies F(E) calculated for all Sn isotopes under discussion (presented in Fig. 3):

- follow definition (10) F(E) have threshold character because of presence of threshold cross section $\sigma(\gamma,2nX)$ in numerator: F(E) = 0 for energies $E < B_{2n}$, at more energies F(E) rapidly increases and reaches maximum value in 2 – 3 MeV;
- for all Sn isotopes investigated F(E) have a maximum ~ 0.46 – 0.48 on the flat energy region with width ~ 4 – 6 MeV; in accordance with definition (10) F(E) must not have values exceeding 0.5; if in corresponding experimental ratio $\sigma^{exp}_{(\gamma,2nX)}(E)/\sigma^{exp}_{(\gamma,xn)}(E)$ value is higher 0.5 that means appearance in partial reaction $\sigma(\gamma,nX)$ cross section of non-physical negative values;
- after the GDR maximum F(E) smoothly and slowly decreases to values ~ 0.40 – 0.45; correlation of correspondent energies with those of B_{3n} values (Table 1) give to one possibility to suppose that those decrease are because of new GDR decay channel with 3 outgoing neutrons opening; deviation from constant value equal to 0.5 describes (3) contribution of $3\sigma(\gamma,3nX)$.

It must be pointed out that for cases when thresholds B_{3n} of reactions (γ,3nX) are especially low and cross sections of reactions with 3 neutrons have noticeable values

proposed treatment could be modified (generalized) by introducing of additional transitional multiplicity functions

$$F_i(E) = \sigma^{\text{reop}}_{(\gamma,inX)}(E)/\sigma^{\text{reop}}_{(\gamma,xn)}(E), \quad (13)$$

each of them will describe the contribution of correspondent i-partial reaction into the total photoneutron yield reaction cross section $\sigma(\gamma,xn)$.

a)

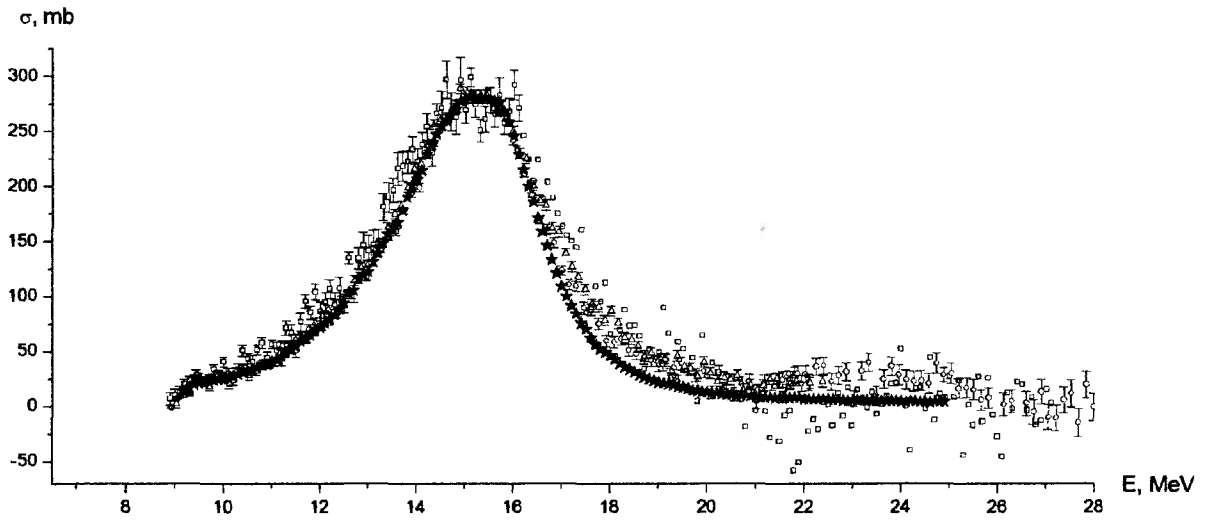

b)

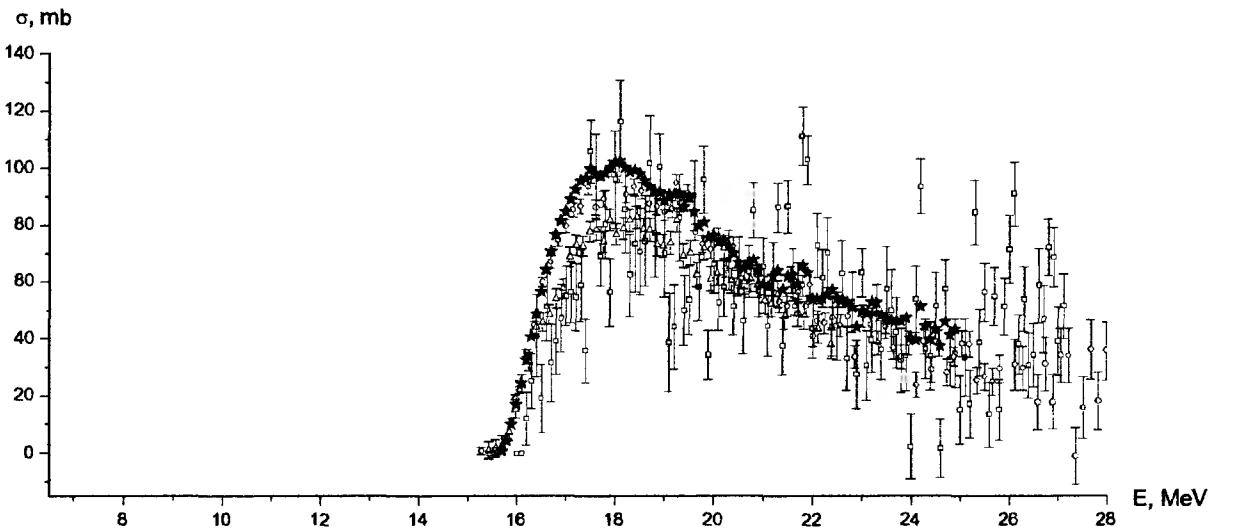

Fig. 1. Comparison of experimental (□ – data from [7], equations (6) and (7), ○ – data from [10], △ – data from [11]) and evaluated ($\sigma^{\text{eval-joint}}$, ★, see further ((11), (12)) partial photoneutron reaction cross sections for ^{120}Sn (B_{2n} = 15.6 MeV)):

a) ^{120}Sn(γ,nX);

b) ^{120}Sn(γ,2nX).

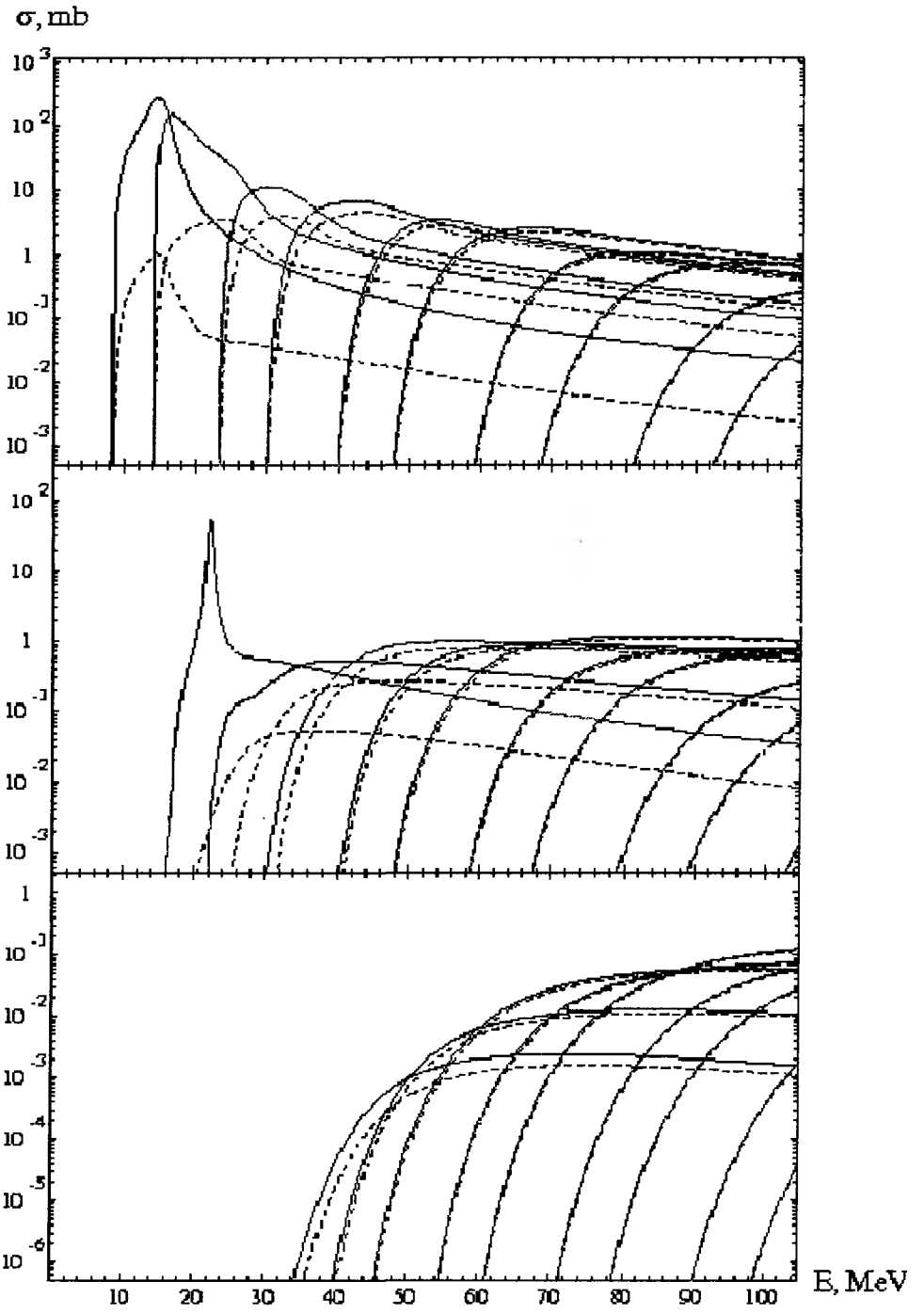

Fig. 2. Calculated [13, 14] cross sections for reactions (γ,0pkn), (γ,1pkn) and (γ,2pkn) – from top to bottom - for ^{124}Sn. Solid line – total cross section. Dotted line – quasideutron component.

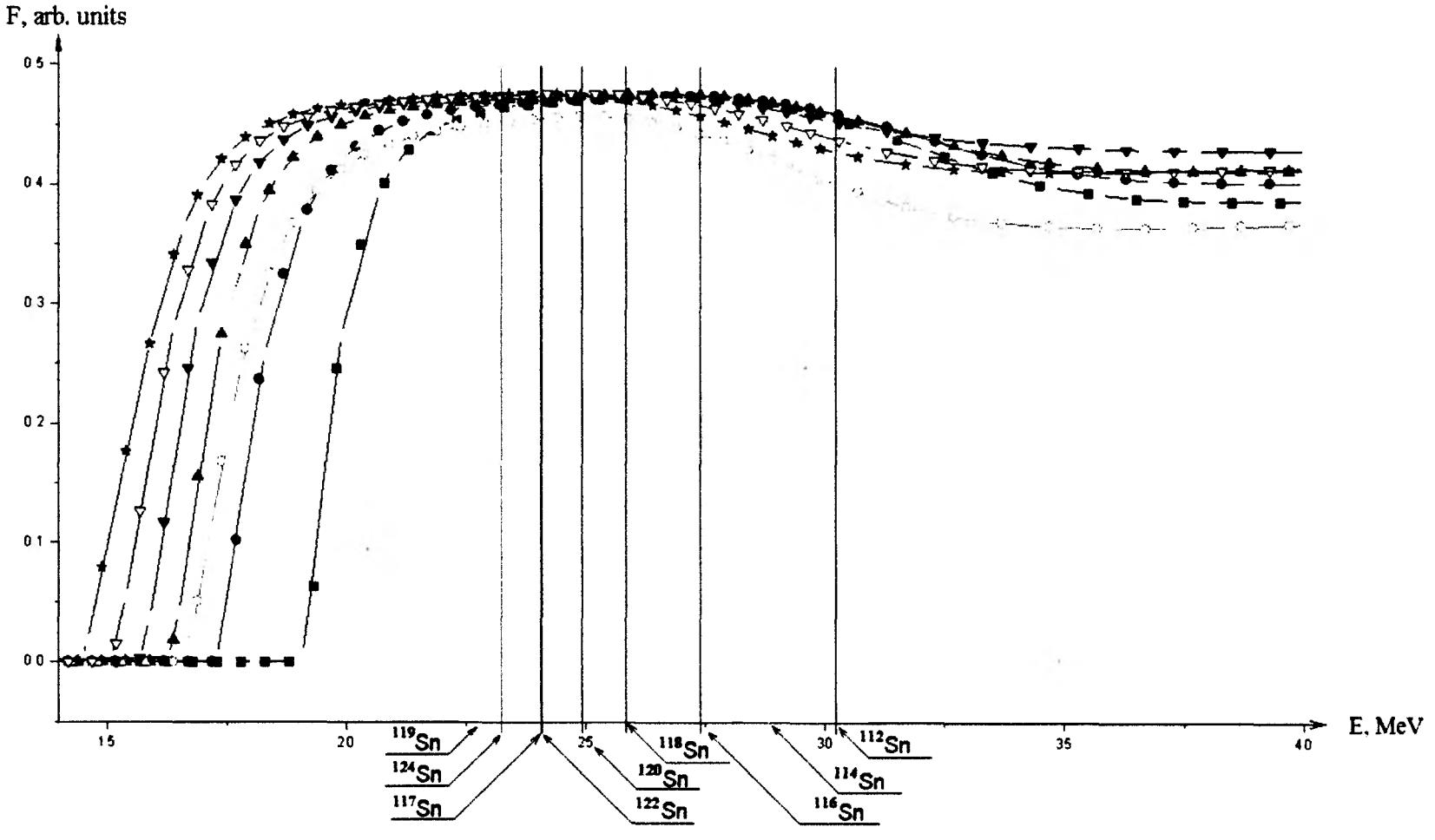

Fig. 3. Energy dependencies of transitional function F(E) describing contribution of partial reaction $\sigma^{theor}(\gamma,2nX)$cross section into the total photoneutron yield reaction cross section $\sigma^{theor}(\gamma,xn)$ for investigated Sn isotopes (arrows point values B_{3n} of thresholds of $(\gamma,3n)$ reactions):

— ■ — ^{112}Sn, — □ — ^{114}Sn, — ● — ^{116}Sn, — ○ — ^{117}Sn,
— ▲ — ^{118}Sn, — △ — ^{119}Sn, — ▼ — ^{120}Sn, — ▽ — ^{122}Sn,
— ★ — ^{124}Sn.

For all investigated isotopes $^{112,114,116-120,122,124}$Sn cross section data for partial reaction cross sections $\sigma_{exp}^{eval}(\gamma,2nX)$ and $\sigma_{exp}^{eval}(\gamma,nX)$ [7, 8], [10], [11] evaluated using correspondent experimental cross sections $\sigma^{exp}(\gamma,xn)$ were compared with experimental data (Fig. 4 is the example for ^{116}Sn). One can see that in general for all investigated Sn isotopes there are good agreement in energy positions, absolute values and shapes for both reaction cross sections $\sigma(\gamma,nX)$ and $\sigma(\gamma,2nX)$ obtained using four different ways:

i) separation of partial reaction cross sections in BR-experiments using statistical theory equations [7, 8];
ii) neutron multiplicity sorting in QMA-experiment using Livermore method [10];
iii) neutron multiplicity sorting in QMA-experiment using Saclay method [11];
iv) experimental-theoretical evaluation of partial reaction cross sections using proposed method.

Because disagreements of various experiments results are not dramatically large all of them were used in procedure of joint evaluation – mean-weighting

$$\sigma^{eval\text{-}joint}(E) = \frac{\sum_i (\Delta\sigma_i(E))^{-2} \cdot \sigma(E)_i}{\sum_i (\Delta\sigma(E)_i)^{-2}} \qquad (14)$$

where i = 1, 2, 3 denotes cross section σ_i ($\sigma_{exp}^{eval}(\gamma,nX)$ or $\sigma_{exp}^{eval}(\gamma,2nX)$) evaluated using method described above with uncertainty $\Delta\sigma_i$:

$$\Delta\sigma^{eval\text{-}joint} = \frac{1}{\sum_i (\Delta\sigma(E)_i)^{-2}} \sqrt{\sum_i (\Delta\sigma(E)_i)^{-2}} \cdot \qquad (15)$$

Comparison of data $\sigma^{eval\text{-}joint}_{(\gamma,nX)}(E)$ and $\sigma^{eval\text{-}joint}_{(\gamma,2nX)}(E)$ evaluated by such a way using the results of several experiments with initial experimental data (an example was presented in Fig 1) confirms that proposed model adequately describes experimental cross section data for both partial reactions corresponding to both main GDR decay channels.

Data on integrated partial reaction cross sections calculated for two energy ranges: B_n - B_{2n} and B_{2n} - B_{3n} are presented in Table 4. They demonstrate complicated competition of processes with escape of one and two neutrons in the range of GDR maximum. So because of arbitrarily low threshold B_{2n} = 19.0 MeV for lightest isotope ^{112}Sn large part of $\sigma(\gamma,nX)$ is in energy region where escape of two neutrons is possible. In going from lightest isotope ^{112}Sn to heaviest one ^{124}Sn B_n is decreasing in 2.3 MeV, B_{2n} in 4.6 MeV, B_{3n} – in 6.9 MeV. That means that in increasing the number of neutrons in isotope energy region in which one neutron decays could be identified definitely permanently became narrow and narrow but the range in which the competition of one and two neutrons escape became wider and wider. So for A > 117 $\sigma_{(\gamma,nX)}(E)$ and $\sigma_{(\gamma,2nX)}(E)$ integrated cross sections for energies B_{3n} - B_{2n} are approximately equal. It must be have in mind that at energies higher ~ 23 – 24 MeV reactions $(\gamma,3nX)$ are added to competitive reactions.

Table 4

Comparison of evaluated integrated cross sections σ_{int} parameters of $\Sigma^{eval\text{-}joint}_{(\gamma,nX)}(E)$ and $\sigma^{eval\text{-}joint}_{(\gamma,2nX)}(E)$, calculated for different energy regions

Nucl	B_n, MeV	$\Sigma_{int}(B_{2n} - B_n)$, MeV·mb	B_{2n}, MeV	$\Sigma_{int}(B_{3n} - B_{2n})$, MeV·mb		B_{3n}, MeV
		(γ,nX)		(γ,nX)	$(\gamma,2nX)$	
^{112}Sn	10.8	1370	19.0	163*	359*	30.2
^{114}Sn	10.3	1150	18.0	249*	442*	28.8
^{116}Sn	9.6	1030	17.1	284	408	27.4
^{117}Sn	6.9	928	16.5	390	402	24.1
^{118}Sn	9.3	851	16.3	339	510	25.8
^{119}Sn	6.5	775	15.8	456	409	22.7
^{120}Sn	9.1	799	15.6	423	607	24.9
^{122}Sn	8.8	591	15.0	456	493	24.1
^{124}Sn	8.5	503	14.4	535	635	23.3

*) measurements till E = 27 MeV (till B_{3n}).

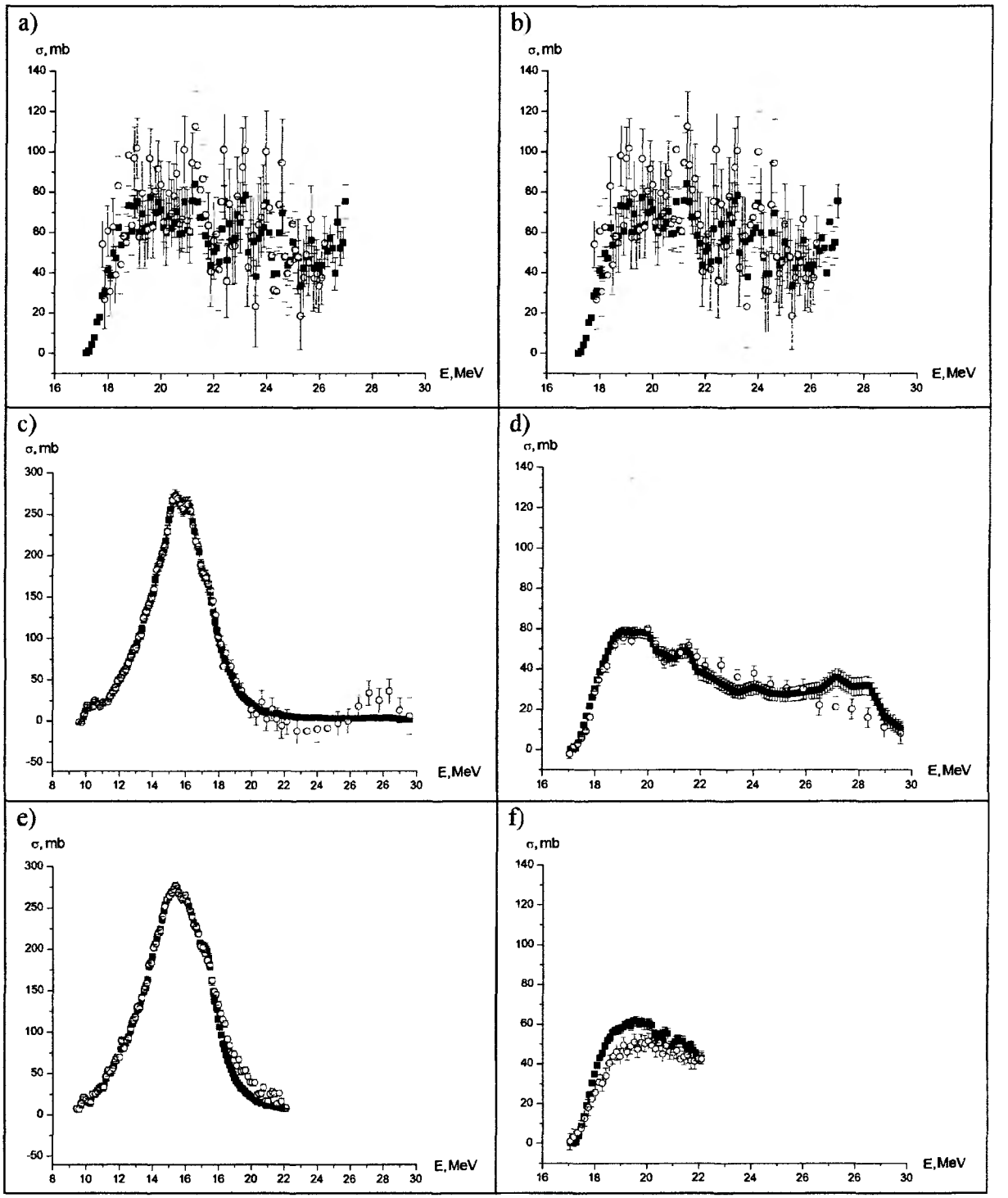

Fig. 4. Comparison of experimental [8, 10, 11] - ○ and evaluated (equations ((11), (12)) - ■ data for partial reaction cross sections $\sigma_{exp}^{eval}(\gamma,nX)$ – left and $\sigma_{exp}^{eval}(\gamma,2nX)$ – rifht for ^{116}Sn:
a) and b)данные [8];
c) and d) данные [10];
e) and f) данные [11].

In Table 5 main parameters of evaluated cross sections for reaction $\sigma^{eval\text{-}joint}(\gamma,sn) = \sigma^{eval\text{-}joint}(\gamma,nX) + \sigma^{eval\text{-}joint}(\gamma,2nX)$, calculated using Lorenz-line approximation are compared with those of experimental [7, 8, 10, 11] cross sections.

In table 6 there is a comparison of experimental and evaluated integrated cross sections.

Table 5

Comparison of main parameters ГДР of GDR in evaluated $\sigma^{eval\text{-}loint}(\gamma,sn) \approx \sigma(\gamma,abs)$ and experimental cross sections (E_m – energy of maximum, σ_m – cross section in maximum, Γ – width of maximum)

	E_m, MeV				σ_m, mb				Γ, MeV			
Nucl	[7, 8]	[10]	[11]	Оц.	[7, 8]	[10]	[11]	Оц.	[7, 8]	[10]	[11]	Оц.
^{112}Sn	15.8	-	-	15.8	268	-	-	270	5.9	-	-	5.3
^{114}Sn	15.7	-	-	15.8	265	-	-	265	7.0*	-	-	5.5
^{116}Sn	15.6	15.7	15.6	15.6	260	266	270	270	6.0*	4.2	5.2	4.7
^{117}Sn	15.4	15.7	15.7	15.6	260	254	255	260	5.5*	5.0	5.3	4.8
^{118}Sn	15.5	15.6	15.4	15.5	272	255	278	265	5.8	4.8	5.0	4.5
^{119}Sn	15.4	15.5	-	15.6	270	253	-	255	6.0*	4.9	-	5.0
^{120}Sn	15.3	15.4	15.4	15.4	297	280	284	285	5.7	4.8	5.3	4.5
^{122}Sn	15.6	-	-	15.2	270	-	-	270	5.0*	-	-	4.3
^{124}Sn	15.5	15.2	15.3	15.1	270	283	275	280	5.5*	5.2	5.0	4.3

*) data absent in original publications taken from [19].

Table 6

Comparison of integrated cross sections σ_{int} of evaluated total photoneutron reaction $\sigma^{eval\text{-}joint}(\gamma,sn) \approx \sigma(\gamma,abs)$ with experimental data

		Integrated cross sections σ_{int} of total photoneutron reaction (γ,sn)					
Nucl	B_{3n}, MeV	[7,8], < 27 MeV	[10], < 30 MeV	[11], < 30 MeV	Eval., (< B_{3n})	Eval., total	Dipole Sum of Rule, 60 NZ/A
	MeV	MeV·mb					
^{112}Sn	30.2	1900*			1893	1893	1661
^{114}Sn	28.8	1860*			1841	1841	1684
^{116}Sn	27.4	1850	1667	1860	1719	1778	1707
^{117}Sn	24.1	1860	1939	1570**	1720	1956	1718
^{118}Sn	25.8	1920	1898	1690**	1700	1840	1729
^{119}Sn	22.8	1860	2078		1640	2042	1739
^{120}Sn	24.9	2070	2092	2140	1855	2013	1750
^{122}Sn	24.1	2030			1685	1887	1770
^{124}Sn	23.3	1930	2077	1620**	1674	1925	1790

*) measurements for energies till B_{3n};
**) data for energies till E = 23 МэВ.

One can see that evaluated cross sections that are well presenting competition of partial reaction cross sections $\sigma^{eval\text{-}joint}(\gamma,nX)$ and $\sigma^{eval\text{-}joint}(\gamma,2nX)$ are in good agreement with data for total photoneutron reaction cross sections. Data presented give to one possibility to do definite conclusions about the character of changing of GDR parameters in going from one isotope to another (A increasing):
- E_m decreasing in accordance with well-known estimations;
- Γ decreasing in connection with closing of neutron number to magic number N = 82;
- σ_m is about constant.

Data obtained show that integrated GDR cross section (evaluated in the frame of described treatment as $\sigma^{eval\text{-}joint}(\gamma,sn) \approx \sigma(\gamma,abs)$) in A increasing practically does not changed. At the same time $\sigma^{eval\text{-}joint}(\gamma,2nX)$ reaction integrated cross section is decreasing but that for $\sigma^{eval\text{-}join}(\gamma,2nX)$ vise versa is increasing (see the Table 4 also), the reason is decreasing of energy range Em – B_{2n} between GDR maximum and threshold of reaction with 2 neutrons.

This work is carried out in the Department of Electromagnetic Processes and Atomic Nuclei Interactions and is supported by Russia Federal Agency on Science and Innovations (Contract 02.740.11.0242), by Grant of support of Science Schools 02.120.21.485-SS, State Contract № 2009-1.1-125-055 and RFBR Grant № 09-02-00368.

СПИСОК ЛИТЕРАТУРЫ

1. MSU SINP CDFE Nuclear Reaction Threshold and Energy Values Calculator and Nucleon Separation Energy Graph Engine.
   URL - http://cdfe.sinp.msu.ru/services/calc_thr/calc_thr.html.
2. A.Bohr, B.Mottelson. Atomic Nucleus Structure. T. 2. M: Мир. 1977.
3. E.Wolynec, M.N.Martins. Revista Brasileira Fisica. 1987. V. 17. P. 56.
4. B.L.Berman, R.E.Pywell, S.S.Dietrich, M.N.Thompson, K.G.McNeill, J.W.Jury. Phys.Rev. 1987. V. C36. P. 1286.
5. V.V.Varlamov, B.S.Ishkhanov. Study of Consistency Between (γ,xn), [(γ,n) + (γ,np)] and (γ,2n) Reaction Cross Sections Using Data Systematics. Vienna, Austria. INDC(CCP)-433, IAEA NDS, Vienna, Austria, 2002.
6. V.V.Varlamov, N.N.Peskov, D.S.Rudenko, M.E.Stepanov. Voprosy Atomnoj Nauki i Tekhniki. Seriya: Yadernye Konstanty. 2003. T. 1-2. C. 48.
7. Yu.I.Sorokin, B.A.Yur'ev. Yadernaya Fizika. 1974. T. 20. C. 233.
8. Yu.I.Sorokin, B.A.Yur'ev. Izvestiya RAN, ser. fiz.. 1975. T. 39. C. 114.
9. Yu.I.Sorokin, V.A.Khrushchev, B.A.Yur'ev. Izvestiya RAN, ser. fiz. 1972. T. 36. C. 181.
10. S.C.Fultz, B.L.Berman, J.T.Caldwell, R.L.Bramblett, M.A.Kelly. Phys. Rev. 1969. V. 186. P. 1255.
11. A.Lepretre, H.Beil, R.Bergere, P.Carlos, A.DeMiniac, A.Veyssiere. Nucl. Phys. 1974. V. A219. P. 39.
12. M.B. Chadwick, P.Oblozinsky, P.E.Hodgson, G.Reffo. Phys. Rev. C 44, 814 (1991).
13. B.S.Ishkhanov, V.N.Orlin. Physics of Elementary Particles and Atomic Nuclei. 2007. T. 38. C. 460.
14. B.S.Ishkhanov, V.N.Orlin. Yadernaya Fizika. 2008. T. 71. C. 517.
15. V.V.Varlamov, B.S.Ishkhanov, V.N.Orlin, V.A.Chetvertkova. Analysis and Evaluation of Cross Sections of Partial Photoneutron Reactions for Sn Isotopes. MSU SINP Preprint-2009-3/847, -M., 2009.
16. B.L.Berman, S.S.Fultz. Rev. Mod. Phys. 1975. V. 47. P. 713.
17. V.V.Varlamov, Yu.Yu.Gudenko, C.Yu.Komarov, N.N.Peskov, M.E.Stepanov. New Evaluations of Competition of Direct and Statistical Processes in GDR Neutron Decay Channel. Abstracts. 56 International Conference "Nucleus-2006" on Problems of Nuclear Spectroscopy and Structure of Atomic Nuclei. 4 - 8 Septemter 2006, Sarov, RFNC RRIEP, 2006, c. 37.
18. J.M.Laget, Lecture Notes in Physics, Vol. 137, edited by H. Arenhovel and A.M. Saruis (Springer-Verlag, Berlin, 1981), p. 148.
19. A.V.Varlamov, V.V.Varlamov, D.S.Rudenko, M.E.Stepanov. Atlas of Giant Dipole Resonances. Parameters and Graphs of Photonuclear Reaction Cross Sections. INDC(NDS)-394, IAEA NDS, Vienna, Austria, 1999.

ON MICROSCOPIC DESCRIPTION OF THE GAMMA – RAY STRENGTH FUNCTIONS

S. Kamerdzhiev, D. Voitenkov

Institute for Physics and Power Engineering, 249033 Obninsk, Russia

Abstract

Using the Theory of Finite Fermi Systems, we obtained a non-magic nuclei generalization of the old theoretical results by J. Speth for magic nuclei dealing with the transitions between excited states and moment values of excited state. Such an extension is quite necessary for microscopic calculations of the gamma ray strength function. The comparison with the standard QRPA has shown that the modern many-body approach gives some new physics. The calculated value of the quadrupole moment of the excited 3_1^- state in ^{208}Pb is agreed satisfactorily with experiment. Some possible improvements of the theory are briefly discussed.

1. Introduction

As a rule, the gamma –ray strength function is used for the statistical studies of gamma transitions from the high-lying nuclear states near the nucleon separation energy.

One of the definitions of the gamma-ray strength function includes the transitions only between the ground and excited states [1]. Such a definition is true, in particular, for the so-called pygmy-dipole resonance which is being investigated at present very actively, both experimentally and theoretically, and is very important, as known, for the description of the radiative neutron capture; see, for example, a recent mini review [2]. Another definition of the gamma-ray strength function, and, in a sense, a conventional one, contains transitions between excited states [3].

In the context of quick and successful development of the nuclear structure microscopic methods and problems of gamma-ray strength function, discussed, for example, in [4, 5], it is necessary to consider modern microscopic feasibilities to calculate gamma-ray strength functions microscopically, which is especially important for the nuclei where there is no experimental information for phenomenological description, first of all, for neutron-rich nuclei. In particular, the question arises whether it is possible to compare microscopic and statistical approaches with the aim to understand limits of their applicability or the applicability of some approximations and hypotheses used. Thus, in order to try to understand the problem microscopically, it is necessary to calculate the transitions between excited states (the microscopic theory for the transitions between ground and excited states is very well developed; see, for example [6, 7, 8, 9]). This is the first motivation of our work. In addition, at present there is a huge number of experimental data in the field of conventional nuclear spectroscopy, which should be understood microscopically, see [10]. This is the second motivation of our work. In any case, it is of great interest to understand the novelty of the modern nuclear many-body theory in this field.

One of the modern nuclear structure microscopic approaches is the Theory of Finite Fermi Systems (TFFS) [6] and its extensions [7, 8, 9]. For the beginning, we would like to revive the old extended TFFS activity [7] at the modern level to calculate transitions between excited states, with each described within the Random Phase Approximation (RPA). In Section 2 we discuss the case of magic nuclei. In Section 3 we consider the case of non–magic nuclei and compare it with the usual Quasiparticle RPA. The first calculations for quadrupole moments of excited states are performed in Section 4.

2. Magic nuclei

We will use the microscopic extended TFFS in the old sense of this term [7, 8]. This version generalizes the standard TFFS [6] to calculate transitions between excited states and static moments of excited states for even-even magic nuclei. In [7], using the formalism of the six-point Green function for magic nuclei, the expression for the matrix element $M_{ss'}$ of the transition between excited states s→s′ was derived, with each described within RPA. It can be written in the graphic form [11, 12]

$$M_{ss'} = M_{ss'}^{(1)} + M_{ss'}^{(2)} \tag{1}$$

$M_{ss'}^{(1)} =$ 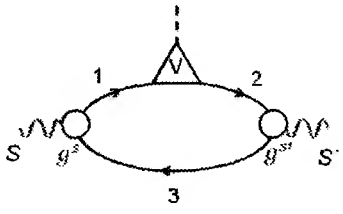

$= \sum_{123} V_{12}\, g_{31}^{s} g_{23}^{s'} A_{123}^{(1)}$ (2)

$M_{ss'}^{(2)} =$ 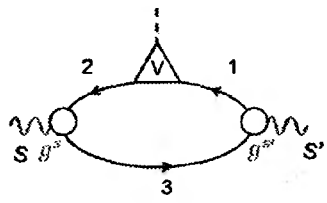

$= \sum_{123} V_{12}\, g_{31}^{s'} g_{23}^{s} A_{123}^{(2)}$ (3)

Here g^s is the matrix element of the phonon creation amplitude with the phonon energy ω_s, V_{12} is the effective field which takes into account the effect of nuclear medium with respect to an external field $e_q V^0$ where e_q is the local quasiparticle charge (for electric fields $e_q{}^p = 1$, $e_q = 0$) [6]. According to [7] the quantities g^s and V should be calculated within the standard TFFS [6], that is, in fact, in RPA. The single –particle indexes for spherical nuclei are $\lambda \equiv \{n, j, l, m\} = \{1\}$. The quantities $A^{(1)}$ and $A^{(2)}$ are given by

$$A_{123}^{(1)}(\omega_s, \omega_{s'}) = \int G_1(\varepsilon) G_2(\varepsilon + \omega) G_3(\varepsilon + \omega_s) d\varepsilon =$$

$$= \frac{(1-n_1)(1-n_2)n_3 - n_1 n_2 (1-n_3)}{(\varepsilon_{31} - \omega_s)(\varepsilon_{32} - \omega_{s'})} +$$

$$+ \frac{1}{\varepsilon_{12} + \omega}\left[\frac{n_1(1-n_2)(1-n_3) - (1-n_1)n_2 n_3}{\varepsilon_{13} + \omega_s} - \frac{(1-n_1)(1-n_3)n_2 - (1-n_2)n_1 n_3}{\varepsilon_{23} + \omega_{s'}}\right] \tag{4}$$

$$A_{123}^{(2)}(\omega_s, \omega_{s'}) = A_{123}^{(1)}(-\omega_{s'}, -\omega_s)$$

where for spherical nuclei the single-particle indexes $\nu_1 = \{n,l,j\} \equiv 1$, $\varepsilon_{12} = \varepsilon_1 - \varepsilon_2$, $\omega = \omega_s - \omega_{s'}$, n_1 are occupation numbers ($n_1 = 0,1$ for magic nuclei).

The case of the static moment of an excited state corresponds to $\omega = 0$. In particular, the quadrupole moment of the excited state s is as follows:

$$Q = \sqrt{\frac{16\pi}{5}} \langle I_s I_s | M | I_s I_s \rangle \tag{5}$$

with the quantity V in the expressions (1), (2), (3)

$$V(\mathbf{r}) = V(r)\, Y_{20} \tag{6}$$

and I_s is the moment value of the excited state s considered.

The main difference between expressions (1), (2), (3) and the RPA case is that instead of the external (or bare) field $e_q V^0$, which should be used in the RPA case, the effective field V is present. As it was stated in [7], the first term on the right side in (4) corresponds to the RPA case with $V= e_q V^0$. Note that this statement can be proved if one uses the property $n_i = n^2_i$, which is true for magic nuclei only. Thus, it is also of interest to find the QRPA case from the appropriate generalization of the approach under consideration (see Sect.3). Of course, it goes without saying that it is necessity to include pairing (non-magic nuclei) in the approach.

3. Non-magic nuclei

As known, for nuclei with pairing it is necessary to use four Green functions G, G^h, $F^{(1)}$, $F^{(2)}$ [6]

$$G_1(\varepsilon) = G_1^h(-\varepsilon) = \frac{u_1^2}{\varepsilon - E_1 + i\delta} + \frac{v_1^2}{\varepsilon + E_1 - i\delta}$$

$$F_1^1(\varepsilon) = F_1^2(\varepsilon) = -\frac{\Delta_1}{2E_1}\left[\frac{1}{\varepsilon - E_1 + i\delta} + \frac{1}{\varepsilon + E_1 - i\delta}\right] \tag{7}$$

where $E_1 = \sqrt{(\varepsilon_1 - \mu)^2 + {\Delta_1}^2}$ and Δ_1 is the gap value, which should be found from the solution of the gap equation, and to add the hp, pp and hh-channels in addition to the ph one of the RPA case , i.e. to consider the full set of QRPA equations and four effective fields V, V^h, $d^{(1)}$, $d^{(2)}$ [6]. Because the pp and hh channels usually give small contributions as compared with the ph and hp ones and create noticeable algebraic complications, here we omit the pp- and hh-channels and, correspondingly, the effective fields $d^{(1)}$ and $d^{(2)}$. In this approximation our matrix element $M_{ss'}$ contains 8 graphs:

$$M_{ss'} = \sum_i M_{ss'}^{(i)} = \tag{8}$$

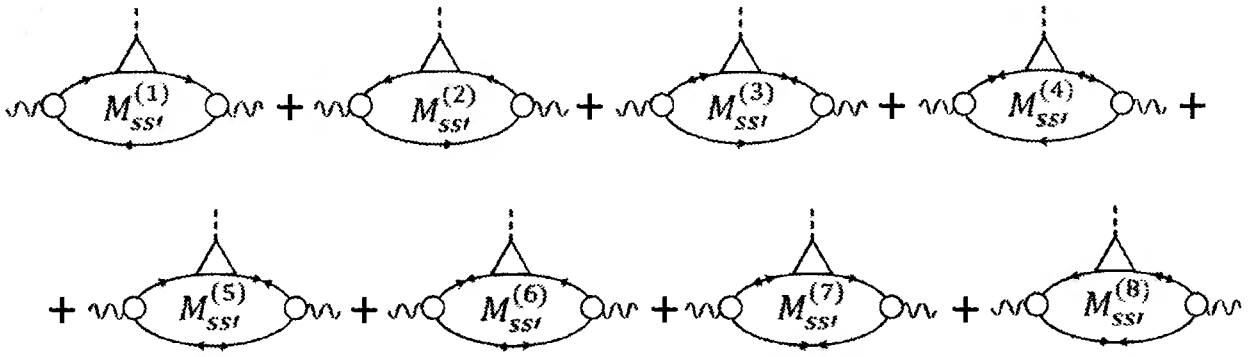

The analytical form for the $M_{ss'}^{(1)}$ is given by

$$M_{ss'}^{(1)} = \sum_{123} V_{12} g_{31}^{s} g_{23}^{s'} A_{123}^{(1)} \tag{9}$$

where

$$A_{123}^{(1)}(\omega_s, \omega_{s'}) = \int G_1(\varepsilon) G_2(\varepsilon + \omega) G_3(\varepsilon + \omega_{s'}) d\varepsilon =$$

$$= \frac{u_1^2 u_2^2 v_3^2}{(\omega_s + E_{13})(\omega_{s'} + E_{23})} - \frac{v_1^2 v_2^2 u_3^2}{(\omega_s - E_{13})(\omega_{s'} - E_{23})} + \tag{10}$$

$$+ \frac{1}{\omega + E_{12}} \left(\frac{u_1^2 v_2^2 u_3^2}{E_{23} - \omega_{s'}} - \frac{u_1^2 v_2^2 v_3^2}{E_{13} + \omega_s} \right) + \frac{1}{\omega - E_{12}} \left(\frac{v_1^2 u_2^2 v_3^2}{E_{23} + \omega_{s'}} - \frac{v_1^2 u_2^2 u_3^2}{E_{13} - \omega_s} \right)$$

For the first graph $M^{(3)}$, which contains the Green function $F^{(1)}$ and $F^{(2)}$, we obtain the corresponding quantity $A^{(3)}{}_{123}$:

$$A_{123}^{(3)}(\omega_s, \omega_{s'}) = -\int G_1(\varepsilon) F_2(\varepsilon + \omega) F_3(\varepsilon + \omega_s) d\varepsilon =$$

$$= -\frac{\Delta_1 \Delta_2}{4 E_1 E_2} \left[\frac{v_3^2}{(\omega_s + E_{13})(\omega_{s'} + E_{23})} + \frac{u_3^2}{(\omega_s - E_{13})(-\omega_{s'} + E_{23})} + \right. \tag{11}$$

$$\left. + \frac{1}{\omega + E_{12}} \left(\frac{v_3^2}{\omega_s + E_{13}} - \frac{u_3^2}{-\omega_{s'} + E_{23}} \right) + \frac{1}{\omega - E_{12}} \left(\frac{v_3^2}{-\omega_{s'} - E_{23}} - \frac{u_3^2}{\omega_s - E_{13}} \right) \right]$$

Here $E_{12} = E_1 + E_2$, $u_1^2 = \frac{E_1 + (\varepsilon_1 - \mu)}{2E_1} = 1 - v_1^2$

The other quantities $A^{(i)}$ are obtained from the relations:

$$A_{123}^{(2)}(\omega_s, \omega_{s'}) = A_{123}^{(1)}(-\omega_{s'}, -\omega_s), \qquad A_{123}^{(4)}(\omega_s, \omega_{s'}) = A_{123}^{(3)}(-\omega_{s'}, -\omega_s),$$

$$A_{123}^{(6)}(\omega_s, \omega_{s'}) = A_{123}^{(5)}(-\omega_{s'}, -\omega_s), \qquad A_{123}^{(8)}(\omega_s, \omega_{s'}) = A_{123}^{(7)}(-\omega_{s'}, -\omega_s) \tag{12}$$

For the case $\omega = 0$ the quantity $M_{ss'}$, like in the RPA case, contains the sum $\Sigma\, A^{(i)}$ of eight terms.

At present there is the QRPA case for $M_{ss'}$ which was studied in work [13]. To compare our results with this case, in each of the $A^{(i)}$ we only take two terms which contain denominators $(E_{13} - \omega_s)(E_{23} - \omega_{s'})$ and $(E_{13} + \omega_s)(E_{23} + \omega_{s'})$ and call it $\Sigma[A(i)]_0$. Using relatively long algebra one can obtain:

$$\sum_i \left[A_{123}^{(i)} \right]_0 = \left[\frac{1}{(\omega_s + E_{13})(\omega_s + E_{23})} + \frac{1}{(\omega_s - E_{13})(\omega_s - E_{23})} \right] \times \tag{13}$$

$$\times \left[u_1^2 u_2^2 v_3^2 - v_1^2 v_2^2 u_3^2 + \frac{\Delta_1 \Delta_2}{4 E_1 E_2} (u_3^2 - v_3^2) + \frac{\Delta_1 \Delta_3}{4 E_1 E_3} (u_2^2 - v_2^2) + \frac{\Delta_2 \Delta_3}{4 E_2 E_3} (u_1^2 - v_1^2) \right]$$

The second square bracket in (13) coincides with the factor $v_{12}^{-}u_{23}^{+}u_{31}^{+}$ in Refs. [13, 14] so that our quantity (13) is proportional to the factor $v_{12}^{-}(\psi_{23}\psi_{31}+\varphi_{23}\varphi_{31})$ in [13], which determines the appropriate matrix element within the QRPA (ψ and φ are phonon amplitudes). Thus, the terms containing factors $(\omega \pm E_{12})^{-1}$ in (10), (11), (12) are added in our approach and, therefore, generalize the standard QRPA. The second generalization of the QRPA is the appearance of the ω dependent effective field $V(\omega)$, with $\omega = \omega_s - \omega_{s'}$ instead of the external field $e_q V^0$, which does not depend on ω.

4. Some calculations for the magic nuclei

Here we consider the case of $\omega = 0$ for magic nuclei and calculate quadrupole moments of excited states in Pb^{208}. Then the quantities $A^{(1)}$ and $A^{(2)}$ in (1), (2), (3), (4) depend on ω_s only and the matrix element M_{ss} contains the sum $\left[A_{123}^{(1)}(\omega_s)+A_{123}^{(1)}(-\omega_s)\right]$.

It is easy to see from (4) that for the case $\omega = 0$ there is an uncertainty at 1=2 in eq. (4) of the kind 0/0. For this reason we should consider the case A_{113} separately:

$$A_{113}^{(1)} = \frac{n_3-n_1}{(\varepsilon_{31}-\omega_s)^2},\quad A_{113}^{(2)} = \frac{n_3-n_1}{(\varepsilon_{31}+\omega_s)^2} \tag{14}$$

We will consider the quantities V and g^s in the following form

$$V(\vec{r}) = V(r)Y_{LM}(\theta,\varphi),\qquad g^s(\vec{r}) = g(r)Y_{I_sM_s}(\theta,\varphi) \tag{15}$$

that is for simplicity we neglect the spin components of these quantities, which is reasonable for the electric fields considered.

After summation over quantum numbers m_1, m_2, m_3 in (1), (2), one can obtain the following for the matrix element M_{ss} :

$$M_{ss} = (-1)^{I_s+L}\begin{pmatrix} I_s & L & I_s \\ -M_s & M & M_s\end{pmatrix}\sum_{123}\begin{Bmatrix} I_s & L & I_s \\ j_2 & j_3 & j_1\end{Bmatrix}\times$$
$$\times\langle 1\|V\|2\rangle\langle 3\|g^s\|1\rangle\langle 2\|g^s\|3\rangle\left[A_{123}^{(1)}(\omega_s)+A_{123}^{(1)}(-\omega_s)\right] \tag{16}$$

Here index 1 stands for $\nu_1 \equiv \{1\} = \{n_1, l_1, j_1\}$, the reduced matrix elements and the quantity $(A^{(1)}+A^{(2)})$ are given by

$$\langle 1\|V\|2\rangle = [V(r)]_{12}\langle 1\|Y_L\|2\rangle$$

$$\langle 3\|g^s\|1\rangle = [g^s(r)]_{31}\langle 3\|Y_{I_s}\|1\rangle$$

$$\langle 1\|Y_L\|2\rangle = \frac{(-1)^{j_2+L+1/2}}{2\sqrt{\pi}}[(2l_1+1)(2L+1)(2l_2+1)(2j_1+1)(2j_2+1)]^{1/2}\times \tag{17}$$
$$\times\begin{pmatrix} l_1 & L & l_2 \\ 0 & 0 & 0\end{pmatrix}\begin{Bmatrix} I_s & L & I_s \\ j_2 & j_3 & j_1\end{Bmatrix}$$

$$A_{123}^{(1)}(\omega_s)+A_{123}^{(1)}(-\omega_s) = (1-\delta_{12})\frac{2}{\varepsilon_{12}}\left[\frac{n_{13}\varepsilon_{13}}{\varepsilon_{13}^2-\omega_s^2}-\frac{n_{23}\varepsilon_{23}}{\varepsilon_{23}^2-\omega_s^2}\right]+\delta_{12}\frac{2n_{31}(\varepsilon_{31}^2+\omega_s^2)}{(\varepsilon_{31}^2-\omega_s^2)^2} \tag{18}$$

where $[V(r)]_{12}$ and $[g^s(r)]_{31}$ are radial integrals.

For the beginning in our calculations we used the following approximations [15]:

$$V(r) = e_{eff} V^0, e^p_{eff} = 2, e^n_{eff} = 1 \tag{19}$$

and the Bohr-Mottelson model for $g^s(r)$:

$$g^s(r) = \frac{\beta_s}{\sqrt{2I_s + 1}} r \frac{\partial U}{\partial r} \tag{20}$$

where U is the single-particle potential.

To calculate the quadrupole moment value we used formulas (5) and (6). Summation over 1,2,3 in (15) was performed within two shells above and two shells below the Fermi energy both for protons and neutrons.

For ^{208}Pb we obtained the following value of the quadrupole moment of the excited state 3^-_1 with the energy $\omega_s = 2.6\ MeV$ and $\beta_s = 0.12$

$$Q_{th}(3^-_1) = -0.12\ e \cdot b$$

The experiment value $Q_{exp}(3^-_1) = -0.34 \mp 15\ e \cdot b$ [10].

We do not think that the consistent use of the RPA approach to calculate V and g^s instead of our approximations (18), (19), (20) can improve considerably the numerical result obtained. There are other physical reasons to improve it. The first is the use of the coordinate representation within the Green function method which allow us to consider the single-particle continuum exactly and omit the questions about the size of the summation limits in our formulas. The second reason is an account for the effects of the so-called tadpole. These effects were introduced and calculated for other problems in the works by the Kurchatov institute group long ago, see [16]. However, they should give a contribution to the problems which have been considered here.

To our knowledge, both of these two physical effects did not account for the problems under consideration.

Conclusion

In this work, we have tried to outline modern feasibilities of the many-body nuclear theory to calculate transitions between excited states and, as a specific case, moment values of the excited state. It has been assumed that these excited states are described within the (Q)RPA. In fact, this assumption has been done for the simplicity and based on theoretical results available; it is possible to consider a more general approach, see for example [14,15].

For magic nuclei, more simple formulas (18) have been derived here than in the pioneering work by Speth [7] and the case of the appearance of the uncertainty has been considered. For non-magic nuclei, an appropriate generalization of the results [7] has been performed and compared with the QRPA approach [13]. This generalization allowed us to directly demonstrate a new physics due to the use of the modern many-body theory.

Our first and approximate calculation of the quadrupole moment of the 3^-_1-level in ^{208}Pb gave a reasonable agreement with the experiment [10] which has relatively large errors. As the approximations used are rather reasonable, we do not think that consistent use of the RPA will give a noticeable change of our numerical result. Of course, these approximations are not true for unstable nuclei which are studied very actively at present. For these nuclei, the self-consistent approaches are necessary and, for example, the extended theory of finite Fermi systems [17] gives some appropriate possibilities.

We think that the two above-mentioned physical effects (coordinate representation and tadpole effects) are quite unknown, very interesting and probably important numerically for

calculation of transitions between excited states and moments of exited states. These effects should be considered first of all for these problems.

We are grateful to J. Speth ant B.A. Tulupov for enlightening and useful discussions.

The work was partly supported by the grants DFG 436RUS113/994/0-1 and RFBR 09-02-91352.

References

1. G. A. Bartholomew , E. D. Earle, A. J. Ferguson, J. W. Knowles, and M. A. Lone, Adv. in Nucl. Phys. v. 7, 229 (1973)
2. A. V. Avdeenkov, S.P. Kamerdzhiev, Phys. At. Nucl. 72, 1332 (2009)
3. G. A. Bartolomew, Annu. Rev. Nucl. Sci. 11, 259 (1961)
4. M. Krtička, F. Bečvař, Proc. of the "Nuclear Physics in Astrophysics III ", J. Phys. G35, 1 (2008), № 14020.
5. 2nd Workshop on Level Densities and Gamma Strength (Oslo, 15 – 20 May 2009), http://oslo.ulo.no/workshop
6. A. B. Migdal, Theory of Finite Fermi Systems and Application to Atomic Nuclei, Wiley, New York 1967
7. J. Speth , Z. Phys. 239, 249 (1970)
8. J. Speth, E. Werner, W. Wild, Phys. Rep. 33, 127 (1977)
9. S. Kamerdzhiev, J.Speth, G. Tertychny, Phys. Rep. 393, 1 (2004)
10. N. J. Stone, Table of Nuclear Magnetic Dipole and Electric Quadrupole Moments, Atomic Data and Nuclear Data Tables, 90, 75 (2005)
11. M. A. Troitsky, A. Ya. Simonov, Sov. Nucl. Phys. 17, 1168 (1973)
12. P. Ring, J. Speth, Nucl. Phys. A235, 315 (1974)
13. V. Yu. Ponomarev, Ch. Stoynov, N. Tsoneva, M. Grinberg, Nucl. Phys. A635, 470 (1998)
14. V. G. Soloviev, Theory of Atomic Nuclei: Quasiparticles and Phonons, Institute of Physics, Bristol and Philadelphia USA, 1992
15. S. P. Kamerdzhiev, Sov. Nucl. Phys. 2, 415 (1965)
16. V. A. Khodel, E. E. Saperstein, Phys. Rep. 92, 183 (1982)
17. A. Avdeenkov, F. Grummer, S. Kamerdzhiev et al., Phys. Lett. B 653, 196 (2007)

PRODUCTION OF THE SHORT-LIVED ISOTOPES ^{12}N AND ^{12}B IN THE ^{14}N(γ,2n), ^{14}N(γ,2p), AND ^{13}C(γ,p) REACTIONS

L.Z.Dzhilavyan[1], A.I.Karev[2], V.D.Laptev[1], V.G.Raevsky[2]
[1] *Institute for Nuclear Research, Russian Academy of Sciences, Moscow, Russia*
[2] *P.N.Lebedev Physical Institute, Russian Academy of Sciences, Moscow, Russia*

1. The production and decay features of ^{12}N-nuclei

Nuclei of the radioactive isotope ^{12}N (β^+-decay; the maximal kinetic energy of β-particles $E_{\beta\,max} \cong 17$ MeV; the half-life $T_{1/2} \cong 11.0$ ms [1]) were for the first time detected and studied, when they were produced in the reaction ^{12}C(p,n)^{12}N [2]. Soon ^{12}N-nuclei were also produced [3] in the photonuclear reaction on ^{14}N (isotopic abundance (IA): ^{14}N-99.63%, ^{15}N-0.37%): $\gamma+^{14}N \rightarrow ^{12}N+2n$ (an incident γ-quantum energy E_γ at the threshold $E_{\gamma\,thresh} \cong 30.6$ MeV [1]). (I)

Decay of ^{12}N-nuclei and ways of their production have (as it was partly noted in [2,3]) a remarkable set of features (especially, when ^{12}N-nuclei are produced at electron accelerators):

a. ^{12}N-nuclei have a very short lifetime (according to [2], the shortest one of any known at that moment β-emitter). When activation takes place at electron accelerators with kinetic energies of outgoing electrons E_e up to ~60 MeV, there are few reactions, which can produced activities with $T_{1/2}$ close to $T_{1/2}$ for ^{12}N [1] (see also about it below). This must help to separate ^{12}N-activity. Moreover, the small absolute value of $T_{1/2}$ for ^{12}N permits to detect ^{12}N-activity from every beam "burst" of a pulsed accelerator (with duration ($10^{-6} \div 10^{-5}$) s, for example) for very short time (for ~100 ms (or even less) between accelerator pulses).
b. ^{12}N-nuclei decay with emitting of β^+-particles (i.e. positrons). So, it is possible for ^{12}N-decay detection to use "in coincidence–registration" of pairs of outgoing γ'-quanta with the energies $E_{\gamma'} \cong 0.511$ MeV each, flying out in opposite directions to each other and produced in annihilation of irradiated substance's electrons with stopped positrons, emitted at ^{12}N-decays. In such a way it is possible to suppress effectively background of rather high levels and to measure even very small activities (see, for example, [4,5]).
c. ^{12}N-nuclei decay, emitting β^+-particles with the very high $E_{\beta\,max}$ (according to [2], which is more than 3 times as high as those for any other known radioactive isotopes to that moment). So, it may be reasonable to detect at registration of ^{12}N-decay outgoing γ'-quanta with rather high energies $E_{\gamma'}$ (from bremsstrahlung, produced by positrons, emitted at ^{12}N-decays).
d. ^{12}N are the neutron-deficient nuclei with A = 2(Z–1) (here A, Z and (A–Z) – numbers of nucleons, protons and neutrons in a nucleus respectively), while, except for the cases of ^{1}H and ^{3}He, we have for all stable nuclei (including light ones) A ≥ 2Z. According to [2,3], stability of ^{12}N-nuclei against proton emission is almost at borderline. So, for production of ^{12}N it is necessary to choose reactions, which are able to provide values Z = 7 and (A–Z) = 5 with increasing of ratios Z/(A–Z) in comparison with those for mother-nuclei. It seems, that rather big cross sections should be for reactions with small number of nucleons (first of all, of neutrons, let us say, with 1 or 2 neutrons) at output of reactions. Among such reactions with relatively big cross sections (including already mentioned ones) there are: ^{12}C(p,n); ^{10}B(^{3}He,n); ^{13}C(p,2n); ^{11}B(^{3}He,2n); ^{10}B(α,2n) and ^{14}N(γ,2n). Thus, production of ^{12}N-activity practically may be connected only with concentrations of a restricted set of light elements.
e. As it was noted in the items "b." and "c.", ^{12}N-decays may be detected using registration of outgoing decay γ'-quanta, which have rather high penetrating ability. So, the maximal thicknesses of irradiated objects are determined by penetrating abilities of incident particles, which are low for cases of incident heavy charged particles, for example,

mentioned above in the item "d.". There is only one exception for the photonuclear reaction (I), for which incident particles are also γ-quanta. Thus, in the last case it is possible to use ^{12}N-activation for rather thick objects, and then the technique will be connected with concentrations of nitrogen.

f. If an incident beam of γ-quanta has small divergence (as, for example, for bremsstrahlung from not-very thick radiators at $E_e > E_{\gamma\,thresh}$ for the reaction (I)) and produces small its "spot" on irradiated objects, we get the common method for localization of nitrogen concentrations.

g. If for detection of ^{12}N-decays registration of (γ'-γ')-coincidences of annihilation photons (see the item "b." above) is used, we may apply this method also to find localization for concentrations of interest together with the common method of the item "f." with achieving better accuracy and additional suppressing of some possible background.

2. The first variant of connected with ^{12}N detectors of hidden explosives

It seems to be quite reasonable that the author of the work [2] could propose (in agreement with the items "a.", "b.", "e.", "f.", "g" above) the idea [6] (which, unfortunately, as far as it is known, was not yet experimentally confirmed) to use for the external not-destroying control the photonuclear detector of hidden explosives (DHE) with "in coincidence–registration" of pairs of annihilation γ'-quanta with $E_{\gamma'} \cong 0.511$ MeV each, emitted "back to back" and connected with decays of ^{12}N-nuclei, which under bombardment by bremsstrahlung beam from a pulsed electron accelerator are produced in the reaction (I) on ^{14}N-nuclei, contained in significant concentrations in widely used modern explosives. We call here the photonuclear DHE, based on ^{12}N-photoproduction and registration of their decays, according to the original idea [6], as the first variant of connected with registration of ^{12}N-activity DHE, and designate it as DHE-1.

The proposition of DHE-1 in [6] was made for control of air-passengers' baggage, but there is also a big interest to the based on registration of ^{12}N-activity DHE for humanitarian demining of territories and for the external not-destroying control of cargo containers. Unfortunately, it seems that for the latter two cases the proposition [6] does not suit. In the case of landmine searching there is no real possibility for registration of both annihilation γ'-quanta, emitted at angle 180° to each other. In the case of cargo containers there is much higher absorption of outgoing γ'-quanta, than that for baggage of air-passengers (see, for example, in [7] estimations for these values of absorption), what makes the proposition [6] for cargo containers, at least, very problematic.

3. The second variant of connected with ^{12}N detectors of hidden explosives

At the further development of a photonuclear DHE, connected with production of ^{12}N-nuclei [7-23], which included also the moderately successful, but encouraging experiments [8,19], the technique was modified so, that instead of "in coincidence–registration" of pairs of annihilation γ'-quanta there was suggested to register single γ'-quanta, accompanying nuclear decays of interest and, first of all, bremsstrahlung photons, produced by decay β-particles in agreement with the items "a.", "c.", "e.", "f." above. We call here the photonuclear DHE, based on photoproduction of radioactive ^{12}N-nuclei and on detection of their decays by registration of single decay γ'-quanta as the second variant of DHE of a type and designate it as DHE-2. The purpose of this modification is to design the universal photonuclear DHE, connected with ^{12}N-activation, for all three directions of its application, pointed out above. Such modification enables the transition to values of E_γ up to, at least, several MeV with significant decreasing (without taking into account advantages from the coincidental technique) of the corresponding in energy gamma-background level, with essential reduction of absorption values for required γ'-quanta in irradiated objects and with an opportunity to use for γ'-quanta registration such detectors able to "cut off" the big part of gamma-background at

small energies as Čerenkov detectors. In this case for providing with useful signals there is addition to the reaction (I) from the reaction (II), which produces also on ^{14}N-nuclei radioactive nuclei ^{12}B (β^--decay; $E_{\beta\ max} \cong 13$ MeV; $T_{1/2} \cong 20.4$ ms [1]), having $T_{1/2}$ and values of decay $E_{\gamma'}$ for registration, close to those for ^{12}N-nuclei, and, hence, being able to give some addition to a useful signal in such DHE:

$\gamma+^{14}N \rightarrow ^{12}B+2p$ ($E_{\gamma\ thresh} \cong 25.1$ MeV [1]). (II)

As it was already noted partly above, at electron accelerators with $E_e < 55$ MeV for outgoing electrons (we choose this value because it is maximal for the pulsed race track microtrone [15-17], which is now under construction in P.N.Lebedev Physical Institute (Moscow), for, first of all, experimental studies of connected with ^{12}N detectors of hidden explosives), there are few reactions, which may produce radioisotopes with values of $T_{1/2}$, laying in approximate limits, let us say, from 7 ms to 30 ms, and with values of $E_{\gamma'}$ for decay γ'-quanta, close enough to those for the cases of ^{12}N and ^{12}B. Except for the reactions (I) and (II) themselves and some reactions on nuclei ^{14}N and ^{15}N, giving small increasing of sensitivity for DHE-1 and/or DHE-2, such radioactive nuclei may be produced in some background nuclear reactions under bombardment by primary bremsstrahlung photons or by secondary neutrons, produced before in photoneutron reactions, induced by primary bremsstrahlung photons. Practically all reactions under bombardment by any other secondary heavy particles are negligible ones (as it was underlined in [6], it is so even for cases, when instead of secondary neutrons there are secondary protons).

Among radioactive nuclei-products of these background reactions may be (taking into account isotopic abundances, values of reaction thresholds, and, to some extent, chemical abundances and branching ratios for these reactions):
as the above-pointed nuclei-products ^{12}N and ^{12}B, but produced on some other nuclei-targets (not on nitrogen), and among these types of reactions there may be:
the photonuclear reactions, including the reactions (IV) and (V), pointed out in [6]:

$\gamma+^{13}C \rightarrow ^{12}B+p$ (IA: ^{12}C-98.89%, ^{13}C-1.11%; $E_{\gamma\ thresh} \cong 17.5$ MeV [1]), (III)

$\gamma+^{16}O \rightarrow ^{12}N+^{3}H+n$ (IA: ^{16}O-99.76%, ^{17}O-0.04%, ^{18}O-0.20%; $E_{\gamma\ thresh} \cong 45.1$ MeV [1]), (IV)

$\gamma+^{19}F \rightarrow ^{12}N+\alpha+3n$ (IA: ^{19}F-100%; $E_{\gamma\ thresh} \cong 45.6$ MeV [1]); (V)

the reaction under thermal neutrons:

$n+^{11}B \rightarrow ^{12}B+\gamma$ (IA: ^{10}B-19.8%, ^{11}B-80.2%; the released energy $\approx$3.4 MeV [1]); (VI)

the reaction under fast neutrons ($E_{n\ thresh}$ – neutron kinetic energies E_n at the reaction threshold):

$n+^{12}C \rightarrow ^{12}B+p$ ($E_{n\ thresh} \cong 12.6$ MeV [1]); (VII)

as some other radioactive nuclei-products, and among these latter types of reactions there may be the photonuclear reactions:

$\gamma+^{16}O \rightarrow ^{13}B+3p$ (β^--decay; $E_{\gamma\ thresh} \cong 43.2$ MeV; $T_{1/2} \cong 17$ ms [1]), (VIII)

$\gamma+^{16}O \rightarrow ^{13}O+3n$ (β^+-decay; $E_{\gamma\ thresh} \cong 52.1$ МэВ; $T_{1/2} \cong 9$ ms [1]). (IX)

At least, for DHE-2 there may be serious background in initial milliseconds after beam pulse [8,19], connected with (n,γ')-reactions, initiated by photoneutrons (after their slowing down). On the other hand, there may be some background from reactions giving radioisotopes with 0.1 s < $T_{1/2}$ < 1 s, in particular, from reactions with escape of three nucleons, especially, the reactions:

$\gamma+^{12}C \rightarrow ^{9}Li+3p$ (β^--decay; $E_{\gamma\ thresh} \cong 46.8$ MeV; $T_{1/2} \cong 178$ ms [1]). (X)

$\gamma+^{12}C \rightarrow ^{9}C+3n$ (β^+-decay; $E_{\gamma\ thresh} \cong 53.1$ MeV; $T_{1/2} \cong 126.5$ ms [1]), (XI)

4. The cross sections of the used reactions and some background reactions

To optimize the technique of DHE, one needs information on the cross sections, in principle, of all reactions (I)÷(XI). The cross sections of the reactions (III) and (VII) were measured in [24-26] (Fig. 1) and [27] (Fig. 2), respectively. Data on the cross section of the

reaction (VI) under thermal neutrons may be found, for example, in [28]. Unfortunately, we did not find original experimental data on the cross sections of the reactions (I), (II), (IV), (V), (VIII)÷(XI).

The compiled data on the cross sections of the reactions (I)÷(III), (VIII), and (IX) were reported in [9,11,14]. The latter of them is more complete as well; therefore, they are reported here (Fig. 3). However, these data give rise to much criticism. First, their sources are not indicated. Second, the data from these three studies are contradictory. Third, the cross sections of the reaction (III) from [14] near their maximum are several times smaller than the well-consistent corresponding cross sections from [24-26]. Fourth, the claims for the „dynamic range" and validity of behavior at relatively high E_γ with respect to the cross section of the reaction (III), made in [14], are, at least, surprising (compare if only with the behavior of the cross section (III) from [24-26], measured in the range from the cross section maximum to $E_\gamma \approx 30$ MeV). A possible reason for the latter fact is that not measured reaction cross sections were reported in [14], but some predicted values (based, for example, on statistical theory), whose exceptional use is doubtful, in particular, because of the presence of direct nucleons in reaction products. So, we need, experimental data on the cross sections of both useful reactions (I) and (II), and the background reactions (IV), (V), (VIII)÷(XI).

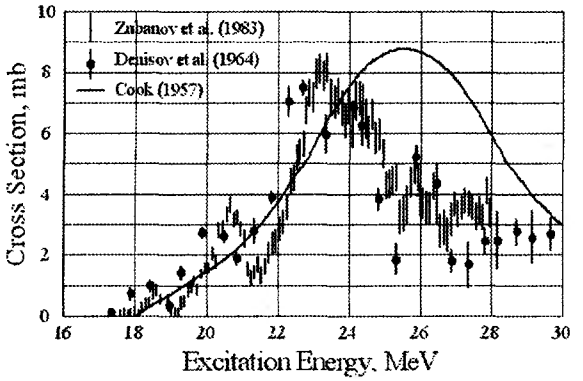

Fig. 1. The cross sections of the reaction (III) in dependence on E_γ [24-26]

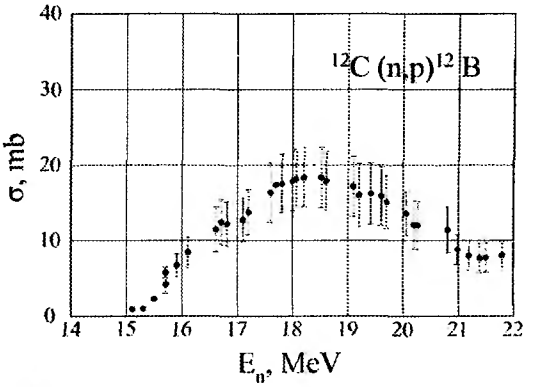

Fig 2. The cross sections of the reaction (VII) in dependence on E_n [27]

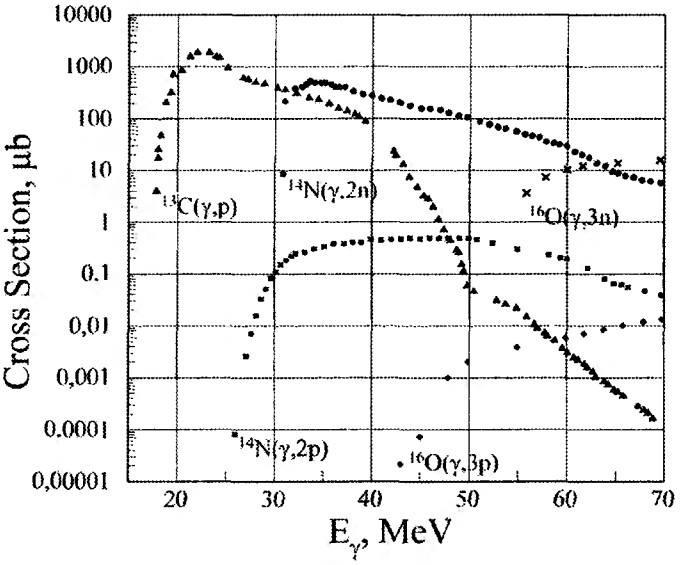

Fig. 3. Compiled data from [14] on the cross sections of the reactions (I), (II), (III), (VIII), (IX) as functions of E_γ

In this technique, some background may be eliminated based on the fact that the thresholds and characteristic E_γ-ranges in the cross sections of the reactions (I) and (II) are much lower than those for the background reaction (IV), (V), (VIII)÷(XI) and another reactions, leading to additional background connected with escape of three nucleons and giving radioisotopes with $0.1\ s < T_{1/2} < 1\ s$. On the other hand, some background may be significantly reduced, because the E_γ thresholds and characteristic ranges for the photonuclear reactions (I) and (II) are much higher, than those for reactions from the giant resonance range (including the reaction (III) and reactions giving the most of photoneutrons (see the cross sections of the latter ones, for example, in [29])).

The small fraction of boron in typical tested objects permits to believe the background from the reaction (VI) to be not very interfering for this technique. The background from the reaction (VII) should be small because (i) the fraction of primary photoneutrons with $E_n > E_{n\ thresh}$ for this reaction is small and (ii) such neutrons with overwhelming probability first undergo scattering; in few of these scattering events, their energy E_n decreases to values below $E_{n\ thresh}$.

As was shown in [16] on the base of analysis of data from [14], the reaction (VIII) is not dangerous due to its small cross sections. We believe, that for background from the reactions (IV,V) situation is the same. In principle, the reaction (IX) may give essential contribution, especially at searching of land-mines, since soil may contain up to 50% of oxygen, but at $E_e <$ 55 MeV this contribution should be small. All background contributions from reactions, giving long-lived isotopes (including the reactions (X,XI)) should be small too, and it seems that their influence may be taken into account by usual procedures of background subtraction.

So, for DHE-2 the most serious background may be from the reaction (III), but, of course, it is very desirable to check situation with all pointed out sources of background experimentally.

5. The third variant of connected with ^{12}N detectors of hidden explosives

Problem of "false signals" is one of the most important for all methods of explosive detection. Its solving to a great extent determines method's efficiency, productivity, and practical importance. As it may be understood from paragraphs 2÷4 in the discussed photonuclear method (with DHE-1 or DHE-2) this problem is reduced to rejection of signals from another substances, containing like explosives nitrogen (N) and/or carbon (C) (see, for example, Table 1). At searching for land-mines, such substances may have vegetable origin and, for example, be wood. At explosive searching in baggage, rejecting of "false signals" is very important because of possible presence of many things in baggage, which are not explosives, but contain also N and/or C.

Table 1. "True" values k_{true} for different substances

substance	chemical formula	k_{true}
explosives		
TNT	$CH_3C_6H_2(NO_2)_3$	0.71
PETN	$C_5H_8N_4O_{12}$	0.82
tetryl	$C_6H_2(NO_2)_4NCH_3$	0.80
hexogen	$N_3(NO_2)_3(CH_2)_3$	0.92
octogen	$N_4(NO_2)_4(CH_2)_4$	0.92
"false" substances		
wood	---	0.03
nitron	$(CH_2CHCN)_n$	0.66
nylon	$(CO(CH_2)_4CONH(CH_2)_6NH)_n$	0.33
capron	$(NH(CH_2)_5CO)_n$	0.49
soap-(Na)	$C_{17}H_{35}COONa$	0.00
shampoo-(K)	$C_{15}H_{31}COOK$	0.00

In the work [11] for DHE-2 to pick out experimentally contributions of background, connected with a presence of C and produced in the reaction (III), there were suggested successive irradiations of tested objects by incident γ-beams with two maximal values of E_γ: $E_{\gamma\,max} = E_e > E_{\gamma\,thresh}$ for the reactions (I) and (II), and then with $E_{\gamma\,max}$ lower, than this values, but higher, than $E_{\gamma\,thresh}$ for the reaction (III). At the first irradiation there will be obtained a sum of signals from N and C, and in the second case – only from C. The similar suggestions were also discussed in [20,21]. Although, in principle, suggestions of a sort seem to be reasonable, but for their realization it is necessary to solve complicated task of operative and precise changing of E_e and keeping in a case a high accuracy control of a γ-intensity. Moreover, it is necessary to take into account changing of spectra for incident γ- and outgoing γ'-quanta in cover-substances, for which usually exact thicknesses and compositions are not known.

Another method to find experimentally for DHE-2 contributions of background, connected with the reaction (III), was suggested also in [11] and is based on differences of energy spectra of γ'-quanta from β-decays of ^{12}N and ^{12}B. For ^{12}N-spectrum of γ'-quanta the upper edge is ~4 MeV higher, than that for ^{12}B. In [11] it is suggested to register secondary decay γ'-quanta independently in three energy intervals: $(\Delta E_{\gamma'})_1 \cong (0.4 \div 0.6)$ MeV, $(\Delta E_{\gamma'})_2 \cong (1.0 \div 4.0)$ MeV, and $(\Delta E_{\gamma'})_3 \approx (4 \div 17)$ MeV. In [11] it is stated, that in $(\Delta E_{\gamma'})_1$ main contribution is from annihilation γ'-quanta with energy ≅0.511 MeV from β^+-decays of ^{12}N; in $(\Delta E_{\gamma'})_2$ main contribution is from decays of ^{12}N and ^{12}B; and in $(\Delta E_{\gamma'})_3$ – from β-decay of only ^{12}N. It is supposed in [11], that ratios of counts, accumulated in these intervals must permit to subtract relative background from C. The grave shortcomings of this method: in $(\Delta E_{\gamma'})_1$ there are also essential contributions from bremsstrahlung γ'-quanta from β-particles, emitted in decays as ^{12}N, as ^{12}B; since absorption of decay γ'-quanta in cover-substances strongly depends on $E_{\gamma'}$, what may give rise to serious distortion of γ'-spectra in a γ'-detector in comparison with original ones, and in particular, to relative suppression of contribution of annihilation γ'-quanta. It seems that altogether these shortcomings make access to high accuracy subtraction of ^{12}B-connected background difficult.

It is important to underling that really at separation of signals from ^{12}N and from ^{12}B even in ideal case we receive separation between respectively a part of signals from N (connected with reaction (I)) and a sum of another part of signals from N (connected with the reaction (II)) and signals from C (connected with the reaction (III)). So, by subtracting ^{12}B-signals from a total quantity of signals, we must receive the same information on N concentration as in the case of DHE-1 (ignoring a difference in efficiencies of decay registration). Let us also remind that both N and C are the basic elements of widely-used explosives (see, for example, Table 1). At least, in principle, it is very desirable to consider signals from C not as background, but as helpful ones in detecting and identification of explosives.

For disclosure and identification of hidden explosives we suggested the third variant of connected with ^{12}N detectors of hidden explosives [30-32], which we designate here as DHE-3, and which consists in registration and analysis of time-distributions of events from photonuclear reactions (I÷III). When a beam pulse of γ-quanta with $E_{\gamma\,max} > 31$ MeV irradiates tested containing N and/or C object, in it as result of the photonuclear reactions, there are produced radioactive nuclei :^{12}N (in the reaction (I)) and/or ^{12}B (in the reactions (II,III)). Relative concentrations of these radioisotopes are unequivocally connected to relative concentrations of N and C in irradiated substances and define unique "portraits" of tested substances. Forms of time-dependences of registered in a case events in γ'-detector are unequivocally determined by values of $T_{1/2}$ for ^{12}N- and ^{12}B-isotopes and by ratios of their initially produced quantities.

In common case a total number N{t} of ^{12}N- and ^{12}B- nuclei, which leave un-decayed to a moment t after an end of irradiation at t = 0, is:

$$N\{t\} = N_{0\,(N\text{-}12)} \times \exp(-\lambda_{(N\text{-}12)} \times t) + N_{0\,(B\text{-}12)} \times \exp(-\lambda_{(B\text{-}12)} \times t), \quad (1)$$

where: $N_{0\,(N\text{-}12)}$, $\lambda_{(N\text{-}12)} = (\ln 2) / (T_{1/2})_{(N\text{-}12)}$ and $N_{0\,(B\text{-}12)}$, $\lambda_{(B\text{-}12)} = (\ln 2) / (T_{1/2})_{(B\text{-}12)}$ – numbers of produced to a moment t = 0 radioactive nuclei, the decay constants, and the half-lives for ^{12}N and ^{12}B, respectively; $N_{0\,\Sigma} \equiv N\{t = 0\} = N_{0\,(N\text{-}12)} + N_{0\,(B\text{-}12)}$.

Analyzing after an end of an irradiation pulse measured time-distributions for an outgoing secondary γ'-radiation from decay of ^{12}B and ^{12}N, one may use this information to determine initial relative concentration of the isotopes ^{12}N and ^{12}B and to identify tested substance. Quantitatively, results of such analysis may be submitted by values of parameter k:

$$k = k_{(N\text{-}12)} = 1 - k_{(B\text{-}12)}, \quad (2)$$

where: $k_{(N\text{-}12)} = \{N_{0\,(N\text{-}12)} / N_{0\,\Sigma}\}$, $k_{(B\text{-}12)} = \{N_{0\,(B\text{-}12)} / N_{0\,\Sigma}\}$ (just k gives produced relative concentration of radioisotopes ^{12}N and ^{12}B and determines unique "portrait" of irradiated substance).

A measured at work of DHE-3 time-distribution of registered by a γ'-detector events from decays of the radioisotopes ^{12}N and ^{12}B is described by:

$$n\{t\} = \lambda_{(N\text{-}12)} \times N_{0\,(N\text{-}12)} \times \exp(-\lambda_{(N\text{-}12)} \times t) \times \Delta t + \lambda_{(B\text{-}12)} \times N_{0\,(B\text{-}12)} \times \exp(-\lambda_{(B\text{-}12)} \times t) \times \Delta t, \quad (3)$$

where Δt – a channel width for a measured time-distribution.

There is a common trouble for variants of photonuclear DHE, using registration of single γ'-quanta, i.e. DHE-2 and DHE-3. As it was already noted above, in several initial milliseconds after an end of irradiation in a γ'-detector, there is rather high background of γ'-quanta from reactions (n,γ'), initiated by photoneutrons. This background may give rise to serious distortions of measurements' results. That is why there is a sense to use not all measured data on distributions n{t}, but only those which are after delay of about several ms, with refusing from direct measurements of $N_{0\,\Sigma}$ -values and respectively from direct calculations of k. Instead of that, we suggest to determine values of k, proceeding, for example, from two measured values n(t), corresponding to pair of moments of time t_i and t_j. In this case, according to (3), we get system of two equations, which are linear ones with respect to unknown values $N_{0\,(N12)}$ и $N_{0\,(B\text{-}12)}$:

$$\begin{cases} n\{t_i\} = \lambda_{(N\text{-}12)} \times N_{0\,(N\text{-}12)} \times \exp(-\lambda_{(N\text{-}12)} \times t_i) \times \Delta t + \lambda_{(B\text{-}12)} \times N_{0\,(B\text{-}12)} \times \exp(-\lambda_{(B\text{-}12)} \times t_i) \times \Delta t, \\ n\{t_j\} = \lambda_{(N\text{-}12)} \times N_{0\,(N\text{-}12)} \times \exp(-\lambda_{(N\text{-}12)} \times t_j) \times \Delta t + \lambda_{(B\text{-}12)} \times N_{0\,(B\text{-}12)} \times \exp(-\lambda_{(B\text{-}12)} \times t_j) \times \Delta t. \end{cases} \quad (4)$$

By solving the system (4), we get values of $N_{0\,(N\text{-}12)}$, $N_{0\,(B\text{-}12)}$, and $k = \{N_{0\,(N\text{-}12)} / N_{0\,\Sigma}\}$. Repeating this procedure to all values of i and j = (i+1), we get a sequence of values of k_i, corresponding to every interval Δt of time-distribution under consideration.

To decrease statistical uncertainties at determination of k, connected with relatively small numbers of counts, accumulated in channels of measured time-distributions, it may be useful to turn from the differential form of describing of a decay process to the integral form. From (1) in this case a difference between quantities of un-decayed nuclei to moments of time t_1 и t_2 ($t_2 > t_1$):

$$N\{t_1\} - N\{t_2\} = N_{0\,(N\text{-}12)} \times [\exp(-\lambda_{(N\text{-}12)} \times t_1) - \exp(-\lambda_{(N\text{-}12)} \times t_2)] + N_{0\,(B\text{-}12)} \times [\exp(-\lambda_{(B\text{-}12)} \times t_1) - \exp(-\lambda_{(B\text{-}12)} \times t_2)] = \sum n_i, \quad (5)$$

where $\sum n_i$ – a sum of events, registered in channels, corresponding to an interval $(t_2 - t_1)$. If to take two time intervals, then from equations (5) we get a system, analogous to (4), from solving of which we get, taking into account (1) and (2), a value of k.

The suggested method of explosive identification, based on analysis of time-distributions of γ'-quanta, registered by their detector, may be considered practically useful, if only k-"portraits" of explosives differ essentially from k-"portraits" of substances, which may give

"false signals". In connection with it, we tried to answer to this question by means of computer simulation of ^{12}N- and ^{12}B- radioisotopes production in objects of interest under bombardment them by bremsstrahlung, generated by incident on radiator electrons with E_e = 55 MeV. In spite of all pointed out above criticism with respect to information on the cross sections of the reactions (I) and (II), as the first step in this simulation, we decided to use for them data from [14] (see also about it below). At small statistical relative uncertainties, there were found values of $N_{0\,(N\text{-}12)}$, $N_{0\,(B\text{-}12)}$, and $N_{0\,\Sigma}$ and calculated values of k, which we call here "true" ones and designate them as k_{true}. Some of found in such a way values of k_{true} are presented in Table 1. We may see that values of k_{true} for explosives differ essentially from those for chemical compounds, which may be in baggage of air-passengers. Values of k_{true} for explosives differ also essentially from those for objects, which have vegetable origin, what is very important at searching for land-mines.

We must to point out, that presented in Table 1 values of k_{true} were calculated within rather rough approximation, in which we not only used doubtful data on some cross sections, but also did not take into account details of some processes, in particular, dependence of physical efficiency of a γ'-detector on $E_{\gamma'}$ and influence of absorption of γ'-quanta in cover-substances on $E_{\gamma'}$-spectra. At practical usage of this technique there is possibility to improve situation considerably by means of special experimental calibrations on a real installation, at which there may be obtained and written into a base of data values of k for substances of interest.

6. Work simulation for the third variant of connected with ^{12}N detectors of hidden explosives

The revealed in previous paragraph differences of values of k_{true} do not mean that at work of real DHE-3 accumulated quantities of counts in channels will be sufficient for calculating of k with accuracy, ensured reliable identification of substances. That is why there was carried out computer simulations of DHE-3 in conditions, imitating baggage inspection in airports at the following main parameters of the installation: E_e = 55 MeV; the electron beam current – 30 mA in the pulse with the duration – 6 μs; the radiator – W with the thickness – 0.35 mm; the surface area of the γ'-detector – 1 m^2; the distance from the tested object to the γ'-detector – 60 cm; the physical efficiency of the γ'-detector – 100%.

It is supposed, that work of this installation consists of consecutive scanning irradiations of a tested object by pulses of γ-radiation and analysis of measured time-distributions of γ'-radiation after each such pulse for receiving express-information on presence of hidden explosives. The following scenario of work was used:

1. The γ'-detector of the installation is switched on with some delay after an end of an accelerator beam pulse, and pulses from the γ'-detector are accumulated in the histogrammic memory of the time-digital converter. An obtained in such a way histogram is written in the computer.
2. Obtained according to the item "1." data are normalized and summed up across all channels with receiving a number N^*_{Σ} . If in this case N^*_{Σ} is less than some threshold $N^*_{\Sigma\,thresh}$, then it is supposed, that in an irradiated region there is no explosives.
3. A removed by the scanning device beam from the next accelerator pulse irradiates the next region of the tested object and initiate new accumulation of data and calculation of the new number N^*_{Σ}. If in this case $N^*_{\Sigma} > N^*_{\Sigma\,thresh}$, then the described above procedure of data processing for registered time-distributions is switched on, and the signals from the previous irradiation are used as background ones.

The presented below results of work simulation for DHE-3 were obtained at the following conditions:

- The connected with produced photoneutrons background signals have time-distribution, described by sum of two exponents. For the first exponent $("T_{1/2}")_1$ = 1.5 ms and the sum

of obtained signals $(N_0)_1 = 700$; for the second exponent – $("T_{1/2}")_2 = 5$ ms and $(N_0)_2 = 800$.

- The useful signals appear from 50 g of trotyl (TNT), covered with the water layer with the thickness – 10 cm. For this registered signals $N_{0\Sigma} = 2100$.
- Accumulation of γ'-detector data beguines at 4 ms after a beam pulse and continues till 19 ms. The channel width for the time-digital converter – 1 ms.

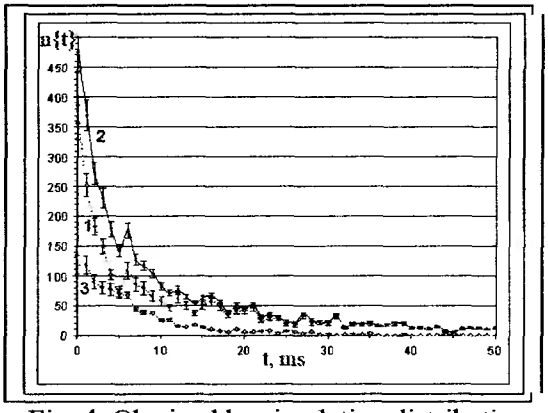

Fig. 4. Obtained by simulation distributions n{t}: and effect (i.e. with an explosive); 3–only effect

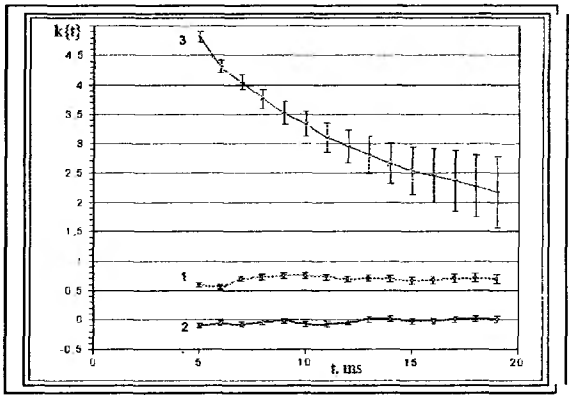

Fig. 5. Obtained from results of simulation $k_{sim}\{t\}$: 1–TNT; 2–carbon; 3–background

The simulated time-distributions are shown on Fig. 4 (the errors are statistical). 1 – background (without explosives); 2 – background and effect (i.e. with an explosive); 3 – only effect.

Usage of described processing of time-distributions permits to calculate values of k_{sim} for every channel in the time interval (5÷19) ms. The results of these calculations of k_{sim} are shown on Fig. 5, where 1 – for 50 g of TNT; 2 – for 50 g of carbon (C). The presented in Table 2 average values of k_{sim} in comparison with the obtained before values of k_{true} demonstrate with convincing effectiveness of the suggested method of substance identification in the conditions, close to work at the restricted quantity of useful signals and the relatively high levels of background.

Table 2. Simulation results of substance identification

substance	k_{true}	k_{sim} (average)	tg(α) (average)
TNT	0.72	0.696 ± 0.062	0.004
carbon	0.0	–0.036 ± 0.070	0.004
background signals	–	2.962 ± 0.062	–0.173

In addition, it is important to point out, that at analysis of signal time-distributions for γ'-detectors, there is one more characteristic, which helps to make identification of explosives. On Fig. 5, except for already described the point groups 1 and 2, there is the group of points 3, corresponding to values of k_{sim} only for the background signals. It is seen, that while for N- and C-containing substances groups of points may be in good approximation presented by straight lines, parallel to t-axis, for background signals tangents to the approximating curve for the corresponding group of points form big angles α with t-axis. This difference is illustrated by the average values of tg(α) for considered cases is presented in Table 2. Therefore, if even because of some reasons at an object test a sum of registered signals receives a sharp increase, but values of k_{sim} are strongly dependent on t, then it means that in the considered part of a tested object ^{12}N- and ^{12}B-nuclei were not produced and it is not explosive.

This method permits to construct new devices with parameters much better than those for existing devices and open perspectives to make detection of explosives totally automatic with separation them from false objects.

At the same described in this paragraph above conditions it was also shown using computer simulation, that when such photonuclear detector of explosives is installed on the moving platform [16,17], it is possible to detect explosives with weight 40 g in ground at depth 20 cm and during 8 hours to test 0.01 km^2 of territory, what is approximately in 500 times more than what the commonly used at humanitarian demining manual method gives.

Usage of stationary installations of a type in the airports permits to get a high efficient and fast acting detector of hidden explosives. For example, the inspection of a baggage unit in airport takes less than 2 s and probability of explosive detecting in a case is much higher than that for the used nowadays methods (different intrascopes, gas analyzers, trained animals, and so on).

Conclusions

The algorithm for substance identification, using measured time-distributions of ^{12}N- and ^{12}B- activities, produced in photonuclear reactions and connected with relative concentrations of nitrogen and carbon in irradiated substances, was considered. It was shown by computer simulation that installations for disclosure and identification of hidden explosives based on photonuclear method can surpass significantly used now for these purposes devices on combined criterion sensitivity-ability for fast acting-trustworthiness. The method is under successful development in LPI RAS.

References

1. Tables of Isotopes. 7-th Edition (edited by C.M.Lederer, V.S.Shirley), Wiley, N.-Y., 1978.
2. L.W.Alvarez. Phys. Rev. 75(1949)1815.
3. W.K.H.Panofsky, D.Reagan. Phys. Rev. 87(1952)543.
4. A.Veyssiere, H.Beil, R.Bergere et al. Nucl. Phys. A227(1974)513.
5. L.Z.Dzhilavyan, N.P.Kucher. Yad. Fiz. 30(1979)294 (in Russian).
6. L.W.Alvarez. Patent US4756866. July 12, 1988.
7. L.Z.Dzhilavyan. Preprint INR RAS 1223/2009. M. 2009 (in Russian).
8. S.Rosander, W.P.Trower. Proc. of the Indo-Soviet Seminar on Microtrons (Indore, India, 1992). ISRN KTH / ALA / PR-92 / 3-SE (1992).
9. W.P.Trower. The Report in P.N.Lebedev Physical Institute, M. 1992.
10. W.P.Trower. Virginia Journal of Science. V. 44, No. 3, Fall 1993, P. 293.
11. W.P.Trower. Nucl. Instr. and Meth. B79(1993)589.
12. W.P.Trower, A.I.Karev, V.N.Melekhin, V.I.Shvedunov, N.P.Sobenin. Nucl.Instr.and Meth. B99(1995)736.
13. E.A.Knapp, A.W.Saunders, V.I.Shvedunov, W.P.Trower. Nucl. Instr. and Meth. B139(1998)517.
14. E.A.Knapp, A.W.Saunders, W.P.Trower. Proc. Conf. «MINE'99», Firenze, Italy, 1999. http://demining.jrc.it/aris/events/mine99/start.htm
15. A.S.Belousov, A.I.Karev, E.I.Malinovsky, V.G.Raevsky, E.I.Tamm, J.A.Konyaev, Yu.M.Kochegarov, V.P.Milovanov, A.S.Rumyantsev, R.R.Iliutchenko, R.G.Maistruk, N.I.Hanyuchenko, A.A.Orlov, S.V.Tverdohlebov. Nauka – proizvodstvu (Science to industry). 2000. № 6. P. 33 (in Russian).
16. A.I.Karev, V.G.Raevsky, J.A.Konyaev, A.S.Rumyantsev, R.R.Iliutchenko. Proc. of NATO Advanced Research Workshop #977941 «Detection of Explosives and Land Mines: Methods and Field Experience», St.-Petersburg, Russia, 2001: NATO-Series book, Kluwer Academic Publisher, Netherlands, 2001.

17. A.Karev, V.Raevsky, J.Konyaev, A.Rumyantsev, A.Averchenko, R.Iliutchenko. Elektronika: Nauka, Tekhnologiya, Biznes (Electronics: Science, Technology, Business). 2002. № 1. P. 54 (in Russian).
18. A.S.Belousov, R.R.Iliutchenko, A.I.Karev, J.A.Konyaev, Yu.M.Kochegarov, E.I.Malinovsky, R.G.Maystruk, V.P.Milovanov, V.G.Raevsky, A.S.Rumyantsev, E.I.Tamm, N.I.Khanyuchenko. Patent RF № 2185614: July 20, 2002.
19. V.M.Alekseev, L.Z.Dzhilavyan, E.E.Zhuravlev, V.D.Laptev, A.N.Lebedev, E.I.Malinovsky, A.I.Karev, V.G.Raevsky, S.G.Raevsky, G.G.Subbotin, A.N.Yakovlev. Report of P.N.Lebedev Physical Institute, RAS, M. 2004 (in Russian).
20. L.Z.Dzhilavyan. Preprint INR RAS 1222/2009. M. 2009 (in Russian).
21. L.Z.Dzhilavyan. Izv. RAN.: Ser. Fiz. 2009. V. 73. No. 6. P. 846 (in Russian).
22. L.Z.Dzhilavyan. Abstracts of the Intern. Conf. «Nucleus 2009», St.-Petersburg, 2009, P. 302 (in Russian).
23. L.Z.Dzhilavyan, A.I.Karev. Abstracts of the Intern. Conf. «Nucleus 2009», St.-Petersburg, 2009, P. 303 (in Russian).
24. B.C.Cook. Phys. Rev. 106(1957)300.
25. N.P.Denisov, A.V.Kulikov, L.A.Kul'chitskiy. JETP 46(1964)1488 (in Russian).
26. D.Zubanov, R.A.Sutton, M.N.Thompson, J.W.Jury. Phys. Rev. C27(1983)1957.
27. E.M.Rimmer, P.S.Fisher. Nucl. Phys. A108(1968)567.
28. N.A.Vlasov. Uspekhi fizicheskikh nauk, Vol. XXXV, issue 4, (1948), P.469 (in Russian).
29. Dietrich S.S., Berman B.L. Atomic Data and Nuclear Data Tables. 38(1988)199.
30. V.G.Raevsky, A.I.Karev, J.A.Konyaev, A.S.Rumyantsev, L.J.Brothers. Patent RF № 2226686: April 10, 2004.
31. A.I.Karev, V.G.Raevsky. Proc.of the 3 Intern. Conf. «Tekhnicheskie sredstva protivodeystviya tekhnicheskim i kriminal'nym vzryvam (Technical means against technical and criminal explosions), St.-Petersburg, 2007, P. 58 (in Russian).
32. L.Z.Dzhilavyan, A.I.Karev, V.G.Raevsky. Abstracts of the Intern. Conf. «Nucleus 2009», St.-Petersburg, 2009, P. 301 (in Russian).

ISOVECTOR EXCITATIONS OF sd-SHELL NUCLEI IN THE PARTICLE-CORE COUPLING VERSION OF SHELL MODEL

N.G. Goncharova
Skobelzyn Institute of Nuclear Physics, Moscow State University,
n.g.goncharova@gmail.com

1. Model input

The giant multipole resonances (MR) are the universal property of the nuclear response to excitation. They represent the most striking feature of the reactions cross sections up to energy excitation E<40 MeV and transferred momentum q< 2.5 Fm^{-1}.

The interpretation of MR complicated structure and its dependence on the individual properties of nuclei is one of the aims of nuclear theory.

Theoretical description of the magnitudes, energy distributions and partial characteristics of multipole resonances (MR) in the frame of multiparticle shell model (MSM) was developed for about 50 years, since first paper [1] on collective dipole states in nuclei. The growth of information on structure of MR has shown that the MSM calculations based on particle-hole configurations are unable to reproduce complicated structure of MR. The usual way to overcome this problem is to expand the basic space and to take into account the interaction of "doorway" states with more complicated configurations, first of all with collective phonons. Applications of this method to the resonances in the middle and heavy closed-shell nuclei were rather successful, but the interpretation of structure and decay properties of MR in open shell nuclei, especially in the deformed ones, represents a challenge to the theory. . Deformations of the target nuclei have very strong influence on the structure of multipole resonances. The excitation of nuclei also leads to the rise of dynamical deformations of nuclear systems which were near to spheres in the ground states. The question is how to take these effects into account is still open. Moreover, due to pairing forces in nuclei the "magic" nuclei are not bona fide completely closed-shell systems.

One of the possible ways to build a set of basic configurations which could be used as doorway states in the microscopic description of multipole resonances in open shell nuclei is to take into account the distribution of the "hole" configurations among the states of residual (A-1) nuclei.

In the "Particle Core Coupling version of Shell Model =PCC SM" these distributions are taken into account in microscopic description of multipole resonances [2, 3].

Wave functions of excited nuclear states in the PCC SM approach are expanded to a set of low-lying states of (A-1) nuclei coupled with a nucleon in a free orbit :

$$\left|J_f,T_f\right\rangle = \sum_{(J'),j} \alpha_f^{(J'),j} \left|(J'E'T')_{A-1} \times (n'l'j'):J_f,T_f\right\rangle \qquad (1)$$

The basic configurations for MR in nuclei under investigation should be built on those states of residual (A-1) nuclei which have non vanishing coefficients of fractional parentage C in the expanding of ground state wave function of target nucleus:

$$\left|J_i,T_i\right\rangle = \sum_{(J'),j} C_i^{(J'),j} \left|(J'E'T')_{A-1} \times (nlj):J_i,T_i\right\rangle \qquad (2)$$

Without violating the Pauli principle, PCC basis can be extended to include the configurations $(J'E'T')_{A-1}$ coupled to low-lying collective excitations of the target nucleus.

Theoretical description of MR in 1p-shell nuclei in the PCC SM has shown good agreement with experimental data for nuclei with A from 7 up to 15 [3]. The same approach to sd-shell nuclei strike against the lack of reliable wave functions for nuclear ground states. The alternative way to estimate the probabilities of the various core states which appears when one of the nucleons would be extracted from nucleus is to use the experimental data on the spectroscopy of direct pick-up reactions. This method was applied to calculations of multipole resonances in sd-shell nuclei and some results of this approach would be discussed in this paper.

The coefficients in the set (2) were estimated as

$$C_i = \frac{S_i}{\sum S_i}, \tag{3}$$

where S_i are the spectroscopic factors of pick-up reaction. The information on distributions of these spectroscopic factors was extracted from review [4] and from [5].

The matrix elements of PCC Hamiltonian involve the excitation energies of the final nuclei levels:

$$\hat{H}_{ij} = (E' + \varepsilon_j + E_c)\delta_{ij} + \hat{V}_{ij}, \tag{4}$$

The estimation of magnitudes of residual interaction matrix elements were based as well on probabilities of pick-up reactions and corresponds to following scheme:

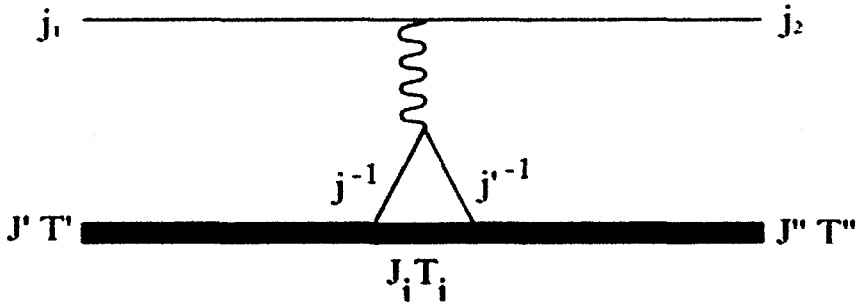

The response functions for multipole excitation of nuclei were calculated as form factors of inelastic electron scattering from target nucleus:

$$F_C^2(q) = \sum_0^{J_{max}} F_{CJ}^2 = (2J_i+1)^{-1} \sum_0^{J_{max}} \left| \langle J_f \| \hat{M}_J^{Coul} \| J_i \rangle \right|^2;$$
$$F_T^2(q) = \sum_1^{J_{max}} (F_{EJ}^2 + F_{MJ}^2) = (2J_i+1)^{-1} \sum_J \left\{ + \left| \langle J_f \| \hat{T}_J^{mag} \| J_i \rangle \right|^2 \right\}. \tag{5}$$

Transverse multipole operators T_J^{mag} and T_J^{el} contain contributions from spin $\hat{A}$ and orbital components $\hat{B}$ of nucleon currents operators [6]:

$$\hat{T}_J^{mag} = \hat{A}_{J-1} + \hat{A}_{J+1} + \hat{B}_J, \qquad \hat{T}_J^{el} = \hat{A}_J + \hat{B}_{J+1} + \hat{B}_{J-1}.$$

$$\hat{A}_J \in j_J(qr)\left[Y_J \times \bar{\sigma}\right]^J, \qquad \hat{B}_J \in j_J(qr)\left[Y_J \times \bar{\nabla}\right]^J. \tag{6}$$

Matrix elements (m.e.) of operators in the space of (1,2) configurations could be represented as sums of m.e. one-particle transitions multiplied on spectroscopic amplitudes Z:

$$Z^J_{TM_T}(j_f j_i) = \sqrt{(2T+1)(2T_i+1)(2J_f+1)}\left\langle T_i M_T T0 \middle| T_f M_T \right\rangle \times$$

$$\sum_{J'T'} C_i^{JT,j_i} \alpha_f^{J'T',j_f} (-1)^{J'-J_i+j_f-J} W(J_i J_f j_i j_f; JJ')(-1)^{T'-T_i+1/2-T} W(T_i T_f \frac{1}{2}\frac{1}{2}; TT'). \tag{7}$$

2. Giant Dipole Resonances in sd-shell nuclei

The calculations of E1 form factors were performed for sd shell nuclei in the frame of particle-core coupling (PCC SM) version of shell model. Results for E1 resonances in ^{28}Si, ^{32}S and ^{40}Ca nuclei [7] have shown good agreement with experimental data.

Nuclei under discussion below have significant deformation β in the ground state

Nucleus	O-18	Ne-22	Mg-24	Mg-26	Al-27
β	0.355[12]	0.562[12]	0.605[12]	0.482[12]	β=0.291[13]

All states of (A-1) nuclei which have non vanishing coefficients of fractional parentage to ground state of A nucleus are included using experimental spectroscopic factors of direct reactions [4,5]. The fixing of energies of final nuclei states is quite reliable, but the error in experimental values of corresponding to these energies S factors are rather high – about 15±20%.

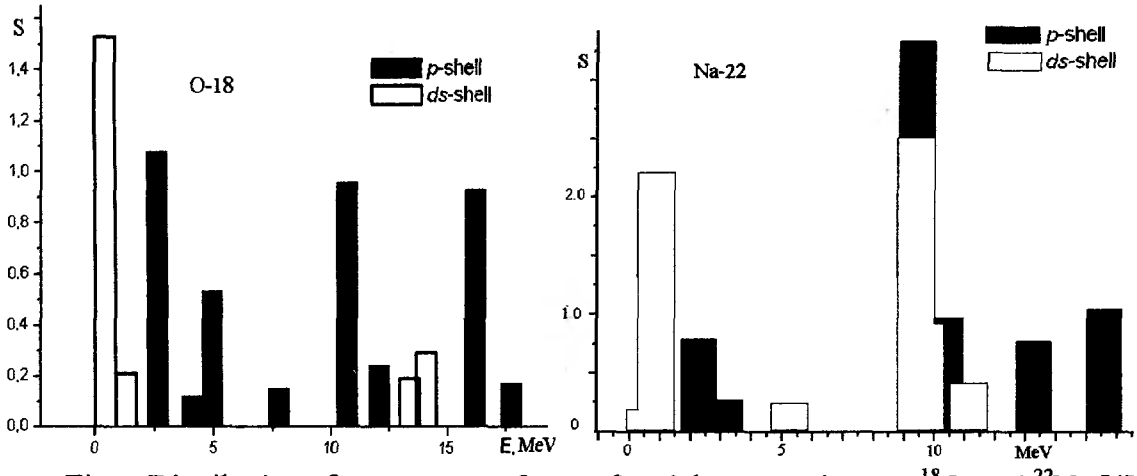

Fig.1. Distribution of spectroscopy factors for pick-up reactions on ^{18}O and ^{22}Ne [4]

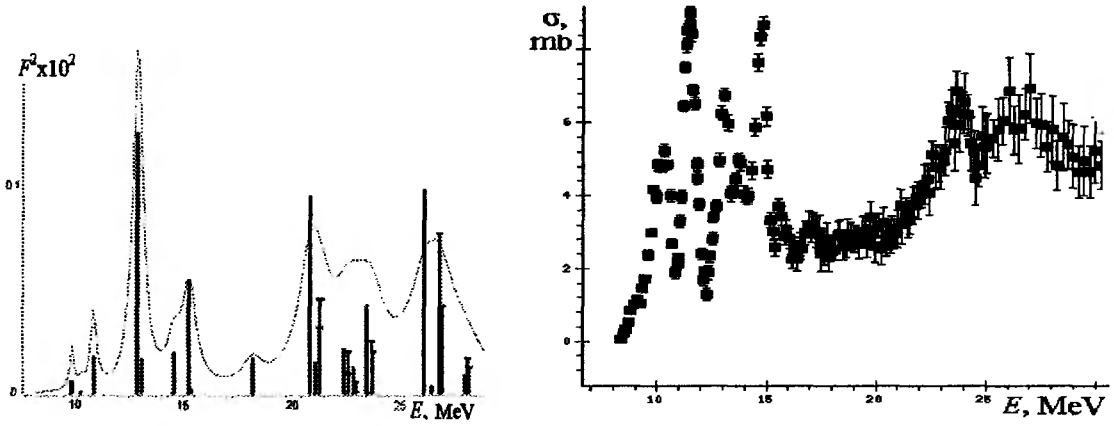

Fig. 2. Distribution of E1 strength in PCCSM and experimental data [8]

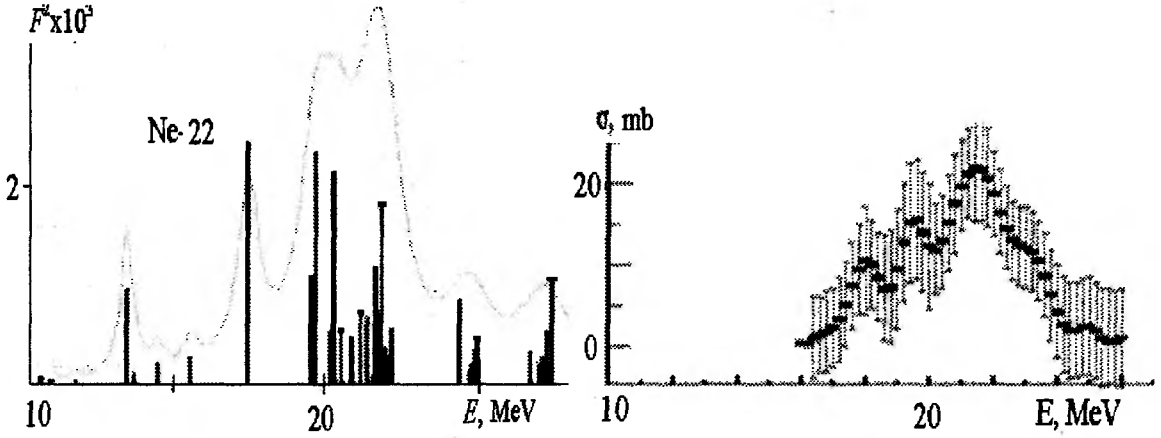

Fig.3. ^{22}Ne F^2(E1) at photopoint and experimental data [10]

PCCSM results for E1 resonances in ^{18}O and ^{22}Ne at photopoint are shown in the fig 2,3. The structure of isovector dipole states in there nuclei is influenced by distribution of S factors (fig.1) and isospin splitting of $T_<$ and $T_>$ states.

Among all sd-shell nuclei calculated in PCC SM ^{24}Mg has the largest deformation displayed in low-lying states of rotational band. Calculations of E1 resonances in ^{24}Mg and ^{26}Mg isotopes in PCC SM successfully explain the main characteristics of these excited states [11] and confirm the validity of used model to description of deformed nuclei.

The fragmentation of the E1 strength in ^{27}Al results from three main factors:

the energy spread of spectroscopic factors over about 60 residual (A=26) nuclei states; isospin splitting and the excitation of six E1 branches.

The results of calculations for E1 in ^{27}Al are presented in Fig.4 along with experimental data [14]. The disintegration of ^{27}Al in direct pick-up reactions leads to a number of excited states in ^{26}Al and ^{26}Mg which are highly deformed. According to the analysis of rotational bands in A=26 nuclei [15], all these states belongs to prolate systems with relations of the lengths for long and short axis ~1.5.

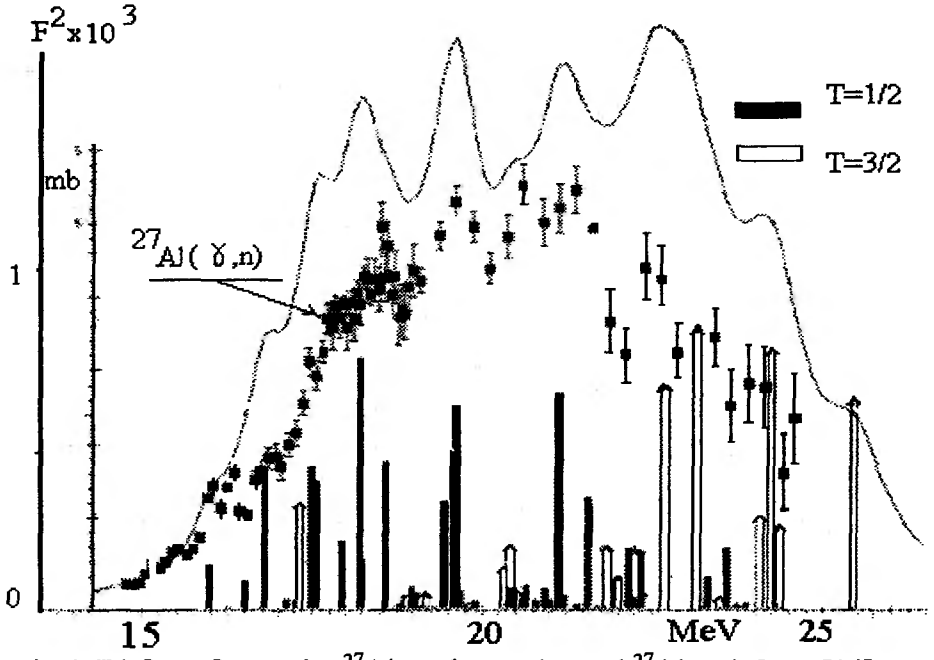

Fig.4. E1 form factors in ^{27}Al at photopoint and ^{27}Al(γ,n) from [14]

3. Magnetic quadrupole states in sd-shell nuclei

While the M1 modes in nuclear electroexcitation have been studied in details for a lot of stable nuclei, much less is known about magnetic quadrupole (M2) resonances. Recently the M2 resonances were investigated in the light and medium nuclei [16,17]. In the excitation of magnetic M2 resonances main role belongs to spin-multipole operators $\hat{A}$. For M2 there are spin-dipole and spin-octupole parts, containing correspondently $A_1 \in [Y_1 \times \bar{\sigma}]^2$ and $A_3 \in [Y_3 \times \bar{\sigma}]^2$ terms. The first one dominates at approximately $0<q<1\text{Fm}^{-1}$, the second one at $q>1\text{Fm}^{-1}$. The strength of M2 mode has as well significant contribution from orbital operator $B \in [Y_2 \times \bar{\nabla}]^2$ m.e.

Orbital modes of M2 excitations were interpreted as nuclear "twist" mode [18]. In the fig.5 are shown contributions of spin (A1+A3) and orbital (B2) terms into M2 form factors for two $1\hbar\omega$ transitions from sd-shell. The interference of orbital and spin parts of M2 operator could be destructive and reveals in disappearance of M2 form factors at some transferred momentum q. Since the positions of these non- diffraction minima depend on configurational structure of the M2 peak, the analysis of q-dependence for M2 states could be used for establishing this structure.

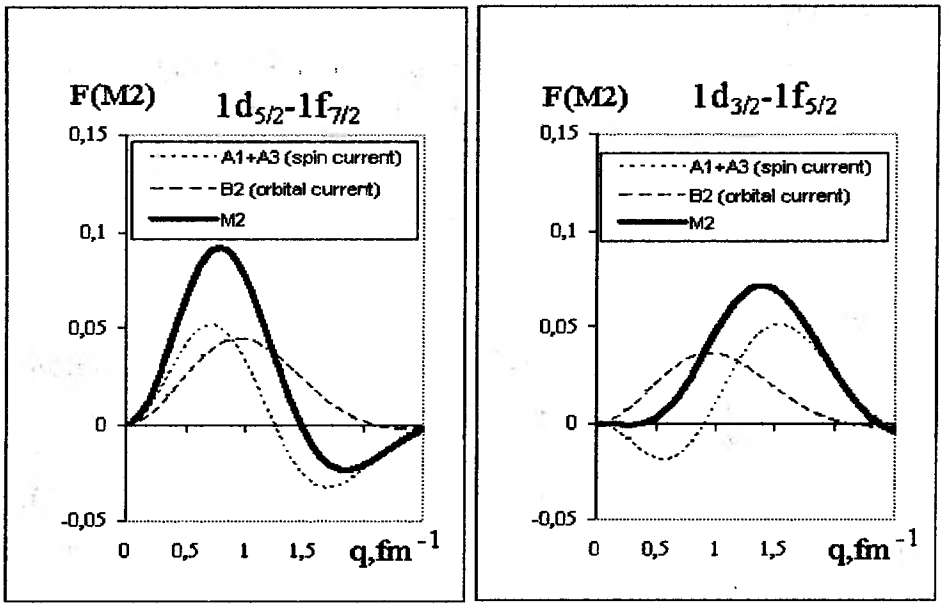

Fig.5. Contributions of spin and orbital currents into M2 form factors

The PCC SM calculations for M2 mode were performed for ^{32}S and ^{24}Mg nuclei. On the Fig.6 are shown the results of PCC SM calculations for M2 form factors in ^{32}S at momentum transfer q=0.6 Fm^{-1} with comparison with results of S-DALINAC experiment [see 17], measured up to energy excitation E=14 MeV. The renormalized value of g-factor $g=0.7g_{free}$ was used.

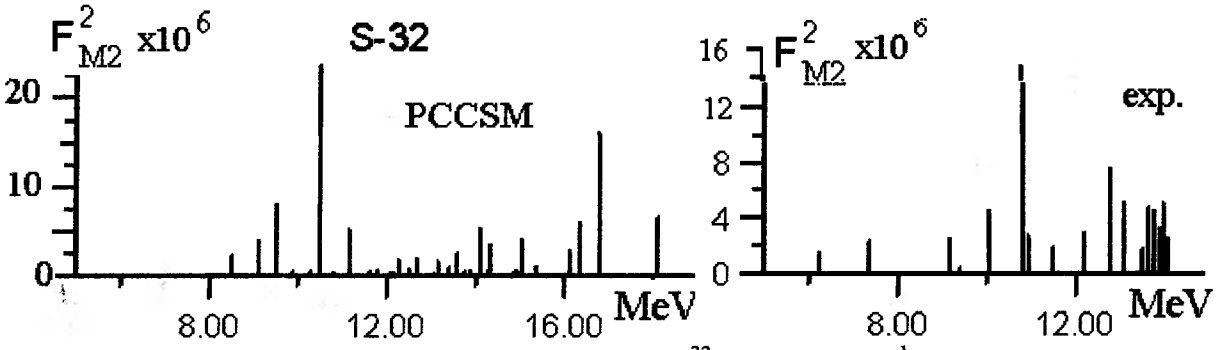

Fig.6. Squared M2 form factors for ^{32}S at q=0.6 Fm^{-1}

The q-dependences of main peaks for $^{32}S(e,e')$ reaction calculated on PCC SM are similar to measured ones (e.g. fir.7)

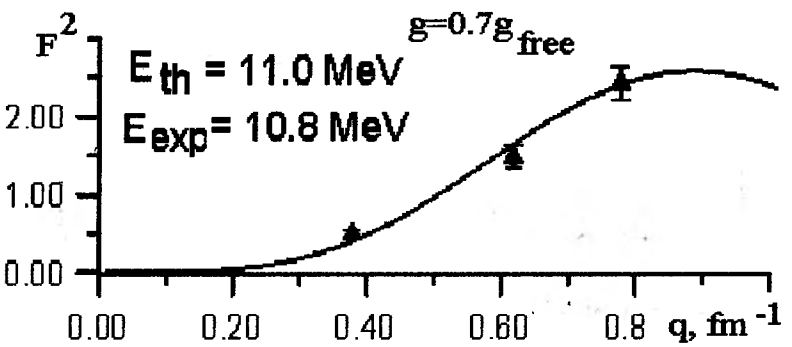

Fig.7. M2 form factors from PCCSM and from S-DALINAC experiment

4. Stretched states in sd-shell nuclei

The maximal spins in $1\hbar\omega$ nuclear excitations appear in so-called stretched states which in sd-shell nuclei reveals as M6 resonances at transferred moments about 1.7±2 fm^{-1}. For excitation of "stretched states" is responsible only the spin component of nucleon current: $\hat{A}_5 \in j_5(qr)\left[Y_5 \times \bar{\sigma}\right]^6$. Their doorway states correspond solely to $1d_{5/2} \rightarrow 1f_{7/2}$ transition. The relatively simple structure of stretched states makes them a reliable test for theoretical model approximations.

In the Fig.8 are shown the results of PCCSM calculation for M6 form factors in ^{40}Ca at q=1.8 fm^{-1} together with distribution of hole states in ^{39}Ca [19]. The fragmentation of 6^- T=1 peak into cluster of 20 levels is a consequence of $1d_{5/2}$ hole spread among a lot of $5/2^+$ states of ^{39}Ca. This distribution explains the fact that 6^- T=1 states were not identified in ^{40}Ca (e,e') reactions. However the presence of M6 in excitation of ^{40}Ca was seen in (p,p') and (p,n) reactions on this nucleus as a broad maximum at about 14 MeV [20,21].

The energy distributions of M6 resonances in ^{32}S are shown on the Fig. 9 near the maximum of F^2(M6) with the results of ^{32}S(e,e') experiment [22]. The spreading of the M6 strength over energies between 11 -16 MeV corresponds to experimental data but this fragmentation based on direct reactions spectroscopy does not exhaust all factors that produce the structure of multipole resonances.

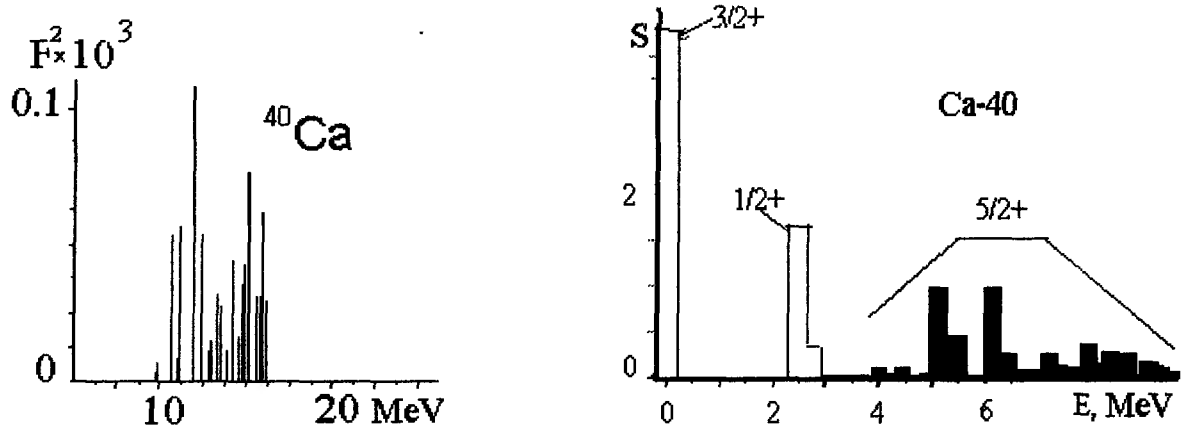

Fig. 8.Distributions of M6 strength in ^{40}Ca (PCC SM) and S factors of ^{40}Ca(d,t)[19]

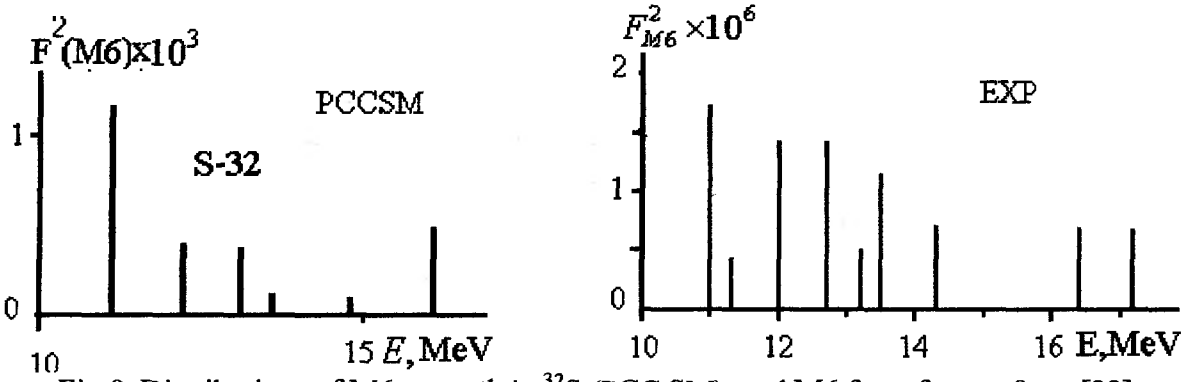

Fig.9. Distributions of M6 strength in ^{32}S (PCC SM) and M6 form factors from [22]

SUMMARY

- The deviation of (A) nucleus from closed shells or subshells reveals in a wide range of energy distribution for "hole" among the (A-1) nuclei states. In the PCC version of SM these distributions are taken into account in microscopic description of multipole resonances in sd-shell nuclei using spectroscopy of pick-up reactions.
- The structure of $1\hbar\omega$ multipole resonances from E1 up to M6 could be realistically reproduced in the PCC SM approach.
- The energy spread of final nuclei states is one of the main origins of the MR fragmentation in open shell nuclei. Comparison of PCC SM results with experimental data on multipole resonances cross sections confirms the validity of this approach for a range of momentum transfer from "photopoint" up to $q \approx 2$ Fm^{-1}.
- The connection between direct and resonance reactions revealed in values and distributions of spectroscopy factors for pick-up processes makes possible to obtain realistic description of multipole resonances in nuclear cross sections.

REFERENCES

1. G.E.Brown,M.Bolsterly, Phys.Rev.Lett. **3** (1959)472
2. N.G.Goncharova, N.P.Yudin, Phys. Lett.**B29**, (1969) 272;
3. N.G.Goncharova, H.-R.Kissener, R.A.Eramzhyan, Sov.J.Part.Nucl.**16** (1985)337
4. P.M. Endt, Nucl. Phys. **A521**, (1990) 1
5. http://www.nndc.bnl.gov
6. T.W.Donnelly, J.D.Walecka, Ann.Rev.Nucl.Sci., **25** (1975)569
7. N.G.Goncharova, A.Dzhioev, Nucl.Phys.**A690** (2001) 247**c**
8 J.H. Kelley *et al*, Nucl. Phys.A**564** (1993)1
9. U. Kneissl, K.H.Leister *et al,* Nucl.Phys.A**272**(1976) 125
10. V.Varlamov, M.E.Stepanov, BRAS Physics **64**, №3 (2000)
11. N.G.Goncharova ,N.D.Pronkina, Phys.At.Nucl. **68** (2005)921;**70,** (2007)671
12. S. Raman *et al,* Atomic Data & Nucl.Data Tables **78,** (2001) 1
13. N.Stone, *Table of New Nuclear Moments. 1997*
14. Y.I.Assafiri, G.F.Egan, M.N.Thompson, Nucl. Phys. **A413**(1984) 416
15. H. Röpke, P.M.Endt, Nucl. Phys.**A632**(1998)173
16. P.von Neumann-Cosel, F.Neumeyer *et al,* Phys.Rev.Lett.**82**(1999)1105
17. F.Hofmann, P.von Neumann-Cosel *et al,* Phys.Rev.**C65**(2002)024311
18. G.Holzwarth,G.Eckart, Nucl.Phys.**A325**(1979)1
19. P.Doll, G.J.Wagner, K.T.Knopfle, Nucl.Phys.**A263**(1976)210
20. B.D.Anderson *et al*,Phys.Lett. **123B** (1983)383
21. T.Saito *et al,* Phys.Rev.**C40**(1989)R1109
22. B.L. Clausen, R.J. Peterson, R.A. Lindgren, Phys. Rev. **C38** (1988) 589

PARTICLE-HOLE OPTICAL MODEL FOR GIANT-RESONANCE STRENGTH FUNCTIONS

M.H. Urin
National Research Nuclear University "MEPhI"
115409 Moscow, Russia

Abstract

An attempt is undertaken to formulate a particle-hole optical model for description of giant-resonance strength functions at arbitrary (but high enough) excitation energies. The model is based on the Bethe–Goldstone equation for the particle-hole Green function. This equation involves a specific energy-dependent particle-hole interaction that is due to virtual excitation of manyquasiparticle configurations. After energy averaging, this interaction involves an imaginary part. The analogy between the single-quasiparticle and particle-hole optical models is outlined.

1 Introduction

Damping of giant resonances (GRs) is a long-standing problem for theoretical studies. There are three main modes of GR relaxation: (i) particle-hole (p–h) strength distribution (Landau damping), which is a result of the shell structure of nuclei; (ii) coupling of (p–h)-type states with the single-particle (s.p.) continuum, which leads to direct nucleon decay of GRs; and, (iii) coupling of (p–h)-type states with manyquasiparticle configurations, which leads to the spreading effect. An interplay of these relaxation modes takes place in the GR phenomenon. A description of the giant-resonance strength function with exact allowance for the Landau damping and s.p. continuum can be obtained within the continuum-RPA (cRPA), provided the nuclear mean field and p–h interaction are fixed [1]. As for the spreading effect, it is described within microscopic and phenomenological approaches. The coupling of the (p–h)-type states, which are the doorway states (DWS) for the spreading effect, with a limited number of 2p–2h configurations is explicitly taken into account within the microscopic approaches (see, e.g., Refs. [2,3]). Some questions to the basic points of the approach could be brought up:

(1) "Ternalization" of the DWS, which form a given GR, i.e. the DWS coupling with manyquasiparticle states (MQPS) (the latter are complicated superpositions of 2p–2h, 3p–3h, ... configurations) is not taken into account. As a result, each DWS may interact with others via 2p–2h configurations. Due to complexity of MQPS one can reasonably expect that after energy averaging the interaction of different DWS via MQPS would be close to zero (the statistical assumption). (2) The use of a limited basis of 2p–2h configurations does not allow to describe correctly the GR energy shift due to the spreading effect. The full basis of these

configurations should be formally used for this purpose. (3) With the single exception of Ref. [4], there are no studies of GR direct-decay properties within the microscopic approaches.

Within the so-called semimicroscopic approach, the spreading effect is phenomenologically taken into account directly in the cRPA equations in terms of the imaginary part of an effective s.p. optical-model potential [5,6]. Within this approach, the afore-mentioned statistical assumption is supposed to be valid and used in formulation of the approach. The GR energy shift due to the spreading effect is evaluated by means of the proper dispersive relationship, and therefore, the full basis of MQPS is formally taken into account [7]. The approach is applied to description of direct-decay properties of various GRs (the references are given in Ref. [6]). In accordance with the "pole" approximation used for description of the spreading effect within the semimicroscopic approach, the latter is valid in the vicinity of the GR energy. However, for an analysis of some phenomena it is necessary to describe the low- and/or high-energy tails of various GRs. For instance, the asymmetry (relative to 90°) of the (γn)–reaction differential cross section at the energy of the isovector giant quadrupole resonance is determined, in particular, by the high-energy tail of the isovector giant dipole resonance [8]. Another example is the isospin-selfconsistent description of the IAR damping. In particular, the IAR total width is determined by the low-energy tail of the charge-exchange giant monopole resonance [9,10].

In the present work, we attempt to formulate the p–h optical model for a phenomenological description of the spreading effect on GR strength functions at arbitrary (but high enough) energies. In this attempt, our formulation is analogous to that of the s.p. optical model [11,12]. The dispersive version of this model [11] is widely used for description of various properties of single-quasiparticle excitations at relatively high energies (see, e.g., Ref. [13]). This model can be also used for description of direct particle decay of subbarier s.p. states [14].

2 Single-particle and particle-hole Green functions

The starting point of the formulation of the s.p. optical model is the Fourier-component of the Fermi-system s.p. Green function, $G(x,x';\varepsilon)$, taken in the coordinate representation (see, e.g., Refs. [11,12]). In analogy with this, we start formulation of the p–h optical model from the Fourier-component of the Fermi-system p–h Green function, $\mathcal{A}(x,x';x_1,x_1';\omega)$, also taken in the coordinate representation. Being a kind of the Fermi-system two-particle Green function (for definitions see, e.g., Ref. [15]), $\mathcal{A}$ satisfies the following spectral expansion:

$$\mathcal{A}(x,x';x_1,x_1';\omega) = \sum_s \left(\frac{\rho_s^*(x',x)\rho_s(x_1,x_1')}{\omega - \omega_s + i0} - \frac{\rho_s^*(x_1',x_1)\rho_s(x,x')}{\omega + \omega_s - i0} \right). \qquad (1)$$

Here, $\omega_s = E_s - E_0$ is the excitation energy of an exact state $|s\rangle$ of the system and $\rho_s(x,x') = \langle s|\widehat{\Psi}^+(x)\widehat{\Psi}(x')|0\rangle$ is the transition matrix density ($\widehat{\Psi}^+(x)$ is the operator of particle creation at the point x). In accordance with the expansion of Eq. (1) the p–h Green function determines the strength function $S_V(\omega)$ corresponding to an external (generally, nonlocal) s.p. field $\widehat{V} = \int \widehat{\Psi}^+(x)V(x,x')\widehat{\Psi}(x')dxdx' \equiv \left[\widehat{\Psi}^+ V \widehat{\Psi}\right]$:

$$S_V(\omega) = -\frac{1}{\pi} Im \left[V^+ \mathcal{A}(\omega) V\right], \qquad (2)$$

where the brackets [...] mean the proper integrations.

The free s.p. and p–h Green functions, $G_0(x,x';\varepsilon)$ and $\mathcal{A}_0(x,x';x_1,x_1';\omega)$, respectively, are determined by the mean field (via the s.p. wave functions) and the occupation numbers (only nuclei without nucleon pairing are considered). Being determined by Eq. (1), the free transition matrix densities $\rho_s^{(0)}(x,x')$ are orthogonal: $\left[\rho_s^{(0)*}\rho_{s'}^{(0)}\right] = \delta_{ss'}$. As applied to transition densities $\rho_s^{(0)}(x=x')$, this statement is false. The RPA p–h Green function, $\mathcal{A}_{RPA}(x,x';x_1,x_1';\omega)$, is determined also by a p–h (local) interaction $\mathcal{F}(x,x';x_1,x_1') = F(x,x_1)\delta(x-x')\delta(x_1-x_1')$, which is responsible for long-range correlations leading to formation of GRs. In particular, the Landau–Migdal forces $F(x,x_1) \to F(x)\delta(x-x_1)$ are used in realizations of the semimicroscopic approach of Refs. [5,6]. The RPA p–h Green function satisfies the expansion, that is similar to that of Eq. (1). In such a case, the RPA states $|d\rangle$ are the DWS for the spreading effect. The local RPA p–h Green function $A(x,x_1;\omega) = \mathcal{A}(x=x';x_1=x_1';\omega)$ determined by the p–h interaction $F(x,x_1)$ is used for cRPA-based description of the GR strength function corresponding to a local external field $\widehat{V} = \int \widehat{\Psi}^+(x)V(x)\widehat{\Psi}(x)dx$ [1].

The s.p. and p–h Green functions satisfy, respectively, the Dyson and Bethe–Goldstone integral equations:

$$G(\varepsilon) = G_0(\varepsilon) + [G_0(\varepsilon)\Sigma(\varepsilon)G(\varepsilon)]\,, \tag{3}$$

$$\mathcal{A}(\omega) = \mathcal{A}_{RPA}(\omega) + [\mathcal{A}_{RPA}(\omega)\mathcal{P}(\omega)\mathcal{A}(\omega)]\,. \tag{4}$$

The self-energy operator $\Sigma(x,x';\varepsilon)$ and the polarization operator $\mathcal{P}(x,x';x_1,x_1';\omega)$ describe the coupling, correspondingly, of single-quasiparticle and (p–h)-type states with MQPS. Analitical properties of G and Σ are nearly the same. A similar statement can be made for $\mathcal{A}$ and $\mathcal{P}$. The quantities $\Sigma(\varepsilon)$ and $\mathcal{P}(\omega)$ both exhibit a sharp energy dependence due to a high density of poles corresponding to virtual excitation of MQPS. Concluding this Section, we present the alternative equation for the p–h Green function:

$$\mathcal{A}(\omega) = \mathcal{A}_0(\omega) + [\mathcal{A}_0(\omega)\left(\mathcal{F}+\mathcal{P}(\omega)\right)\mathcal{A}(\omega)]\,, \tag{5}$$

which follows from Eq. (4) and from the equation for $\mathcal{A}_{RPA}$. The latter is similar to Eq. (4) and containes the p–h interaction $\mathcal{F}$.

3 Transition to the optical models

Since the density of MQPS, ρ_m, is large and described by statistical formulae, only the quantities $\overline{\Sigma}(x,x';\varepsilon)$ and $\overline{\mathcal{P}}(x,x';x_1,x_1';\omega)$ averaged over an interval $J \gg \rho_m^{-1}$ can be reasonably parameterized. As applied to $\overline{\Sigma}(\varepsilon) = \Sigma\left(\varepsilon + iJSgn(\varepsilon-\mu)\right)$, it is done, e.g., in Refs. [11,12]:

$$\overline{\Sigma}(x,x';\varepsilon) = Sgn(\varepsilon-\mu)\left\{-iw(x;\varepsilon) + p(x;\varepsilon)\right\}\delta(x-x'). \tag{6}$$

Here, μ is the chemical potential and $w(x;\varepsilon)$ is the imaginary part of a (local) optical-model potential. Assuming that the radial dependencies of p and w are the same, i.e. $w(x;\varepsilon) \to w(r)w(\varepsilon)$ and $p(x;\varepsilon) \to w(r)p(\varepsilon)$, the intensity of the real addition to the mean field, $p(\varepsilon)$, has been expressed in terms of $w(\varepsilon)$ via the corresponding dispersive relationship [11]. It is noteworthy, that the optical-model addition to the mean field can be taken to be local, i.e. $\overline{\Sigma}(x,x';\varepsilon) \sim \delta(x-x')$, in view of a large momentum transfer (of order of the Fermi momentum) at the "decay" of single-quasiparticle states into MQPS. The energy averaged

s.p. Green function $\overline{G}(x,x';\varepsilon)$ satisfies to the Eq. (3), which involves in such a case the quantity $\overline{\Sigma}$ of Eq. (6). Actually, $\overline{G}$ is the Green function of the Schrödinger equation, which involves the addition to the mean field considerated above.

The energy-averaged polarization operator can be parameterized similarly to Eq. (6):

$$\overline{\mathcal{P}}(x,x';x_1,x_1';\omega) = \{-i\mathcal{W}(x,x';\omega) + P(x,x';\omega)\}\,\delta(x-x_1)\delta(x'-x_1'). \qquad (7)$$

Assuming that the coordinate dependencies of the quantities P and $\mathcal{W}$ are the same, i.e. $\mathcal{W}(x,x';\omega) \to \mathcal{W}(x,x')\mathcal{W}(\omega)$ and $P(x,x';\omega) \to \mathcal{W}(x,x')P(\omega)$, we can express $P(\omega)$ in terms of $\mathcal{W}(\omega)$ via the corresponding dispersive relationship. The example of such a relationship is given in Ref. [7]. In accordance with Eqs. (4), (5), (7) the energy-averaged p–h Green function satisfies to the equivalent equations:

$$\overline{\mathcal{A}}(\omega) = \mathcal{A}_{RPA}(\omega) + \left[\mathcal{A}_{RPA}(\omega)\overline{\mathcal{P}}(\omega)\overline{\mathcal{A}}(\omega)\right], \qquad (8)$$

$$\overline{\mathcal{A}}(\omega) = \mathcal{A}_0(\omega) + \left[\mathcal{A}_0(\omega)\left(\mathcal{F} + \overline{\mathcal{P}}(\omega)\right)\overline{\mathcal{A}}(\omega)\right]. \qquad (9)$$

Formally, Eqs. (7)–(9) are the basic equations of the p–h optical model. In particular, the energy-averaged strength function is determined by Eq. (2) with substitution $\mathcal{A}(\omega) \to \overline{\mathcal{A}}(\omega)$.

To realize the model in practice, a reasonable parametrization of $Im\overline{\mathcal{P}}$ should be done with taking the statistical assumption into account. For this purpose, we consider the quantity $\mathcal{A}_{RPA}$ within the discrete–RPA (dRPA) in the "pole" approximation. In accordance with Eq. (1), we have

$$\mathcal{A}_{RPA}(x,x';x_1,x_1';\omega) \to \sum_d \rho_d^*(x',x)\rho_d(x_1,x_1')(\omega-\omega_d+i0)^{-1}. \qquad (10)$$

The statistical assumption $\left[\rho_d^*\overline{\mathcal{P}}\rho_{d'}\right] \sim \delta_{dd'}$ is fulfilled, provided that: (i) the intensity $\mathcal{W}(x,x';\omega)$ is nearly constant within the nuclear volume, i.e. $\mathcal{W}(x,x';\omega) \to \mathcal{W}(\omega)$; and, (ii) the dRPA transition matrix densities are orthogonal, i.e. $[\rho_d^*\rho_{d'}] = \delta_{dd'}$. Under these assumptions, the solution of Eq. (8) can be easily obtained in the pole approximation: $\overline{\mathcal{A}}(\omega) = \mathcal{A}_{RPA}(\omega-\omega_d+i\mathcal{W}(\omega)-P(\omega))$. As a result, the energy-averaged strength functions is the superimposition of the DWS resonances:

$$\overline{S}_V(\omega) = -\frac{1}{\pi}Im\sum_d \left|\left[V^+\rho_d\right]\right|^2 (\omega-\omega_d+i\mathcal{W}(\omega)-P(\omega))^{-1}. \qquad (11)$$

The quantity $2\mathcal{W}$ can be considered as the mean DWS spreading width $\langle\Gamma_d^{\downarrow}\rangle$, which might be larger than the mean energy interval between neighbouring DWS resonances.

A few points are noteworthy in conclusion of this Section. Formally, the p–h optical model is valid at arbitrary (but high enough) excitation energy. The low limit is determined by the possibility of using the statistical formulae to describe the MQPS density. Within the semimicroscopic approach, the substitution like $\omega \to \omega + i\mathcal{W}(\omega) - P(\omega)$ is used in the cRPA equations to take the spreading effect phenomenologically into account in the "pole" approximation together with the statistical assumption [6,7]. Within the s.p. optical model the statistical assumption for "decay" of different s.p. states with the same angular momentum and parity into MQPS seems to be valid. At high excitation energies $|\varepsilon-\mu|$, when the empirical value of $w(\varepsilon)$ is comparable with the energy interval between the aforementioned s.p. states, the empirical radial dependence $w(r)$ becomes nearly constant within the nuclear volume (see, e.g., Refs. [13]).

4 "Single-level" giant resonance

The p–h optical model can be simply realized in terms of the energy-averaged local p–h Green function $\overline{A}(x,x_1;\omega)$ to describe the strength function of a "single-level" GR, because in such a case there is no need for the statistical assumption. Being more simple, the equations like (4), (5), (7)–(9) are actually the straight-forward extension of the corresponding cRPA equations. In practice, within the cRPA it is more convenient to use the equation for the effective field $\overline{V}(x,\omega)$, which corresponds to a local external field $V(x)$ and is determined in accordance with the relationship: $[V\overline{A}(\omega)] = [\overline{V}(\omega)A_0(\omega)]$. The effective field determines the strength function:

$$\overline{S}_V(\omega) = -\frac{1}{\pi} Im\left[V_0 A_0(\omega)\overline{V}(\omega)\right], \tag{12}$$

and satisfies to the equation:

$$\overline{V}(\omega) = V + \left[\left(F + \overline{\Pi}(\omega)\right) A_0(\omega)\overline{V}(\omega)\right]. \tag{13}$$

The energy-averaged local polarization operator is parameterized similarly to Eq. (7):

$$\overline{\Pi}(x,x_1;\omega) = C\left\{-iW(x;\omega) + P(x;\omega)\right\}\delta(x-x_1). \tag{14}$$

Here, $C = 300\,\mathrm{MeV\,fm^3}$ is the value often used in parametrization of the Landau–Migdal forces; W and P are the dimensionless quantities, which can be parameterized as follows: $W(x;\omega) \to W(r)W(\omega)$ and $P(x;\omega) \to W(r)P(\omega)$, where $P(\omega)$ is determined by $W(\omega)$ via the corresponding dispersive relationship [7].

Due to strong coupling with s.p. continuum the high-energy GRs (they are mostly the overtones of corresponding low-energy GRs) can be roughly considered as the "one-level" ones. Being the IAR overtone, the charge-exchange (in the β^--channel) giant monopole resonance ($\mathrm{GMR}^{(-)}$) is related to these GRs. Within the isospin-selfconsistent description of the IAR damping [9,10], the low-energy "tail" of the $\mathrm{GMR}^{(-)}$ in the energy dependence of the "Coulomb" strength function $\overline{S}_C^{(-)}(\omega)$ determines the IAR total width Γ_A via the nonlinear equation:

$$\Gamma_A = 2\pi S_A^{-1}\overline{S}_C^{(-)}(\omega = \omega_A). \tag{15}$$

Here, $S_A \simeq (N-Z)$ is the IAR Fermi strength, ω_A is the IAR energy, and the "Coulomb" strength function corresponds to the external field $V(x) \to V_C^{(-)} = \left(U_C(r) - \omega_A + \frac{i}{2}\Gamma_A\right)\tau^{(-)}$, where $U_C(r)$ is the mean Coulomb field. Strength function $\overline{S}_C^{(-)}(\omega)$ exhibits a wide resonance corresponding to the $\mathrm{GMR}^{(-)}$. In Fig. 1, we present the strength function calculated for the ^{208}Pb parent nucleus within: (i) the cRPA (in such a case the strength function $S_C^{(-)}(\omega = \omega_A)$ determines the IAR total escape width found without taking the isospin-forbidden spreading effect into account [16]); (ii) the semimicroscopic approach [10] and, (iii) the p–h optical model by Eqs. (12)–(14). All the model parameters, parameterization of the imaginary part of the effective s.p. optical-model potential $I(r;\omega)$ [10] and parameterization of $W(r;\omega)$ in Eq. (14) are taken the same in both approaches. The intensities of $I(r;\omega)$ and $W(r;\omega)$ are chosen to reproduce in calculations the observable total width of the $\mathrm{GMR}^{(-)}$ in ^{208}Bi ($\simeq$ 15 MeV). Both approaches lead to the similar results, which are not exactly the same for the low-energy "tail" of the $\mathrm{GMR}^{(-)}$ at $\omega \simeq \omega_A$. Irregularities in the energy dependence of $\overline{S}_C^{(-)}(\omega)$ calculated within the p–h optical model are explained by the fact that the $\mathrm{GMR}^{(-)}$ can be roughly considered as the "one-level" one.

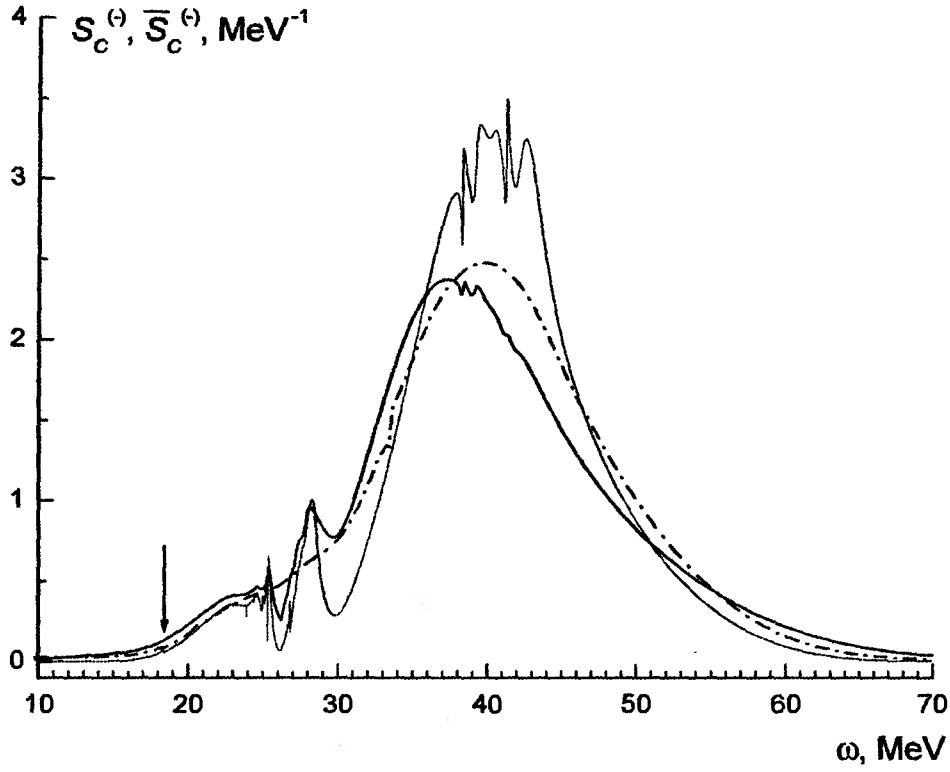

Fig 1. The "Coulomb" strength function calculated for the ^{208}Pb parent nucleus within the cRPA (thin line), the semimicroscopic approach (dash–dotted line), and p–h optical model (full line). The arrow indicates the IAR energy. .

5 Summary and perspectives

In the present work, the particle-hole optical model for giant-resonance strength functions has been formulated in terms of the energy-averaged nonlocal particle-hole Green function. The equation for this Green function contains a specific energy-dependent particle-hole interaction, which is due to virtual excitation of manyquasiparticle configurations. The intensity of the imaginary part of this interaction should be taken nearly constant within nuclear volume to satisfy to the statistical assumption on the independent spreading of different particle-hole-type states that form a given giant resonance. The strength function of the "single-level" giant resonance can be described in terms of the energy-averaged local particle-hole Green function.

Along with numerical realizations, the particle-hole optical model can be extended to describe direct particle decays of giant resonances. These points are under consideration.

The author thanks M.L. Gorelik for the calculation leading to the results presented in Fig. 1, and V.S. Rykovanov for his kind help in preparing the manuscript.

This work is partially supported by RFBR under grant 09-02-00926-a.

References

[1] S. Shlomo, G. Bertsch, Nucl. Phys. A 243, 507 (1975).

[2] G.F. Bertsch, P.F. Bortignon, R.A. Broglia, Rev. Mod. Phys. 55, 287 (1983).

[3] S. Kamerdzicv, J. Speth, G. Tertychny, Phys. Rep. 393, 1 (2004).

[4] G. Colò et al., Phys. Rev. C 50, 1496 (1994).

[5] M.L. Gorelik, I.V. Safonov, M.H. Urin, Phys. Rev. C 69, 054322 (2004).

[6] M.H. Urin, Nucl. Phys. A 811, 107 (2008).

[7] B.A. Tulupov, M.H. Urin, Phys. At. Nucl. 72, 737 (2009).

[8] M.L. Gorelik, B.A. Tulupov, M.H. Urin, Phys. At. Nucl. 69, 598 (2006).

[9] I.V. Safonov, M.G. Urin, Bull. Rus. Acad. Sci. Phys. 67, 44 (2003).

[10] M.L. Gorelik, V.S. Rykovanov, M.G. Urin, Bull. Rus. Acad. Sci. Phys. 73, N.11 (2009).

[11] C. Mahaux, S. Sartor, Adv. Nucl. Phys. 20, 1 (1991).

[12] M.G. Urin, "Relaxation of nuclear excitations", Energoatomizdat, Moscow, 1991 (in Russian).

[13] E.A. Romanovskii et al., Phys. At. Nucl. 63, 399 (2000); O.V. Bespalova et al., Phys. At. Nucl. 69, 796 (2006).

[14] G.A. Chekomazov, M.H. Urin, Phys. Lett. B 349, 400 (1995); Phys. At. Nucl. 61, 375 (1998).

[15] A.B. Migdal, "Theory of Finite Fermi-Systems and Applications to Atomic Nuclei", Interscience, New York, 1967.

[16] M.L. Gorelik and M.H. Urin, Phys. Rev. C 63, 064312 (2001).

THE SEMIMICROSCOPIC DESCRIPTION OF THE SIMPLEST PHOTONUCLEAR REACTIONS WITH GIANT DIPOLE RESONANCE EXCITATION

B.A.Tulupov[1], M.H.Urin[2]

[1]*Institute for Nuclear Research RAS, Moscow, Russia*

[2]*National Research Nuclear University "MEPhI", Moscow, Russia*

The main goal of the presented talk is the further development of the semimicroscopic approach for better description of the simplest photonuclear reactions in the energy region of the giant dipole resonance (GDR). Various versions of the semimicroscopic approach based on the continuum random-phase approximation (cRPA) were intensively used during last years for the studies of these reactions (see, e.g., [1, 2]). Saying of the simplest photonuclear reactions we mean, first of all, the total photoabsorption and the direct or inverse single-particle reactions. Though during these studies the important results have been obtained, all of them are characterized by one essential shortcoming. It appeared that it is impossible to obtain the proper position of the GDR energy in the framework of cRPA in the form adopted in the finite Fermi-system theory (FFST) using the residual Landau-Migdal partical-hole interaction in the following form:

$$F^{ph}(\mathbf{r},\mathbf{r}') = C\delta(\mathbf{r}-\mathbf{r}')[f(\mathbf{r}) + f'(\mathbf{r})\vec{\tau}\cdot\vec{\tau}'] \quad , \tag{1}$$

where $f(\mathbf{r})$ and $f'(\mathbf{r})$ are the dimensionless parameters determining the intensities of the isoscalar and isovector interactions, respectively.

The decision of this problem is prompted by the general principles of the FFST. In the first edition of Migdal book [3] the following relations between the energy (ω_M), the integrated total photoabsorption cross section ($\sigma_{E1,int}$) and parameter f_1' determining the intensity of momentum-dependent forces have been obtained in a model way:

$$\omega_M^2 = \omega_0^2(1+\frac{2}{3}f_1') \quad , \quad \sigma_{E1,int} = \sigma_0(1+\frac{2}{3}f_1') \quad . \tag{2}$$

Here ω_0 and σ_0 are the GDR energy and its integrated cross section, respectively, calculated without account of momentum-dependent forces. As follows from Eq.(2) these forces should play an important role in the GDR formation and its properties.

The first study of the simplest photonuclear reactions in the GDR energy region with the momentum-dependent forces account has been carried out in Ref. [4], where the rather satisfactory description of the experimental photoabsorption and partial (n,γ)-reaction cross sections for some nuclei has been obtained, in particularily, for ^{208}Pb isotope. However, the calculated energy behaviour of the total photoabsorption cross section for this nucleus is characterized by the feature similar to the resonance peak splitting in the strongly deformed nuclei. Besides, the approach used in Ref. [4] has the certain shortcomings. For instance, introduction of the smearing parameter (the mean doorway-state spreading width)

$$I(\omega) = \alpha(\omega-\Delta)^2/[1+(\omega-\Delta)^2/B^2] \tag{3}$$

(its form is similar to that proposed in Ref. [5]) leads in calculations to the appearance of the additional terms $\mp(i/2)I(\omega)I(r)$ in the potential $U(x)$ used for the calculations of the cRPA certain ingredients (Green's functions and continuum-state wave functions). As $I(r)$ is usually used the Woods-Saxon function $f_{WS}(r, R^*, a)$. In the mentioned approach [4] the cutoff radius R^* was chosen as $R^* = 2R$ in the calculations of the Green's functions and $R^* = R$ in the calculations of the partial reaction amplitudes. Such choice of R^* is not quite justified and makes the used approach rather inconsistent. It is necessary to notice also that the smearing parameter $I(\omega)$ is an imaginary part of the polarization operator $\Pi(\omega) = -(i/2)I(\omega) + \mathrm{Re}\,\Pi(\omega)$, which determines the relaxation of the particle-hole degree of freedom. The quantity $\mathrm{Re}\,\Pi(\omega)$ which can be determined through $I(\omega)$ with the help of the certain dispersion relation [6] also gives a contribution $\mathrm{Re}\,\Pi(\omega)I(r)$ to the potential $U(x)$.

Therefore the account of the above made remarks has been chosen as the first step to improve the approach of Ref. [4]. As it is well known in the FFST the effective fields V satisfy to the following equations (in symbolic form):

$$V = V_0 + FAV \quad , \tag{4}$$

where V_0 is the external field, $\mathcal{A}$ is the response function and F is the residual particle-hole interaction. In the presented approach the isovector part of this interaction is chosen in the form having the separable momentum-dependent part [7]:

$$F(1,2) \to \left(F'\delta(\vec{r}_1 - \vec{r}_2) + \frac{k'}{mA}(\vec{p}_1\vec{p}_2)\right)(\vec{\tau}_1\vec{\tau}_2) \quad , \tag{5}$$

where $F' = f' \cdot 300\,\mathrm{MeV\,fm^3}$, k' is the dimensionless intensity of the momentum-dependent separable forces, m is the nucleon mass and A is the number of nucleons. In the case of the GDR excitation the external field $V_0(x)$ is taken as following:

$$V_0(x) = -\frac{1}{2}rY_1(\Omega)\tau^{(3)} \quad ,$$

('x' means the set of space, spin and isospin variables). Assuming the operator equality $\vec{p} = md\vec{r}/dt$, in the cRPA from Eqs. (4),(5) the following relations may be obtained after separation of isobaric and spin-angular variables:

$$\tilde{V}(r,\omega) = V(r,\omega) + V_k(r,\omega) \quad , \tag{6}$$

$$V(r,\omega) = r + \frac{2F'}{r^2}\int[\mathcal{A}(r,r',\omega) + \mathcal{A}_k(r,r',\omega)]V(r',\omega)dr' \quad , \tag{7}$$

$$V_k(r,\omega) = \frac{k\omega^2}{1 + k' - \omega^2 k\int r\mathcal{A}(r,r',\omega)r'drdr'} \cdot r\int r\mathcal{A}(r,r',\omega)V(r',\omega)drdr' \quad , \tag{8}$$

$$\mathcal{A}_k(r,r',\omega) = \frac{k\omega^2}{1 + k' - \omega^2 k\int r\mathcal{A}(r,r',\omega)r'drdr'}\int \mathcal{A}(r,r',\omega)r'dr'\int r\mathcal{A}(r,r',\omega)dr \quad . \tag{9}$$

Here $k = \frac{8\pi m}{3\hbar^2 A}k'$. The small correction to the equality $\vec{p} = md\vec{r}/dt$ caused by the spin-orbit part of the nuclear mean field can be neglected [7]. All ω-dependent single-particle quantities in Eqs. (6)-(9) are determined by the potential, including the above mentioned additional terms.

Using Eqs. (6)-(9) it is possible to find the dipole strength function

$$S(\omega) = -\frac{1}{\pi} Im \int r\mathcal{A}(r,r',\omega)\tilde{V}(r',\omega)drdr' \quad , \tag{10}$$

where ω is a photon energy and, hence, the total photoabsorption cross section in the energy region of the GDR:

$$\sigma(\omega) = \frac{8\pi^3}{3}\frac{e^2}{\hbar c}\omega S(\omega) \tag{11}$$

Unfortunately the results for photoabsorption cross section in ^{208}Pb isotope obtained in this version of the presented approach happened to be practically similar to those obtained in Ref. [4] (Fig. 1).

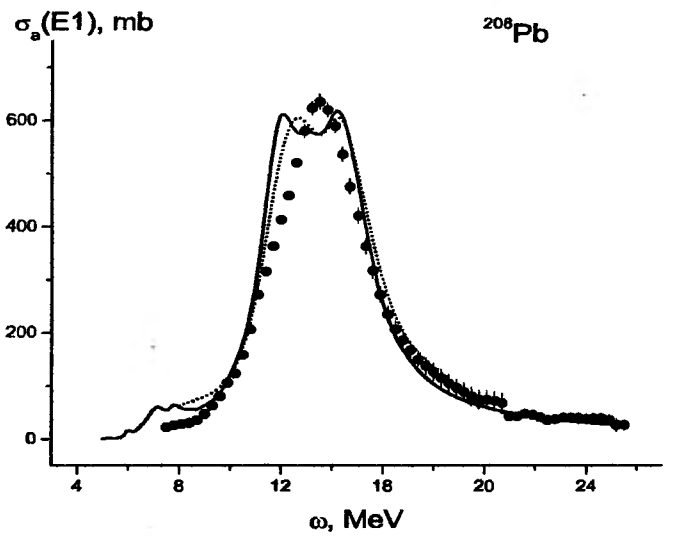

Fig 1. The total photoabsorption cross section in ^{208}Pb calculated in the first version of the presented approach (solid line) in comparison with corresponding results of Ref.[4] (dotted line) and the available experimental data [8].

Due to that an attempt has been made to reconsider one of the principal foundation of the approach: to change the potential used for the calculations of all cRPA ingredients. This procedure has been carried out in Ref. [9] on the base of new phenomenological potential proposed in Ref. [10]. In this potential the mean field $U(x)$ consists of pure nuclear parts, containing the isoscalar and isovector spin-orbit interaction, Coulomb field, the symmetry energy and is written in the following form:

$$U(x) = U_0(r) + (U_0^{SO}(r) + \frac{1}{2}U_1^{SO}(r)\tau^{(3)})\vec{l}\vec{s} + \frac{1}{2}\mathrm{v}(r)\tau^{(3)} + \frac{1}{2}(1-\tau^{(3)})U_C(r) \tag{12}$$

The space dependences of central field $U_0(r)$ and spin-orbit interactions U_0^{SO} and U_1^{SO} are determined by the Woods-Saxon function $f_{WS}(r; R^*, a)$ and its derivative $df_{WS}(r)/dr$, respectively. As to the symmetry potential $\mathrm{v}(r)$ and Coulomb field $U_C(r)$, they are calculated in a self-consistent way. The choice of all parameters determining every part of the potential $U(x)$ is made by means of the minimization of the differences between calculated position of the energy levels and the experimental ones (for the details of the total procedure and obtained

values of potential parameters see Ref. [9]). It is worthwhile to notice that obtained value of the isovector constant f' is equal to 1.09 in contrast to the previously used value 1.0 (see,e.g., Ref. [4]).

The approach developed on the base of this new potential includes only two parameters which should be treated as the adjustable ones: the intensity of the momentum-dependent forces k' and the intensity of the smearing parameter α (the values of Δ and B are taken to be the same as in Ref. [4]). To determine them the experimental data on the photoabsorption cross section for ^{208}Pb isotope [8] has been chosen as the most authentic ones. The corresponding calculations of the $\sigma(\omega)$ has been carried out on the base of Eqs. (6)-(11) using the newly defined potential. The comparison of the obtained results with the experimental data in Fig. 2 allows to define the values of α and k': $\alpha = 0.1\,\mathrm{MeV}^{-1}$, $k' = 0.4$.

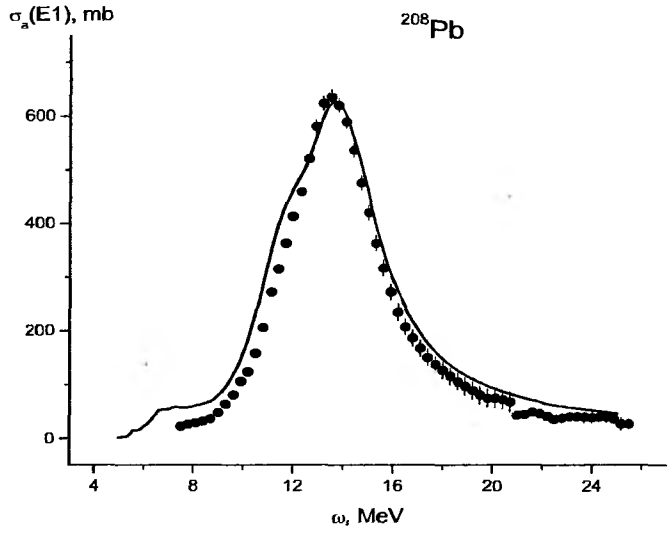

Fig 2. The calculated total photoabsorption cross section for ^{208}Pb (solid line) in comparison with available experimental data [8].

To check the possibilities of the presented approach the available partial (n,γ) reaction cross sections for ^{208}Pb isotope have been also investigated in the energy region of the GDR. The reaction amplitude which has been calculated on the base of Eqs. (6)-(9) has the following form:

$$M_c(\omega) = < (\lambda)||Y_1||(\mu) > \int \chi^{(-)}_{\varepsilon(\lambda)}(r)\tilde{V}(r,\omega)\chi_\mu(r)\mathrm{d}r \quad , \tag{13}$$

where $c = \{\varepsilon(\lambda), \mu\}$ is the set of the reaction-channel quantum numbers, $\mu = \{\varepsilon_\mu, (\mu)\}$ is the set of quantum numbers for single-particle state, $\chi_\mu(r)$ is the radial wave function of the populated bound state with energy ε_μ and $\chi^{(+)}_{\varepsilon(\lambda)}(r)$ is the corresponding to this channel and normalized to the δ–function of energy the scattering radial wave function of incident nucleon with energy $\varepsilon = \omega + \varepsilon_\mu$ (for other notations see, e.g. [4]). The bound state wave function is calculated with new potential (12) while the scattering wave function - with potential (12) and additional terms connected with $I(\omega)I(r)$ and $\Pi(\omega)I(r)$ (see above). The cross sections of these reactions can be then presented in the following form:

$$\frac{d\sigma_c(\varepsilon,0)}{d\Omega} = \frac{8}{3}\pi^{5/2}\frac{e^2}{\hbar c}\omega \cdot \frac{\omega^2}{2mc^2\varepsilon}\sum_L A_L(\varepsilon,\mu)P_L(cos\theta) \quad , \tag{14}$$

$$A_L(\varepsilon,\mu) = \sum_{(\lambda)(\lambda')} i^{l-l'}(-1)^{j_\mu+j}(1-111|L0)W(jj'11;Lj_\mu) < (\lambda)||Y_L||(\lambda') > M_c(\omega)M_{c'}^*(\omega) \quad .$$

Here, $P_L(cos\theta)$ are the Legendre polynomials, $(1-111|L0)$ and $W(jj'11;Lj_\mu)$ are the Clebsch-Gordan coefficient and Racah coefficient, respectively.

The relults of these cross section calculations are shown in Figs. 3,4 in comparison with the available experimental data [11] and some results from Ref. [4]. As it is seen from Figs. 3,4 the presented approach based on the use of new potential [9] allows us to describe

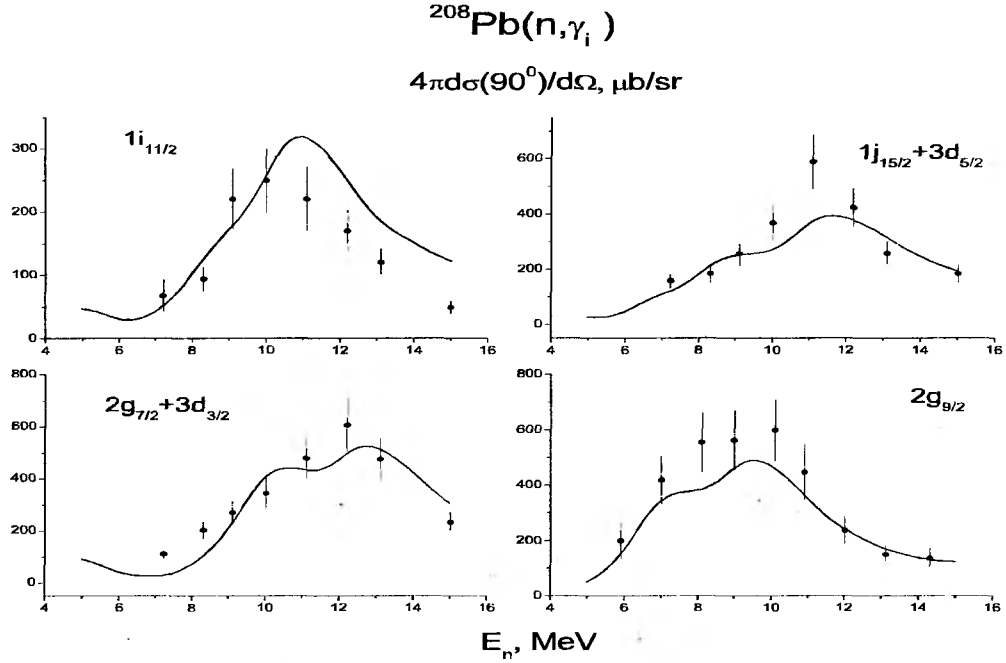

Fig 3. The calculated on the base of the presented approach the partial (n,γ) reaction cross sections at 90^0 to some single-particle states in ^{209}Pb in comparison with the available experimental data [11].

satisfactorily the studied photonuclear reactions: (i) the splitting of the GDR peak in ^{208}Pb is absent; (ii) the obtained cross sections of partial (n,γ) reactions appreciably better agree with the available experimental data than those from Ref. [4]. The energy-averaged (due to the use of the smearing parameter $I(\omega)$) differential cross sections for neutron radiative capture, $d\sigma_\mu/d\Omega$, are calculated without use of any adjustable parameters. Each calculation of the cross section is carried out with account of the experimental spectroscopic factor value, S_μ, of the final product-nucleus single-particle state populated after the capture. The corresponding experimental data are taken from Ref. [12].

As a conclusion one could say the following. In the presented approach a reasonable description of the experimental data on the total photoabsorption cross section and the partial (n,γ) reactions for ^{208}Pb isotope is obtained. In the future it is planned to expand the such investigations on the other medium-heavy mass nuclei having the similar structure. Besides, it is supposed to carry out these studies on the base of the potential [9] using the new set of parameters. Finally, it is planned to perform in a framework of the presented approach some predictive investigations, for instance, of (γ,n) reactions where there are some appropriate experimental data.

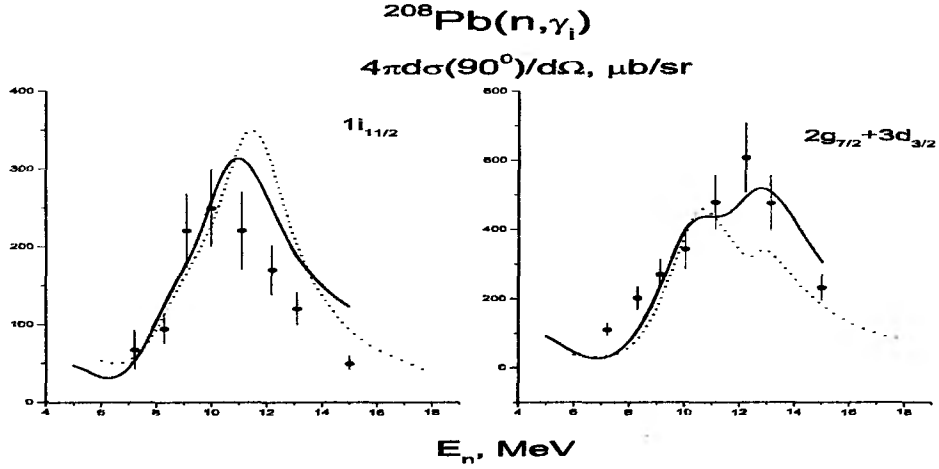

Fig 4. The calculated partial cross sections at 90^0 for neutron radiative capture (solid lines) to some single-particle states in ^{209}Pb in comparison with the corresponding results of Ref. [4] (dotted lines) and the available experimental data [11].

This work was supported in part by the Russian Foundation for Basic Research (project no. 09-02-00926-a).

References

[1] S.E. Muraviev and M.H. Urin, Nucl. Phys. **A572**, 267 (1994).

[2] S. Kamerdzhiev et al., Phys.Rep. **393**, 1 (2004).

[3] A.B. Migdal, *Theory of Finite Fermi Systems and Properties of Atomic Nuclei* (Nauka, Moscow, 1965) (in Russian) (English Translation: A.B. Migdal, *Theory of Finite Fermi-Systems and Applications to Atomic Nuclei*, Interscience, New York, 1967).

[4] V.A. Rodin and M.H. Urin, Phys. Rev. C **66**, 064608 (2002).

[5] C. Mahaux and R. Sartor, Nucl. Phys. **A503**, 525 (1989).

[6] B.A. Tulupov and M.H. Urin, Phys. At. Nucl. 72, 737 (2009).

[7] V.A. Rodin and M.H. Urin, in: *Contemporary Problems of Nucleus and Particle Physics*, 33 (Edition of INR RAS, Moscow, 1999).

[8] R. Bergère et al., Nucl. Phys. **A159**, 561 (1970).

[9] S.Yu. Igashov and M.H. Urin, Bull.Rus.Acad.Sci.Phys., 70, 212 (2006).

[10] V.I. Isakov et al., Phys. At. Nucl. 67, 1856 (2004).

[11] I. Bergqvist, D.M. Drake and D.K. McDaniels, Nucl. Phys. **A191**, 641 (1972).

[12] A. Likar and T. Vidmar, Nucl. Phys. **A 637**, 365 (1998).

FOLDING POTENTIALS IN ^{6}He+p AND ^{6}Li+n CHANNELS WITH A=6 CLUSTERS IN GROUND AND EXCITED STATES

Afanasyeva N.V.
al-Farabi Kazakh National University, Almaty, The Republic of Kazakhstan

Nowadays there are a number of experimental data on the photodisintegration of ^{7}Li: ^{7}Li(γ,p)^{6}He [1,2], ^{7}Li(γ,n)^{6}Li [3-7] and ^{6}He(p,γ)^{7}Li radiative capture reaction with the formation of ^{7}Li in the ground and first excited states [8]. It is significant, that the (γ,p) and (γ,n) processes have a general feature: the formation of the residual nuclei ^{6}He and ^{6}Li respectively in the ground state absolutely dominates only in the near-threshold energy region of gamma quantum γ. As the excitation energy is increasing, in the theoretical calculations of the characteristics for these reactions it is necessary to take into account the channels where ^{6}He$_{exc}$ and ^{6}Li$_{exc}$ nuclei are in the excited states, because all available experimental data are inclusive.

Thereupon the question might come to mind about the correct description of ^{6}He$_{exc}$ + p and ^{6}Li$_{exc}$ + n scattering channels. As the using of direct experimental data on the scattering in these channels are not available, it is actual to construct the corresponding interaction potentials by using the folding-model, basing on the realistic microscopic nucleon-nucleon and nucleon-cluster potentials with nuclear density functions.

The interaction potentials between the nucleons and nuclei with mass number A=6 are obtained in the general form on the basis of the self-consistent folding model. Also the folding-potentials are obtained for several particular cases: ^{6}He$_{exc}$ + p and ^{6}Li$_{exc}$ + n. The self-consistency is provided by the carrying out of the folding for V_{NN} and $V_{\alpha N}$ potentials, which have been used for the construction of the three-body αNN wave functions of above nucleus built within the multicluster dynamical model with Pauli-projection (MDMP) [9].

In Figure1 the relative coordinates for {αNN}+N systems are presented.

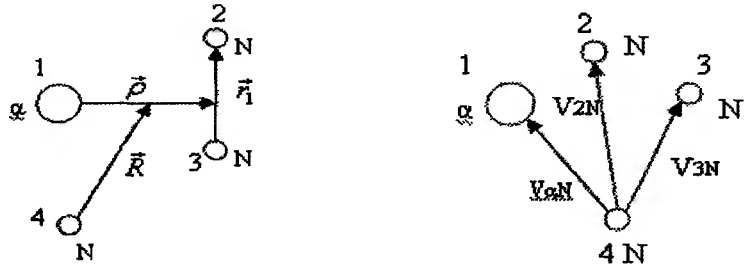

Fig. 1. Relative coordinates for {αNN}+N systems. (T-axis set and V-axis set).

For the description of ^{6}Li and ^{6}He nucleus being in the states with total angular momentum j and its projection m_j we use the wave MDMP functions obtained in [9], i.e. αNN -presentation:

$$\Psi_{jm_j}(\vec{r}_1,\vec{\rho}) = \sum_{\substack{\lambda\mu,lm,\\ LM,SM_S}} (\lambda\mu lm\,|\,LM)(LMSM_S\,|\,jm_j)\,\chi_{SM_S}(2,3)\,\Phi_{\lambda\mu lm}(\vec{r}_1,\vec{\rho}) \qquad (1)$$

The interaction potential is calculated as the average value by the wave function $\Psi_{jm_j}(\vec{r}_1,\vec{\rho})$ of the sum of partial αN- and NN-potentials:

$$\upsilon_{iN}=v_{\alpha N}(\vec{r}_{\alpha N})+v_{2N}(\vec{r}_{2N})+v_{3N}(\vec{r}_{3N}) \tag{2}$$

In other words the folding-potential is calculated as the overlap integral:

$$V_{AN}=<jm_j;\frac{1}{2}m_N\,|\,\mathrm{v}\,|\,jm_j;\frac{1}{2}m_N> \tag{3}$$

Then, we introduce the spin channel S_c quantity. Thus, the folding-potential is given by the following expression:

$$V_{AN}=\sum_{s_cm_c}(jm_j\,\frac{1}{2}m_N\,|s_cm_c)^2\cdot V_{s_cm_c}\,, \tag{4}$$

where
$$V_{S_cm_c}=<j\frac{1}{2}:S_cm_c\,|\,\mathrm{v}\,|\,j\frac{1}{2}:S_cm_c>. \tag{5}$$

Then the potential given by expression (5) is factorized on the spin and coordinate (radial) parts.

As a result of the complete theoretical calculations the averaged folding-potential is given by the next general formula:

$$\bar{V}_{AN}=\frac{1}{2(2j+1)}\sum_{S_c}(2S_c+1)V_{S_cm_c} \tag{6}$$

The folding-potential for the specified values of spin in $^6\mathrm{He}_{\mathrm{exc}}(2^+,1)$+p channel has the form:

$$\bar{V}_{^6He+p}=\sum_{s_c}\frac{(2s_c+1)}{2\cdot(2j+1)}\bar{V}_{j\frac{1}{2};s_c}=\frac{2}{5}\bar{V}_{2\frac{1}{2};\frac{3}{2}}+\frac{3}{5}\bar{V}_{2\frac{1}{2};\frac{5}{2}}\,,\quad \vec{s}_c=\vec{j}+\frac{1}{2}\Rightarrow\ s_c=3/2;\ 5/2 \tag{7}$$

and the folding-potential for the specified values of spin in $^6\mathrm{Li}_{\mathrm{exc}}(3^+,0)$+n channel has the following form:

$$\bar{V}_{^6Li+n}=\sum_{s_c}\frac{(2s_c+1)}{2\cdot(2j+1)}\bar{V}_{s_c}=\frac{3}{7}\bar{V}_{\frac{5}{2}}+\frac{4}{7}\bar{V}_{\frac{7}{2}}\,,\quad s_c=5/2;\ 7/2 \tag{8}$$

It is important to note that the analytical presentation of folding-potentials is obtained by using the Gaussian parameterization of the partial potentials $\upsilon_{i4}(\vec{r}_{i4})$:

$$\upsilon_{i4}(\vec{r}_{i4})=\sum_l A_l e^{-\gamma_{i4}^{(l)}\vec{r}_{i4}^{\,2}} \tag{9}$$

The visual presentation of the folding-potentials for $^6Li_{exc}(3^+,0)$+n and $^6He_{exc}(2^+,1)$+p channels is shown in Fig. 2.

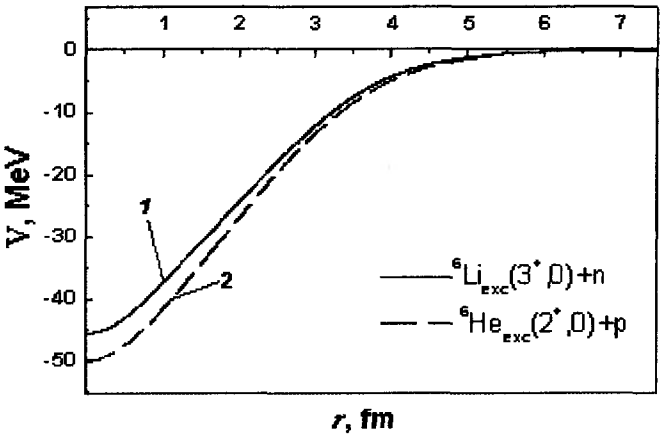

Figure 2. Folding-potentials for $^6Li_{exc}(3^+,0)$+n and $^6He_{exc}(2^+,1)$+p channels.

The view of calculated folding potentials resembles the Woods-Saxon potential of the form $V_{WS} = -V_0/\{1+\exp[(r-R_0)/a]\}$, but actually it is not possible to reduce the folding-potentials to the exact Woods-Saxon.

Further optimization of obtained folding-potentials assumes the probing their in calculations of various characteristics of nuclear reactions.

In addition on basis of obtained folding-potentials we can research the dynamic clusterization of nuclei.

Reference:

1. Junghans G., Bangert K., Berg U.E.P., Stock R., Wienhard K. The photodisintegration of ^6Li and ^7Li. // Z. Physik A. 1979. V. 291. P 353-365.
2. Denisov V.P., Kulchitskiy L.A. Neutrons-, deuterons- and tritons-emitting reactions in the process of photodisintegration of ^{7}Li. // Nucl. Phys. A. 1967. V.5. N 3. P. 490-497.
3. Barker F.C.Neutron and proton capture by ^{6}Li. // Aust. J. Phys. 1980. V. 33. P. 159-176.
4. Bramblett R.L., Berman B.L., Kelly M.A., Caldwell J.T., Fultz S.C. Photoneutron cross sections for ^{7}Li. // Proc. Int. Conf. Photonucl. React. Appl. California. 1973. V. 1. P.175.
5. Ferdinande H., Sherman N.K., Lokan K.H., Ross. C.K. Photoneutron cross sections in ^{7}Li. // Can. J. Phys. 1977. V. 55. P.428-433.
6. Siddiqui S.A., Dytlewski N., Thies H.H. The photoneutron cross section of ^{7}Li. // Nucl. Phys. A. 1986. 458. 1986. P. 387-396.
7. Karataglidis S., Zubanov D., Harty P.D., Thompson M.N. The $^7Li(\gamma,n_0)^6Li$ cross section near threshold. // Nucl. Phys. A. 1989. V.501. P. 108-117.
8. Sauvan E. et al. Radiative proton capture on ^{6}He. // Phys. Rev. Lett. 2001. V. 87, N 4. P.042501-1-042501-4.
9. Kukulin V.I., Pomerantsev V.N. et al. Detailed study of the cluster structure of light nuclei in a three-body model (IV). Large space calculation for A=6 nuclei with realistic nuclear forces. // Nucl. Phys. A. 1995. V.586. P. 151-189.

SUPERCONDUCTING RF ELECTRON RECIRCULATOR FOR NUCLEAR AND PARTICLE PHYSICS RESEARCH AS UPGRADE OF THE ACCELERATOR COMPLEX OF LEBEDEV PHYSICAL INSTITUTE IN TROITSK

E.G. Bessonov[1], V.G. Kurakin[1], A.I. L'vov[1], G.A. Sokol[1], V.G. Nedorezov[2], B.S. Ishkhanov[3], E.M. Leikin[3], V.I. Shvedunov[3], A.I. Malakhov[4]

[1]Lebedev Physical Institute, Moscow; [2]Institute for Nuclear Research, Moscow; [3]Skobeltsin Institute for Nuclear Physics, MSU, Moscow; [4]Joint Institute for Nuclear Research, Dubna

A project of a CW electron accelerator with superconducting RF cavities and recirculation loops is described as a possible upgrade of the Lebedev Physical Institute accelerator complex in Troitsk. An energy recovery system has to reduce a radiation background and to save the RF power. Steps of project realization are discussed.

Introduction

The electron synchrotron S25R [1] (also known as the synchrotron "Pakhra" named after a nearby river) in the town of Troitsk, with the maximum energy 1.3 GeV is the last in the series of synchrotrons build at the P.N. Lebedev Physical Institute since the resonance acceleration principle was discovered by V.I. Veksler in 1944. With the previous accelerators S3, S25, S60 of that series build in 1946-1959, many fundamental studies of phase focusing, meson physics, electromagnetic interactions of nuclei and elementary particles, synchrotron radiation, etc., have been made. S25R is under operation since the mid of 1970s and it also allowed to do a few remarkable experiments such as studying pion polarizabilities and η-mesic nuclei. Some further experiments on photonuclear and solid-state physics are running or planning there, so that this machine will be yet maintained for some time [2]. In parallel we study a possibility to build a completely new accelerator in the existing environment (i.e. accelerator and experimental halls, power supply, etc.) [3,4] in order to continue exploration of electromagnetic properties of particles and nuclei, properties of hadrons in the nuclear matter, to test new ideas such as the tagged meson method, and last not least to provide means to create a powerful light source for numerous applications. Aims for such a machine are outlined in more detail in our accompanying contribution to the Conference.

The subject of the present paper is a possible layout of the new accelerator. The accelerator schema based on a generalized microtron principle is described and the main accelerator parameters are given. The extraction schema to deliver electron beams to experimental areas is suggested. Beam energy recovery is also discussed.

Accelerator schema

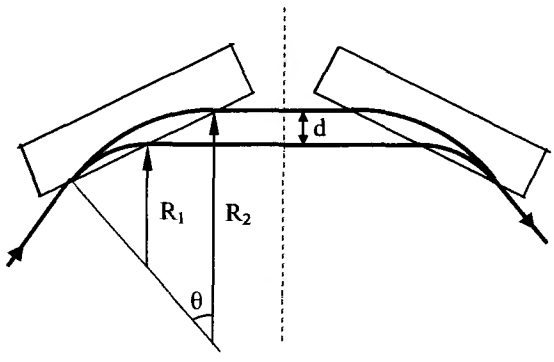

Fig. 1: Electron trajectories in a polytron.

The best solution for nuclear physics research is a cw beam with deep energy changing. Modern accelerator technologies suggest power tools for such an accelerator. To date, superconducting rf cavities operate with the high accelerating gradient up to 30 MV/m and more [5], thus making it possible to build up a compact machine using a beam recirculation schema. Many projects of electron recirculators have been suggested in the world based on superconducting rf cavities and various magnet systems. Presently we focuse our attention on a generalized microtron schema (polytron principle) [6] for several reasons, compactness being the most important one. In general, the polytron consists of N rf accelerating

structures and N pairs of dipole magnets arranged in a polygon, in which electrons are transferred from a previous linac to the next one by an achromatic dipole pair as shown in Fig. 1. In order to accelerate electrons from different orbits, the synchronism condition has to be satisfied,

$$\Delta E(\mathrm{MeV}) = 1.5B(\mathrm{T})g\lambda\frac{1}{\theta-\sin\theta}, \tag{1}$$

that, like in a classical microtron, simply means the orbit lengthening in the magnet pair by an integer number g of accelerating wave length λ after each turn. Here $\theta = 2\pi/N$, where N is polytron order. The next formulae also take place:

$$\Delta R = g\lambda\frac{1}{2(\theta-\sin\theta)}, \quad d = \frac{g\lambda}{2}\frac{1-\cos\theta}{\theta-\sin\theta}, \tag{2}$$

where d is orbit spacing in dispersive part of electron orbits and ΔR is a radius increase in the dipole magnet after every new passage.

The fourth-order polytron is the most optimal solution for square geometry of the existing accelerator hall of 25x25m^2. The corresponding accelerator layout is shown in Fig. 2, while the main parameters of the machine are collected in the Table 1.

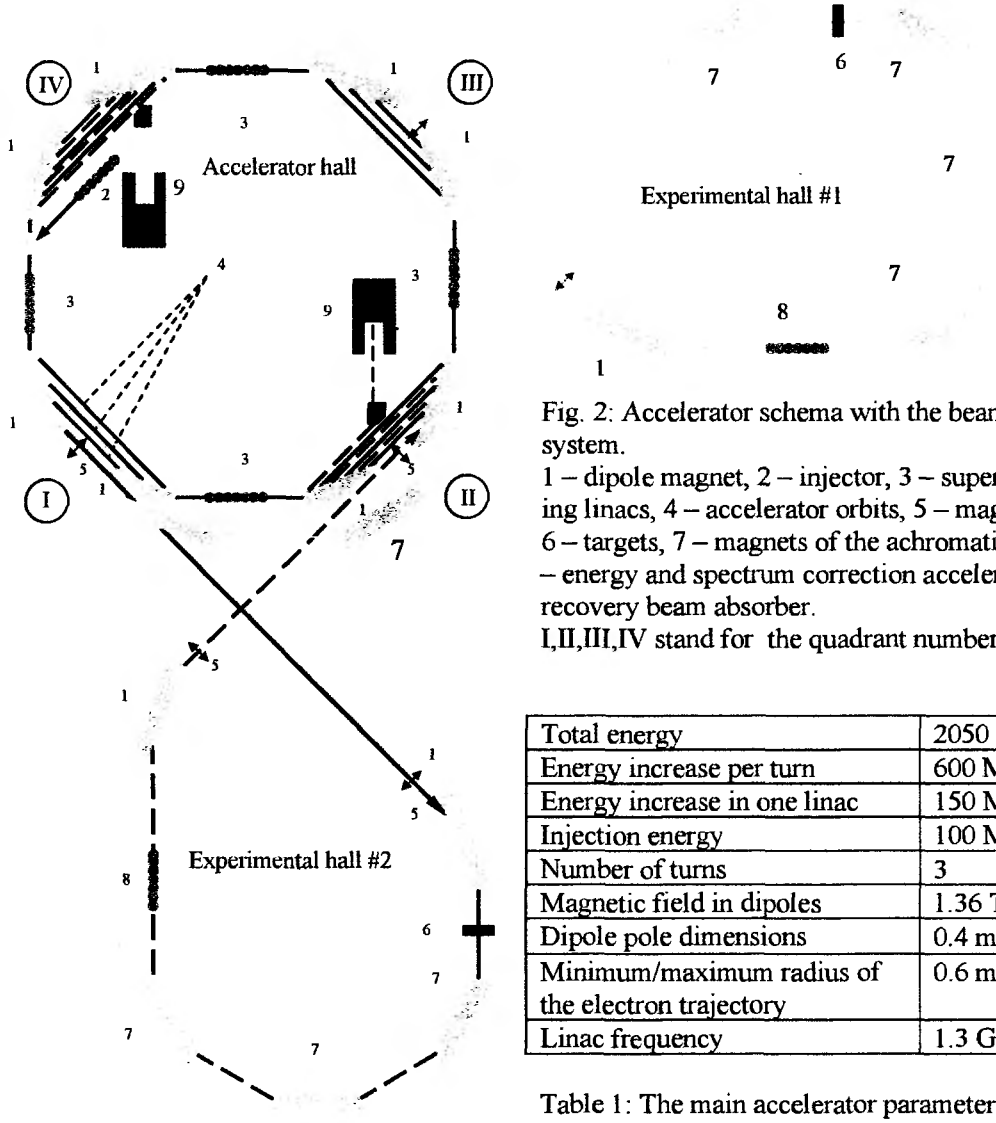

Fig. 2: Accelerator schema with the beam recovery system.
1 – dipole magnet, 2 – injector, 3 – superconducting linacs, 4 – accelerator orbits, 5 – magnetic lens, 6 – targets, 7 – magnets of the achromatic system, 8 – energy and spectrum correction accelerator, 9 – recovery beam absorber.
I,II,III,IV stand for the quadrant number.

Total energy	2050 MeV
Energy increase per turn	600 MeV
Energy increase in one linac	150 Mev
Injection energy	100 MeV
Number of turns	3
Magnetic field in dipoles	1.36 T
Dipole pole dimensions	0.4 m x 3.6 m
Minimum/maximum radius of the electron trajectory	0.6 m / 4.7 m
Linac frequency	1.3 GHz

Table 1: The main accelerator parameters.

Bunched electrons from the injector 2 directed onto the axis of the first linear accelerator (linac) 3 are transferred after acceleration by a dipole magnet pair to the entrance of the next linac, the rotation angle being 90°. After three full loops and the fourth passage of the first-period linac the electron beam is extracted from the accelerator due to a shorter pole of the second magnet of the first quadrant. In the case the magnet at the extracted beam path (the distributing magnet) is off, electrons are directed from an achromatic translation magnet pair to a target in the experimental hall #2. In the case the distributing magnet is on, the appropriate achromatic translation system directs the electron beam to the experimental hall #1.

Accelerating structure

We consider using TESLA or similar type cavity [7,8] that had been developed in the frame of the project TTF (TESLA Test Facility). This R&D project at DESY in the end of the 20th century that was aimed to prove a possibility of a linear electron-positron collider with high gradient superconducting linacs had finished with very promising results in the field of SRF (superconducting radio frequency). An industrially produced multi-cell cavity had been developed with the average accelerating gradient as high as 25 MV/m and more. The high purity niobium with RRR of the order of 300 and usual chemical polishing followed by high pressure water rinsing was used. To date, a modern technology of cavity surface preparation with electro-chemical polishing results in the accelerating gradient as high as 30 MV/m and more. The main cavity parameters are given in Table 2.

Table 2: Main parameters of the SRF cavity.

Resonance frequency	1300 MHz
Number of cells	9
Shunt impedance $R/Q = V_{ac}^2/P_{dis} \times Q$	1 kΩ
Quality factor Q at bath temperature 2.0 K	$> 5 \times 10^9$
Accelerating gradient (MV/m)	> 25
Iris diameter d	70 mm
Equator diameter D	206.6 mm
Active length L	1.038 m

Energy recovery system and beam optics

In most cases, only a small portion of the electron beam energy is absorbed in the target material in nuclear physics experiments, especially in the case of measurements with a polarized target. The used beam is directed into a beam absorber where it looses its energy via producing an electromagnetic shower in the absorber material. We suppose to use a beam energy recovery system in order to save the rf power and to reduce the radiation background.

The recovery system as well the recovery process looks as follows. After interaction with the target, the electron beam is picked up by an achromatic magnet system consisting of three magnets 7 (see Fig. 2) and directed into the linac 8 that serves for correcting the beam energy and spectrum [4]. Then, with a dipole magnet quite similar to those used in the recirculator, the used beam is directed to the second dipole magnet of the accelerator itself in the quadrant II or III (depending on the experimental hall where the beam was used for the experiment) and then it enters the first decelerating linac. The energy of the used beam is adjusted in a way that forces the beam to pass over the same orbits as during its acceleration, or between them with equal intervals from them. After the decelerated beam reaches the energy equal to the injection energy, it is absorbed in an absorber.

Table 3. Evolution of the beam energy during acceleration and deceleration. E_a – the electron energy during the acceleration stage; E_{d1} and E_{d2} – the same during deceleration from the hall #1 and #2, respectively; E_i – the injection energy (MeV).

Quadrant#	I				II				III				IV			
Passage#	1	2	3	4	1	2	3	4	1	2	3	4	1	2	3	4
$E_a - E_i$	150	750	1350	1950	300	900	1500	–	450	1050	1650	–	600	1200	1800	–
$E_{d1} - E_i$	1350	750	150	–	1800	1200	600	0abs	1650	1050	450	–	1500	900	300	–
$E_{d2} - E_i$	1650	1050	450	–	1500	900	300	–	1950	1350	750	150	1800	1200	600	0 abs

Thus, in the discussed schema the maximum possible recovery efficiency is equal to $(E_{max} - E_{inj})/E_{max}$ or 0.95 for the accelerator parameters given in Table 1. The beam energy evolution during acceleration and deceleration (recovery process) is shown in some detail in Table 3.

Conclusion

The presented paper is a further development of the conceptual design of the cw electron accelerator for nuclear physics research at Lebedev Physical Institute [3]. A significant progress in the field of superconducting rf during the last two decades makes it possible to build such an accelerator in the existing environment that includes buildings, power supply, cooling systems and so on. Unfortunately, the appropriate new superconducting rf cavity technology is not yet available in Russia, and the fastest way of its formation here is seen in moving this technique from Europe. A step by step policy is foreseen. We could start with a rf superconducting stand that includes a helium cryostat for a vertical cavity test and an appropriate environment – a clean room, a chemical room, a gas helium collection system, etc. An electron accelerator of the energy 20-30 MeV with a single multi cell cavity might be the second step. This machine would help us to acquire appropriate experience and even start some scientific applications including accelerator and nuclear physics as well as radiophysicsl. A full scale injector with the following recirculation loops and a recovery system would allow to do elementary particle physics in the energy range up to several hundreds MeV. All these steps are compatible with the existing synchrotron S25R. The synchrotron will be dismantled at the last step of the full scale project under discussion.

Nowadays, the recovery technique is widely discussed in the world in connection with a new generation of light sources ultra high intensity and brightness in the Roentgen range [9]. Two or three orders of magnitude of the electron beam intensity compared to that needed for nuclear physics applications are required for proceeding this technology. The schema under discussion allows us to go in that direction too.

References

[1] K.A. Belovintsev et al. "Cascade electron storage system". LPI preprint #45, 1967 (in Russian).

[2] V.M. Alekseev, V.P. Busygin, A.V. Koltsov, V.G. Kurakin, P.V. Kurakin, G.G. Subbotin, E.I. Tamm. "Lebedev Physical Institute synchrotron to the energy of 1.3 GeV automation as the first step of the accelerator upgrade". In Proc. 18th Russian Conf. on Charged Particle Accelerators (Obninsk, 2004), vol. 1, pp. 345-350 (in Russian); Atomic Energy, vol. 93, #6 (2002) pp. 464-468 (in Russian).

[3] V.G. Kurakin, G.A. Sokol, V.G. Nedoresov, B.S. Ishkhanov, V.I. Shvedunov. "Superconducting RF Electron Recirculator for Nuclear Physics Research at Lebedev Physical Institute", in Proc. RuPAC08 (Zvenigorod, Russia, Sep 28 - Oct 3, 2008), pp. 107-109.

[4] V.G. Kurakin, A.V. Koltsov. "Ecologically Clean Accelerator for Nuclear Physics Research", in Proc. RuPAC08 (Zvenigorod, Russia, Sep 28 - Oct 3, 2008), pp. 376-378.

[5] A. Jamamoto. "Global R&D Effort for the ILC Linac Technology" in Proc. EPAC08 (Genoa, Italy, June 23-27, 2008), pp. 12-16.

[6] K.A. Belovintsev, A.I. Karev, V.G. Kurakin. "The Prospect of the segment magnets use in high energy electron recirculators". Letters to the Soviet Journal of Technical Physics, vol. 10, No 7, pp.439-442 (in Russian).

[7] S. Bauer et al. "Production of Superconducting 9-Cell Cavities for the TESLA Test Facility", Stanford University and Forschungszentrum Rossendorf.

[8] W. Anders, J. Knobloch, O. Kugeler, A. Newmann. "CW operation of superconducting TESLA cavities", in Proc. 13th Workshop on RF Superconductivity (Beijing, China, Oct 14-19, 2007), http://web5.pku.edu.cn/srf2007/proceeding.html

[9]. E.G. Bessonov. "4th Generation Light Sources and Elementary Particle Physics", http://arxiv.org/abs/0906.1683

SEARCH FOR THE Δ-ISOBAR COMPONENT IN ^{12}C AND ^{16}O GROUND STATE

I.V. Glavanakov[1], P. Grabmayr[2], Yu.F. Krechetov[1a], A.N. Tabachenko[1]
[1]*Nuclear Physics Institute at Tomsk Polytechnic University, 634050 Tomsk, Russia*
[2] *Institute of Physics, Tübingen University, D-72076 Tübingen, Germany*
[a]*E-mail: krechet@npi.tpu.ru*

1. INTRODUCTION

The nontrivial substructure of a nucleon in nuclei manifests itself in the existence of the internally excited states, i.e. baryon resonances or isobars (see [1, 2]). One possibility to describe these subnucleonic effects in modern nuclear models is the addition of exotic components, the so-called isobar configurations to the conventional nuclear wave functions. The exchange of the π and ρ mesons may result in virtual $N\Delta$ and $\Delta\Delta$ states. In 1971, S. Gerasimov suggested using the process of isobar knocking-out by high-energy particles for studying the isobaric degrees of freedom in nuclei [3]. Theoretical estimates [4, 5] and the results of a few experiments on setting off the mechanism of direct isobar knocking-out [6 - 8] gave a value of 0.5–4% for the contribution of Δ-isobaric states to the wave function of *p*-shell nuclei.

The photo- and electroproduction processes as a test of Δ admixture in nuclei were considered for the first time in [9]. In [10] a combined study of (e, e' Δ^{++}) und (e, e' Δ^{0}) reactions on ^{3}He was proposed by J. M. Laget.

The small size of the isobar admixture in nuclei hampers the experimental observation of the Δ component. The main difficulty consists in separating the background mechanisms of the reaction leading to an identical final state. Before we have solved this problem by measuring the photoproduction cross section for π^+p pairs in the reaction γ + nucleus $\rightarrow \pi^+ + p + X$ in the kinematical region of high momentum transfer to the residual nuclear system *X* [11]. The idea of the experiment is that the direct production of $\pi^+ p$ pairs by the nucleons in a nucleus is forbidden for this reaction, whereas the background is concentrated in the small-momentum transfer range.

In this work we present the results of the measurement of the reaction (γ, π^+p) differential yield on ^{16}O. The data are analyzed in the frame of the model under the assumption that the formation of the π^+p pairs may be interpreted as a process which takes place on a Δ preexisting in the target nucleus. The results of the measurement of the reaction ^{12}C(γ, π^+p) differential yield obtained early are analyzed also in the similar kinematical conditions [12].

2. EXPERIMENT

Measurements of the differential yield of the reaction $^{16}O(\gamma, \pi^+ p)$ were performed at the Tomsk synchrotron at electron beam energy E_e = 450 MeV. The experimental setup includes two coplanar arms detecting the positive pion and the proton in coincidence.

A strong focusing magnetic spectrometer was set at an angle 54° with respect to the photon beam in order to positive pions select with mean momentum 181.3 MeV/c. The solid angle of the magnetic spectrometer covered $3 \cdot 10^{-3}$ sr and the momentum acceptance was 24%. The pion momentum was measured to a precision of about 2% with the aid of a scintillation hodoscope arranged in the focal plane of the magnetic spectrometer.

The proton channel included a (ΔE, E) plastic scintillation spectrometer and two auxiliary counters with absorbers intended for monitoring the proton channel stability.

The ΔE counter of the spectrometer in front defined the solid angle of the proton channel to 0.26 sr. The mean polar angle of the proton channel with respect to the photon beam and its angular coverage were $\theta_p = (75 \pm 19)^\circ$, respectively.

Within the range of the proton energy $T_p = 50 \pm 130$ MeV the analysis of the signals from the photomultipliers of the ΔE and E counters allowed one to determine the polar angle and the energy of the detected proton with position independent accuracies better than $\sigma(\theta_p) = 3^\circ$ and $\sigma(T_p) = 4$ MeV, respectively. The accuracy of the azimuthal angle ϕ was determined by the vertical ΔE counter dimension to $\sigma(\phi) \sim 2^\circ$.

The level of the cosmic background was less 1%. The total energy of the photon flux during the runs was measured by the Gauss-quantameter in with the accuracy of 3%.

3. DATA ANALYSIS

In the present experiment fifty-five π^+p events have been selected for the analysis. Figure shows the differential yield of the ^{16}O(γ, π^+p) reaction averaged over the proton emission angles as a function of the proton kinetic energy. In the kinematical conditions our experiment the high energy of the protons T_p correspond to high momentum transfer to the residual nuclear system. The analysis of the contributions from the background π^+p-production mechanisms was carried out with the aim of determining the kinematic region where the reaction mechanisms caused by non-nucleon degrees of freedom dominate. For this purpose, we employed so-called Valencia model described in [13]. This model takes into account the one-, two-, and three-nucleon modes of incident-photon absorption and the single-pion production on nucleons, as well as the pion and nucleon re-scattering by the residual nucleus. The background is mainly due to the π^+n- or π^0p-pair production followed by charge exchange re-scattering of a neutron into a proton or a π^0 meson into a π^+ meson. As one can see in figure, according to the calculation the background is concentrated in the range of small momentum transfer.

The results for the $^{16}O(\gamma,\pi^+p)$ and $^{12}C(\gamma,\pi^+p)$ reactions have been analyzed on the basis of the model of the pion photoproduction on the nuclei, which takes into account the isobar configuration for the ground states of the nuclei with the closed shells. According to this model the photon interacts with the Δ-isobar of the correlation ΔN system. Such system is result of the mutual polarization or deformation of the bound nucleons in nuclei due to close collisions within nuclei. The wave function $\Psi_{\Delta N}$ of the ΔN system was received from the generalized Schrodinger equation [14-16]. According this approach bound nucleons in the nucleus, in addition to the spatial, spin, and isospin coordinates are characterized also by the intrinsic coordinate. Hamiltonian H for the system of N particles acts on spatial, spin, isospin, and intrinsic coordinates. The operators the kinetic energy and the two-particle interaction unlike those of standard nuclear physics depend also on the intrinsic degrees of freedom. Besides, Hamiltonian contains the part stipulated by the introduction of the intrinsic degrees of freedom. As result, nuclei can be considered as system of nucleons, the wave function of which have the additional to purely nucleon, isobar configurations. The π- and ρ- exchange potential have been used.

In our model one-particle transition operator was found using the amplitude of the elementary process $\gamma\Delta \rightarrow \pi N$. The elementary amplitude was obtained within the diagrammic approach. It was based on the coupling of the photons to pions, nucleons and Δ isobars using effective Lagrangians.

The final-state interaction takes into account the absorption of the produced particles π^+ and p inside the nucleus. It depends on the pion and proton energies and their opening angle.

The π^+p pair photoproduction in this model is the result of the interaction:
a) of the photon and Δ^{++}-isobar in the A(γ, π^+p)B* reaction;
b) of the photon and Δ^{++} - or Δ^+-isobar in the A(γ, π^+p)nB* reaction.
In figure together with experimental data we present the calculation for the ^{16}O(γ, π^+p) reaction.

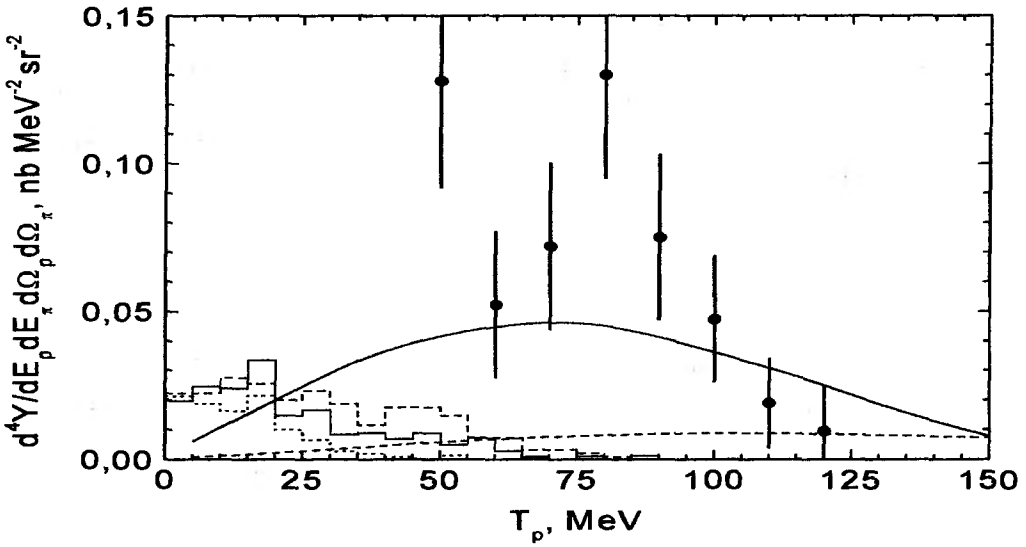

Figure. Differential yield for the $^{16}O(\gamma, \pi^+ p)$ reaction as a function of the kinetic proton energy: the dots represents the experimental data; the results of the Valencia model at $E_\gamma = 400$, 420 and 450 MeV are shown by the dotted, solid and dash histograms; the solid curve corresponds to the calculation with two nucleons in the final state; and the dash curve corresponds to the calculation with one nucleon in the free state.

The probability W of the excitation of Δ–isobar as result of the interaction the bound nucleons in the ground states was found by the two methods. In the first method the probability W was calculated as norm of the wave function $\Psi_{\Delta N}$ of the isobar configuration of the nucleus. In this approach the probability of the Δ–isobar configurations per nucleon W is $W_{Th} = 0.015$. In second method the value W was estimated from the comparison between the experimental and theoretical reaction yields in the framework of our model. The norm of the wave function $\Psi_{\Delta N}$ (*x1*, *x2*) in this case is a normalization parameter. The estimation of the value W was made by the least-squares method using the experimental data for the proton energy above 55 MeV, where the contribution of the background reaction under Valencia model is very small. We obtained $W_{ex} = 0.018 \pm 0.004$. The analogous analysis was made for the $^{12}C(\gamma, \pi^+ p)$ reaction. We obtained next estimations for the ^{12}C nucleus $W_{Th} = 0{,}013$ and $W_{ex} = 0.012 \pm 0.005$.

As one can see, the theoretical and experimental estimations for ^{16}O and ^{12}C differ less than one-standard-deviation.

This work part was supported by the Federal Agency for Science and Innovation (contract No 02.740.11.0245).

REFERENCES

1. A.M.Green. Rep. Progr. Phys., 39 (1976) 1109.
2. H.J. Weber, H.Arenhovel. Phys. Rep., 36 (1978) 277.
3. S.B.Gerasimov. Pis'ma v Zhurnal Éksper. i Teoret. Fiziki, 14 (1971) 385.
4. G. Horlacher, H. Arenhovel. Nucl. Phys., A.300 (1978) 348.
5. M.R. Anastasio et al. Nucl. Phys., A322 (1979) 369.
6. I. Amelin et al. Phys. Lett., B337 (1994) 261.
7. C.I. Morris et al. Phys. Lett., B419 (1998) 25.
8. E.A. Pasyuk et al. nucl-ex/9912004 (1999).
9. H.J. Lipkin, T.-S.H. Lee. Phys.Lett., B183 (1987) 22.
10. J.M. Laget. Preprint Saclay, DAPNIA/SPhN 95-44 (1995).
11. A. Fix, I. Glavanakov, Yu. Krechetov. Nucl. Phys., A646 (1999) 417.
12. V. Bystritsky et al. Nucl. Phys., A705 (2002) 55.
13. R. Carrasco. Nucl. Phys., A570 (1994) 701.
14. G. Horlacher, H. Arenhovel. Nucl. Phys., A300 (1978) 348.
15. A.N. Tabachenko. nucl-th/0512057 (2005).
16. A.N.Tabachenko, Russian Physics Journal, 50 (2007) 305.

THE REACTION $D(\gamma,\pi^0 n)p$ AT THRESHOLD ENERGIES

M.I.Levchuk

B.I. Stepanov Institute of Physics, Belarussian Academy of Sciences, Minsk, Belarus

Pion photoproduction on nucleons is a very important source of information on their electromagnetic structure. Nowadays, an open question is the threshold value of the S-wave electric dipole amplitude $E_{0+}^{\pi^0 n}$ in the $\pi^0 n$-channel. There is a notable disagreement in theoretical predictions for $E_{0+}^{\pi^0 n}$. Chiral perturbation theory (ChPT) and dispersion theory (DT) give, respectively, 2.13 [1] and 1.19 [2] in units of $10^{-3}/\mu_{\pi+}$. At the same time, both models agree quite well in their predictions for $E_{0+}^{\pi^0 p}$, producing -1.16 and -1.22, respectively.

Because of absence of dense, stable, free neutron targets, measurements of the reaction $\gamma n \to \pi^0 n$ are forced to deal with neutrons bound in deuterium. There are two possible channels for the study of this reaction, namely coherent, $\gamma D \to \pi^0 D$, and incoherent, $\gamma D \to \pi^0 np$, photoproduction. First measurement of total and differential cross sections for the $D(\gamma,\pi^0)$ channel at threshold energies was performed in Ref. [3]. After subtraction theoretically predicted values for the incoherent channel from measured ones, total and differential cross sections for the $D(\gamma,\pi^0)D$ reaction were obtained. They then were used to extract, in particular, the threshold amplitude E_d in $\gamma D \to \pi^0 D$. Although, formally a relation between E_d and $E_{0+}^{\pi^0 n}$ looks very simple, like $E_d = \Delta E + a E_{0+}^{\pi^0 n}$, in fact it is not easily to calculate reliably the coefficients ΔE and a. So, authors of Ref. [3] were not in a position to extract $E_{0+}^{\pi^0 n}$.

Another option for extracting the threshold value of $E_{0+}^{\pi^0 n}$ provides the incoherent channel $D(\gamma,\pi^0 n)p$ when registering the coincidence of the neutron and decaying π^0-meson. Such a method was discussed in a proposal of 2004 and in a letter of intent of 2008 to the MAX-lab PAC [5].

Below we present our first theoretical estimations for the differential cross section of the above reaction at threshold energies. The model is close to that built in Ref. [7] where the semi-exclusive process $D(\gamma,\pi^0)np$ at threshold energies was studied.

All calculations refer to the lab frame. We denote by $k = (E_\gamma, \vec{k})$, $p_d = (M, 0)$, $q = (\varepsilon_\pi, \vec{q})$, $p_p = (\varepsilon_p, \vec{p}_p)$, and $p_n = (\varepsilon_n, \vec{p}_n)$ the 4-momenta of the photon, deuteron, pion, proton, and neutron, respectively. As independent kinematical variables we take the 3-momentum of the neutron $\vec{p}_n$ and pion angles (Θ_π, ϕ_π). One has for the value of the pion momentum

$$|\vec{q}| = \frac{1}{D}\left[AC \pm B\sqrt{A^2 - \mu^2 D}\,\right], \tag{1}$$

where

$$\begin{aligned} A &= \frac{M^2 + \mu^2 + m_n^2 - m_p^2}{2} + (E_\gamma - \varepsilon_n)M - k\cdot p_n, \\ B &= M + E_\gamma - \varepsilon_n, \quad C = (\vec{k} - \vec{p}_n)\cdot\hat{\vec{q}}, \quad D = B^2 - C^2, \end{aligned} \tag{2}$$

and μ, m_n, and m_p being, respectively, the meson, neutron, and proton masses. Equations (1) and (2) restore the 3-momentum of the pion $\vec{q}$ and, therefore, the full kinematics. Threshold values of the momenta and kinetic energies of final particles are

$$q^{\rm th} = 9.5\ {\rm MeV}/c,\ E_\pi^{\rm th} = 0.3\ {\rm MeV},\ p_n^{\rm th} \simeq p_p^{\rm th} = 66.4\ {\rm MeV}/c,\ E_n^{\rm th} \simeq E_p^{\rm th} = 2.3\ {\rm MeV}. \tag{3}$$

Note that at threshold energies all final particles move in the forward cone.

The differential cross section reads

$$\frac{d^3\sigma}{dE_n d\Omega_n d\Omega_\pi} = \frac{1}{(2\pi)^5}\,\frac{m_n m_p |\vec{p}_n||\vec{q}|^3}{4E_\gamma|\varepsilon_\pi q\cdot p_p - \mu^2\varepsilon_p|}\,\frac{1}{6}\sum_{spins}|T|^2. \tag{4}$$

In the present work we have taken into account contributions to the reaction amplitude from diagrams displayed in Fig. 1. The deuteron wave function and the amplitude of π^0-photoproduction on the nucleon are needed at evaluation of the pole diagram $1(a)$. The CD-Bonn potential [4] is used to generate the former. The low-energy photoproduction amplitude in the c.m. frame is

$$T_{\gamma N\to\pi N} = \frac{4\pi W_{\pi N}}{m}\left[i\vec{\sigma}\cdot\vec{\epsilon}\,(E_{0+} + \vec{k}\cdot\vec{q}\,p_1) + i\vec{\sigma}\cdot\vec{k}\,\vec{q}\cdot\vec{\epsilon}\,p_2 + \vec{q}\cdot(\vec{k}\times\vec{\epsilon})\,p_3\right], \qquad (5)$$

where $W_{\pi N}$ is the total energy of the πN-system, and p_1, p_2 and p_3 are the P-waves. We use a parametrization for E_{0+} given in Ref. [6]:

$$E_{0+}^{\pi^0 N}(W_{\pi N}) = a_0 + a_1(W_{\pi N}^2 - W_{\pi^0 N}^{\rm th\ 2}) + ia_2\frac{q_+}{\mu_{\pi^+}}, \qquad (6)$$

where $W_{\pi^0 N}^{\rm th} = \mu + m_N$ is the threshold energy for the $\pi^0 N$-channel, q_+ is the πN c.m. momentum (which is imaginary below the charged pion threshold), and a_i are energy-independent parameters which were evaluated in Ref. [6] to reproduce ChPT and DT predictions for the $\pi^0 p$-and $\pi^0 n$-channels. The last term in Eq. (6) is responsible for the so-called cusp effect. The P-wave amplitudes are taken to be the same as in Table 1 of Ref. [7]. The amplitude (5) is used at energies $W_{\pi N}$ corresponding to lab photon energies up to 170 MeV for the $\gamma N \to \pi^0 N$ reaction.

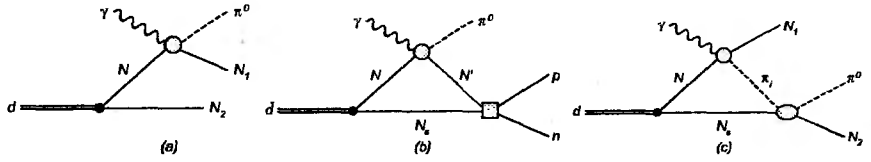

Figure 1: Pole (a) and one-loop (b–c) diagrams of the reaction $\gamma D \to \pi^0 np$. Permutation $N_1 \leftrightarrow N_2$ is not shown.

Diagram $1(b)$ has also to be taken into account because of very strong np-final state interaction (FSI) at threshold energies. One new block needed at evaluation of this diagram is the half-off-shell np-scattering amplitude. It has been build for the CD-Bonn potential. It is wort mentioning that we have found results to be insensitive to the choice of a NN-potential. This is a consequence of the smallness of nucleon momenta involved in the reaction mechanisms. Also one needs a parametrization of the π^0-photoproduction amplitude above 170 MeV. Such energies emerge at the integration over nucleon momenta in the loop in diagram $1(b)$. We use the well-known Blomqvist-Laget model [8] in this region.

Although the s-wave πN-scattering lengths are about two order smaller than those for np-scattering, a contribution of diagram $1(c)$ with πN-FSI is not suppressed in comparison to that of $1(b)$. The reason is that the intermediate π-meson in this diagram can be both neutral and charged, and the photoproduction amplitude for the latter in the threshold region is about 30 times larger than that for the former. We have evaluated diagram 1(c) using the Blomqvist-Laget model for charged pion photoproduction and a separable parametrization of the πN-scattering amplitude from Ref. [9].

Some results of the calculation are presented in Fig. 2. One observes a huge effect of np-FSI. The sharp peak at $E_n \simeq 1.7$ MeV corresponds to the kinematics where the relative energy of the np-pair is close to zero. Notable decrease of the cross sections above 3 MeV stems from πN-FSI. The predictions are very sensitive to the parametrization of the amplitude. DT produces only about a half of the ChPT cross section at all E_n.

Of course, the present calculation is not complete. As was shown in Ref. [7], two-loop diagram $3(a)$ with charge pion photoproduction in the intermediate state is very important

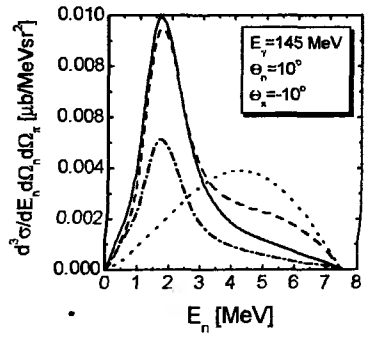

Figure 2: Differential cross section as a function of the neutron kinetic energy E_n at $E_\gamma = 145$ MeV, $\Theta_n = 10°$, and $\Theta_\pi = -10°$ in coplanar geometry. The dotted line is the contribution of the pole diagram $1(a)$ if the ChPT parametrization is used in Eqs. (5) and (6). Successive addition of the diagrams $1(b)$ and $1(c)$ gives the dashed and solid lines, respectively. The dash-dotted line is obtained with the DT parametrization.

at threshold energies. There is another two-loop mechanism shown in Fig. $3(b)$ that expected to give a notable contribution to the reaction amplitude when again the charged π-meson is produced in the intermediate state. As to third two-loop diagram $3(c)$, we suppose it to be safely neglected at threshold energies. Evaluations of two-loop diagrams $3(a)$ and (b) are underway now.

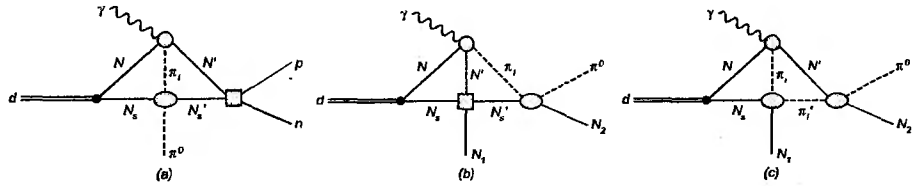

Figure 3: Two-loop diagrams of the reaction $\gamma D \to \pi^0 np$. Permutation $N_1 \leftrightarrow N_2$ is not shown.

The work was supported by Belarusian Republican Foundation for Fundamental Research (grant No. F09-051).

References

[1] V.Bernard, N.Kaiser, U.-G.Meißner. Phys. Lett. B378 (1996) 337.

[2] O.Hanstein, D.Drechsel, L.Tiator. Phys. Lett. B399 (1997) 13.

[3] J.C.Bergstrom, R.Igarashi, J.M.Vogt, N.Kolb, R.E.Pywell, D.M.Skopik, E.Korkmaz. Phys. Rev. C57 (1998) 3203.

[4] R.Machleidt. Phys. Rev. C63 (2001) 024001.

[5] See http://www.maxlab.lu.se/kfoto/ExperimentalProgram/props.html

[6] M.Benmerrouche, E.Tomusiak. Phys. Rev. C58 (1998) 1777.

[7] M.I.Levchuk, M.Schumacher, F.Wissmann. Phys. Rev. A675 (2000) 621.

[8] I.Blomqvist, J.M.Laget. Nucl. Phys. A280 (1977) 405.

[9] S.Nozawa, B.Blankleider, T.-S.H.Lee. Nucl. Phys. A513 (1990) 459.

γD SCATTERING AND POLARIZABILITIES OF THE NUCLEON

M.I. Levchuk[1], A.I. L'vov[2]

[1]*P.N. Lebedev Physical Institute, Moscow, Russia;*
[2]*B.I. Stepanov Institute of Physics, Minsk, Belarus*

Revised and corrected results of our earlier calculation [1] of elastic γd scattering are presented. For the first time all existing data on that reaction below 100 MeV are successfully described. A two-parameter fit for isospin-averaged dipole electric and magnetic polarizabilities of the nucleon gives $\alpha_N = 13.7 \pm 1.1$, $\beta_N = 3.2 \pm 1.1$ (in the units of 10^{-4} fm^3). With the constraint $\alpha_N + \beta_N = 14.6$ (Baldin sum rule) a one-parameter fit gives $\alpha_N - \beta_N = 9.4 \pm 1.6$.

1. A possibility to measure electromagnetic polarizabilities of the neutron in the reaction of elastic γd scattering was considered during last years in several theoretical works, in which different methods of taking into account effects of the nuclear environment have been tried. Part of these analyses relied on realistic, high-quality phenomenological nucleon-nucleon potentials (see [1] and references therein). In other approaches methods of effective field theories, including chiral perturbation theory, have been applied [2,3].

In our opinion, among all of these investigations, our calculation [1] still remains the most complete and precise (up to a bug in the computer code, see below). In that work the amplitude of elastic γd-scattering was found in a model of NN-interaction represented by the Bonn one-boson-exchange (OBE) potential, with the corresponding realistic wave functions of the np-system both in the discrete and continuous spectrum, with the use of meson-exchange currents and seagulls (effective two-photon vertices) consistent with the given OBE NN-interaction, with inclusion of main relativistic corrections, corrections for retardation, effects of the Δ-isobar excitation, etc. Many of the effects that we consider sizeable and deliberately take into account have been neglected in works of other authors.

Generally, the dipole electric and magnetic polarizabilities of the nucleon, α and β, are structure parameters characterizing the particle's ability to get induced electric and magnetic dipole moments in external soft electromagnetic fields. These parameters enter the low-energy expansion of the nucleon Compton scattering amplitude to second order in the photon energy. The proton polarizabilities have been successfully measured in dedicated experiments on low-energy γp-scattering in 1960–2001. Similar measurements of γn-scattering can be done with neutrons weekly bound in deuterons. The deuteron is clearly very good as a neutron container owing to minimal distortions introduced by nearby protons and owing to a good theoretical control over the distortion effects.

Our analysis of the reaction of low-energy elastic γd scattering, in which a coherent sum of γp- and γn-scattering amplitudes is probed, is carried out using a nonrelativistic diagrammatic approach with a nonrelativistic version OBEPR of the Bonn potential. This potential suggests a simple diagrammatic picture of strong interaction via meson exchanges from which meson-exchange currents (MEC) and seagulls consistent with the potential can be straightforwardly constructed. Those MEC as well as a related technique of loop calculations have already been carefully tested [4] in applications to the reaction of deuteron photodisintegration, including polarization observables.

Actually, deuteron-structure dependent effects in low-energy γd scattering are strongly dominated by a well-known long-ranged single-pion exchange. Moreover, electromagnetic interactions related with a short-range part of the NN-interaction (the latter is parameterized by heavy-meson exchanges and form factors in the Bonn OBE potential) are mostly fixed at

low energies in a unique way by gauge invariance and its consequence — Siegert theorem. For this reason, a model dependence related with unreliably known features of the short-range NN-interaction and with therefore somewhat arbitrary choice of the NN-potential is not large provided the used potential includes the long-ranged single-pion exchange and the short-range part is adjusted to give an accurate description of the binding energy and the NN-scattering amplitude.

Having fixed the strong and electromagnetic interactions in the specific Bonn model, we take into account a full set of diagrams (up to four loops) thus guaranteeing the gauge invariance of the resulting amplitude of $\gamma d \to \gamma d$. Beyond that additional two-body contributions due to Δ-isobar excitation and retardation in pion-exchange diagrams are added. One-photon interaction of the free nucleon is considered together with the important spin-orbital term which is the most essential relativistic correction in the considered problem. Two-photon structure of the free nucleon is accounted through its dipole electric and magnetic polarizabilities (also together with a relativistic correction) describing effects to second order in the photon energy. Important higher-order corrections are also included using results of phenomenological calculations through dispersion relations for spin, quadrupole, etc., polarizabilities.

In the previous version of the calculation we met a problem with a description of the Saskatoon laboratory data [5] on γd-scattering at 94 MeV. Recently we have found that this failure is caused by a sign mistake in the computer code for the Δ-isobar contribution to the two-body electromagnetic current in crossed diagrams that resulted in a noticeable underestimation of the differential cross section at backward angles and a strong shift of extracted polarizabilities of the nucleon. After correction of this mistake we arrive at a very satisfactory agreement with all the data (see below).

Another shortcoming of the previous calculation was in using a too poor approximation for four-loop diagrams with two meson-exchange currents and intermediate NN-rescattering. Actually, in order to facilitate four-loop computations, a simplified off-shell NN-rescattering amplitude was used, namely the amplitude found with a separable NN-potential built as a truncation of another, the Paris potential. As a result of using different NN-potentials in different pieces of the whole amplitude, some mismatch appeared between the resonance and seagull parts at all energies, so that gauge invariance was not exactly maintained and the corresponding low-energy theorem was also not exactly fulfilled. For example, at zero energy and the forward scattering angle we have got the spin-averaged amplitude of deuteron Compton scattering to be -0.47 (in the units of e^2/M, M is the nucleon mass) instead of the correct value of -0.50. With the advent of faster computers, we are capable today to do four-loop calculations directly, thus avoiding the Paris-potential separable approximation and using the NN-rescattering amplitude consistently as it is in the Bonn model. In the presented now results, the mentioned mismatch is cured and the total Compton scattering amplitude obeys nicely the low-energy theorem within the accuracy of numerical calculations.

2. We omit further computational details that can be found in Ref. [1]. Our present (corrected) main results are as follows.

Considering the isospin-averaged nucleon dipole polarizabilities α_N and β_N as the only free parameters, we fit available data on the differential cross section of γd scattering [5–7] and obtain

$$\alpha_N + \beta_N = 16.9 \pm 1.5, \quad \alpha_N - \beta_N = 10.5 \pm 1.7 \tag{1}$$

(in the units of $10^{-4}\,\mathrm{fm}^3$) with combined statistical and systematic uncertainties and a very satisfactory $\chi^2/\mathrm{d.o.f} = 33/(29-2)$. Actually the obtained numbers slightly depend on the

explicit version of the Bonn potential used.

A one-parameter fit with the theoretical constraint $\alpha_N + \beta_N = 14.6$ (Baldin sum rule) gives a consistent value $\alpha_N - \beta_N = 9.4 \pm 1.6$.

In contrast to previous (erroneous) results in [1] the obtained difference $\alpha_N - \beta_N$ is now in a good agreement with the proton's value ($\alpha_p - \beta_p = 10.1 \pm 0.6$ [8]) that means the absence of a visible isovector component in the nucleon dipole polarizabilities α and β.

It is remarkable that for the first time a good description of all available data on γd scattering is obtained (see Fig. 1) including data points at the highest energies and backward angles where all previous calculations failed. This might be important for theoretical interpretation of expected new data at energies 40–110 MeV and angles 30–150° from MAX-lab (Lund) [9].

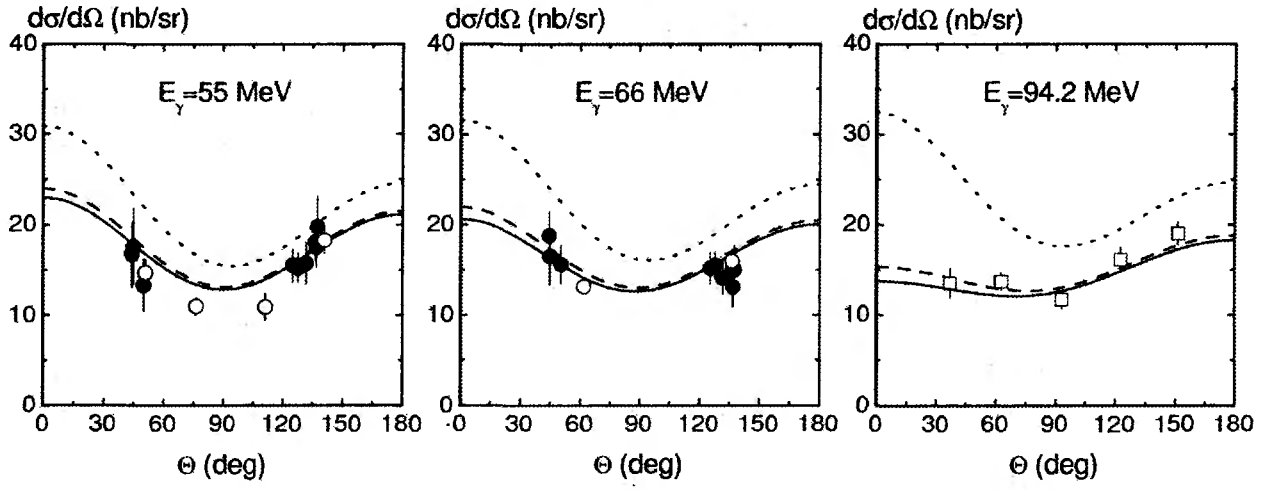

Figure 1: The differential cross section of γd-scattering at three selected energies. Dotted lines: the nucleon dipole polarizabilities are turned off. Dashed lines: $\alpha_N + \beta_N = 14.6$ and $\alpha_N - \beta_N = 9.4$. Solid lines: $\alpha_N + \beta_N = 16.9$ and $\alpha_N - \beta_N = 10.5$. Data are from Urbana [6] (○), Lund [7] (•) and Saskatoon [5] (□).

[1] M.I. Levchuk and A.I. L'vov, Nucl. Phys. **A674**, 449 (2000).

[2] S.R. Beane *et al.*, Nucl. Phys. **A747**, 311 (2005).

[3] R.H. Hildebrandt *et al.*, Nucl. Phys. **A748**, 573 (2005).

[4] M.I. Levchuk, Few-Body Syst. **19**, 77 (1995).

[5] D.L. Hornidge et al., Phys. Rev. Lett. **84**, 2334 (2000).

[6] M.A. Lucas, PhD thesis, University of Illinois at Urbana-Champaign, 1994.

[7] M. Lundin et al., Phys. Rev. Lett. **90**, 192501 (2003).

[8] Review of Particle Physics (C. Amsler *et al.*), Phys. Lett. B **667**, 1 (2008).

[9] L. Isaksson, talk at this Conference.

SEMI-INCLUSIVE CHARGED PION ELECTROPRODUCTION OFF THE PROTON

M. Osipenko[1,2]
(The CLAS Collaboration)
[1]*INFN, Sezione di Genova, 16146 Genova, Italy*
[2]*Moscow State University, Skobeltsyn Institute of Nuclear Physics, 119899 Moscow, Russia*

The semi-inclusive electroproduction of hadrons off the nucleon, $eN \to e'hX$, is an important tool allowing to study simultaneously the internal structure of the target nucleon and hadron creation mechanism. In Deep Inelastic Scattering (DIS) regime the semi-inclusive electroproduction of hadrons can be described by perturbative quantum chromodynamics (pQCD) combining our knowledge of non-perturbative distribution/fragmentation/fracture functions. Indeed, the inclusive lepton scattering off the nucleon and hadron production in e^+e^- collisions allow one to study separately the momentum dependence of the parton distribution functions in the nucleon and the parton fragmentation functions, respectively. The electroproduction of hadrons in the current fragmentation region combines these two and provides additional information about hadronization and nucleon structure.

The data were collected at Jefferson Lab in Hall B with the CEBAF Large Acceptance Spectrometer (CLAS) [1] using a 0.354 g/cm^2 liquid-hydrogen target and a 5.75-GeV electron beam. The average luminosity was 10^{34} cm^{-2}s^{-1}. The CLAS can detect and identify charged particles with momenta down to 0.2 GeV/c for polar angles between 8° and 142°, while the electron-pion separation is limited up to about 50°. The total angular acceptance for electrons is about 1.5 sr. The momentum resolution is a function of the polar scattered angle and varies from 0.5% to 1%. The angular resolution is approximately constant, approaching 1 mrad for polar and 4 mrad for azimuthal angles.

Using these data we performed a measurement of semi-inclusive π^+ electroproduction [2] with broad coverage in all five independent kinematic variables: four-momentum transfer Q^2 from 1.4 to 5.7 GeV^2, Bjorken x from 0.15 to 1, z from 0.07 to 1, p_T^2 from 0 to 1.5 GeV^2 and full coverage from 0 to 2π in the azimuthal distributions. The measurement of fully (five-fold) differential cross sections allowed us to study all possible correlations between dynamical dependencies in five kinematic variables. Moreover, the complete coverage in the azimuthal distributions was very important to separate the three contributions to the total cross section:

$$\frac{d^5\sigma}{dxdQ^2dzdp_T^2d\phi} = \sigma_T(1+\epsilon R)\left\{1 + 2\langle\cos\phi\rangle\cos\phi + 2\langle\cos 2\phi\rangle\cos 2\phi\right\}, \qquad (1)$$

ϕ-independent part ($\sigma_T(1+\epsilon R)$ with ϵ being the virtual photon polarization), $\cos\phi$ and $\cos 2\phi$ terms.

The ϕ-independent part of the cross section falls off exponentially in p_T^2. This has been predicted in Ref. [3] to arise from the intrinsic transverse momentum of partons. We observe no deviation from this exponential behavior over the entire kinematic domain of our data. At large z the mean transverse momentum $\langle p_T^2\rangle$ (the exponential slope) is found to be almost x and Q^2-independent and it rises with z as expected within the naive parton model. In the low-z region, $\langle p_T^2\rangle$ is altered by the limited phase space.

In order to compare the measured ϕ-independent part of the cross section with pQCD calculations we integrated it in p_T^2 and extracted the structure function H_2 by using the known ratio R of longitudinal to transverse virtual photon cross sections [4]:

$$\int \sigma_T(1+\epsilon R)dp_T^2 = \frac{2\pi\alpha^2}{xQ^4}(1+(1-y)^2)\frac{H_2}{1+R}\,. \qquad (2)$$

Obtained structure function $H_2 = \sum_i c_i^2 x f_i(x) \otimes D_i^h(z)$ was compared to LO and NLO pQCD calculations given in Ref. [5], where the parton distribution function $f(x)$ were taken from Ref. [6] and the fragmentation function $D(z)$ were taken from Ref. [7]. In the NLO calculations we included a systematic uncertainty due to arbitrary factorization/renormalization scale variations, indicating the size of possible higher order effects. NLO calculations within their uncertainty lie closer to the data in the low-z region than LO ones. The difference between the data and NLO pQCD is at most about 20% and it leaves room for an additional contribution from target fragmentation of <20% in the low-z region. However, this difference is comparable to systematic uncertainties in the calculations due to higher-order corrections and the favored fragmentation assumption. The multiplicity ratio H_2/F_2 (the ratio of semi-inclusive and inclusive cross sections) demonstrates the same level of agreement between data and pQCD calculations as H_2 alone. This demonstrates that the differences between the data and theory do not cancel in the ratio.

Because the agreement between pQCD calculations and our data was rather poor even at large-z we could explore only qualitative behavior of the structure functions to search for the target fragmentation contribution. One can naively define all hadrons produced in the direction of the struck quark to be in the current fragmentation region, whereas those produced in the direction of the spectator diquark to be in the target fragmentation region. In the CM frame, the variable z mixes backward-angle production with the production of low-momentum forward-going hadrons [8]. In the left panel of Fig. 1 we compared measured Feynman x_F distributions with the LO pQCD calculations combined with a Gaussian p_T-distribution. The theory describes approximately the $x_F > 0$ behavior beginning from the $x_F \sim 0$ peak. At negative x_F values the theoretical curve is almost constant and deviates strongly from the data. This is because at $x_F < 0$, z is close to zero and varies slowly, making $D(z)$ nearly constant. In order to distinguish target and current fragmentation, one can use a different variable [8]. This can still be interpreted as the parton momentum fraction carried by the measured hadron, similar to that in e^+e^- collisions. By simply using the fragmentation function $D(z_G)$ for both forward and backward regions, one obtains a qualitative agreement between theoretical and experimental x_F distributions (see the right panel of Fig. 1). Hence the target fragmentation term is similar to the standard "current fragmentation" contribution.

The ϕ-dependent terms are typically less than a few percent of the ϕ-independent part of the semi-inclusive cross section. The $\langle\cos 2\phi\rangle$ moments are generally compatible with zero within our systematic uncertainties, excluding the low-z and high-p_T region where they are definitely positive. The $\langle\cos\phi\rangle$ moments are more significant due to smaller systematic uncertainty and they are negative at large-p_T. These data were compared to the theoretical prediction based on phenomenological models of two different mechanisms: Cahn and Berger effects. The Cahn effect arises from the simple kinematic consideration of partons with intrinsic transverse momentum and can be calculated explicitly in the limits $Q^2 \to \infty$ and $z \to 1$. The Berger effect is due to the exclusive production of a single hadron from a free quark. The formation of this hadron through one-gluon exchange yields a ϕ-dependence

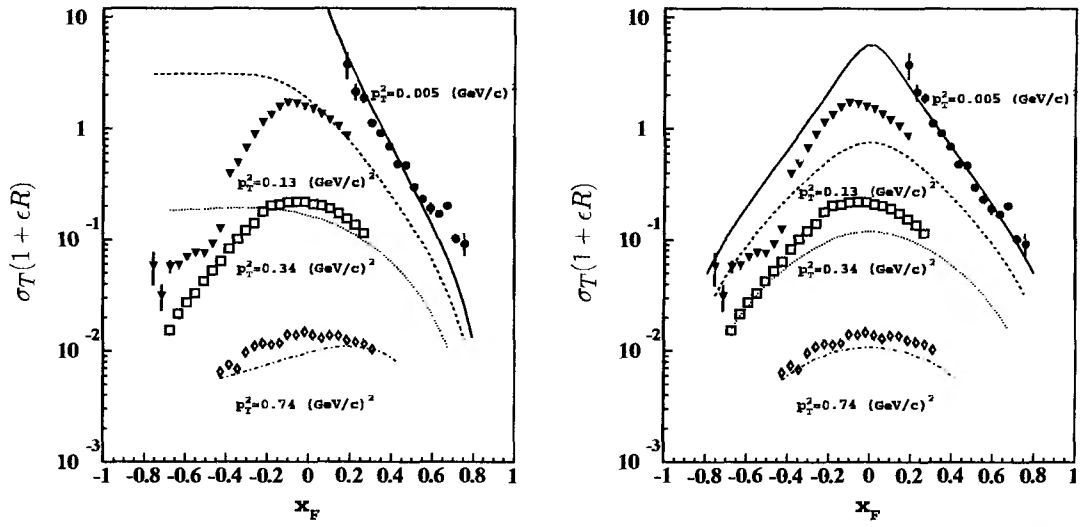

FIG. 1: The x_F-dependence of the ϕ-independent term $\sigma_T(1+\epsilon R)$ at $Q^2 = 2$ (GeV/c)^2, $x = 0.26$ and different values of p_T^2. The data are compared to LO pQCD calculations combined with a Gaussian p_T-dependence. The theoretical curves on the left panel are using the fragmentation function $D(z)$, while on the right panel $D(z_G)$.

proportional to the hadron wave function. Since such production mechanism does not require any intrinsic transverse momentum of partons it is completely orthogonal to the Cahn effect. Theoretical predictions on the $\langle\cos\phi\rangle$ are in strong disagreement with our data. Both data and theory suggest negative $\langle\cos\phi\rangle$, but the theory overestimate its magnitude by many standard deviations over much of the kinematics. This is due to the dominant, negative Cahn effect contribution. Theory predicts very small $\langle\cos 2\phi\rangle$ values partially due to cancellation between the Cahn and Berger effect contributions. These predictions are generally in agreement with our data. The data points at large p_T and low z lie above the theoretical curves, this difference reaches 2-3 systematic deviations.

The comparison with higher energy data taken at $Q^2 \simeq 30 - 60$ GeV^2 in Ref. [9] reveals the striking difference between the two measurements of $\langle\cos\phi\rangle$, whereas both measurements of $\langle\cos 2\phi\rangle$ at large and small Q^2 are compatible with zero. At large Q^2 the absolute values of $\langle\cos\phi\rangle$ reach 0.05-0.1 and seem to follow the expected $1/Q^2$ behavior. However, our data at lower Q^2 do not follow this trend having values compatible with zero.

---

[1] B. Mecking et al., Nucl. Instr. and Meth. **A503**, 513 (2003).
[2] M. Osipenko et al., Phys. Rev. **D80**, 032004 (2009).
[3] R. N. Cahn, Phys. Rev. **D40**, 3107 (1989).
[4] C. J. Bebek et al., Phys. Rev. Lett. **38**, 1051 (1977).
[5] W. Furmanski and R. Petronzio, Z. Phys **C11**, 293 (1982).
[6] H. L. Lai et al., Eur. Phys. J. **C12**, 375 (2000).
[7] S. Kretzer, Phys. Rev. **D62**, 054001 (2000).
[8] D. Graudenz, Fortsch. Phys. **45**, 629 (1997).
[9] J. J. Aubert et al., Phys. Lett. **B130**, 118 (1983).

SILICON VERTEX TRACKER FOR THE TJNAF HALL B UPGRADE

M. Merkin, A. Voronin, D. Karmanov, S. Rogozhin
Skobeltsyn Institute of Nuclear Physics, Moscow State University, Moscow, Russia

The Silicon Vertex Tracker is a part of the Thomas Jefferson National Accelerator Facility Hall B upgrade project. Jefferson Lab operates the CEBAF accelerator with a continuous electron beam; the upgrade increases the beam energy to 12 GeV and the luminosity reaches $10^{35}\ {}^{1}/_{s \cdot cm^2}$. The current CLAS detector complex in Hall B is comprised of drift chambers, time-of-flight scintillators and Cherenkov counters. The upgraded version of the detector complex is dubbed CLAS12; it provides for reliable 4π particle registration at high luminosity.

The SVT is a key element of CLAS12 [1]. It consists of two sections: the barrel and the disc, each section is assembled from standard wafers – see Fig. 1. The barrel part is comprised of four superlayers (each superlayer is made of two sensor layers with intersecting strips to determine two spatial coordinates). The fourth superlayer is redundant, however, it significantly decreases the probability of track loss. The disc part consists of three superlayers. It operates in conjunction with the forward detector complex, therefore losing one point in the tracker is less critical, at the same time adding a fourth layer would decrease the accuracy of the whole detector.

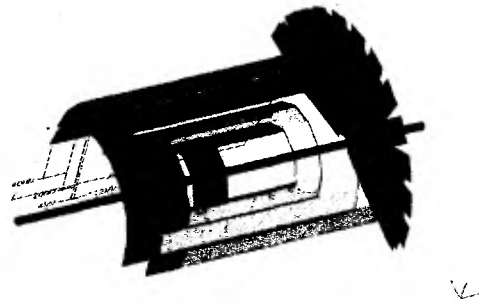

Fig. 1. Layout of the Silicon Vertex Tracker.

It should be noted that a silicon tracker is the only system able to provide the required resolution of 50 μm in the limited space available. This resolution can be achieved with a strip pitch of 150 μm. If 300 μm thick wafers are used, the effects of multiple scattering are negligible.

The readout ASIC for the SVT needs to operate with CEBAF's continuous beam. Most integrated circuits that are used in silicon sensor arrays operate with fixed-time bunch crossings. It should be noted that despite the high luminosity radiation hardness is not an important parameter with an electron beam.

The main candidate for the DAQ system is the FSSR2 ASIC. The FSSR2 has 128 input channels, each channel is equipped with a preamplifier, a shaper, a 3-bit ADC and a discriminator. The shaping time can be set to 65, 85, 100 or 125 ns; the overall dynamic range of the amplifier is circa 2 MIP for the 300 μm wafers used. The most important feature of the FSSR2 is its self-triggering mechanism: if a signal exceeds the discriminator threshold, the ASIC transmits the hit data: the hit channel number, the signal magnitude and a time stamp. Thus, it is able to operate continuously (until a certain input rate is reached). The FSSR2 ASIC is controlled by two clocks: the slow clock (designed to run at 132 ns) operates the chip's core logic; the fast clock (70 MHz) drives the data readout. Data is transmitted in 24-bit words, either status words transmitted by default, or data words with information

corresponding to a single event. Other characteristics of the FSSR2 are its low noise levels and low power dissipation (500 mW).

In order to evaluate the FSSR2's performance, a computer simulation of its data rate handling capability was performed [2]. The test program generated events evenly distributed across the ASIC's input channels and processed them in the way the chip's logic does. Two possible causes for data loss were studied. First, two hits in a single channel over a short period of time cannot be distinguished. Second, the FSSR2 has no pipeline, therefore hit acquisition is stopped while data is being read out.

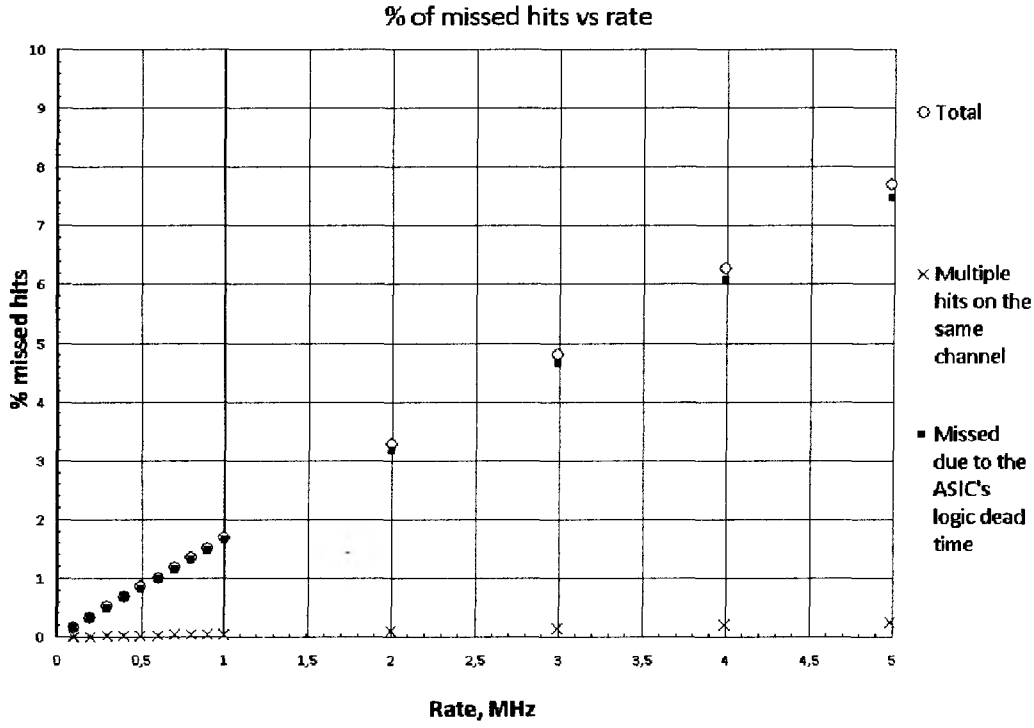

Fig. 2. Percentage of hits lost as a function of the hit rate.

Results are presented in Fig. 2. At a rate of 1 MHz per ASIC 0.05% hits are lost due to multiple events and 1.65% hits due to the chip logic's dead time. GEANT4 simulations indicate an expected rate of 1 MHz per ASIC in the inner regions of the tracker.

Noise measurements were performed to determine the amplifier noise sensitivity to the sensor capacitance. The common method of measuring noise is by calculating the distribution of output signal magnitude at a certain input signal level and certain ADC thresholds. However, this method is not applicable due to the low resolution of the FSSR2's ADC. The discriminator threshold, on the other hand, has a better resolution of 8 bits. Therefore, a different method was used. The hit rate was measured as a function of the discriminator threshold. The obtained distribution is called the complementary error function and is the signal rate distribution integrated. Taking noise into account, the initial signal rate distribution is Gaussian with the μ and σ parameters corresponding to the input pulse and the amplifier noise.

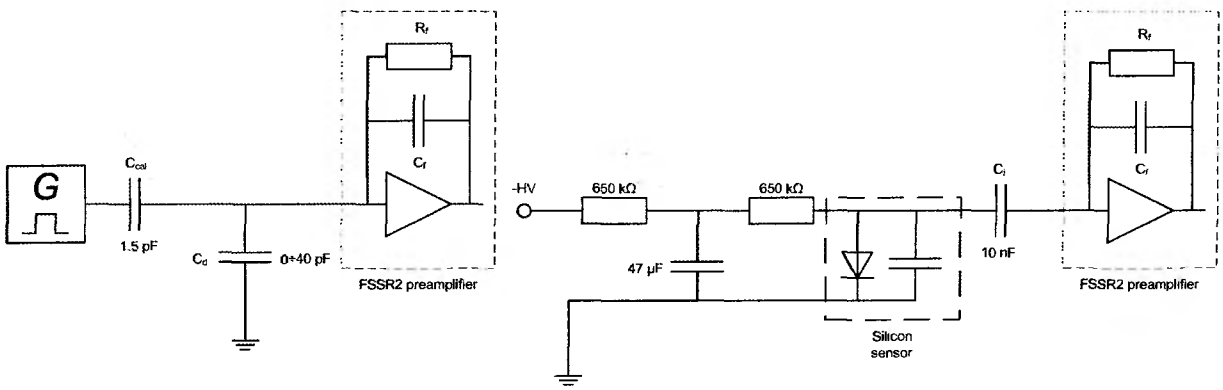

Fig. 3. Diagrams of the charge injection circuit (left) and readout chain with sensor attached (right).

A test stand was assembled to perform the measurements – see Fig. 3. A square pulse with a frequency of 100 kHz was injected through a special calibrating capacitor C_{cal} to imitate charge collected from a sensor. The calibrating capacitance needs to be relatively small in order not to increase the noise levels. A sensor strip capacitance is estimated to be 20 pF, therefore, a 1.5 pF capacitor was used. The pulse magnitude was equivalent to a MIP signal (3.6 fCl in 300 µm of silicon). A set of sensor equivalent capacitors C_d with capacitances ranging from 0 to 40 pF was installed after the calibrating capacitor.

A special software was developed to perform the test. The software adjusted the discriminator level from minimum to maximum and measured the hit rate. The obtained distribution was numerically differentiated and the µ and σ parameters were calculated. The µ parameter corresponded to the injected signal, the σ parameter to the noise level which was recalculated in electrons – see Fig. 4. Measurements were performed at different shaping times. Noise levels are consistent with previous measurements [3]. Reducing the shaping time increases the noise, however, the signal-to-noise ratio remains acceptable at all capacitances.

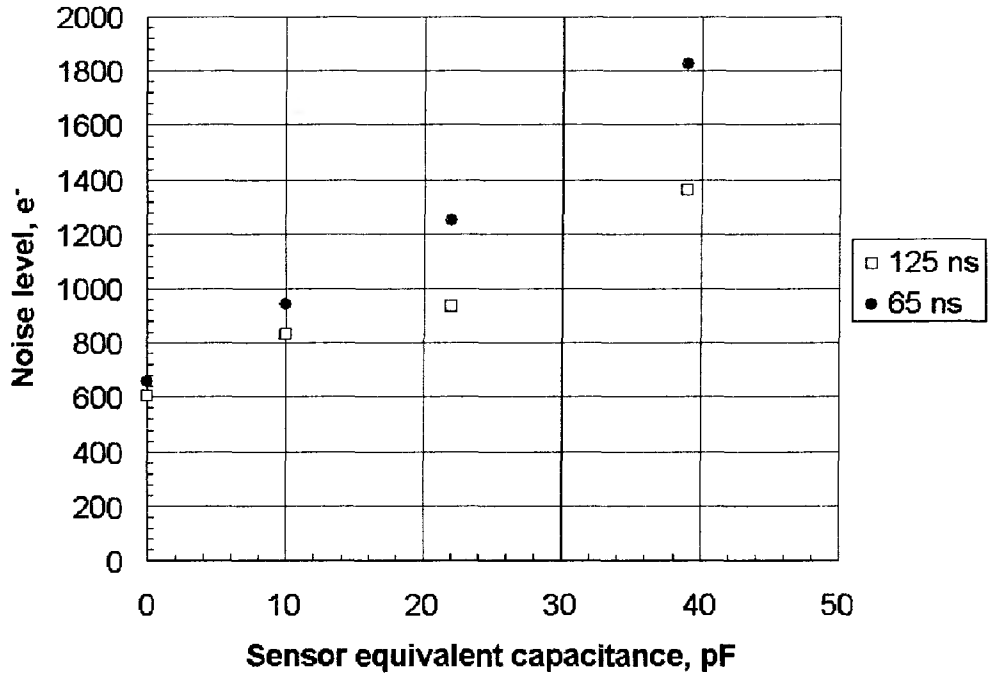

Fig. 4. Noise level as a function of sensor capacitance at 65 ns and 125 ns shaping times.

To imitate particle detection, a laser test stand was assembled. A single-channel silicon sensor was attached to the ASIC – see Fig. 3. The sensor is drawn as a reverse-biased diode

and a capacitor (the sensor's capacitance was estimated at 20 pF). High voltage (- 50V) is applied through a special filter.

The laser was driven by pulses with a frequency of 100 kHz and a duration of 80 ns. The pulse amplitude was calibrated to be equivalent to a MIP. The above described method was used to obtain signal rate distribution. The results are presented in Fig. 5, the generator signal with a 20 pF equivalent capacitor is presented for reference.

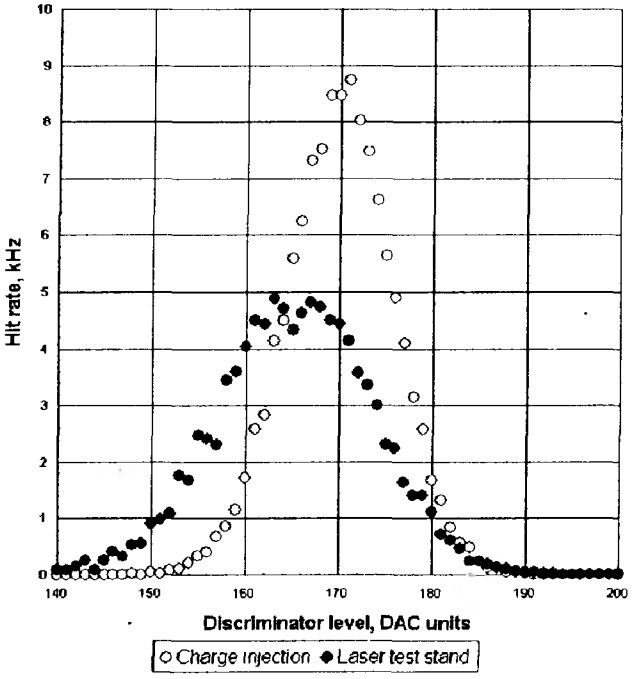

Fig. 5. Signal rate distributions for the laser test stand and an injected signal.

[1] The Hall B 12 GeV Upgrade. Preconceptual Design Report. Jefferson Lab – December, 2005.

[2] S. Rogozhin et al., Data Rate Handling Capability of the FSSR2 ASIC-based Data Acquisition System of the Silicon Vertex Tracker, CLAS-Note 2008-028

[3] V. Re et al., FSSR2, a Self-Triggered Low Noise Readout Chip for Silicon Strip Detectors, IEEE Trans. Nucl. Sci., vol. 53, no. 4, pp. 2470-2476, Aug. 2006

PHOTOPRODUCTION OF $\pi^0\pi^+$ ON THE PROTON AND DEUTERON AT $E_\gamma = 0.7 - 1.5$ GEV

A. Mushkarenkov for the GRAAL collaboration

Institute for Nuclear Research, 117312 Moscow, Russia

Abstract

The preliminary results obtained by the GRAAL collaboration for the $\pi^0\pi^+$ photoproduction on the free and quasi-free proton (deuteron) at $E_\gamma = 0.7 - 1.5$ *GeV* are presented. The total cross section of the $\gamma p \to \pi^0\pi^+ n$ reaction and invariant mass spectra for the $\pi^+\pi^0$, $\pi^+ n$ and $\pi^0 n$ systems are presented in the photon energy range from 0.7 to 1.5 GeV. These results are in good agreement with the 2π-MAID calculations.

Double pion photoproduction processes give the main contribution to the total photoabsorption cross section at E_γ= 0.7–1.5 GeV. They provide new information on the cascade channels of the nucleon resonances decays. e.g. $N^* \to (\Delta\pi, \rho N, \sigma N) \to \pi\pi N$. This information can highlight resonances which are not seen in the πN or ηN channels and brings additional constraints for the theoretical models of the nucleon.

The $\pi^0\pi^+$ process on the proton has been experimentally studied using DAPHNE and TAPS detectors at MAMI [1, 2, 3] for E_γ below 0.8 GeV. These unpolarized measurements have been complemented in the work [3] with the helicity dependent cross-sections $\sigma_{1/2}$ and $\sigma_{3/2}$, corresponding to the absorption of circularly polarized photons by longitudinally polarized nucleons with anti-parallel and parallel relative spin orientations, respectively. It has been found that the model [4] can well describe experimental data for $\sigma_{3/2}$, for which the processes $\gamma p \to D_{13} \to (\pi\Delta, \rho^+ n) \to \pi^0\pi^+ n$ are largely responsible, but fails to describe $\sigma_{1/2}$ indicating non-resonant mechanisms of the reaction which are not fully accounted in the model.

The experiment was performed at the GRAAL facility which uses a tagged photon beam with E_γ=500–1500 MeV (ΔE_γ=16 MeV) obtained from the laser-induced Compton backscattering of storage ring electrons with an energy of 6 GeV. A schematic view of the GRAAL detection system is shown on fig. 1. This detector is described in details in work [5]. Detection efficiencies of the LAGRANγE detector for charged particles and photons are $\approx$70–100% depending on the software reconstruction conditions. Neutron detection efficiency amounts to $\sim$60% for the BGO ball [6] and $\sim$22% for the shower detector [7].

Data collected on the proton and deuteron targets were analysed in a very similar way to select candidates of the $\pi^0\pi^+$ photoproduction process. A signal from the tagging detector together with two photons of π^0 decay in the BGO ball, as well as a neutron and π^+ detected in the central or forward direction were required. Events with a two photons invariant mass within the range 0.1–0.18 MeV were selected as those that containing a π^0 in the final state (see fig. 2). The measured energy and momentum of the π^0 and the measured angles of the π^+ and neutron provided, for each event, the necessary constraints for a 3-body kinematical fit that was performed to determine the unmeasured π^+ and neutron energies. In addition, the following cuts were applied: $30^\circ \leq \Delta\theta_n \leq 30^\circ$ and $40^\circ \leq \Delta\varphi_n \leq 40^\circ$, where $\Delta\theta_n$ and $\Delta\varphi_n$ are differences between measured and calculated polar and azimuthal angles, respectively (figs. 3 and 4).

A special attention was devoted to evaluate of the LAGRANγE detector acceptance. It was found that π^0 mesons with $\theta \lesssim 20^\circ$ were not detected by our apparatus. This indicates

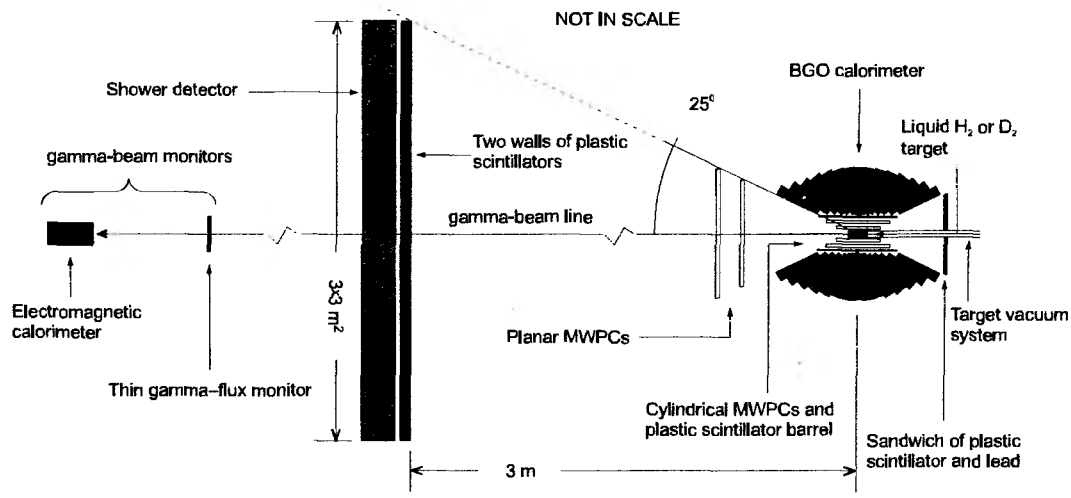

Fig. 1. Schematic view of the GRAAL detection system.

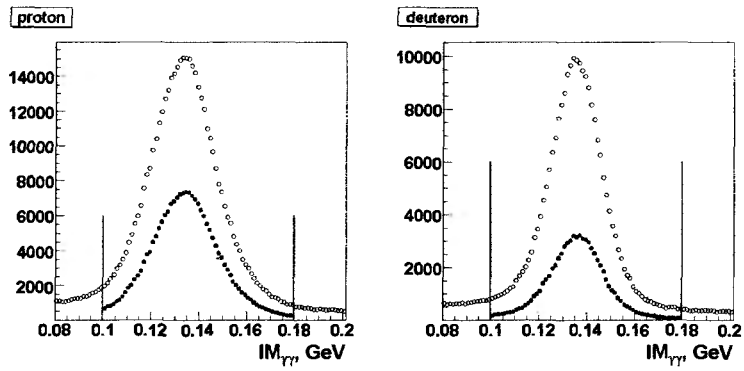

Fig. 2. 2γ invariant mass distributions for selected $\pi^0\pi^+$ events. The left (right) plot is from the proton (deutron) target. Open and closed circles correspond to the data before and after the kinematical cuts applied, respectively. The vertical lines show the selected ranges.

that an extrapolation using a theoretical prediction is needed for the calculation of the total cross section.

Fig. 5 shows a comparison of the invariant mass spectra for the $\pi^0\pi^+$, $\pi^0 n$ and $\pi^+ n$ systems measured at the 3 different E_γ energy regions on the proton (closed circles) and deutron (open circles) targets. The detector acceptance correction are not applied. No sizeable nuclear effects can be deduced from this comparison.

Fig. 6 shows a comparison between the experimental invariant mass spectra with the ones simulated using the GEANT3 code. In the simulation, the $\pi^+\Delta^0$, $\pi^0\Delta^+$, $\rho^+ n$ and $\pi^0\pi^+ n$ (with a uniform phase space distribution) intermediate mechanisms were implemented. The contribution of each partial channel was deduced from a fit of the total photoabsorption cross-section on the proton using a sum of 6 Breit-Wigner resonances plus a smooth non-resonant background [8]. The simulated data were analysed in the same way as the experimental one. It was found that this simple phenomenological model could fairly well describe the invariant mass sprectra for both the $\pi^0 n$ and $\pi^+ n$ systems while the $\pi^0\pi^+$ spectra indicate an slight model overestimation of the $\rho^+ n$ channel contribution. Due to its good agreement with the experimental data, this model was used to evaluate both the detection efficiency and the extrapolation correction of the data into the unmeasured kinematical region.

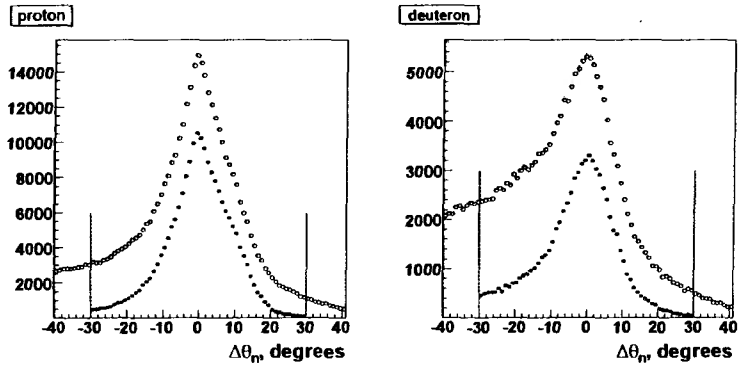

Fig. 3. Differences between the calculated and measured neutron θ angles for all selected events. Notations are the same as in fig. 2.

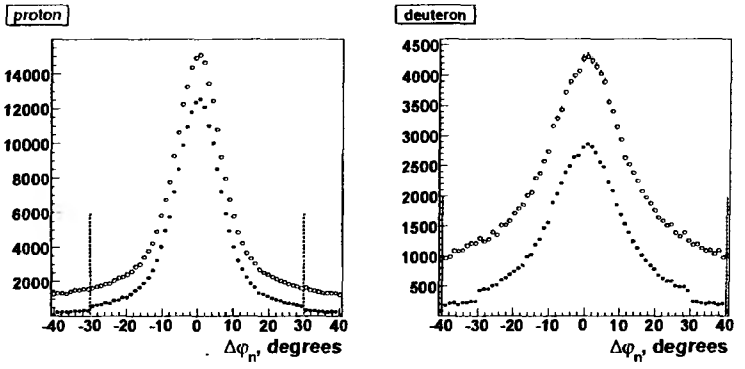

Fig. 4. Differences between the calculated and measured neutron φ angles for all selected events. Notations are the same as in fig. 2.

The preliminary results of the total cross-section for the $\gamma p \to \pi^0\pi^+ n$ reaction are presented on the fig. 7. In this preliminary phase, only a relative normalization was evaluated for these data. The absolute normalization value was obtained by scaling to the total cross-section values obtained at MAMI. In fig. 7 the data that were thus abtained are compared with the 2π-MAID model calculation [9]. One can see the model can well describe the basic trend of the observed data but there is a 5-10 μb overestimation. Above 1.4 GeV there is an increase of the experimental data while the model still predicts a decreasing behaviour. Accornding to the 2π-MAID model, the peak at ~0.75 GeV corresponds to the internediate $D_{13}(1520)$ resonance excitation and the broad bump centered at E_γ=1-1.1 GeV is due to the excitation of the $F_{15}(1680)$ resonance and to the non-resonant ρ^+ production.

As it was said above, the obtained total cross-section values depend on the model selected for the detection efficiency calculation. Therefore, the detection efficiency calculation has to be done taking into account the some other different models that may provide us with a systematic error related to the model chosen.

This work was supported by Russian Foundation for Basic Research, grant no. 08-02-00646-a.

References

[1] A. Braghieri et al., *Phys. Lett. B* **363** (1995) 46.

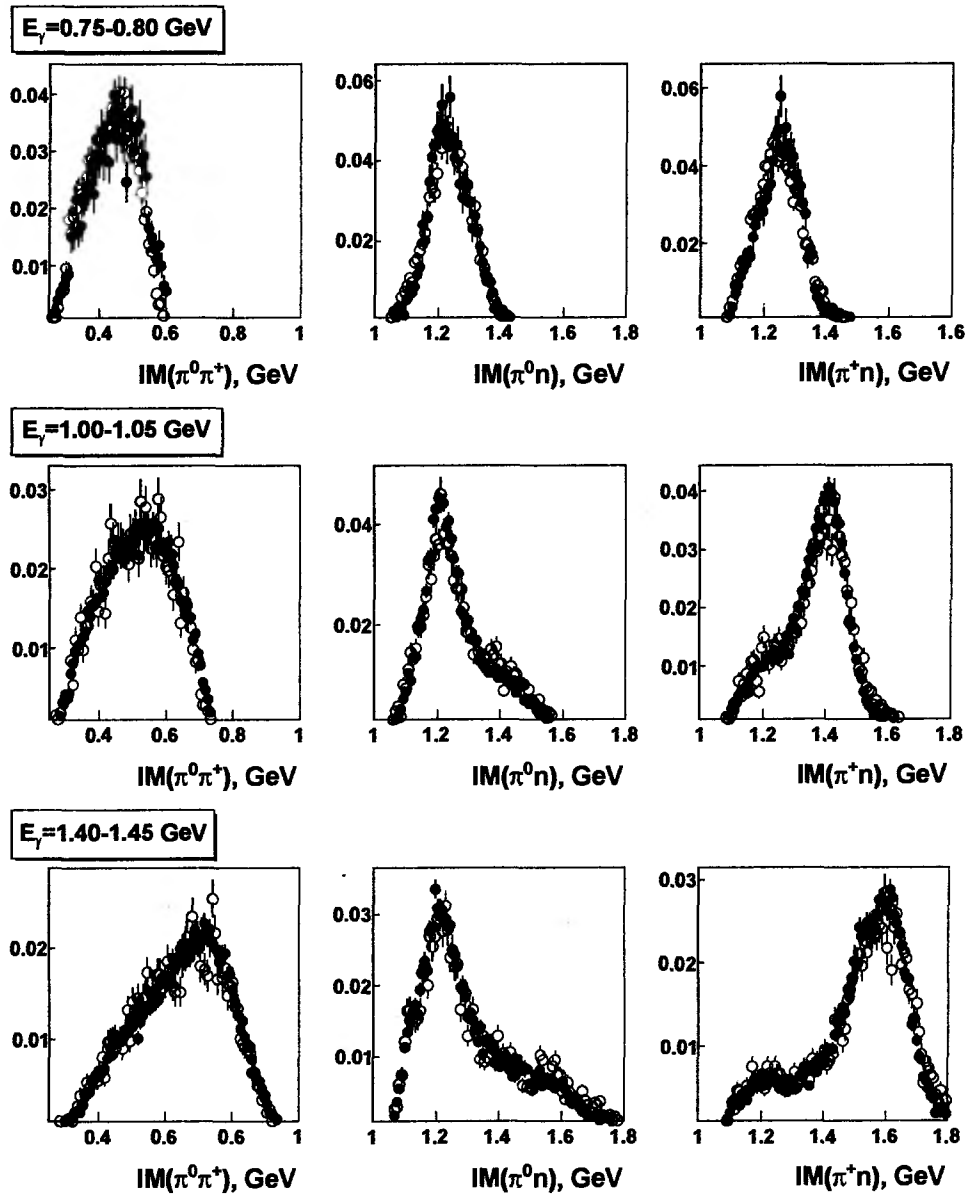

Fig. 5. The invariant mass spectra for the $\pi^0\pi^+$, $\pi^0 n$ and $\pi^+ n$ systems for the 3 different E_γ energy range. Closed and open circles correspond to proton and deuteron targets, respectively.

[2] W. Langgärtner et al., *Phys. Rev. Lett.* **87** (2001) 052001.

[3] J. Ahrens et al., *Phys. Lett. B* **551** (2003) 49.

[4] J. C. Nacher, et al., *Nucl. Phys. A* **695** (2001) 295.

[5] O. Bartalini et al., *Eur. Phys. J. A* **26** (2005) 399.

[6] O. Bartalini et al., *Nucl. Inst. and Meth. A* **562** (2006) 85.

[7] V. Kuznetsov et al., *Nucl. Instrum. Methods A* **487** (2002) 396.

[8] N. Bianchi et al., *Phys. Rev. C* **54** (1996) 1688.

[9] A. Fix and H. Arenhovel, *Eur. Phys. J. A* **25** (2005) 115.

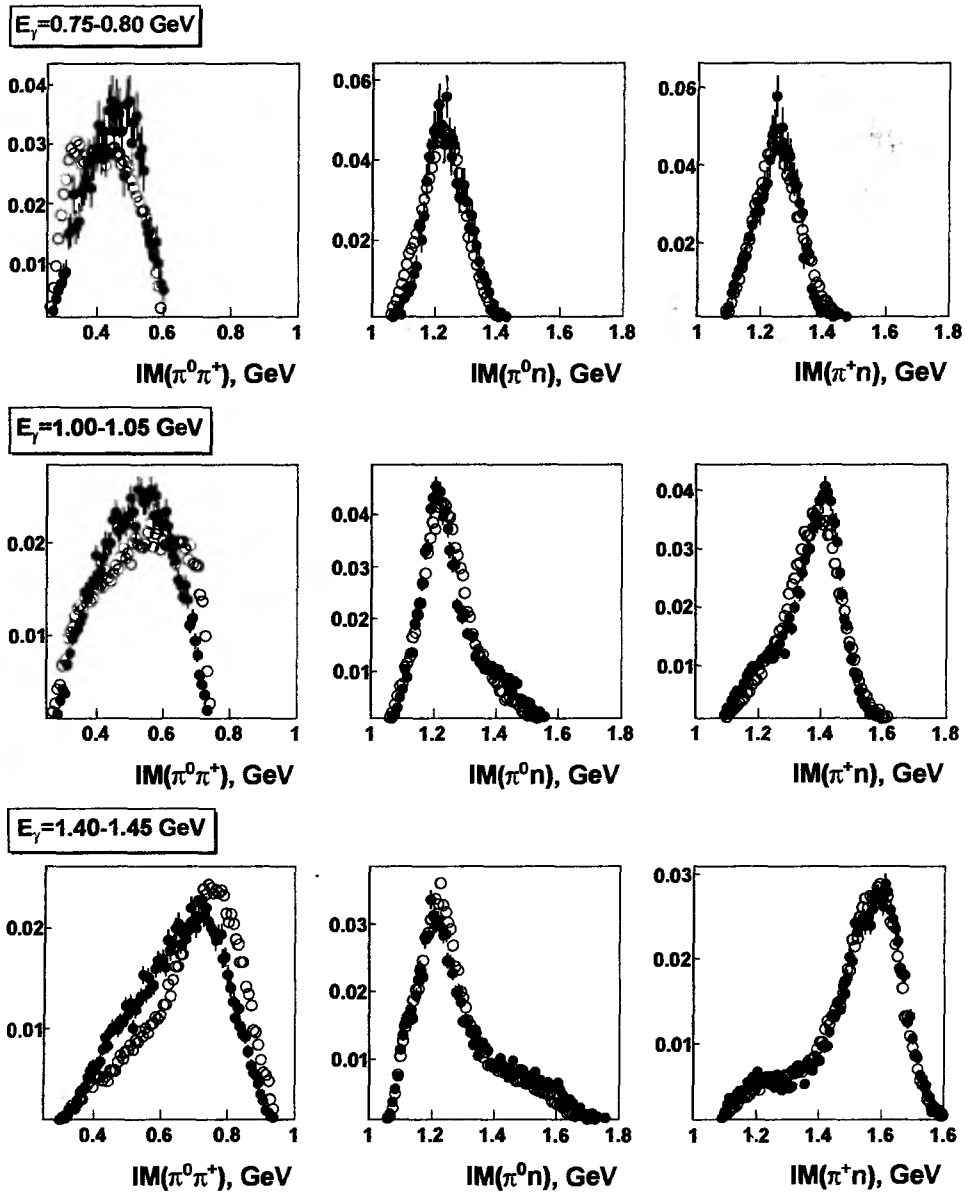

Fig. 6. The invariant mass spectra for the $\pi^0\pi^+$, $\pi^0 n$ and $\pi^+ n$ systems for the 3 different E_γ energy range. Closed and open circles correspond to experimental data on the proton and simulation, respectively.

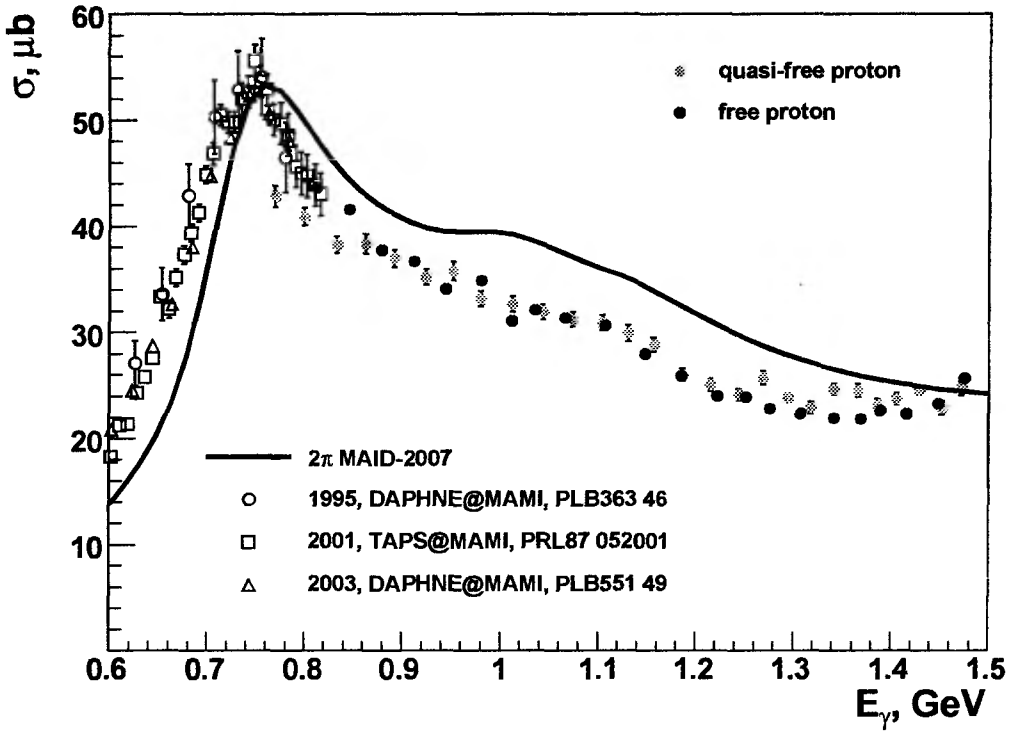

Fig. 7. The total cross-section of the reaction $\gamma p \to \pi^0\pi^+ n$. The back and grey circles show the results of this work for the proton and deuteron targets, respectively. The open markers show the data previously obtained at MAMI [1,2,3]. The solid line shows 2π-MAID calculation [9].

The coherent dissociation of relativistic nuclei ^{7}Li to the ^{3}H + ^{4}He channel

N.G. Peresadko, V.N. Fetisov, Yu.A. Alexandrov,
S.G. Gerasimov, V.A. Dronov, V.G. Larionova, E.I. Tamm, S.P. Kharlamov
P.N. Lebedev Physical Institute Russian Academy of Sciences, Moscow, Russia

Abstract

The coherent dissociation of relativistic nuclei ^{7}Li at the momentum of 3A GeV/c to ^{3}H + ^{4}He was studied by the photoemulsion technique. Results on the total (31± 4 mb) and differential vs the momentum transfer Q cross sections are presented. The observed Q-dependence of cross section is interpreted within the cluster model and the Akhieser-Sitenko-Glauber approach mainly as the superposition of two individual nuclear diffractional patterns from light (C,N,O) and heavy (Br, Ag) nuclei. The contributions to cross section due to the electromagnetic (the Bertulani-Baur theory) and nuclear interactions are well separated in the variable Q. Calculated values are correspondingly 4 mb (Q≤ 50 MeV/c) and 40.7 mb (Q≤ 400 MeV/c).

PACS: 25.75.-q, 25.70.Mn, 21.60.Gx, 24.10.Ht, 29.40.Rg

The study of nucleus properties and reaction mechanisms in Coulomb and nuclear interactions at the nucleus-nucleus collisions has more than half a century history [1–4]. In recent years these investigations are steeply expanding to relativistic energies [5–8].

It has been known that at the energies of hundreds MeV and above in parallel with the Coulomb interaction the nuclear diffractional reaction mechanism becomes important at small momentum transfer Q. It is analogous to the optical diffraction and has been predicted in the mid-1950s [9–12]. A distinguishing feature of diffraction is oscillations observed in the elastic particle or nucleon scattering cross sections ($d\sigma/dQ$) with the main maximum at small angles of order $\vartheta \simeq \lambda/R$, where λ is the de Broglie wave length of an incident particle and R is the size of interaction region. In this case the nuclear and Rutherford cross sections overlap considerably. It was suggested earlier [12] that the diffractional mechanism can produce the coherent disintegration of incident nucleus (without the target nucleus excitation) and the particle production also. The coherent dissociation of ^{12}C to three α-paricle has been observed in nuclear emulsion (p_0 = 4.5A GeV/c) and in propan bubble chamber (p_0 = 4.2A GeV/c) [13, 14] but a proper theoretical analysis of the Coulomb and nuclear contributions was not presented. It should be noted that the direct observation of diffractional pattern by a counter technique for processes of nuclear disintegration is a complicated task and was not implemented up to the present. In counter experiments the energy spectra of charged particles are usually measured for fixed emission angles [15, 16].

From many reactions detected in the emulsion (multifragmentation, meson production) we selected two-body final channel ^{3}H + ^{4}He corresponding to two-cluster structure of

the projectile ^{7}Li which is suitable for checking the current cluster model, the relativistic Coulomb excitation theory and nuclear diffractional approaches for very small $\lambda \simeq 0.01$ fm.

In this experiment the coherent dissociation cross section $d\sigma/dQ$ for the ^{7}Li projectile is measured with the goal to reveal special features of the nuclear and electromagnetic contributions. As is shown in the previous paper [8] very small emission angles of clusters are typical to this reaction at elativistic energies and therefore one could expect a joint noticiable manifestation of both the nuclear and electromagnetic reaction mechanisms [5]. Theoretical approaches [5,10,17,18] and the two-cluster model of ^{7}Li with the Pauli forbidden bound states [19,20] enables one for the first time to determin the regions in the variable Q of the nuclear and electromagnetic contributions to the studied reaction.

The emulsion stack was composed of layers of nuclear photoemulsion BR-2 which is sensetive to minimum ionization of the singly charged particles and irradiated in the ^{7}Li 3A GeV/c beam provided by the JINR synchrophasotron. In this photoemulsion the nuclei ^{7}Li and the singly and doubly charged particles are easily distinguished visually according to the ionization density on their tracks. For the determination of masses A_f of fragments the multiple Coulomb scattering of particles was measured. The detailed description of the identification procedure of protons, deuterons and ^{3}H, ^{3,4}He nuclei by this technique is given in Ref. [8].

From the total number of 3730 observed inelastic interactions only 85 events of the coherent disintegration of ^{7}Li to ^{3}H+^{4}He were separated. The nuclear emulsion contains $1.03 \cdot 10^{22}$cm^{-3} nuclei Br or Ag and $2.85 \cdot 10^{22}$cm^{-3} nuclei C,N,O. The pathes of the recoil nuclei Ag, Br having momenta less than 1 GeV/c are very small and they were not detected. The nuclei C,N,O with the momenta above 200-300 MeV/c have pathes more than 2 μm and they can be identified. For events collected the momentum transfer Q$\leq$ 400 MeV/c and recoil nuclei were not seen. Interactions of ^{7}Li with the protons were identified but not analyzed.

These 85 events were detected at the examination of the beam tracks with the total length 548.37 m that corresponds to the mean free path 6.5±0.7 m for the reaction channel considered. The cross section averaging over all photoemulsion nuclei is determined as the ratio the number of events to the total number of nuclei on the length of examinated tracks σ=85/(5.4837·10^4·4.91·10$^{22-3}$)=31±4 mb.

The transverse momentum transfer Q is equal to the vector sum of the transverse momenta of ^{3}H and ^{4}He. Their values are determined by the relation $p_t = p_0 A_f sin(\theta)$ where θ is the emission fragment angle relative to the progectile momentum. The accuracy of measurements of Q is about 10 MeV/c. The experimental cross section $d\sigma/dQ$ is shown in Fig.1 together with the theortical curves the meaning of which will be explained below. The characteristic non-monotonous Q-dependence has the peak in the range 100-170 MeV/c and the minimum at ~200 MeV/c. This shape is conserved at the variation of the histogram interval ΔQ in the range 15-40 MeV/c.

The nuclei ^{6,7}Li ^{7}Be are the lightest ones of the 1p-shell. I has been known that two-cluster probabilities for them have a high level (~ 0.8–1.0) [21]. In this paper the ^{7}Li nucleus and the states of ^{3}H, ^{4}He in continuum are described using the potential cluster model with the Pauli forbidden states formulated in Refs. [19, 20]. Previously this model was successfully used to describe the properties of ^{6,7}Li, photodisintegration process and scattering phase data [22, 23].

The interaction potential of clusters is written as the sum of the central V, spin-orbit V_{so}

and Coulomb V_c parts

$$\mathrm{V(r)} = -\mathrm{V_0}(1 + exp[(r - R_c)/a])^{-1}, \quad \mathrm{V}_{so}(r) = -\mathrm{V_1 ls}\,\frac{d}{r\,dr}V(r), \tag{1}$$

$$V_c(r) = \begin{cases} \frac{Z_1 Z_2 e^2}{2R_c}(3 - \frac{r^2}{R_c^2}), & r \leq R_c \\ \frac{Z_1 Z_2 e^2}{r}, & r > R_c. \end{cases} \tag{2}$$

with the parameters taken from Refs. [19, 24]

$$\begin{aligned} &\mathrm{V_{00}}=98.5\ \mathrm{MeV},\ \Delta V=11.5\ \mathrm{MeV},\ R_c=1.8\ \mathrm{fm},\ a=0.7\ \mathrm{fm}, \\ &\mathrm{V_0}=V_{00}+\Delta V(-1)^{l+1},\ V_1=0.015(3+(-1)^{l+1})\ \mathrm{fm}^2. \end{aligned} \tag{3}$$

In calculations with this potential we use the bound state wave functions of two allowed states $P_{3/2}$(-2.36 MeV, the ground state of ^{7}Li), $P_{1/2}$(-1.59) and six forbidden states $S_{1/2}$(-57.4), $S_{1/2}$(-15.9), $P_{3/2}$(-34.4), $P_{1/2}$(-32.3), $D_{5/2}$(-13.7), $D_{3/2}$(-11.1) obtained in Ref. [24].

The important assumption of the relativistic Coulomb dissotiation theories developed in [17] and [25] (the quantum and semiclassical versions) is a negligible value of the Coulomb amplitude compared with nuclear one for impact parameters $b \leq R$ where the value of R is of the order of a sum of collision nuclei radii. It is assumed that for these b the nuclear dissotiation becomes dominant.

The electromagnetic disintegration cross section calculation for ^{7}Li to the ^{3}H+^{4}He channel was done in the framework of the Bertulani-Baur formalism [5, 17] using the multipole expansion of the interaction. The main contribution gives two E1-transitions $P_{3/2} \to S_{1/2}, D_{3/2}, D_{5/2}$. After the integration of the initial expression for the cross section [5, 17] over angular variables of emission particle momenta we obtain

$$\frac{d\sigma_C}{dQ} = \frac{32}{9}\left(\frac{Ze^2}{\hbar v}\right)^2 c_d Q R^2 \int_0^\infty \frac{\xi^2}{(\xi^2 + (QR)^2)^2}(I_2^2(k) + \frac{1}{2}I_{0,1/2}^2(k))(f_1^2 + \frac{1}{\gamma^2}f_0^2)k^2 dk. \tag{4}$$

The functions f_n and the radial integrals $I_{l,j}(k)$ for dipole transitions are

$$f_n = \xi J_n(QR)K_{n+1}(\xi) - QRJ_{n+1}(QR)K_n(\xi), \quad I_{l,j}(k) = \int_0^\infty R_{l,j}(k,r)R_i(r)r^3 dr, \tag{5}$$

where J_n and K_n are the Bessel functions of the different type, l, j are the orbital and total momenta, R_i $R_{l,j}$ are the cluster wave functions for the ground state (the binding energy $E_b^{exp.} = 2.47$ MeV) and for continuum. In the integrals $I_{2,j} = I_2$ a small difference of the $D_{3/2}$ and $D_{5/2}$ states is neglected. Without final state interaction the radial functions $R_{l,j}(k,r)$ transform to spherical Bessel functions $j_l(kr)$. In the expression (4) Z is the number of protons in the target nucleus, v is the velocity of ^{7}Li, the coefficient $c_d = (Z_1\beta_1 - Z_2\beta_2)^2$ ($\beta_{1(2)} = m_{2(1)}/(m_1+m_2)$, m_i are masses of clusters) defines the dipole moment of two-cluster nucleus, additional notations are $\gamma = (1-(v/c)^2)^{-1/2}$, $\xi = (\omega R)/(\gamma v)$, $\omega = E_b + (\hbar k)^2/(2\mu_{\alpha t})$. The average values $\bar{R}$=5.0 fm, $\bar{Z}$=7 (CNO) and $\bar{R}$=8.1 fm. $\bar{Z}$=41 (AgBr) were accepted. The calculated Q-dependence of cross section covering the very narrow interval Q$\leq$ 50 MeV/c with the maximum at Q$\simeq$3.5 MeV/c is shown in Fig.1 by the curve C. For the emulsion (58%CNO and 42%AgBr) the calculated total cross section is 4 mb. The interval Q$\leq$ 30 MeV/c includes only 6 events. This fact gives a rought estimate of cross section for the target (Ag,Br) σ_C=6/(5.4837·10^{4}cm·2.06·10^{22}cm^{-3})=5$\pm$2 mb. This value is somewhat less than calculated one (9.1 mb) for these nuclei. The small values of σ_C and the corresponding Q-interval show the need to consider the nuclear frgmentation.

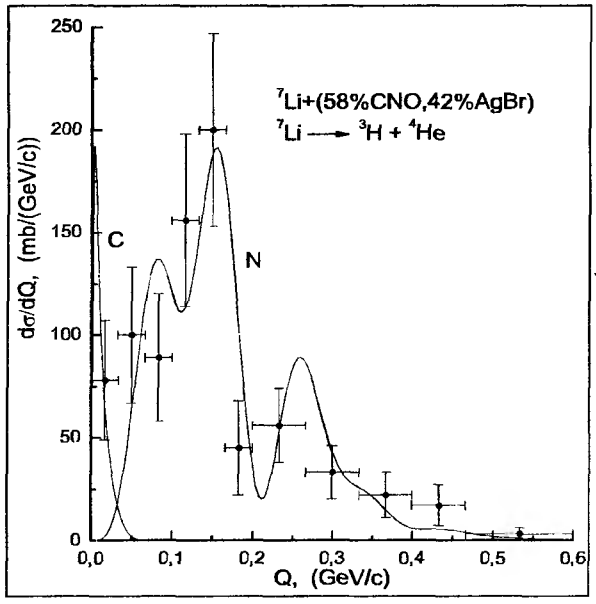

Figure 1: Experimental data and theoretical curves showing the cross sections of the Coulomb (C) and nuclear diffractional (N) disintegration of ^{7}Li.

Within the Akhieser-Sitenko formalism [10] developed recently [18] in application to the diffractional scattering of two-cluster nuclei the cross section is determined by matrix elements of the combination of the profile functions $\omega(b)$

$$\omega_\alpha(b_\alpha) + \omega_t(b_t) - \omega_\alpha(b_\alpha)\omega_t(b_t), \qquad \omega_i(b) = 1 - exp(i\chi_i(b)). \tag{6}$$

The phase shift functions χ_i for the collision of nuclei with the mass numbers A_1 and A_2 were calculated in the first order optical limit of the Glauber-Sitenko theory using the folding integral for nuclear form factors $S_{A_i}(q)$ and NN-amplitude [26]

$$i\chi(b) = -\frac{A_1 A_2 \sigma_N}{8\pi^2}(1 - i\rho)\int exp(-i\mathbf{qb} - a_N q^2/2)K(q)S_{A_1}S_{A_2}d^2q. \tag{7}$$

The form factors of (α, t)-clusters and nuclei C,N,O were calculated in the oscillator shell model with the center-of-mass correlation function $K(q)$. The Fermi single nucleon density distribution was used for heavy nuclei Ag,Br. Parameters of the oscillator model and Fermi distribution were inferred by a standard way [27,28] from the root mean square nuclear radii values [29]: $\bar{r}_t$=1.7 fm, $\bar{r}_\alpha$=1.67 fm, $\bar{r}_{CNO}$=2.54 fm, $\bar{r}_{Br}$= 5.1 fm, $\bar{r}_{Ag}$=5.62 fm. Accepted values of NN-interaction parameters are σ_N=43.0 mb, ρ=-0.35, a_N=0.242 fm^2 [28]. Due to a small difference of ω_α and ω_t for a choosed target nucleus we use a half sum of them as the equal value of $\omega(b)$ for (α,t)-clusters. The real and imaginary parts of $\omega(b)$ are displayed in Fig.2 for light and heavy nuclei. In Eq. (6) two first terms corresponding to the impulse approximation gives the main contribution to the cross section

$$\frac{d\sigma_N}{dQ} = A\Big(1 + I_0(Q) - \frac{3}{2}\sum_{lj,L}(I_L^{lj}(\beta_1 Q) + (-1)^L I_L^{lj}(\beta_2 Q))^2 \hat{l}\hat{j}(10l0|L0)^2 \begin{Bmatrix} j & l & 1/2 \\ 1 & 3/2 & L \end{Bmatrix}^2\Big) \tag{8}$$

where

$$\frac{A}{4\pi Q} = \left|\int_0^\infty \omega(b)J_0(Qb)bdb\right|^2, \; I_0(q) = \int_0^\infty j_0(qr)R_i^2 r^2 dr, \; I_L^{lj}(q) = \int_0^\infty j_L(qr)R_{lj}R_i r^2 dr. \tag{9}$$

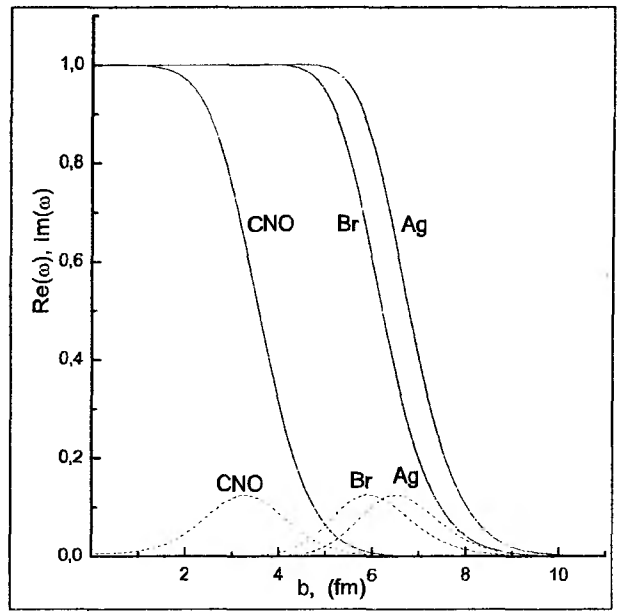

Figure 2: The real parts Re(ω) (full lines) and imaginary parts Im(ω) (dotted lines) of profile functions.

Eq. (8) was derived using a complete set of states of two-cluster Hamiltonian to avoid the integration in matrix elements over the relative momentum in continuum and to reduce them to matrix elements over all bound (l, j)-states. In Eq. (8) the factors following after term $\hat{l}\hat{j} = (2l+1)(2j+1)$ are the Clebsh-Gordon coefficient and 6j-simbol squared. Alternating contribution to cross section from the third term in Eq. (6) does not exceed 1–2%.

Cross sections $d\sigma_N/dQ$ for the light (C,N,O; σ_N=31.6 mb) and heavy target-nuclei (Br, σ_N=50.6 mb; Ag, σ_N=56.0 mb) fall within the interval Q$\leq$ 0.4 GeV/c and have the oscillative form with intervals along Q which are close to zeros of $J_1(QR)$ where R is of the order of the profile function Re($\omega(b)$) dimensions. The imaginary parts Im(ω) give small contributions which are evident in the minimums of cross sections. It is of interest to note that the cross section is proportional to $J_1^2(QR)$ in the black nucleus model having a sharp surface. However we found that this strong absorption model does not describe data since it predicts many oscillations in a very wide diffractional cone ($Q \leq 2$ GeV/c) and gives too large value of cross section of the order 250 mb. In calculations presented in this work we use the realistic form of profile functions corresponding to diffuse shape of the nuclear surface. It predicts two maximums in the cross section for nuclei C,N,O at $Q \simeq 120$ 280 MeV/c with the ratio of intensities 1:0.34 and four maximums for heavy nuclei Br,Ag at $Q \simeq 70$. 170, 270 360 MeV/c with the approximate ratio 0.7:1.0:0.5:0.15. The differnt oscillating structure of cross sections is explained by the large difference of nuclear radii and profile functions. This pattern of the inelastic coherent diffraction differs from the elastic one where zero angle peak is dominating.

The resulting curve of the cross section (N) taking account of the nuclear content of emulsion and experimental data are shown in Fig.1. The nuclear and electromagneic theoretical cross sections were normalized by the coefficient k=0.7 to the total experimental cross section. Fig.1 shows that the observed Q-dependence of the cross section is explained by the superposition of two diffractional patterns of oscillating forms arising from the ^{7}Li interaction with light and heavy nuclei of nuclear emulsion. The Q-variable regions responsible for the Coulomb and nuclear mechanisms are well separated and their interference, disregarded here, is expected in the narrow interval $0 \leq Q \leq 50$ MeV/c. It should be noted that the

total cross section calculated $\sigma_N+\sigma_C$=44.7 mb is somewhat larger than the experimental one 31±4 mb. It seems plausible that this difference is connected with the plane wave impulse approximation used for the inital and final nuclear systems [4]. It can not be excluded that the extent of (α,t)-clusterization in ^{7}Li is less than unity.

Presented results show that the two-cluster projectile ^{7}Li may be used like deuteron as a probe nucleus to check the theories of electromagnetic and diffractional disintegrations and to extract the information on surface layers of nuclei. It is of interest to investigate the diffractional patterns of the coherent dissociation of ^{7}Li to the (α,t)-channel on pure target nuclei in a wide range of mass numbers by the counter technique with the higher statistics.

Authors are deeply grateful to A.V. Pisetskaya and L.N. Shesterkina for the great work on a search of events and microscopic measurements in emulsion. We are very indebted to Prof. V.G. Neudatchin for the valuable information about investigations of the NPI MSU theoretical group on the cluster structure of light nuclei and fruitful discussion of results. The work was supported by the Russian Foundation for Basic Research, grant 07-02-00871-a.

References

[1] L.D. Landau, Phys. Zs. Sovietun. **1**, 88 (1932).

[2] R. Serber, Phys. Rev. **72**, 1008 (1947).

[3] K. Alder and A. Winther, Electromagnetic Excitation (North-Holland, Amsterdam, 1975).

[4] A.G. Sitenko, Theory of Nuclear Reactions (World Scientific,Singapore, 1990).

[5] C.A. Bertulani and G. Baur, Phys. Rep. **163**, 299 (1988).

[6] L.S. Azhgirey and N.P. Yudin, Fiz. Elem. Chastits. At. Yadra **37**, 1012 (2006).

[7] The BECQUEREL Project, http://becquerel.jinr.ru/.

[8] .I. Adamovich, Yu.A. Alexandrov, S.G. Gerassimov *et al.*, J. Phys. G **30**, 1479 (2004).

[9] A.I. Akhieser, A.G. Sitenko, Sci. Papers. of Kharkov Univ. **64**, 9, (1955).

[10] A.I. Akhieser and A.G. Sitenko, Phys. Rev. **106**, 1236, (1957).

[11] R. Glauber, Phys. Rev. **99**, 1515 (1955).

[12] I.Ya. Pomeranchuk, E.L. Feinberg, Dokl. Akad. Nauk SSSR **93**, 439, (1953); E.L. Feinberg, Zh. Ekxp. Teor. Fiz. **29**, 115, (1955); E.L. Feinberg, I.Ya. Pomeranchuk, Suppl. Nuovo Cimento **3**, 652, (1956).

[13] V.V. Belaga, A.A. Bendjaza, V.V. Rusakova *et al.*, Yad. Phys. **58**, 2014, (1993).

[14] V.V. Belaga, A.I. Bondarenko, T. Kanarek *et al.*, Yad. Phys. **59**, 869, (1996).

[15] H. Okamura *et al.*, Phys. Rev. C, **58**, 2180 (1998).

[16] N. Heide, D.K. Srivastava and H. Rebel, Phys. Rev. Lett., **63**, 601, (1985).

[17] C.A. Bertulani and G. Baur, Nucl. Phys., **A442**, 739, (1985).

[18] V.V. Davidovsky, M.V. Evlanov, V.K. Tartakosky, Yad. Fiz. **69**, 252, (2006) and references therein.

[19] V.G. Neudatchin, Yu.F. Smirnov, Modern problems of optics and nuclear physics, (Kiev, p.225, 1974).

[20] V.I. Kukulin, V.G. Neudatchin, Yu.F. Smirnov, Fiz. Elem. Chastits. At. Yadra **10**, 1236, (1979).

[21] V.G. Neudatchin, Yu.F. Smirnov, Nucleon Associations in Light Nuclei (Nauka, Moscow, 1969).

[22] S.B. Dubovichenko, Properties of light nuclei in the potential cluster model (Denker, Almaty, 2004).

[23] N.A. Burkova, K.A. Zhaksybekova, M.A. Zhusupov, Fiz. Elem. Chastits. At. Yadra **36**, 821, (2005).

[24] S.B. Dubovichenko, M.A. Zhusupov, Izv. Akad. Nauk KazSSR, ser. fiz.-mat. 4, 44, (1983).

[25] A. Winther and K. Alder, Nucl. Phys. **A319**, 518, (1979).

[26] V. Franco and A. Tekou, Phys. Rev. C **16**, 658, (1977).

[27] L.J.Tassie and F.C. Barker, Phys. Rev. **111**, 940, (1958).

[28] V. Franco, Phys. Rev. **6**, 748, (1972).

[29] R.C. Barrett and D.F. Jackson, Nuclear Sizes and Structure, 1977.

PHYSICS OF ELECTROMAGNETIC INTERACTIONS AT ELECTRON ACCELERATOR OF LEBEDEV PHYSICAL INSTITUTE: CURRENT STATUS AND PROSPECTS

E.G. Bessonov[1], V.N. Fetisov[1], L.V. Filkov[1], V.G. Kurakin[1], A.I. Lebedev[1], A.I. L'vov[1], E.I. Malinovsky[1], V.A. Petrunkin[1], G.A. Sokol[1], V.G. Nedorezov[2], B.S. Ishkhanov[3], E.M. Leikin[3], V.I. Shvedunov[3], A.I. Malakhov[4]

[1]Lebedev Physical Institute, Moscow; [2]Institute for Nuclear Research, Moscow; [3]Skobeltsin Institute for Nuclear Physics, MSU, Moscow; [4]Joint Institute for Nuclear Research, Dubna

1. First electron synchrotrons (S3, S25 and S60) at Lebedev Physical Institute have been constructed in 1947-1959 under leadership of V.I. Veksler soon after his remarkable discovery of the principle of phase stability (1944). These machines have extensively been used for studying nuclear photoreactions at E_γ up to ~250 MeV and for obtaining pioneer data on photo-disintegration of deuteron and helium-4, meson photoproduction and proton Compton scattering. In the middle of 1970's, a newer LPI electron synchrotron S25R (or synchrotron "Pakhra") with the maximum energy $E_{e\,max}$=1.2 GeV was built in Troitsk, near Moscow. Among others, pioneer data on pion Compton scattering and eta-mesic nucleus formation have been obtained at this machine.

Currently S25R continues to work and it provides possibilities for doing further experiments on eta-meson physics with a high-energy bremsstrahlung photon beam up to ~850 MeV and those on low-energy pion photoproduction with an extracted electron beam (up to ~600 MeV) and a photon tagging system. Also, works on condensed state physics with synchrotron radiation (in the vacuum ultraviolet and soft Roentgen range) and a 7-11 MeV electron beam of the microtron injector are carried out. A quasi-storage mode of the synchrotron operation was tested as a regime for producing a smoother synchrotron radiation, with a duty factor ~1. Other opportunities of the accelerator complex include another microtron with E_e=7-35 MeV used in particular as a driver for Free Electron Laser in the Theraherz range, and a new 55-MeV microtron which has to start working soon for applied studies of photonuclear reactions.

Considering an option to build in Troitsk, using an existing infrastructure, a new electron accelerator like a CW superconducting-RF recirculator with E_e ~ 2-3 GeV and the energy-beam recovering [1], we briefly discuss here some physical goals for such a machine.

2. Till now there are many open problems in the contemporary physics of strong interactions. Among them:

- a theory of strong interactions at low energies (nonperturbative QCD) is not sufficiently developed for making first-principle calculations of the main hadron properties and reaction cross sections. Confinement of color is not proven.
- efficient models replacing the strict theory are also not fully satisfactory. Even effective degrees of freedom determining hadron properties at medium energies are not fully established. Valence quarks and gluons, diquarks, gluon tubes are often used in phenomenology; Goldstone bosons jointly with low-lying vector and axial mesons and, in the baryon sector, with low-lying baryon resonances (e.g., the Delta) are also often considered as appropriate degrees of freedom. The very existence of many different models demonstrates that there are difficulties and ambiguities.
- many baryon states predicted by the quark model are not yet found or identified. Structure of mesons, especially that of the scalar mesons, is not understood; in particular, their mixing angles and wave functions ($q\bar{q}$, $q\bar{q}q\bar{q}$) are not firmly established.

- exotic states such as $qqq\bar{q}$, $qqqq\bar{q}$, $q\bar{q}g$, gg, dibaryons, etc., which have to exist in QCD are not yet found; instead, an unexpected (within quark models) rich family of meson resonances is discovered in the annihilation channel of $N\bar{N}$ ...

In order to solve the mentioned and many not mentioned here problems, a further development of both the theory and experiment is clearly needed. New experimental data may help to make new guesses and to formulate new ideas. Studying electromagnetic processes with hadrons is a possible and attractive way to obtain such data on the structure of hadrons that has its own advantages as discussed below.

3. It is worth to say that ion and proton beams as well as electron and secondary particle beams (inverse Compton photons, bremsstrahlung) compliment each other in nuclear and particle physics experiments with fixed targets. Nowadays, hadron or nuclear beams are used to produce and investigate high-density and high-temperature nuclear media – hadron and quark-gluon plasma in equilibrium and non-equilibrium states. In these reactions, the primary nuclear object is destroyed, and a new knowledge concerning strong interaction is extracted from the behavior of the produced substance. On the other side, photon as well as electron beams are very suitable for precise studying particle structures and composite constitutions because:

- of a very small size of the probe ($<10^{-16}$ cm) that is significantly less than the nucleon radius;
- electrons and photons interact with other objects electromagnetically, and the form of this interaction is well known from Quantum Electrodynamics and alike;
- perturbation of the object under investigation is weak and for this reason the primary beam does not fully destroy the object.

4. There are many electromagnetic processes in which various aspects of the structure of hadrons and nuclei can be investigated. They include electron scattering off nucleons and nuclei (including deep-inelastic reactions), photo- and electroproduction of mesons, real and virtual Compton scattering. Structure functions, generalized parton distributions, resonance excitation amplitudes, transition formfactors, ordinary and generalized polarizabilities, P and T-odd effects, modification of hadron properties in the nuclear matter, chiral symmetry and its restoration at high densities can be learnt in these studies.

Such a plenty of processes and observables provides a big space for their parallel studies at different accelerators in different laboratories. Undoubtedly, many of these problems will remain
open and newer ones will also arise to the time when the future machine is ready.

Based on our tradition and previous experience, we can plan to continue a research in the meson-nuclear physics, electromagnetic interaction being the basis for such a research. Nowadays there are many evidences of the influence of nuclear media on meson properties [2], and this influence seems to be a good subject for a further research directed to clarification of many problems in the physics of strong interaction. A direct proof of changing the meson mass in nuclear media requires specific conditions to be fulfilled [3]. First, specific types of mesons produced by an incident particle in the nucleus have to be chosen. For such experiments we suggest to select mesons with a narrow width and a pronounced decay into two photons or two charged particles. In such a case, double coincidence method provides a confident detection of the decay products during measurements. Second, the recoilless kinematics has to be selected. In other words, the velocity of the meson produced by the incident particle must be close to zero in order to guarantee its decay inside the nucleus. In contrast to meson production in interactions of the incident beam with free nucleons, the condition of recoilless kinematics can be satisfied in nucleus approximately only due to the nucleon Fermi motion inside the nucleus. Under such

kinematical conditions, decay particles are distributed uniformly, and spectrometer position might be chosen from the lowest background considerations. At last, a target material has to contain hydrogen atom(s) besides the main element. This allows one to have measurements of the meson mass in the nucleus media in comparison with that of a free meson. For many reasons the meson group η, η', ω, and φ is most suitable for this purpose provided cw electron as well as photon beams up to 2 GeV are available.

Among fresh and perspective lines of research one can also mention studies of meson-nucleon interaction in the nuclear matter using some kind of tagging. For example, using an ordinary tagged photon beam and detecting a knocked-out proton one can produce and identify in the reaction $\gamma p \rightarrow \eta p$ inside a nucleus a η-meson with a controlled energy-momentum. Then one can identify and study interactions of such tagged mesons with other nucleons in the nucleus, like the reaction $\eta N \rightarrow K\Sigma$ which is of a big interest for understanding the nature of some baryon resonances and for developing dynamical chiral models of the meson-baryon interaction.

Another perspective line is studies of quasi-bound states of mesons in nuclei, including the η, η', ω, ϕ mesons.

For investigation of many different reactions and channels, with tagging, with detecting final particles in coincidence, high-intensity cw accelerators in a few-GeV range with fixed targets are very suitable. Constructing polarized beams and targets is highly desirable. Detectors with the 4π-geometry and data acquisition in wide kinematical ranges is also a necessity.

5. A conceptual design of a cw accelerator in the energy range of a few GeV and the electron current up to hundreds mA was discussed in the Lebedev Physical Institute and the Soviet Academy of Science since the beginning of 1980's. Our contemporary vision of the project including the use of superconducting rf cavities is described in some detail in [1].

Of course, many of the physical problems outlined above can be solved at existing accelerators (in Mainz, Bonn, Jefferson lab, etc.). Participance in joint researches in such centers is at the moment the main way Russian scientists can do (and do!) fundamental nuclear and particle physics at the appropriate level. Nevertheless, we consider the building up a new cw electron accelerator vital for several reasons. First of all, this allows to increase scientific activity in many fields of physics (including applied physics and technology with a powefull Light Source), to bring the research to a higher scientific level, and to enhance appropriate technologies. The latter is important because the related scientific environment did not renew for a long period. Second, this would help us to recruit students at all steps of the project realization. At last, this will stimulate a development of the rf superconducting technology that does not actually exist in Russia today.

[1] E.G. Bessonov et al., Superconducting rf electron recirculator for nuclear and particle physics research as upgrade of the accelerator complex of Lebedev Physical Institute in Troitsk, contribution to EMIN-2009.

[2] M. Kotulla, nucl-ex/0609012;
D. Trnk et al., Phys. Rev. Lett. 94, 192303 (2005);
R. Nasseripour et al., nucl-ex/07072324;
V. Metag, nucl-ex/0711.4709;
S. Schadmand, nucl-ex/0709.2903;
T. Mertens et al., nucl-ex/0810.2678.

[3] G.A. Sokol, E.M. Leikin, nucl-ex/09021408.

FEYNMAN PROPAGATOR FOR PARTICLE IN MAGNETIC FIELD

Yu. I. Sorokin

Institute for Nuclear Research RAS, 117312 Moscow, Russia.

Feynman ([1], P.78) had got propagator for particle with mass m and charge $e = Ze_0$ in constant homogeneous magnetic field B, z-axis direct:

$$G(x,y,z,T,x_0,y_0,z_0,0) = (\frac{m}{2\pi i\hbar T})^{3/2}\frac{\omega T}{2\sin(\omega T/2)}\exp(iS/\hbar), \qquad (1)$$

$$S = \frac{m}{2}\{\frac{(z-z_0)^2}{T} + \frac{\omega}{2}ctg(\frac{\omega T}{2})[(x-x_0)^2+(y-y_0)^2] + \omega(yx_0 - xy_0)\}. \qquad (2)$$

$T = t - t_0 > 0$, $\omega = (eB)/(mc)$ - cyclotron frequency.

Warning: the formula (3.64), [1], P. 78, hold excess ω before embrace. For correcting had been taken path integrals once more.

Two factors may get from the propagator (1,2): G_B and G_z - for circular motion in plane xy and free motion along z-axis.

If in plane xy particle moved at first with velocity v along x-axis, and its spatial indefiniteness was described with Gauss distribution with dispersion Δ and centre in $\bar{x}, \bar{y}$, it is necessary, in according to [2], to bring in initial wave function data about velocity, presence magnetic field and angular momentum relatively reference point.

As result square root from initial Gaussian function got phase:

$$\Psi_0(x_0,y_0) =$$

$$= \frac{1}{\sqrt{2\pi}\Delta}\exp[-\frac{(x_0-\bar{x})^2+(y_0-\bar{y})^2}{4\Delta^2} + \frac{imvx_0}{\hbar} + \frac{im\omega}{2\hbar}(y_0\bar{x} - x_0\bar{y})],$$

that, in according to [1], [2], give wave function:

$$\Psi(x,y,T) = \int G_B(x,y,T,x_0,y_0,0)\Psi_0(x_0,y_0)dx_0dy_0 =$$

$$\int \exp\{\frac{im\omega}{2\hbar}[ctg(\frac{\omega T}{2})\frac{(x-x_0)^2+(y-y_0)^2}{2} + (yx_0 - xy_0)]\}\frac{m\omega\Psi_0(x_0,y_0)dx_0dy_0}{4\pi i\hbar\sin(\omega T/2)} =$$

$$= \frac{m\omega\Delta}{\sqrt{2\pi}(i\hbar\sin\frac{\omega T}{2} + m\omega\Delta^2\cos\frac{\omega T}{2})}\cdot$$

$$\cdot\exp(-\frac{[x-\bar{x}-2\rho\sin\frac{\omega T}{2}\cos\frac{\omega T}{2}]^2 + [y-\bar{y}+2\rho\sin^2\frac{\omega T}{2}]^2}{4\Delta^2\cos^2\frac{\omega T}{2} + 4i\hbar\sin\frac{\omega T}{2}\cos\frac{\omega T}{2}/m\omega} +$$

$$+imvx + \frac{im\omega}{4\hbar}\{2(\bar{x}y - \bar{y}x) - [(x-\hat{x})^2 + (y-\bar{y}+2\rho)^2]tg\frac{\omega T}{2}\}). \qquad (3)$$

It is visible, that centre of distribution move along circle of radius $\rho = v/\omega$ with circular frequency $\omega = eB/mc$. Result wave function (3) may be use, for

example, description move particle in cyclotron and illustration Hall effect, conform to Quantum mechanics, for example, instead of [3], P. 263. Warning: propagator (1,2) and wave function (3) accord to Hamiltonian for exercise 11.1, [3], P. 274, and does not accord Hamiltonians (11.1),P.255, and (11.66), P.273. [1] had not written Hamiltonian.

At $\omega T \ll 1$ wave function (3) become wave function free move on plane xy, along x-axis with velocity v.

Free move along z-axis particle with beginning velocity v_z describe z - component of wave function:

$$\Psi(z,T) = \sqrt{\frac{\Delta/\sqrt{2\pi}}{\frac{i\hbar T}{2m}+\Delta^2}}\exp[-\frac{(z-v_zT)^2}{4(\Delta^2+\frac{i\hbar T}{2m})}]\cdot\exp[\frac{i}{\hbar}(mv_zz-\frac{mv_z^2T}{2})]. \quad (4)$$

Physical senseis present density function:

$$\Phi(z,T) = \{2\pi[(\frac{\hbar T}{2m\Delta})^2+\Delta^2]\}^{-1/2}\exp\{-\frac{(z-v_zT)^2}{2[\Delta^2+(\hbar T)^2/(2m\Delta)^2]}\}. \quad (5)$$

Three-dimensional wave function, corresponding to propagator (1,2), is formed by product (3) and (4). Physical sense is present density function $\Phi(z,T)$, (5), multiplied $\Phi(x,y,T)$:

$$\Phi(x,y,T) = \mid \Psi(x,y,T) \mid^2 = [2\pi(\Delta^2\cos^2\frac{\omega T}{2}+\frac{\hbar^2\sin^2\frac{\omega T}{2}}{\Delta^2m^2\omega^2})]^{-1}\cdot$$

$$\cdot\exp\{-\frac{[x-\bar{x}-2\rho\sin\frac{\omega T}{2}\cos\frac{\omega T}{2}]^2+[y-\bar{y}+2\rho\sin^2\frac{\omega T}{2}]^2}{2\Delta^2\cos^2\frac{\omega T}{2}+2(\hbar\sin\frac{\omega T}{2})^2/(m\omega\Delta)^2}\}$$

It is visible, that after half-turn distribution focus with dispersion $\sigma = \hbar/(m\omega\Delta)) = \hbar c/(Ze_0B\Delta)$, smoothing break of a curve in response function of mass spectrometer [4], P. 105.

Absolute focus is so much the better (its dispersion σ is smaller), then large was beginning dispersion. For example, L-electrons internal conversion focus better, then K-electrons, K-electrons internal conversion focus better, then β-particles, and thermoemission electrons focus more better.

Moreover, so long as cyclotron frequency ω inversely mass, dispersion of focus does not depend on mass. For example, dispersion of semicircular focus for proton and positron may be equal. In other side, so far as cyclotron frequency depend on charge, focus actinide fission fragments with $Z = 40$ may be better in twenty time, then α-particles.

This focus is result Feynman amplitude interference from different path.

Relative focus $\delta = \sigma/\rho = \hbar/(mv\Delta)$ does not depend on magnitude magnetic field. Comparison with experimental relative resolution α-particles from Bi^{212} (kinetic energy $W = mv^2/2 \approx 6MeV$, $\delta < 0.003$ [4], P. 183), give uncertainty initial location of particle:

$$\Delta > \hbar/mv\delta = \frac{\hbar}{\delta\sqrt{2Wm}} = \frac{\hbar c}{\delta\sqrt{2Wmc^2}} \approx 3 \cdot 10^{-11} cm,$$

that almost two order of magnitude large nuclear dimension and correspond exterior size Coulomb potential barrier at level

$$\frac{Z_\alpha(Z_{Bi}-2)e^2}{\Delta} = \frac{Z_\alpha(Z_{Bi}-2)e_0^2\delta\sqrt{2Wmc^2}}{\hbar c} < 0.8MeV.$$

Last result may be utility for understanding properties of high-spin state, giant resonance [5] and photoproton reaction [6].

[1] Р.Фейнман, А.Хибс. *Квантовая механика и интегралы по траекториям.* (Мир, Москва, 1968), пер. с англ. *Quantum Mechanics and Path Integrals* by R.P.Feynman, A.R.Hibbs. (McCraw Hill Book Company. New York,1965).

[2] Ю.И.Сорокин. Вестник РУДН (Bulletin of Peoples' Friendship University of Russia), сер. Физика. $N^0$1(13), 113(2005).

[3] Ч. Киттель. *Квантовая теория твердых тел.* (Наука, Москва, 1967), пер с англ. *Quantum Theory of Solids.* by C. Kittel. (John Wiley and Sons, Inc. New York - London. 1963)

[4] *Альфа-, бета- и гамма-спектроскопия.* Под редакцией К.Зигбана, вып.1. (Атомиздат, Москва, 1969) пер с англ. *Alpha-, Beta- and Gamma-ray spektroscopy.* Volum 1. Edited by Kai Siegbahn. (North-Holland publishing company. Amsterdam. 1965)

[5] Ю.И.Сорокин, Б.А.Юрьев. ЯФ(Sov.J.Nucl.Phys.), Т. 20 , 233(1974)

[6] Ю.И.Сорокин, В.А.Хрущёв, Б.А.Юрьев. ЯФ, Т. 14 , 1118-1122 (1971)

GIANT RESONANCES ON EXCITED STATES OF NUCLEI (REVIEW)

B.S. Dolbilkin
Institute for Nuclear Research RAS, Moscow, Russia

1. Introduction

Giant Dipole Resonances (GDR) on ground nuclear states of cold nuclei, which have represented an excitation of collective vibrations from external oscillating electromagnetic fields, has intensively been studied, after it were discovered, in photonuclear reactions during long time after fifties of the last century. For this time GDR parameters at many nuclei and their systematic were established. However, according Axel-Brink hypothesis, global features of GDR reflect basic foundations of nuclear forces and does not depend from an excitation way. Later such GDR was really experimentally found in different reactions on excited states of nuclei, as single and double pion charge-exchanged ones or reactions with heavy ions [1, 2]. GDR2, excited on known GDR, was firstly measured at (π^+,π^0) and (π^+,π^-) reactions. Later GDR, like GDR2, at hot nuclei were investigated in heavy ion reactions. As in cold nuclei case, multipole giant resonances (MGR) were found in hot ones. Their parameters, such as the Sum Rules, resonance energies, although with bigger uncertainties, are not strongly different from GDR in cold nuclei, but width for spherical nuclei in cold ones (~ 4 MeV) is increased up to ~ 10-12 MeV at excitations ~ 100 MeV or more. Results of these experiments are described and discussed.

2. Double isovector Giant Dipole Resonances (GDR2) at (π^+,π^0) and (π^+,π^-) reactions

A special case is, when the excited state on which the GDR is built – a giant resonance itself, so called GDR2. It has been experimentally found on ^{93}Nb at single and double pion charge-exchanged reactions, at LAMPF, using pion spectrometer EPICS[2]. The spectrometer detected pions in a kinetic energy range 100-300 MeV with energy resolution ~140 KeV(Fig.1).. Three resonances over extrapolated background after its subtraction are seen at the bottom of the Fig. At a simple model of double charge-exchanged reactions (DCHOR), it has presented as two consecutive single charge-exchanged reactions (SCHOR), which two neutrons are changed on two protons in. Since every process strongly excites GDR and IAS, therefore they well excite GDR2. GDR2 has a width ~ 8 – 10 MeV, ~ 2 times larger, than usual GDR, what is close to theoretical estimates with taking in account two-phonon states. The GDR2 energy is connected with GDR +IAS resonances by a simple equation: $|Q_{GDR}| = 2|Q_{GDR+IAS}| - |Q_{IAS}|$

Experimental energies of GDR2 are in a good agreement with it, which gives additional support for the proper identification of the resonances. The GDR energy for a large interval of mass numbers A is ~ Q = - 25 MeV. The GDR2 one is equal two GDR energies:

$$Q_{\pi+\pi-(GDR2)} \approx 2 \times Q_{\pi\pm\pi^0(GDR)} \approx |50| \text{ MeV},$$

what coincides with the GDR2 maximum energy in Fig.1.

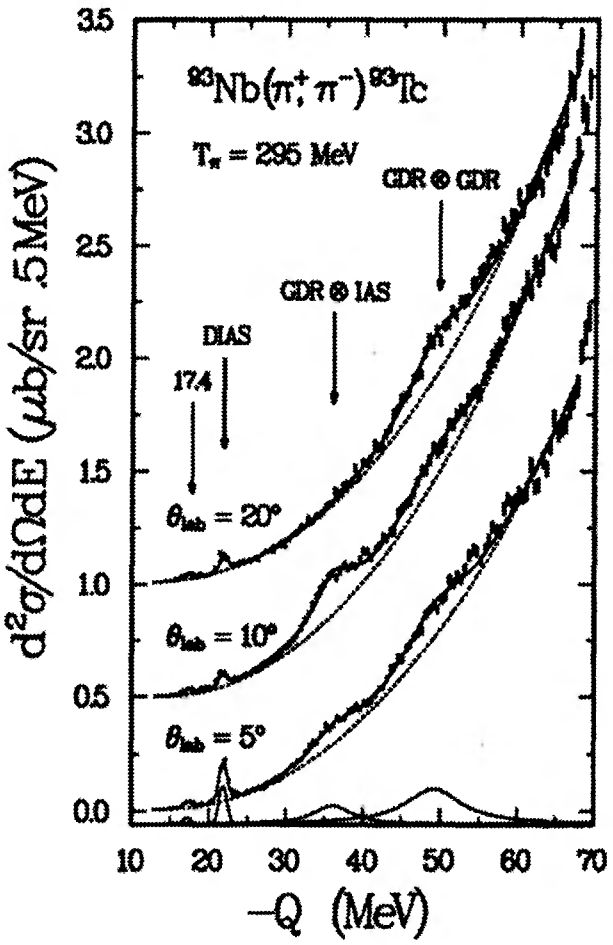

Fig.1. The twice differential cross sections of $^{93}Nb(\pi^+,\pi^-)$ reaction at pion kinetic energy 295 MeV and angles θ_{lab} = 5,10,20 ^{0} in dependence from -Q value. The arrows show energetic positions of three resonances, observed at experiment [3]. Statistical errors are done. The smooth background was fitted by polynoms of 3-rd order.Resonances after background subtraction are shown at the bottom [3]

An additional test for the GDR2 identification has been made by measurement of (π^- , π+) inverse reaction on the ^{40} Ca target with ΔT =+2. They both were measured at the same experimental conditions at θ_{lab} = 5^0 and incoming pion energy 295 MeV. The GDR2 peaks were fitted with a Lorentzian shape of variable width. The fit has given Γ (GDR2) = 9.0 MeV for both reactions.. The background was fitted by a third-order polynomial function of the Q-value. In the reaction ^{40} Ca(π^+,π^-)GDR2 has maximum at the energy of ~ 52 MeV and practically does not depend from *A*, since the GDR2 resonance energy is reached by adding two E1 vibrational energies and two Coulomb ones to the ground state of target-nucleus. The first energy decreases with *A*, the Coulomb energy increases. So two effects practically cancel each other [3].

GDR2 and GDR1, built on the isobaric analog state, have different angular distributions. GDR1 shows a dipole behavior, whereas GDR2 has a quadrupole distribution. This resonance is absent on ^{40}Ca (and other self-conjugate nuclei), because no IAS is exist on a $T = 0$ nuclei. A good agreement of experimental results and theoretical calculations is observed, which supports, that GDR2, built on the ground state GDR, was really found.

3. Giant resonances-GDR2,GDR,GQR in reactions with heavy ions

Soon after a discovery GDR2 in pion charge-exchanged reactions [2,3], they were also found in reactions with heavy ions at few experiments, including LAND and TAPS collaborations in GSI [5,6] (Darmstadt, Germany) .

Identical GR, built on top each other, might be understood as an existence two or more-phonon oscillator states. In the harmonic approximation their oscillation amplitudes increase as $\sim\sqrt{n}$ and they are distinct from single GR in hot nuclei. The questions to multiphonon states are: to which extent the harmonic approximation is valid; nuclei can bear the collective motion of increasing amplitude; in which way follows a dynamics of spreading width, especially, since higher-phonon states are embedded into a continuum of non-resonant states of exponentially increasing level density. The measured cross sections in pion-exchanged reactions were ~ a few mb. For a GDR2 cross sections, which are up to hundreds mb, are expected to result from a two-step excitation mechanism, induced by the strong electromagnetic field, which is due to the high nuclear charge of the interacting ions. Results for ^{136}Xe from LAND collaboration are presented on Fig.2. The aim of the experiments [5,6] was to make an exclusive measurement of electromagnetic excitations in pheripheral heavy ion collisions and the subsequent decay process. The apparatus was sooner made to measure the excitation of projectile.

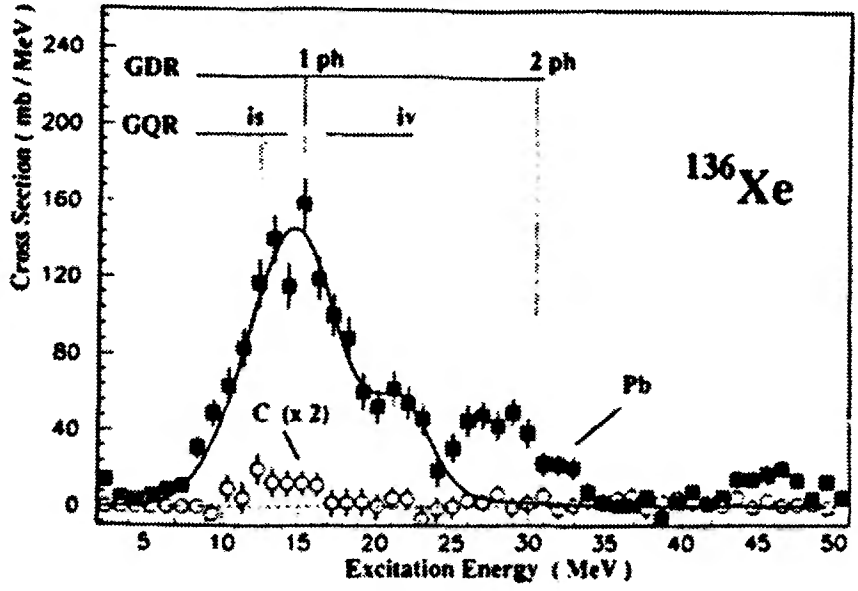

Fig.2. ^{136}Xe projectile excitation on a Pb (squares) and a C (circles) targets. Statistical errors are shown. Spectrum for the C target is multiplied by a factor 2 for better observation. The resonance energies for GDR, GDR2 and the isoscalar/ isovector quadrupole resonance are indicated. The solid curve is the result of calculations for Pb target, including only single-step electromagnetic excitations

In heavy nuclei such as Xe or Pb GDR decay by neutron emission. For such measurements a large area (2 ×2 m^2) detector LAND was made with high neutron efficiency (85-90%) and the overall resolution ~ 2-4 MeV. It has 200 elements and resolved reactions, involving up to 4 neutrons. The projectiles ^{136}Xe had bombarding energy of 700 *A* [5] MeV. TAPS is consisted from 256 BaF_2 detectors and the FOPI detector system, to not detect nuclear interactions.
The GDR2 in ^{136}Xe is seen after of a background subtraction. The quantization of the harmonic oscillator gives for n-phonon resonance energy E_n = nE and E (GDR2) = 2 E (GDR).

The relative width Γ(GDR2)/Γ(GDR) from assumption of an independent decay of the two phonons and a sequential one-phonon excitation was expected to be ~2. The experimental values however, except for *Au*, are nearer to a smaller value, ~ 1.5, although data are not enough for good systematic

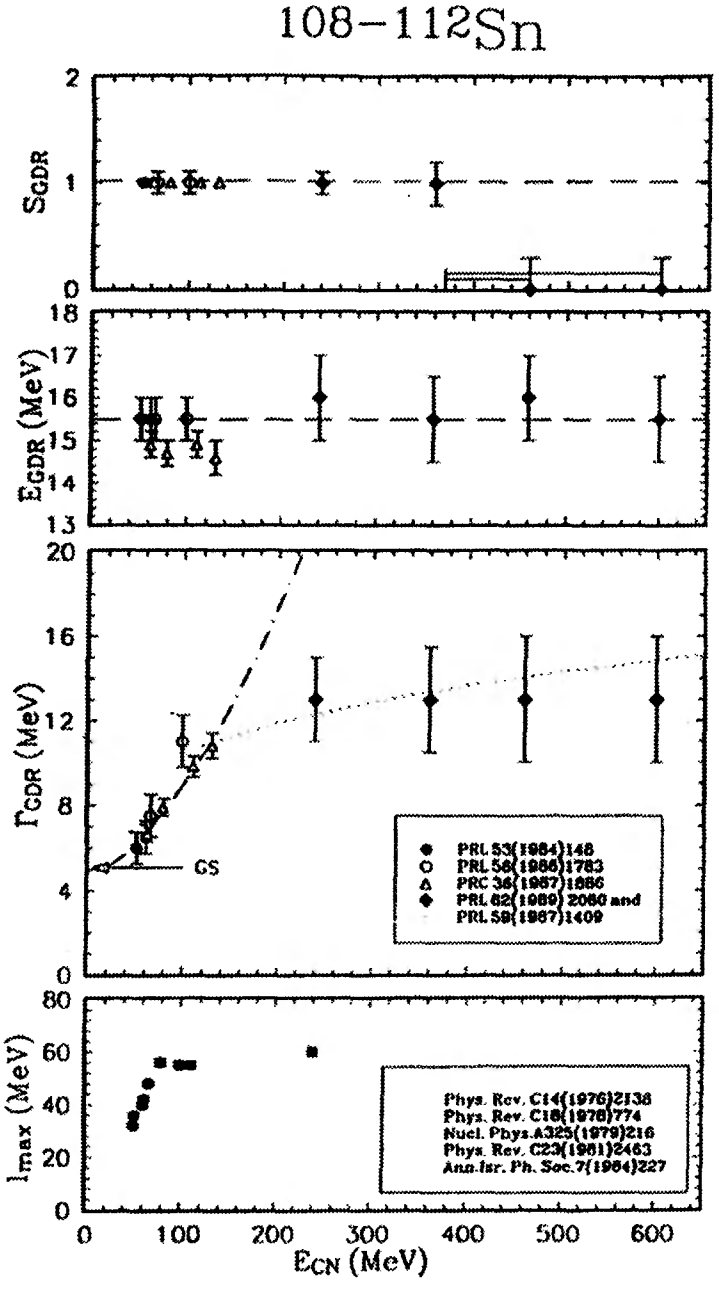

Fig.3.Systematic of the GDR parameter as a function of the excitation energy of the formed compound system (and therefore as a function of the angular momentum) for the $^{108-112}$Sn isotopes [2 and ref. in the Fig.]. From up to down:
- strength in units of the classical sum rule;
- centroid energy,
- width dependence from the excitation energy.
- analogical angular momentum dependence.

After giant resonances (GR) have been found in highly excited nuclei at heavy ion interactions, for last few years many experiments were made [7,8]. An aim was to use the nuclear basic collective modes GR for an exploration of the physics of the atomic nucleus,

when it contains a large amount of thermal energy. The parameters for $^{108-112}$Sn isotopes are shown in Fig.3. In contrast to ground state GDR, properties of GDR in hot nuclei are studied as a function of not only mass, but also excitation energy and rotational angular momentum *J*. From Fig. follows, that the measured GDR strength is strongly reduced at excitation energy higher of 300 MeV, the width is increased from ~ 5 MeV in the ground state GDR, as a function of the excitation energy (angular momentum) of the compound nucleus, to ~ 12 MeV up to ~ 250 MeV and a constant in error limits at energies up to 600 MeV. These peculiarities are probably connected with a mechanism of collective state excitation in highly excited quantum system, consisting from a finite number of nucleons. Here some new physics could be developed. In connection with it, a sensitivity of heavy ions results, studied the GDR and multi-phonon GDR, is desirable to improve, f.ex. by (γ,γ) coincidences experiments.

In summary, in reactions with heavy ions GDR and GDR2 were discovered and for a few *A* investigated. Earlier hot compound nuclei are considered as chaotic systems. Instead it regular collective characteristics were found as in cold nuclei. GDR parameters, except widths, weakly depended from nuclear excitation energy, although their uncertainties are yet too large.

Reference:

1. G.F. Bertsch and R.A.Broglia, Physics today **39,** 8 (1986)
2. J. J. Gaardhoje, Ann.Rev.Nucl. Part. Sci **42**, 483 (1992)
3. S. Mordechai et al., Phys Rev C **43**, 1111 (1991)
4. H. Ward et al, Phys. Rev. Lett. **70**, 3209 (1993)
5. R. Schmidt et al., Phys.Rev. Lett. **70**, 1767 (1993)
6. J. Ritman, Phys.Rev.Lett. **70**, 533 (1993)
7. H.J. Hoffmann et al, Nucl. Phys. A**571**, 301 (1994)
8. T. Baumann et al, Nucl.Phys. A **635**,428 (1998)

PHOTOPROTON REACTION ON ^{9}BE NEAR THRESHOLD

N.A. Burkova, K.A. Zhaksybekova, Ch.Z.Kabytayev
Al-Farabi Kazakh National University, Almaty, Kazakhstan

Investigation of photoproton reaction on ^{9}Be and comparison with experimental data are presented. Explanation of the set of resonances near threshold of ^{9}Be(γ,p)^{8}Li reaction is suggested. Consideration of that process is based on wave functions of multicluster dynamic model with Pauli projection [1, 2] and formalism of photodisintegration.

The process ^{9}Be(γ,p)^{8}Li was investigated in 1962 by experimental group of Clikeman et al [3]. According to these data the integral cross section near threshold has a pronounced resonance structure (Fig. 1).

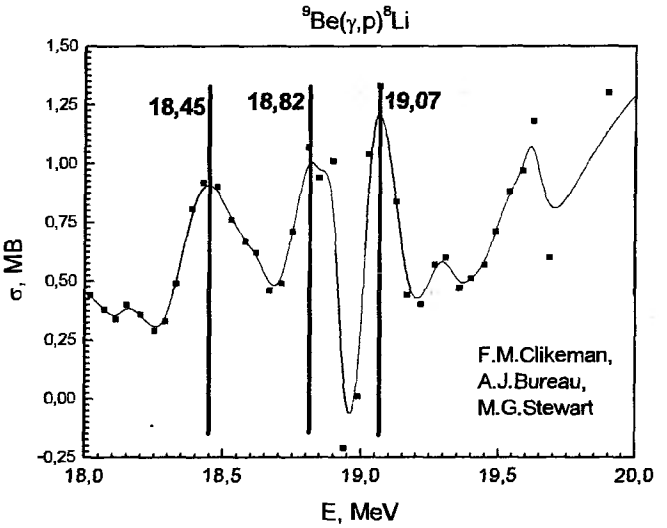

Fig. 1. The integral cross section of ^{9}Be(γ,p)^{8}Li near the threshold [3]
Investigated resonances are marked with the vertical bars

Our objective was to explain that resonance structure by theoretical means, namely we used wave functions which had been constructed in multicluster dynamic model with Pauli projection. Furthermore we made some assumptions about order of scattering waves.

The wave function in the 2αn-model of ^{9}Be nucleus in the ground state with quantum numbers $J_i^\pi, T_i = \frac{3^-}{2}, \frac{1}{2}$ can be written as:

$$\Psi_{J_i M_i}\left(\vec{x},\vec{y},\vec{\xi}\right) = \Phi_{000}\left(\vec{\xi}_1,\vec{\xi}_2,\vec{\xi}_3\right)\Phi_{000}\left(\vec{\xi}_4,\vec{\xi}_5,\vec{\xi}_6\right)\sum_{LM_L,\lambda\mu,lm,m_n} C^{J_i M_i}_{LM_L\,1/2m_n}\, C^{LM_L}_{\lambda\mu\, lm}\times$$
$$\times\Phi_{\lambda\mu lm}(\vec{x},\vec{y})\cdot\chi_{00}^{S_1T_1}(\alpha_1)\chi_{00}^{S_2T_2}(\alpha_2)\chi^{\sigma}_{1/2,m_n}(n)\chi^{\tau}_{1/2,-1/2}(n) \qquad (1)$$

Here $\Phi_{000}(\vec{\xi})$ is internal WF of α-particles, $\chi^{ST}_{M_S M_T}$ are spin-isospin functions of clusters, $\chi^{\sigma}_{1/2,m_n}$, $\chi^{\tau}_{1/2,-1/2}$ are spin-isospin functions of neutron. Finally $\vec{\xi}$ - is the set of internal Jacobi coordinates for α-particles (Fig.2).

Radial function of the clusters relative motion is constructed in the form of the expansion in the Gaussian basis and can be written in the following:

$$\Phi_{\lambda\mu lm}(\vec{x},\vec{y}) = \sum_{ij} C_{ij} e^{-\alpha_i x^2} Y_{\lambda\mu}(\vec{x})\, e^{-\beta_j y^2} Y_{lm}(\vec{y}) \qquad (2)$$

Coefficients C_{ij} and variable parameters $\alpha_i^{(\lambda)}$, $\beta_j^{(l)}$ were extracted from the papers [4, 5].

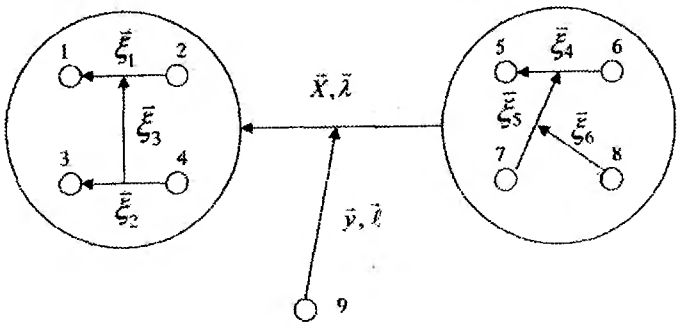

Fig.2. Jacobi coordianates for ^{9}Be in 2α n model

Then we need a "structured" α-particle. Let us construct it for the case of fragmentation on tritium (5,6,7 nucleons) and proton p (nucleon 8):

$$\Phi_{000}(\vec{\xi}_4,\vec{\xi}_5,\vec{\xi}_6)=\Phi_{000}(\vec{\xi}_4,\vec{\xi}_5)\cdot \mathrm{N}_{00}(\xi_{06})\cdot\sum_{n=1}^{N_{\max}} C_n\, e^{-\varpi_n \xi_{56}^2} Y_{00}(\Omega_{\vec{\xi}_6}) \qquad (3)$$

Wave function in cluster channel "Li isotope + c" (where c is light fragment) is factorized on internal wave functions of corresponding lithium isotopes and separable cluster (proton in our case), and can be written in the following:

$$\Psi_{jm_j,s_cm_c}(\vec{\rho},\vec{\eta};\vec{\xi}) \qquad (4)$$

where $\vec{\xi}$ - is coordinates of internal WF of α-particle and tritium (Fig. 2); relative coordinates $\vec{\rho}$ и $\vec{\eta}$ are defined for ^{8}Lip channel in correspondence with Figure 3:

$$\left\{\vec{\rho},\vec{\eta}\right\}=\left\{\vec{R}_{\alpha t},\vec{R}_{\eta_{Lin}}\right\} \qquad (5)$$

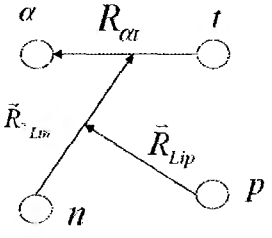

Fig. 3. Set of Jacobi coordinates for 8Lip cluster channel

In order to obtain the wave function of "Li+c" relative motion it is necessary to calculate following integral $\Psi_{J_iM_i}^{jm_j,s_cm_c}(\vec{R})=\left\langle\Psi_{jm_j,s_cm_c}(\vec{\rho},\vec{\eta};\vec{\xi})\middle|\Psi_{J_iM_i}(\vec{x},\vec{y},\vec{\xi})\right\rangle$.

Finally for the wave function of relative motion we obtain:

$$\Psi_{jm_j,s_cm_c}^{3/2M_i}(\vec{R})=\sum_{\substack{\lambda\ell L,\tilde{\lambda}\tilde{\ell}\tilde{L},\tilde{S}\\ sm_s,\kappa m_\kappa}}(-1)^L C_{s_cm_cjm_j}^{sm_s} C_{sm_s\kappa m_\kappa}^{3/2M_i}\prod_{\tilde{S}jsL}\begin{Bmatrix}\tilde{S}\,\tilde{L}\,j\\ s\,s_c\,1/2\end{Bmatrix}\begin{Bmatrix}L1/23/2\\ s\;\kappa\;\tilde{L}\end{Bmatrix}\times$$

$$\times Y_{\kappa m_\kappa}(\Omega_R)\,\mathrm{I}_{\lambda\ell L,\tilde{\lambda}\tilde{\ell}\tilde{L}}^{(\kappa)}(R)$$

According to the paper [3] the ^{9}Be(γ,p)^{8}Li process in low energies E_γ=18-20 MeV has a pronounced resonance structure. Especially we are interested in resonances with energies E_γ ($E_{c.m.}$): 18,44 (1,56), 18,82 (1,93) и 19,07 (2,18) MeV (Fig. 1).

The first our assumption is that resonance structure corresponds to resonances in p-waves (L=1) near the threshold. But we have shown that it is impossible to find a fit between parameters of Woods-Saxon potential and scattering phase.

The second assumption was more successful. Resonance structure corresponds to resonances in d-wave (L=2). The fit between parameters of Woods-Saxon potential and scattering phase of d-wave was successfully found (a=0,4; V_0=124,4; 121,7; 126,2).

Results of our calculations of integral cross-section for ^{9}Be(γ,p)^{8}Li process at energies E_γ=18-20 MeV are shown in Fig. 4:

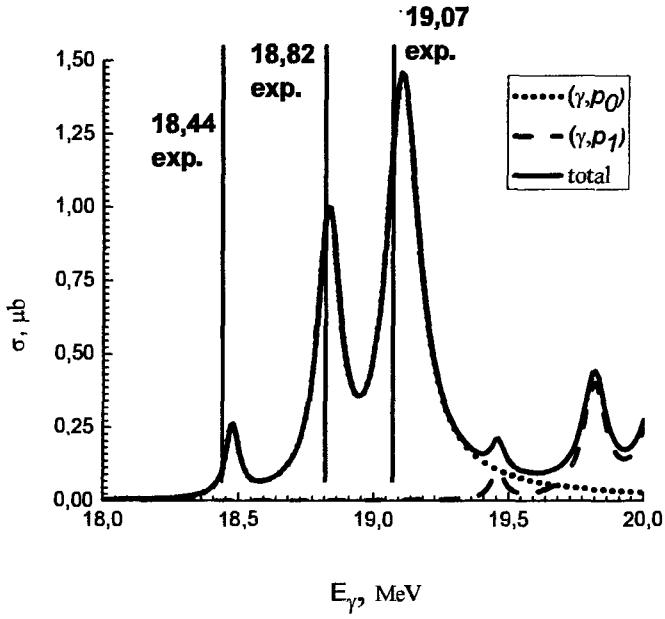

Fig. 4. Calculations of integral cross-section for ^{9}Be(γ,p)^{8}Li process at energies E_γ=18-20 MeV

Vertical black lines correspond to experimental resonance values

Investigation of of ^{9}Be(γ,p)^{8}Li process in the frame of the multicluster dynamical model with Pauli projection allows to conclude: Resonance structure of ^{9}Be(γ,p)^{8}Li process near threshold is caused by resonant d-wave (L=2). E1-transition leads to resonant d-wave and process of photoproton emission ^{9}Be(γ,p)^{8}Li in the region of low energies caused by combination of two transitions: in the first one (γ, p_0) ^{8}Li nucleus is in the ground state, in the second one ^{8}Li nucleus is in the first excited state.

Further research of ^{9}Be(γ,p)^{8}Li can be important due to huge applications of Beryllium as a strategic material.

[1] V. T. Voronchev, V. I. Kukulin, V. N. Pomerantsev, Kh. D. Razikov, and G. Ryzhikh, "Study of the Structure and Properties of Nuclei with A = 9 (9Be–9B) in Terms of Multicluster Dynamic Model 2α + N," Yad. Fiz. 57, 1964–1980 (1994) [Phys. At. Nucl. 57, 1890 (1994)];

[2] Kukulin V.I., Vorontchev V.T., Pomerantsev V.N. Three body calculations of A=9 nuclei with super-symmetric $\alpha\alpha$ -potentials // Few-Body Syst. - 1995. - Vol. 18. - P. 191-202.

[3] Clikeman F.M., Bureau A.J., Steart M.G. Photoproton reaction in Be^9 // Phys. Rev. C. - 1962. - Vol. 126, № 5. - P. 1822-1825.

[4] Kukulin V.I., Krasnopol'sky V.M., Voronchev V.T., Sazonov P.B. Detailed study of the cluster structure of light nuclei in a three-body model: (I). Ground state of ^{6}Li // Nucl. Phys. A. - 1984. - Vol. 417. - P. 128-156.
[5] Kukulin V.I., Voronchev V.T., Kaipov T.D., Eramzhyan R.A. Detailed study of the cluster structure of light nuclei in a three-body model: (III). Electromagnetic structure of ^{6}Li // Nucl. Phys. A. - 1990. - Vol. 517. - P. 221-263.

Труды XII Международного семинара
по электромагнитным взаимодействиям ядер
ЭМИН-2009

Ф-т 60x84/8. Уч.-изд.л 14,0 Печ.л. 20,5 Зак. № 22066 Тираж 70 экз. Бесплатно

Отпечатано на компьютерной издательской системес электронной версии,
предоставленной авторами и редколлегией

Учреждение Российской академии наук
Институт ядерных исследований

Издательский отдел
117312, Москва, проспект 60-летия Октября, 7а